ADVANCED IMAGING AND ARTIFICIAL INTELLIGENCE FOR DIAGNOSTIC AND PROGNOSTIC BIOMARKERS IN GLIOBLASTOMA

by

MARKAND DIPANKUMAR PATEL

A thesis submitted to the University of Birmingham for the degree of

DOCTOR OF PHILOSOPHY

Institute of Cancer and Genomic Sciences

College of Medical and Dental Sciences

University of Birmingham

October 2021

Abstract

Conventional magnetic resonance imaging (MRI) has a pivotal role in diagnosis and post-treatment management of glioblastoma, however it has limitations. This work investigates the use of advanced MRI techniques that assess the tumour microenvironment, and artificial intelligence (AI) techniques that compute quantitative features, as potential imaging biomarkers in key clinical issues faced by clinicians, through several retrospective studies. Results show that advanced multiparametric MRI is superior to current standard-of-care imaging for the diagnosis of glioblastoma, and in treatment response assessment. Results of AI techniques on pre-operative imaging show the ability to differentiate between glioblastoma and metastasis with an accuracy of 88.7%, prediction of overall survival with a high level of accuracy, and stratification of patients into high- and low-level groups of MGMT promoter methylation with accuracies between 45-67%. In the early post-treatment phase, AI analysis of imaging can distinguish between disease progression and pseudoprogression with an accuracy of 73.7%, compared to neuroradiologist accuracy of 32.9%. Integrating these techniques into routine clinical practice is essential to improve patient outcomes. Further work is required to validate advanced imaging and AI biomarkers, towards the longer-term goal of using these as clinical decision support tools, to benefit patients with glioblastoma and other brain tumours.

Dedicated to my gurus

His Holiness Pramukh Swami Maharaj

and

His Holiness Mahant Swami Maharaj

"*In the joy of others, lies our own.*

In the progress of others, rests our own.

In the good of others, abides our own."

- His Holiness Pramukh Swami Maharaj

Acknowledgements

I would like to sincerely thank my research supervisors Professor Vijay Sawlani and Professor Andrew Peet who have always been available, for their encouragement, tireless support and guidance. I also appreciate the time given by individual patients and carers who reviewed the study proposal and provided comments through the Brain Tumour Charity's Research Involvement Network, which were extremely positive and encouraging.

This work would not have been possible without the fantastic opportunity and funding I received to undertake the Institute of Translational Medicine starter fellowship and the ongoing support from Birmingham Health Partners. I would also like to thank Mike Hammond, Chief Executive of Queen Elizabeth Hospital Birmingham (QEHB) Charity for logistic support, public and patient involvement in artificial intelligence research, and funding for the PhD fellowship. I would also like to acknowledge Professor Simon Ball, Executive Medical Director and Hilary Fanning, Director of Research Development and Innovation at University Hospitals Birmingham NHS Foundation Trust, for facilitating this research.

I am grateful to the Microsoft Project InnerEye team in particular to Kenji Takeda, Antonio Criminisi, Anton Schwaighofer and Raj Jena of Microsoft Research, Cambridge, for their collaboration, infrastructure, and support, which has been central to the work. I would also like to thank Professor Vinay Duddalwar from the University of Southern California Radiomics Lab, who has provided me with direction and guidance whilst planning and during this work.

I am also grateful to all the clinicians at QEHB in Clinical Oncology, Neurosurgery and Pathology who make up the Neuro-Oncology multi-disciplinary team and have given their support and guidance, particularly Dr Paul Sanghera, Dr Helen Benghiat, Dr Sara Meade, Professor Colin Watts, Professor Garth Cruickshank, Mr Ismail Ughratdar, Miss Victoria Wykes, Dr Ute Pohl and Dr Santhosh Nagaraju. In addition to this, members of the Medical Physics, Clinical Computing, and Imaging teams at QEHB have facilitated the work, providing invaluable support and infrastructure setup, in particular to Kal Natarajan, Nigel Davies, Robert Flintham, Roman Wesolowski, and Jane Herbert.

I have learned a great deal about machine learning from Dr Jinfeng Zhan and Dr Yiping Lu, Jo-Li Fellows in Neuroradiology at QEHB, who attended from The Affiliated Hospital of Qingdao University and Huashan Hospital Fudan University, China, respectively, and would like to sincerely thank them for their invaluable training and support with this work. Members of Professor Andrew Peet's Brain Tumour Research Group have also provided support and feedback, for which I am extremely grateful, in particular to James Grist, Chris Bennett, Heather Rose, Dadi Zhao, Sonal Nandanwar, Rebecca Sawbridge and Lara Worthington. I would also like to thank Marie Kershaw for her help as a medical student.

Lastly, I would like to thank my family; my parents Dipan and Harsha, my brother Kirtan, my grandparents, as well as my extended family, who I am very grateful for and have all supported me through this journey.

Funding

Funding received from Birmingham Health Partners for the Institute of Translational Medicine starter fellowship (February 2017, post reference number 57866). This work was supported by an equipment grant from the University of Birmingham as part of the College of Medical and Dental Sciences Research Development Fund preliminary data award grant (January 2018). Funding was also received for a PhD fellowship from QEHB Charity (August 2018, grant number 16-5-836).

Contribution to publications

I have widely researched and contributed significantly to the publications related to my thesis topic and in the field of brain tumours. I was first author for the publication "Machine learning-based radiomic evaluation of treatment response prediction in glioblastoma" (*Clinical Radiology*, 2021); Chapter 7 is an adapted version of this publication.

I was co-first author for the publication "Machine learning-based radiomic, clinical and semantic feature analysis for predicting overall survival and MGMT promoter methylation status in patients with glioblastoma" (*Magnetic Resonance Imaging*, 2021); I have contributed substantially to data collection, analysis, setting up the radiomics analysis and machine learning pipeline and writing the paper. Chapter 5 is an adapted version of this publication.

I was second author and contributed significantly to writing, data collection, analysis and image curation for the publication "Multiparametric MRI: practical approach and pictorial review of a useful tool in the evaluation of brain tumours and tumour-like lesions" (*Insights into Imaging*, 2020); I have reviewed more than 1000 cases of multiparametric MRI with my supervisor and contributed to writing this extensive review. Parts of Chapter 3 and some images from Chapter 6 are adapted from this publication.

I was second author and contributed significantly to writing, data collection, analysis and image curation for the review article publication "Role of postoperative imaging in neuro-oncology" (*International Journal of Neuro-oncology*, 2021); there are only two authors on this publication, and I have made a substantial contribution to this publication. Sections 2.9 and 2.10 of Chapter 2 are adapted from this publication.

List of Achievements

Below is the list of achievements during the course of the PhD.

Journal publications

Patel M, Zhan J, Natarajan K, Flintham R, Davies N, Sanghera P, Grist J, Duddalwar V, Peet A, Sawlani V (2021) **Machine learning-based radiomic evaluation of treatment response prediction in glioblastoma**. *Clin Radiol* 76:628.e17-628.e27.

Sawlani V, Patel M (2021) **Role of postoperative imaging in neuro-oncology**. *Int J Neurooncol* 4(3):30.

Sawlani V, Scotton S, Nader K, Jen JP, Patel M, Gokani K, Denno P, Thaller M, Englezou C, Janjua U, Bowen M, Hoskote C, Veenith T, Hassan-Smith G, Jacob S (2021) **COVID-19-related intracranial imaging findings: a large single-centre experience**. *Clin Radiol* 76:108.

Lu Y, Patel M, (Co-first author) Natarajan K, Ughratdar I, Sanghera P, Jena R, Watts C, Sawlani V (2020) **Machine learning-based radiomic, clinical and semantic feature analysis for predicting overall survival and MGMT promoter methylation status in patients with glioblastoma**. *Magn Reson Imaging* 74:161–170.

Sawlani V, Patel MD, Davies N, Flintham R, Wesolowski R, Ughratdar I, Pohl U, Nagaraju S, Petrik V, Kay A, Jacob S, Sanghera P, Wykes V, Watts C, Poptani H (2020)

Multiparametric MRI: practical approach and pictorial review of a useful tool in the evaluation of brain tumours and tumour-like lesions. *Insights Imaging* 11:84.

Sawlani V, Davies N, Patel M, Flintham R, Fong C, Heyes G, Cruickshank G, Steven N, Peet A, Hartley A, Benghiat H, Meade S, Sanghera P (2019) Evaluation of Response to Stereotactic Radiosurgery in Brain Metastases Using Multiparametric Magnetic Resonance Imaging and a Review of the Literature. *Clin Oncol* 31:41–49.

Sawlani V, Patel M (2019) Three-dimensional double inversion recovery magnetic resonance sequence detects perilesional gliosis better than 3D-FLAIR and postcontrast T1 imaging in calcified neurocysticercosis. *Neurol India* 67:74–75.

Patel M, Sawlani V (2017) Can arterial spin labelling really replace dynamic susceptibility contrast perfusion techniques for assessing brain tumours in clinical practice? *Neurol India* 65:977–978.

Invited talks

- Royal College of Radiologists (RCR) Annual Conference, Liverpool, October 2019

  Patel M, Zhan J, Natarajan K, Flintham R, Davies N, Sanghera P, Grist J, Cruickshank G, Ughratdar I, Duddalwar V, Schwaighofer A, Peet A, Sawlani V. AI for glioblastoma treatment response in the session: 'Artificial Intelligence (AI) and its impact on imaging'.

Conference presentations (oral)

- British Neuro-Oncology Society (BNOS) Annual Meeting, Birmingham, July 2021

  Patel M, Zhan J, Natarajan K, Flintham R, Davies N, Sanghera P, Grist J, Duddalwar V, Peet A, Sawlani V. **Artificial intelligence for early prediction of treatment response in glioblastoma.**

  Patel M, Rajapakse D, Jen JP, Meade S, Benghiat H, Hartley A, Petrik V, Ughratdar I, Watts, C, Sanghera P, Ramalingam S, Sawlani V. **Delayed contrast and multiparametric MRI for treatment response assessment in brain metastases following stereotactic radiosurgery.**

  Jen JP, Patel M, Bowen M, Pohl U, Nagaraju S, Wykes V, Watts C, Sawlani V. **T2-FLAIR mismatch sign for diagnosis of 1p19q non-codeleted or ATRX mutant astrocytoma.**

- British Society of Neuroradiologists (BSNR) Annual Meeting, Cardiff, October 2019.

  Patel M, Bowen M, Nagaraju S, Pohl U, Davies N, Flintham R, Wesolowski R, Kennedy J, Herbert J, Zisakis A, Kay A, Ughratdar I, Watts C, Sawlani V. **Early detection of malignant transformation in non-enhancing low-grade gliomas using multiparametric MRI.**

  Lu Y, Patel M, Schwaighofer A, Natarajan K, Sanghera P, Jena R, Watts C, Sawlani V. **Machine learning-based radiomic, clinical and semantic feature analysis for predicting methylation status and overall survival in glioblastoma.**

- Royal College of Radiologists (RCR) and British Institute of Radiology (BIR), 'Artificial Intelligence in 2019: Where we are now?' Meeting, London, March 2019.

  Patel M, Zhan J, Natarajan K, Flintham R, Davies N, Sanghera P, Cruickshank G, Ughratdar I, Peet A, Sawlani V. **Radiomics and machine learning in glioblastoma: predicting treatment response.**

- British Neuro-Oncology Society (BNOS) Annual Meeting, Winchester, July 2018

  Patel M, Zhan J, Natarajan K, Flintham R, Davies N, Sanghera P, Cruickshank G, Ughratdar I, Duddalwar V, Sawlani V. **Radiomic evaluation of treatment response in patients with glioblastoma: a pilot study.**

Conference presentations (poster)

- British Society of Neuroradiologists (BSNR) Annual Meeting, Cardiff, October 2019.

  Sawlani V, Grist J, Patel M, Flintham R, Herbert J, Harley M, Davies N. **Overcoming challenges in adopting magnetic resonance spectroscopy into routine clinical practice.**

- American Society of Neuroradiology (ASNR) Annual Meeting, Boston, May 2019.

  Bowen M, Patel M, Butler B, Murphy J, Herbert J, Davies N, Flintham R, Harley M, Moussa A, Ughratdar I, Sawlani V. **Multiparametric MRI assessment of lesions affecting the corpus callosum.**

- Post-graduate British Chapter of ISMRM (PG BC-ISMRM) Symposium, Birmingham, April 2019).

Sawlani V, Grist J, Patel M, Flintham R, Wesolowski R, Herbert J, Harley M, Davies N. **Overcoming challenges for adopting magnetic resonance spectroscopy into routine clinical practice.**

- European Congress of Radiology (ECR), Vienna, February 2019.

  Patel M, Zhan J, Natarajan K, Flintham R, Davies N, Sanghera P, Peet A, Duddalwar V, Sawlani V. **Radiomic evaluation of treatment response in patients with glioblastoma: a preliminary study.**

  Patel MD, Sawlani V. **How to perform radiomic studies in the clinical setting taking imaging and biological factors into account.**

  Harley M, Patel MD, Bowen M, Muhammad W, Jacob S, Douglas M, Ughratdar I, Herbert J, Sawlani V. **Role of Multiparametric MRI in brainstem lesions.**

- Joint Irish/British Society of Neuroradiologists (ISNR/BSNR) Annual Meeting, Dublin, October 2018).

  Patel M, Sawlani V. **How to perform radiomic and radiogenomic studies in the clinical setting taking imaging and biological factors into account**.

  Patel M, Bhatt N, Sawlani V. **Big Data and AI: Should we be concerned about patient identification from MRI head scans?**

Butler B, White D, Patel M, Muhammad W, Hayton T, Ramalingam S, Jacob S, Sawlani V. **Autoimmune glial fibrillary acidic protein (GFAP) astrocytopathy presenting as meningoencephalomyelitis: A review of two cases from the UK.**

Bowen M, Sadiq N, Fazal J, Muhammad W, Patel M, Jacob S, Sawlani V. **Bickerstaff's brainstem encephalitis - part of anti-GQ1b spectrum disorder: Imaging review of an overlooked diagnosis**.

Awards

- **Commendation for oral presentation** "Artificial Intelligence in Brain Tumour Imaging: Predicting Treatment Response", Institute of Cancer and Genomic Sciences Research Festival, University of Birmingham (2019)

- **Travel bursary for European Congress of Radiology** to present "Radiomic evaluation of treatment response in patients with glioblastoma: a preliminary study", Royal College of Radiologists (2019)

- **First prize for scientific poster presentation** "Radiomic evaluation of treatment response in patients with glioblastoma: a pilot study", British Neuro-Oncology Society (2018)

- **Sankey runner-up research prize for oral presentation** "Artificial intelligence in brain tumour imaging: predicting treatment response – pilot study", University Hospitals Birmingham NHS Foundation Trust Grand Round (2018)

Table of Contents

List of illustrations

List of tables

List of common abbreviations

ADC	Apparent diffusion coefficient
AI	Artificial intelligence
CE-T1WI	Contrast-enhanced T1-weighted imaging
Cho/Cr	Choline/Creatine
CT	Computerised tomography
DWI	Diffusion-weighted imaging
IDH	Isocitrate dehydrogenase
MGMT	O^6-methylguanine DNA methyltransferase
MRI	Magnetic resonance imaging
MRS	Magnetic resonance spectroscopy
OS	Overall survival
psPD	Pseudoprogression
PWI	Perfusion-weighted imaging
rCBV	Relative cerebral blood volume
tPD	True progression

1. INTRODUCTION

1.1 Motivation

I have been fascinated by imaging for many years; more than 15 years ago, I wrote a report on medical imaging during my A-levels. At medical school, this curiosity led me to undertake an intercalated BSc in radiological sciences with a project in diffusion tensor imaging, an advanced neuroimaging technique. The collaborative approach between scientists, physicists, mathematicians, and clinicians was valuable, each offering unique perspectives towards a unified goal. During my core training as a specialty registrar in clinical radiology, naturally, I gravitated towards neuroimaging, and spent time in the neuroradiology department at the Queen Elizabeth Hospital Birmingham, and started working with my current supervisor, Professor Vijay Sawlani, to assess the role of advanced neuroimaging techniques in inflammatory conditions of the brain. I attended various neuroradiology multi-disciplinary team (MDT) meetings, which gave me a clearer insight into the key clinical issues faced by clinicians, and this also highlighted the limitations of current imaging techniques, which can greatly impact patient care. These were largely uncertainties surrounding diagnosis and post-treatment imaging. One of the most important issues I witnessed on numerous occasions was the uncertainty around differentiating treatment-related changes from tumour progression in patients who had undergone treatment for brain tumours. My supervisor had previous experience in using advanced magnetic resonance imaging (MRI) in this field; I was fortunate to have his expertise and guidance, as well as being at one of the largest centres for treating

brain tumours in the UK, and now a Tessa Jowell Centre of Excellence for brain tumours. We decided to investigate further, and I put forward a PhD proposal to look into the use of advanced MRI techniques to better assess glioblastoma treatment response, trying to keep a clinical focus and provide solutions that are directly relevant in practice. During the planning phase of the project in 2017, I came across the early use of artificial intelligence (AI) in healthcare, for example the use of radiomic texture analysis and machine learning to predict whether similar appearing lung nodules on imaging would remain stable or become malignant over time. I realised that this could potentially be applied to imaging of glioblastoma, as treatment-related changes and tumour progression appeared similar on imaging yet are distinct pathologies with very different outcomes. This led me to widen the scope of my research to also incorporate and investigate the use of AI techniques as well as advanced imaging in this PhD project, for their role in the diagnosis and prognostication of patients with glioblastoma, whilst maintaining a strong focus on clinically relevant research.

1.2 Aim

The aim is to further the understanding of advanced imaging and AI techniques to identify more accurate, predictive, and clinically relevant imaging biomarkers in neuro-oncology, towards the longer-term goal of using these as validated clinical decision support tools to benefit patients with glioblastoma and other brain tumours.

1.3 Thesis structure and objectives

Chapter 2: Glioblastoma

This chapter provides a background to glioblastoma, the diagnostic features clinically, on conventional imaging, and on histopathology, followed by the recent 2021 updates to the World Health Organisation integrated diagnostic criteria. The role of imaging throughout the patient pathway is presented, and a brief overview of current treatment strategies as well as experimental approaches to diagnostics and therapeutics is highlighted.

Chapter 3: Advanced imaging in the diagnosis of glioblastoma

A clinical challenge faced by radiologists is differentiating between various brain tumours and other non-tumoural lesions. This chapter provides a review of the role of advanced MRI techniques for the diagnosis of glioblastoma and differentiating it from other intracranial lesions including neoplastic, infective, inflammatory, and vascular-related lesions which can mimic its appearances on conventional imaging.

Chapter 4: Machine learning-based radiomic analysis for distinguishing between glioblastoma and metastasis

One of the most frequently observed clinical issues is differentiating between glioblastoma and a single brain metastasis on conventional MRI. In this chapter, a study is presented to investigate the use of machine learning and quantitative radiomic features to distinguish between glioblastoma and brain metastasis on conventional imaging. It also introduces

artificial intelligence techniques and the process involved in machine and deep learning studies.

Chapter 5: Machine learning-based radiomic evaluation of pre-operative imaging for prediction of MGMT methylation promoter status and overall survival

With the growing role of molecular markers in tumour classification, survival prediction and treatment strategies, imaging biomarkers that can accurately reflect molecular markers of tumours could provide a 'virtual biopsy' of lesions. This chapter provides a study investigating machine learning with a combination of sub-regional radiomic features and clinical features to predict O^6-methylguanine-DNA methyltransferase (MGMT) promotor methylation status in glioblastoma, from conventional pre-operative imaging and also the combination of all features including MGMT promotor methylation status through machine learning to predict overall survival.

Chapter 6: Advanced MRI techniques for early prediction of treatment response

The use of advanced MRI techniques have been suggested for treatment response assessment in the latest brain tumour guidelines published by the National Institute for Health and Care Excellence (NICE). This chapter provides a study to evaluate the utility of advanced MRI techniques using diffusion-weighted imaging (DWI), perfusion-weighted imaging (PWI) and magnetic resonance spectroscopy (MRS) in clinical practice for assessing treatment response in patients with glioblastoma.

Chapter 7: Machine learning-based radiomic evaluation of early treatment response prediction

This chapter provides a study investigating the use of machine learning with sub-regional quantitative radiomic features from conventional imaging and DWI in combination with clinical features and MGMT promotor methylation status to predict treatment response assessment in patients with glioblastoma.

Chapter 8: Conclusions

Finally, a summary of the work, its clinical relevance and suggestions for future work are presented.

1.4 Patient and carer opinions

In December 2017, during the design of this research, I approached the Brain Tumour Charity and provided a research proposal summary. This was reviewed by the Brain Tumour Charity's research team and sent to patients and carers within their Research Involvement Network for feedback and comments. There were 13 responses, of which 77% strongly agreed that the research was worth pursuing, and the remaining 23% agreed that the research was worth pursuing. Feedback was used to improve the study design, and individual comments from patients and carers are provided below:

- “Pseudoprogression was one of the main sources of anxiety for my family during the treatment – definitely a relevant topic.”
- “Really liking the radiomics sounds superb. If it closes or narrows the window of uncertainty and gives more clarity around growth and treatment will be a god send.”
- “I have concerns that the process will be too machine led. There needs to be a certain amount of human lead work.”
- “Really good to see progression in this area. One of the most frustrating periods is scan time, and the difficulties then faced as doctors are unable to tell the difference re true tumour progression or not is significant.”
- “I am aware of the problems posed by the current inaccuracy of MRI scans soon after surgery.”
- “Whereas this seems highly promising, we must continue to recognise the ineffectiveness of current treatments.”
- “This study will be very useful.”
- “This seems like a fantastic use for AI and could be something with a fairly quick turnaround.”
- “Anything to help diagnosis is surely worthwhile.”
- “It seems the validity for the research will be gained early as it will involve retrospective scans and if it works it is a big thumbs up for AI and brain tumours.”
- “This was one of the clearest and best worded summary document I've read as part of the research involvement network.”

2. GLIOBLASTOMA

Parts of this chapter (Sections 2.9 and 2.10) are adapted from [1], previously published by *International Journal of Neuro-oncology* (licensed under CC BY-NC-SA 4.0).

2.1 Epidemiology

2.1.1 Central nervous system tumours

The Office for National statistics recorded 9,737 new cases of primary tumours affecting the central nervous system (CNS) in England in 2017 [2]. A breakdown of the type and sites of tumours are shown in Table 1 and a breakdown of the number of cases by age group and sex is shown in Figure 1. There is a peak incidence between the 65-to-74-year age groups, and there is largely similar proportion of males and females affected.

Type and site of tumours	Number of cases
Malignant neoplasm of brain	4,568
Benign neoplasm of meninges	2,443
Benign neoplasm of brain and other parts of CNS	953
Benign neoplasm of pituitary gland	822
Neoplasm of uncertain or unknown behaviour of brain and CNS	475
Neoplasm of uncertain or unknown behaviour of meninges	272
Malignant neoplasm of spinal cord, cranial nerves and other parts of CNS	141
Malignant neoplasm of meninges	60
Benign neoplasm of pineal gland	3

Table 1. Registrations of newly diagnosed cases of CNS neoplasm by type in England in 2017.

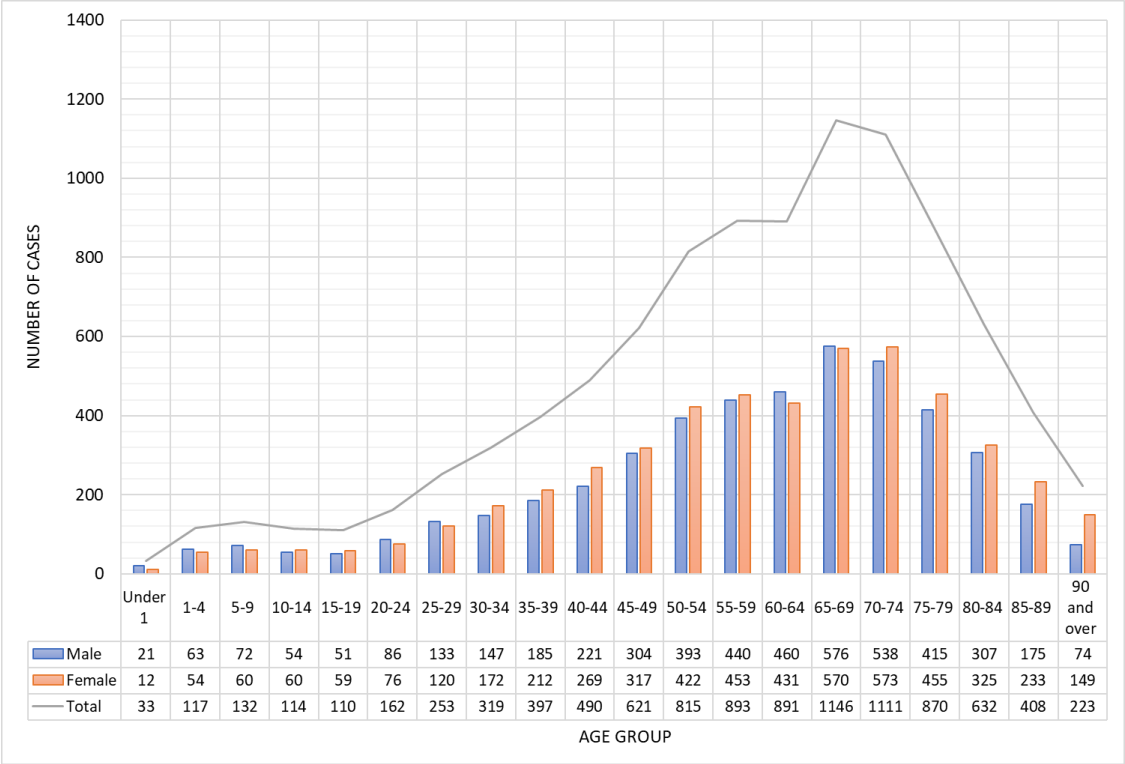

	Under 1	1-4	5-9	10-14	15-19	20-24	25-29	30-34	35-39	40-44	45-49	50-54	55-59	60-64	65-69	70-74	75-79	80-84	85-89	90 and over
Male	21	63	72	54	51	86	133	147	185	221	304	393	440	460	576	538	415	307	175	74
Female	12	54	60	60	59	76	120	172	212	269	317	422	453	431	570	573	455	325	233	149
Total	33	117	132	114	110	162	253	319	397	490	621	815	893	891	1146	1111	870	632	408	223

Figure 1. Number of new central nervous system tumour cases by age group and sex in England in 2017.

2.1.2 Malignant primary brain tumours

Malignant primary tumours of the brain make up the highest group of cases of all CNS tumours, at a proportion of 47%, or 4,568 new cases in 2017. A breakdown of the number of cases by age group and sex is shown in **Figure 2**. The peak incidence of cases is between the ages of 65 and 74, with a greater proportion of males affected than females (ratio 1.4:1).

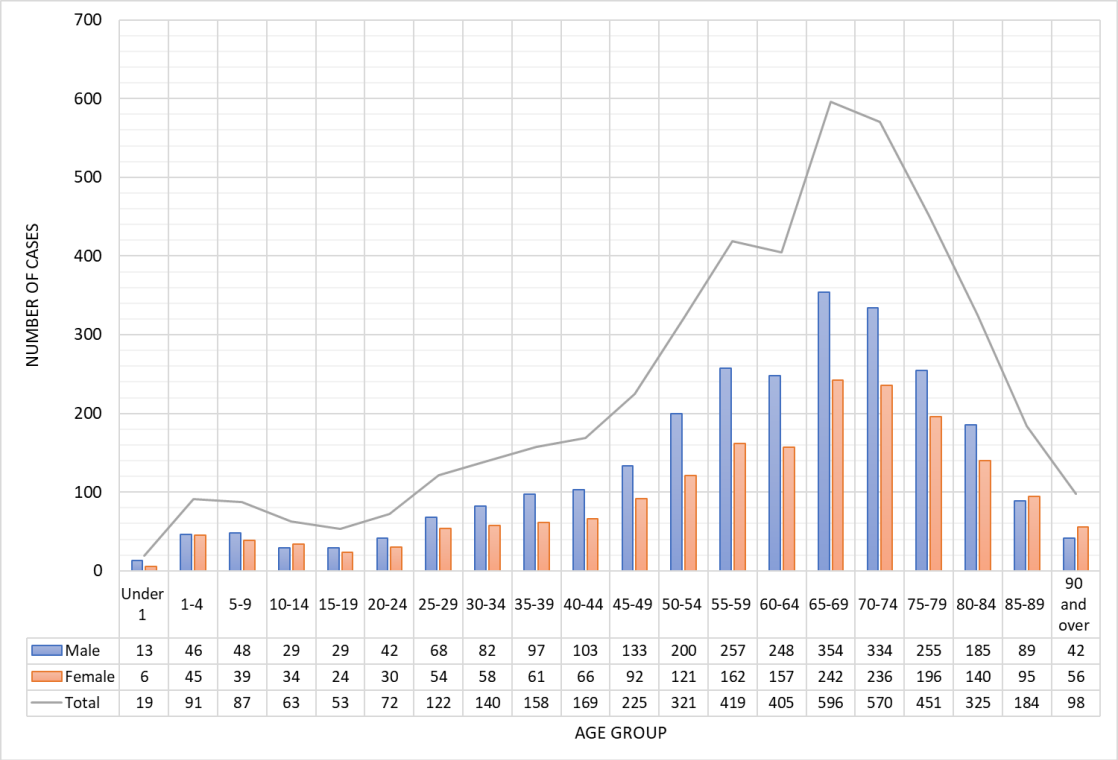

	Under 1	1-4	5-9	10-14	15-19	20-24	25-29	30-34	35-39	40-44	45-49	50-54	55-59	60-64	65-69	70-74	75-79	80-84	85-89	90 and over
Male	13	46	48	29	29	42	68	82	97	103	133	200	257	248	354	334	255	185	89	42
Female	6	45	39	34	24	30	54	58	61	66	92	121	162	157	242	236	196	140	95	56
Total	19	91	87	63	53	72	122	140	158	169	225	321	419	405	596	570	451	325	184	98

Figure 2. Number of new malignant tumour cases of the brain by age group and sex in England in 2017.

2.1.3 Glioblastoma

Glioblastoma is the most common malignant primary brain tumour. Approximately 55% of malignant brain tumours are glioblastoma [3], equating to more than 2,500 new cases per year and an age standardised incidence of 5 per 100,000 per year in England [4]. The incidence rate has more than doubled between 1995 and 2015, with a percentage rise similar across all age groups, suggesting environmental or lifestyle factors may be contributing to this increase [5]. Until recently, glioblastoma had been classified as “primary glioblastoma”, seen in about 90% of patients as *de novo* development of the disease, without any evidence of a precursor lesion and a mean age at diagnosis of 62 years [6]. The remaining 10% of patients were categorised as “secondary glioblastoma” from a precursor diffuse astrocytoma or

anaplastic astrocytoma, and are usually younger at time of presentation with the mean age of 44 years and better prognosis [6]. However, there has since been a shift in classification based on genetic markers, which will be detailed ahead in Section 2.5.

2.2 Causal and risk factors

High-dose ionising radiation has been associated with an increased incidence of all brain tumours and an established risk factor for developing glioblastoma [7]. Evidence for this is largely from exposure of the population to atomic bomb irradiation and high-dose radiotherapy. There is no conclusive evidence regarding exposure to medical imaging-related diagnostic radiation, however the cumulative effects of diagnostic exposures from computerised tomography (CT) imaging is of concern, given the increasing incidence of ionising radiation-related medical imaging within the population [8].

The increased incidence of glioblastoma over time may be explained by few possible factors. Long-term exposure to traffic-related air pollution has been associated with the development of glioblastoma in 12 cohorts from six European countries through the European Study of Cohorts for Air Pollution Effects [9]. Increased indoor radon exposure as a result of double-glazed windows and house sealing leading to lower exchange with outside air may also explain the increase in incidence over time [10,11].

In 2011, the International Agency for Research on Cancer classified radiofrequency fields as a possible carcinogen for increasing the risk of glioma in those with a heavy cellular phone use [12]. There has been mixed evidence since this review was published, and no clear association

determined yet, however given the unknown latency period, the risk of non-ionising radiation from cellular phones is still under review [13]. In addition, extremely low frequency electromagnetic fields have raised possible association with glioblastoma, which is also under investigation [14].

There have been inconsistent findings for occupational exposure of chemicals and pesticides for glioblastoma risk, however certain occupations have demonstrated an increase in glioma risk, including butchers, meat cutters, salesperson, record clerk, waitress, farmer and women associated with employment in agriculture, textile, electronics and retail [8].

Monogenic Mendelian disorders such as Lynch syndrome and Li-Fraumeni syndrome have been associated with an increased risk of glioblastoma, but make up only a small proportion of cases, and genome-wide association studies have identified common genetic variations in seven genes for glioma risk [8]. There is also some evidence linking mitochondrial dysfunction and metabolic disease to drive genetic changes and increased risk of glioma formation [5].

There is also some evidence for potential viral triggers such as cytomegalovirus as a causative factor for development of glioblastoma [15,16]. A large meta-analysis has shown that a history of allergies or atopic disease appears to have a protective effect against developing glioblastoma, with a reduced risk of almost 40% [17].

2.3 Clinical presentation

The majority of patients present with a short history of symptoms, usually between 3-6 months in duration [7]. In some patients, symptoms appear acutely, mimicking stroke. In

patients with secondary glioblastoma from low-grade tumour transformation, symptoms can occur over a number of years. The clinical presentation varies depending on the size of the lesion, location, speed of growth and whether or not there are any secondary effects or complications related to the tumour.

Early symptoms are non-specific, and patients may present several times to healthcare services before being referred for investigation. The mean length of clinical symptoms is four months in isocitrate dehydrogenase-wildtype (IDH-wildtype) glioblastoma, formerly known as primary glioblastoma, and 15 months in IDH-mutant glioblastoma, formerly referred to as secondary glioblastoma [6]. Low-grade gliomas that can undergo transformation to glioblastoma are also picked up incidentally on head and neck imaging performed for other reasons.

More than 95% of patients present with glioblastoma in the supratentorial compartment, with the highest incidence in the frontal lobes, followed by multiple overlapping lobes, followed by the temporal lobes, parietal lobes and lastly the occipital lobes [18]. At presentation, 35% of patients with glioblastoma with have multiple lesions [19].

Signs and symptoms from direct involvement of the brain tissue is as a result of necrosis, giving focal neurology in the majority of cases. Tumours involving eloquent areas of the brain will cause symptoms earlier and are diagnosed sooner and as smaller lesions. Parietal lobe location of tumour can cause sensory disturbance, hemineglect and spatial disorientation, whereas tumours involving any part of the optic radiations can cause visual field defects [20]. Seizures are a presenting feature in 22% of patients with glioblastoma, thought to be related

to temporal lobe or cortical location [21,22]. In other areas such as the frontal lobe, temporal lobe or corpus callosum there are often more subtle symptoms such as personality change, mood disorders and short-term memory deficits which can lead to delays in imaging and diagnosis, and consequently tend to be larger lesions when diagnosed [20,22].

In a small number of cases, glioblastoma can occur within the posterior fossa, brainstem, and spinal cord, leading to cerebellar signs, cranial nerve palsy, or long tract signs. Leptomeningeal involvement is rare and usually occurs late in the disease, and distant metastatic disease arising from glioblastoma is also rare [23].

Secondary effects of glioblastoma can include raised intracranial pressure due to large tumour size and associated peritumoural oedema. This can cause mass effect and shift of intracranial contents, typically associated with a dull, unilateral progressive headache which is worse in the early morning or at night, seen as a presenting feature in 30-50% of patients [7,23]. Papilloedema and vomiting are late-stage signs of the raised intracranial pressure and now rarely seen. Obstruction of the ventricular system and associated hydrocephalus is another complication of the mass effect, which will give a similar clinical presentation. Intracranial haemorrhage as a presenting feature of glioblastoma is possible but rare [24].

There are various published red flag symptoms and criteria for imaging referral. Table 2 summarises several important red flag symptoms which warrant rapid referral for investigation, and the recommended guidance in the UK primary care setting for investigating a potential brain tumour is shown in Figure 3. The frequency of reported symptoms in primary care leading up to the diagnosis of a brain tumour is shown in Figure 4.

New, severe or persistent headache, significantly different from previous headaches
Associated fever or other systemic symptoms
New headache in adults, especially those aged over 50 years of age
Headache on exertion, at night or in the early morning
Headache with meningism
Headache with neurological signs
Headache exacerbated by Valsalva manoeuvre
Progressively worsening headache
New headache in the older adults or children

Table 2. Red flag symptoms for brain tumours. (Adapted from [25]).

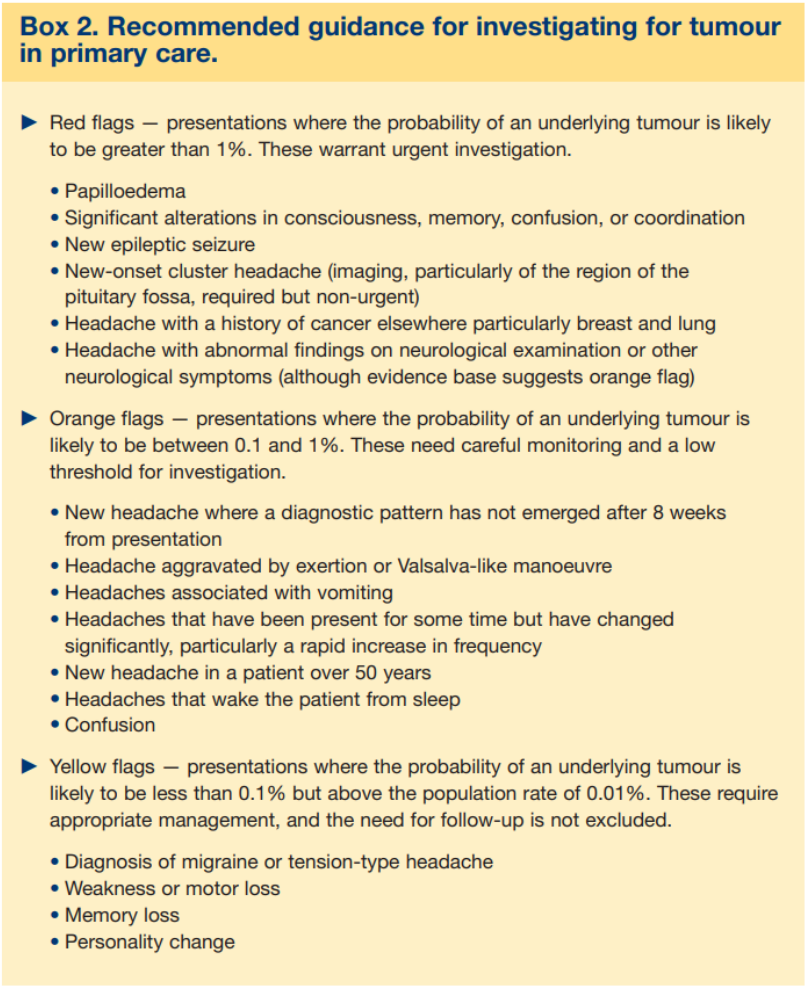

Box 2. Recommended guidance for investigating for tumour in primary care.

- Red flags — presentations where the probability of an underlying tumour is likely to be greater than 1%. These warrant urgent investigation.
  - Papilloedema
  - Significant alterations in consciousness, memory, confusion, or coordination
  - New epileptic seizure
  - New-onset cluster headache (imaging, particularly of the region of the pituitary fossa, required but non-urgent)
  - Headache with a history of cancer elsewhere particularly breast and lung
  - Headache with abnormal findings on neurological examination or other neurological symptoms (although evidence base suggests orange flag)
- Orange flags — presentations where the probability of an underlying tumour is likely to be between 0.1 and 1%. These need careful monitoring and a low threshold for investigation.
  - New headache where a diagnostic pattern has not emerged after 8 weeks from presentation
  - Headache aggravated by exertion or Valsalva-like manoeuvre
  - Headaches associated with vomiting
  - Headaches that have been present for some time but have changed significantly, particularly a rapid increase in frequency
  - New headache in a patient over 50 years
  - Headaches that wake the patient from sleep
  - Confusion
- Yellow flags — presentations where the probability of an underlying tumour is likely to be less than 0.1% but above the population rate of 0.01%. These require appropriate management, and the need for follow-up is not excluded.
  - Diagnosis of migraine or tension-type headache
  - Weakness or motor loss
  - Memory loss
  - Personality change

Figure 3. Recommended guidance for investigating for tumour in primary care. (Reprinted from [26], with permission).

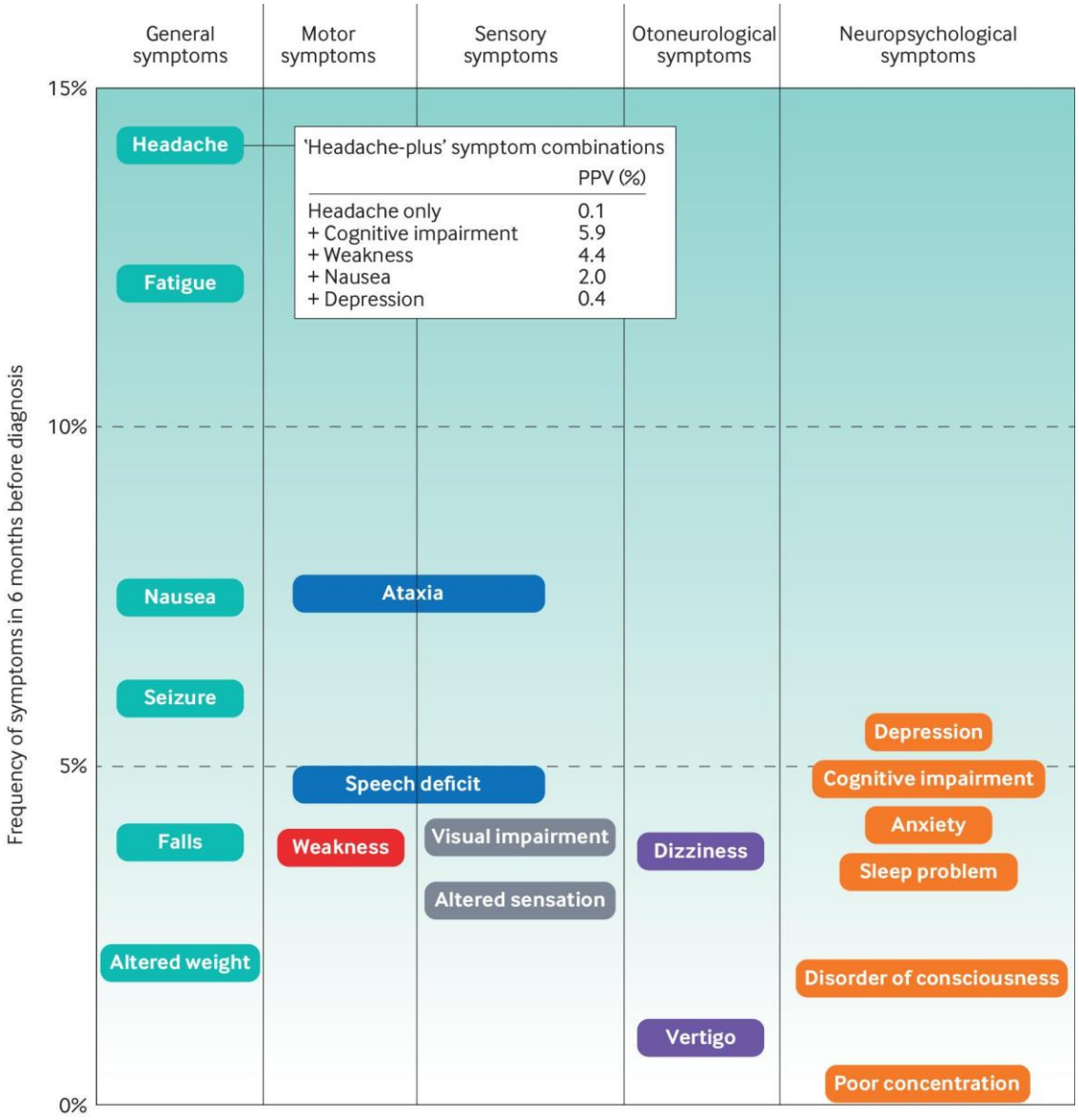

Figure 4. Frequency of symptoms reported to general practitioners in the six months before brain tumour diagnosis. (Reprinted from [27], with permission).

2.4 Diagnosis

2.4.1 Conventional imaging

Depending on the clinical presentation, first-line investigations can involve CT or MRI of the brain. CT is generally performed in acute situations where a patient may have been referred to hospital with focal neurology or seizures and there is concern of acute haemorrhage, acute infarct, hydrocephalus, or when MRI is not available or contraindicated. Contraindications may include the presence of a non-compatible cardiac device, certain implants and metallic foreign bodies within the orbits. MRI of the brain is generally performed in patients with more long-term signs or symptoms or headache with red flag symptoms. According to the current NICE guidelines, the recommended structural imaging for a suspected glioma is MRI with the following sequences unless MRI is contraindicated [28]:

- T2-weighted imaging (T2WI)
- Fluid-attenuation inversion recovery (FLAIR)
- Diffusion-weighted imaging (DWI)
- Pre-contrast T1-weighted imaging (T1WI)
- Contrast-enhanced T1WI (CE-T1WI)

Appearances of glioblastoma on CT is typically that of a mass lesion with central hypodensity which represents the area of necrosis, surrounded by irregular isodense or hyperdense margins, representing the area of cellularity. There is usually associated mass effect and peritumoural vasogenic oedema. Post contrast CT imaging will typically demonstrate intense heterogenous enhancement peripherally (**Figure 5**).

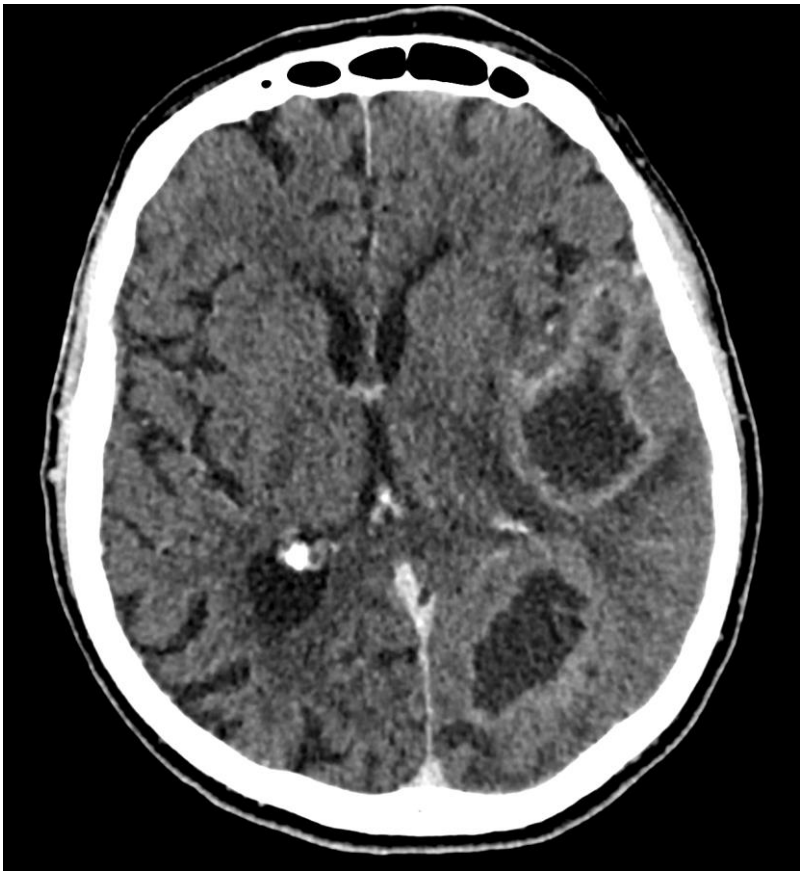

Figure 5. Post-contrast CT appearances of glioblastoma. Large, centrally necrotic areas demonstrating irregular rim enhancement and some surrounding vasogenic oedema.

Similar appearances are seen on MRI (Figure 6), with T2WI/FLAIR hyperintensity representing central necrosis, peripheral irregular and nodular enhancement following gadolinium contrast and T2WI/FLAIR hyperintensities within the surrounding white matter representing surrounding tumour infiltration and vasogenic oedema.

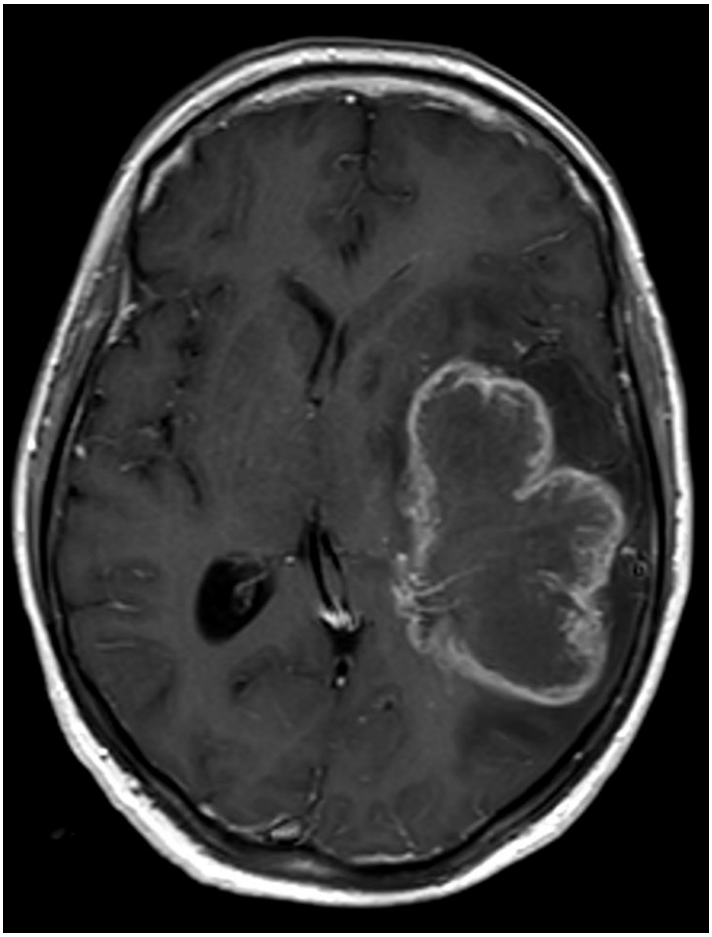

Figure 6. Typical MRI appearances of glioblastoma on CE-T1WI. Large necrotic lesion within the left cerebral hemisphere with mass effect and surrounding vasogenic oedema/infiltration. Central necrosis and irregular peripheral enhancement are demonstrated.

Single lesions are seen in 65% of patients and multiple lesions are seen 35% of patients. Multiple lesions can be categorised into multifocal disease, when there is a clear path of spread, usually through areas of T2WI/FLAIR hyperintensity, which is seen in 87% of patients with multiple lesions. The second is multicentric disease, when there is no clear path of spread, seen in 13% of those with multiple lesions [19].

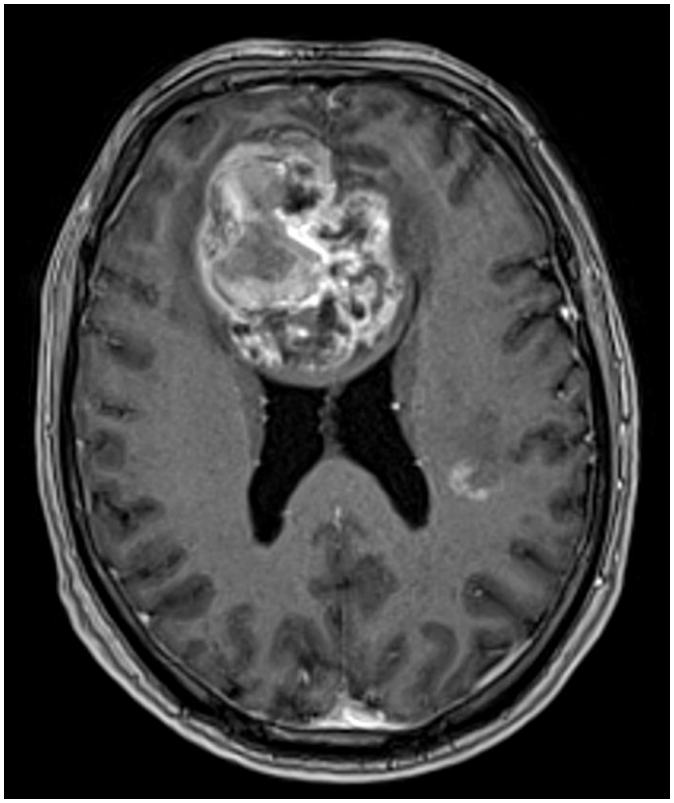

Figure 7. Multicentric disease in glioblastoma. Large necrotic enhancing mass lesion centred on the genu of the corpus callosum. There is a distant enhancing lesion in the left parietal white matter indicating multicentric disease.

Although the typical appearance of glioblastoma is a large necrotic periphery enhancing mass lesion, rarely, in the early stages of the disease the appearances are of a small hyperintense lesion on T2WI with no or poor contrast enhancement, which develops into a more typical mass lesion with necrosis, ring enhancement and peritumoural oedema within a short period of time, reported to be 2.5 to 6 months [29]. Calcification and haemorrhage are rarely seen and is represented by hyperdensity on CT imaging, hyperintensity on pre-contrast T1WI (Figure 8) or susceptibility artefact on T2* or susceptibility-weighted imaging (SWI). On T2*/SWI imaging, a hypointense rim may be seen from blood products, which is irregular and incomplete when present and located inside the peripheral enhancing component [30].

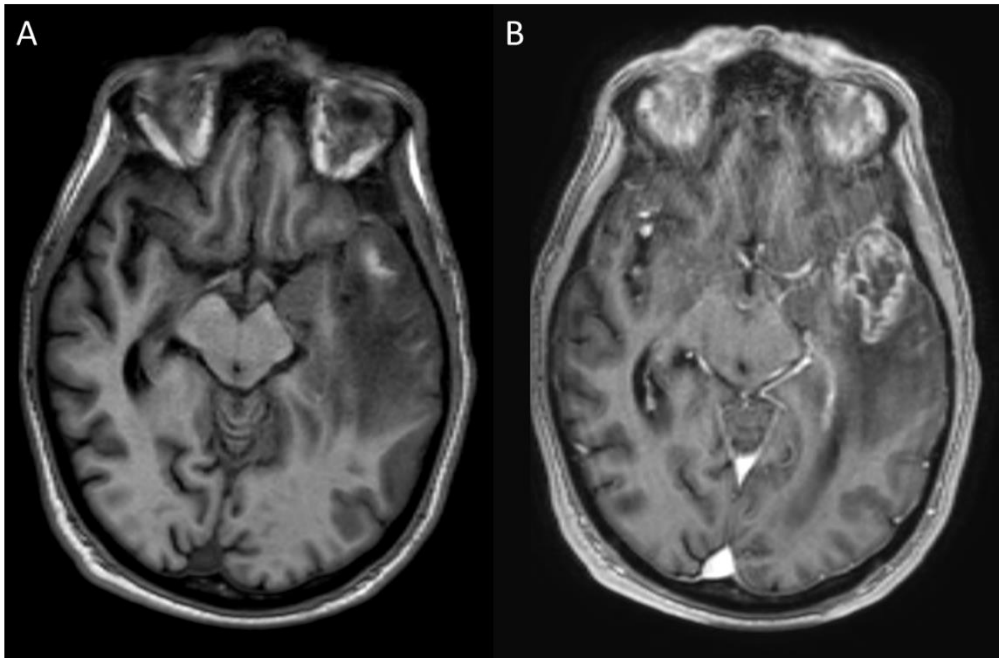

Figure 8. Haemorrhage within glioblastoma. (A) Pre-contrast T1WI showing hyperintensity in the left temporal pole indicating haemorrhage and vasogenic oedema throughout the left temporal lobe. (B) CE-T1WI confirms the haemorrhage to be within an irregular necrotic mass lesion in the left temporal pole.

Previously termed IDH-mutant glioblastoma, usually demonstrates a large bulky non-enhancing lesion with cortical infiltration with a predilection for the frontal and temporal lobes (Figure 9), and only limited peritumoural oedema and necrosis [22]. In a proportion of cases, glioblastoma may not show any contrast enhancement and mimic the appearances of a low-grade lesion [31], which is further detailed in Section 3.3.3.

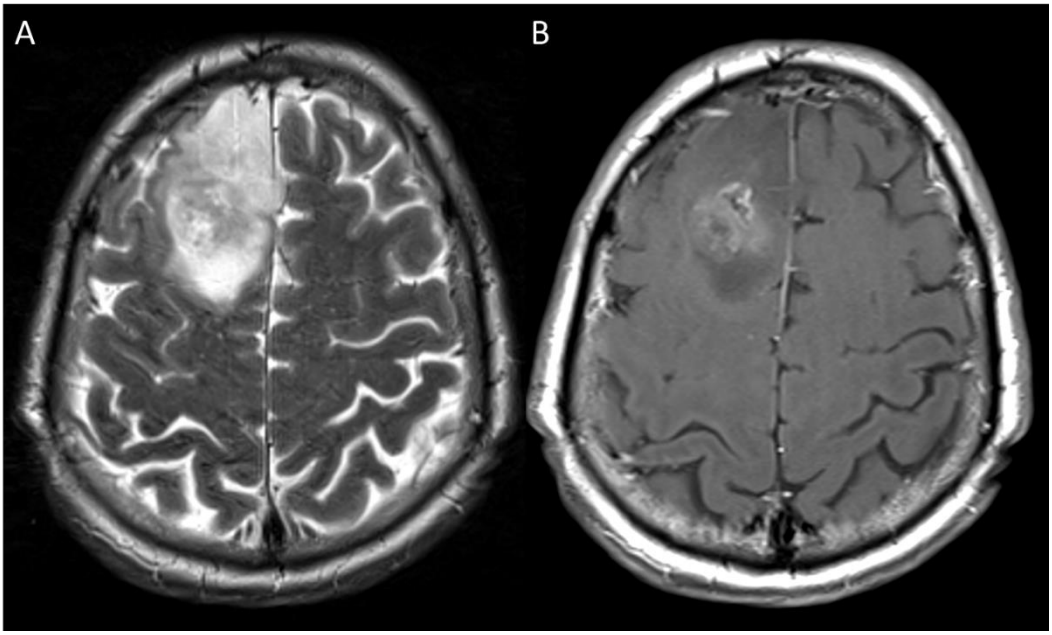

Figure 9. IDH-mutant glioblastoma. (A) Bulky infiltrative right frontal lesion showing predominant high signal on T2WI and central heterogeneous low signal. (B) Faint central patchy enhancement within the area of signal abnormality.

2.4.2 Differential diagnosis

The differential diagnosis for a single or multiple rim-enhancing mass lesions within the brain changes according to the patients age, presence of comorbidities, clinical presentation and differences in imaging characteristics. The main differential diagnoses are between other neoplastic lesions, infections, inflammatory and vascular lesions. In all cases of suspected brain tumours, a CT examination of the thorax, abdomen and pelvis is performed to look for the presence of primary malignancy elsewhere. When body imaging does not provide additional information, distinguishing between the aforementioned intracranial pathological processes are difficult based on conventional imaging alone and therefore additional techniques such advanced imaging can be used. Advanced MRI techniques can be useful when there is a diagnostic dilemma regarding diagnosis, for example when the risk of biopsy

is high due to location of the tumour in an eloquent or deep location, patient co-morbidities or a lesion that mimics another pathology. This is discussed further in Chapter 3, and the use of AI techniques to help address this issue is investigated in Chapter 4.

2.4.3 Histopathology

Currently, tissue samples obtained from surgical resection or biopsy forms the mainstay of diagnosis. Glioblastoma is typically a large, irregular lesion arising from the white matter which is macroscopically heterogenous, containing haemorrhage, necrosis, cystic and gelatinous regions, some of which appear yellow and soft, whereas other areas are white and firm [7]. Microscopically, glioblastoma is an intrinsic lesion that has no distinct brain-tumour interface under microscopy and infiltrates diffusely along vessels and white matter tracts which can be apparently normal on MRI [32]. Microscopy typically gives the cellular morphology of an anaplastic astrocytoma, with pleomorphism, mitotic activity, vascular endothelial cell proliferation and necrosis [22]. In some cases, cellular morphology may represent oligodendroglial or primitive neuroectodermal tumour features [22].

2.4.4 Experimental approaches to diagnosis

Studies have shown that through liquid biopsy of blood plasma, cerebrospinal fluid (CSF) and urine, cell-free circulating tumour deoxyribonucleic acid (DNA) can be obtained. This can be used as a minimally invasive tool for metabolic profiling to identify risk of developing glioblastoma, asymptomatic screening, obtaining a genetic diagnosis of glioblastoma, personalised treatment planning and monitoring response to treatment [33–35]. However,

currently there are no validated liquid biopsy biomarkers for the detection or prognostication of glioblastoma, and in order to translate this promising technology into clinical practice, more sensitive techniques including the integration of multiple biomarkers, standardised approaches, more cost-effective methods and large prospective studies are required [36]. Large-scale pilot screening programmes are being performed worldwide, and commencing within the UK National Health Service (NHS) in 2021 to further investigate blood biomarkers of malignancy using a test targeting key regions of the genome [37,38].

2.5 World Health Organisation classification

2.5.1 2016 classification

Until 2016, the World Health Organisation (WHO) classification of brain tumours was based on morphological appearances of histology on microscopy, though mitoses, microvascular proliferation and necrosis. In 2016, there was an update to the classification of brain tumours, based on a combination of microscopic morphology, as well as molecular and genetic features [39]. The WHO defined three categories for glioblastoma based on IDH status, determined using immunohistochemistry and/or sequencing: [1] glioblastoma IDH-wildtype, [2] glioblastoma IDH-mutant and [3] glioblastoma NOS, which is reserved for diagnosis when IDH evaluation cannot be performed or is inconclusive. The simplified algorithm for diagnosis is shown in **Figure 10** [6].

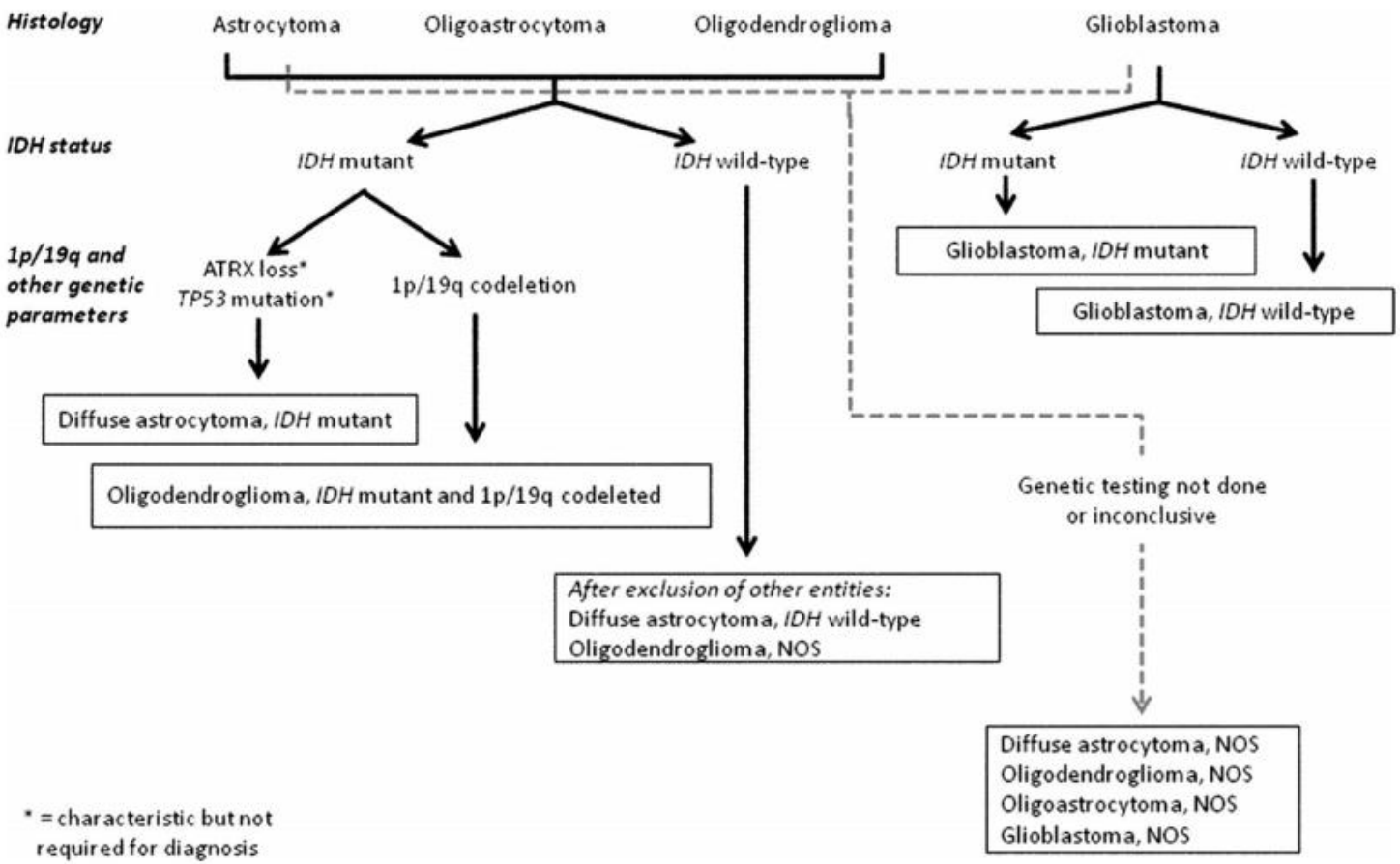

Figure 10. A simplified algorithm for classification of the diffuse gliomas based on histological and genetic features. (Reprinted from [6], with permission).

2.5.2 2021 classification

Since the 2016 WHO classification, there had been multiple proposed interval updates by the Consortium to Inform Molecular and Practical Approaches to CNS Tumor Taxonomy (cIMPACT-NOW) [40]. In May 2021, the changes were incorporated and published in the 5th edition of the WHO Classification of Central Nervous System Tumours [41], and there are several important updates specifically relevant to the classification of glioblastoma. There has now been discontinuation of the term 'Glioblastoma, IDH-mutant', and currently three main distinct entities within the diffuse glioma group:

- Astrocytoma, IDH-mutant
- Oligodendroglioma, IDH-mutant and 1p/19q-codeleted
- Glioblastoma, IDH-wildtype

IDH-mutant diffuse tumours are now considered as 'Astrocytoma, IDH-mutant' and graded between 2-4. Previously, grading was based on histological features alone, however molecular markers provide useful prognostic information and therefore these are now used for grading and combined with histological features to come to an integrated diagnosis [42]. In addition, the presence of a molecular marker even in the absence of specific histological features can enable classification of the tumour. The presence of any of the following would lead to designation of a tumour as 'Astrocytoma, IDH-mutant, WHO grade 4':

- Microvascular proliferation (histological)
- Necrosis (histological)

- Cyclin dependent kinase inhibitor 2 (CDKN2) A/B homozygous deletion (genetic alteration)

The diagnosis of 'Glioblastoma, IDH-wildtype, WHO grade 4' can now made in cases of IDH-wildtype diffuse astrocytic tumours, if there is the presence of at least one of the following histological features, or one of the three genetic alterations being present: [40]

- Microvascular proliferation (histological)
- Necrosis (histological)
- Telomerase reverse transcriptase (TERT) promoter mutation (genetic alteration)
- Epidermal growth factor (EGFR) gene amplification (genetic alteration)
- Both the gain of entire chromosome 7 and loss of entire chromosome 10 (genetic alteration).

Other key biomarkers include O^6-methylguanine DNA methyltransferase (MGMT) promoter methylation, co-deletion of the short arm of chromosome 1 and the long arm of chromosome 19 (1p/19q), and loss of alpha-thalassemia/mental retardation syndrome X-linked (ATRX) gene. The molecular heterogeneity is thought to reflect patient sensitivity to treatment and prognosis, but the overlap of biomarkers complicates assessment of the role of these individual alterations [8,43].

The update also classifies a missense mutation of glycine for arginine or valine at position 34 of the histone H3.3 protein as "Diffuse glioma, H3.3, G34-mutant" [40], and being distinct from IDH-wildtype glioma, IDH-mutant glioma and H3 K27M-mutant diffuse midline glioma.

The mean overall survival (OS) in patients with H3.3 G34-mutant diffuse glioma is longer than that compared to IDH-wildtype glioblastoma, but shorter compared to patients with WHO grade 4 IDH-mutant glioma [44]. A summary of the integrated diagnosis and classification pathway in the 2021 update is shown in **Figure 11**.

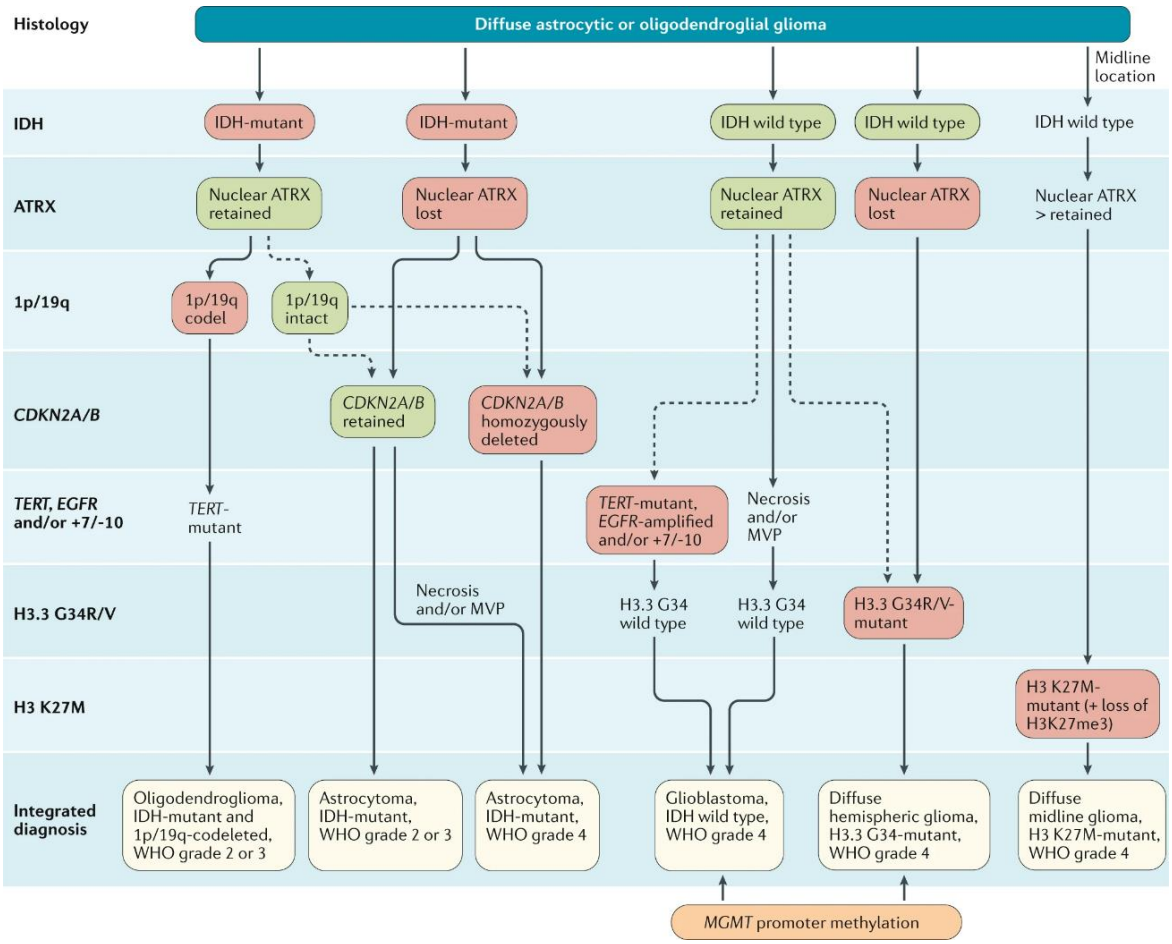

Figure 11. Diagnostic algorithm for the integrated classification of the major diffuse gliomas in adults. (Reprinted from [45], licensed under CC BY 4.0).

2.6 Prognosis

Glioblastoma has the highest average years of life lost per patient for any cancer, at just over 20 years [46]. More than two thirds of patients will die within two years of diagnosis [47], and only about 5% of patients survive beyond five years [20]. Patients with single lesions have a greater mean OS compared to patients with multiple (multifocal/multicentric) lesions, at 18 months and 10 months respectively [19]. Patients with multicentric lesions have the worst prognosis, with a mean OS of three months [19].

2.7 Molecular biomarkers

There is an array of molecular markers associated with glioma, however the three most reliable and reproducible predictive markers include IDH mutations, MGMT promoter methylation, and 1p/19q co-deletion. Patients who are triple-positive have a much more favourable prognosis than those who are in the triple-negative group [48]. There are also a number of other molecular biomarkers and emerging biomarkers which have been less studied, and the clinical impact is less clear. An understanding of the relationship between mutations and tumour characteristics is important for moving towards personalised treatment for patients with glioblastoma.

2.7.1 IDH

Somatic mutations in IDH 1/2 occur at arginine residues, at codon 132 of IDH1 and at codon 172 of IDH2 [43]. The IDH1 and IDH2 mutations affect tumour metabolism, encouraging the reduction of α-ketoglutarate to 2-hydroxyglutarate (2-HG) [49], leading to a genome-wide

glioma cytosine–phosphate–guanine island methylator phenotype (G-CIMP), hypermethylation at a large number of loci, and is predictive of better response to chemotherapy [8]. IDH-mutant tumours also have lower levels of hypoxia-inducible factor 1α and lactate dehydrogenase A, which results in a slower growing tumour and improved prognosis [43].

IDH mutations are seen in more than 80% of WHO grade II/III gliomas [50], and according to the previous WHO 2016 classification, they were markers of secondary glioblastoma, and only seen rarely in primary glioblastoma, in less than 5% of cases [43,51]. Previous studies comparing OS based on the previous classification have shown that the presence of IDH mutation confers an improvement in OS, with a median of 31 months in IDH-mutant glioblastoma following surgery and chemoradiotherapy (CRT) compared to a median OS of 15 months in patients with IDH-wildtype glioblastoma [6]. In patients only having surgery and radiotherapy, the median OS in IDH-mutant glioblastoma is 24 months, compared with 9.9 months in IDH-wildtype glioblastoma [6]. This is summarised in Table 3.

	Median overall survival (months)	
Treatment	IDH-wildtype glioblastoma	IDH-mutant glioblastoma
Surgery and radiotherapy	9.9	24
Surgery and CRT	15	31

Table 3. Median OS for glioblastoma according to IDH status and treatment.

2.7.2 MGMT promoter methylation

The MGMT gene on chromosome 10q26 encodes a DNA repair protein that removes alkyl groups from the O^6 position of guanine, which is important for DNA alkylation [52]. Epigenetic silencing of the MGMT gene through promoter methylation is found in 40% of glioblastoma [53], and results in loss of MGMT expression (low MGMT levels) and increases the effects of alkylating chemotherapy agents such as temozolomide (TMZ), and is an important factor in response to treatment and increased OS [52]. Three-class stratification of MGMT levels into unmethylated (methylation <9%), intermediate (9–29%) and highly methylated (>29%) has a prognostic impact with a median progression-free survival (PFS) of 8, 12 and 15 months respectively and median OS of 13, 16 and 20 months respectively [54].

2.7.3 Co-deletion of 1p and 19q

In IDH-mutant glioblastoma, the loss of the short arm of chromosome 1 (1p) and the long arm of chromosome 19 (19q), referred to as 1p/19q deletion is most commonly found in tumours with oligodendroglial morphology, approximately 80% of cases [55], and is associated with better OS [56].

2.7.4 EGFR

The EGFR gene is a major activator of signalling pathways and responses. EGFR has been found to be amplified in 40% of glioblastoma, overexpressed in 60% and deleted or mutated in 24-67% of cases [57]. It is rarely seen in IDH-mutant glioblastoma. About half of patients with EGFR amplification have a mutation due to deletion of exons 2–7 (EGFRvIII) [58]. Recent

studies have shown associations between high levels of EGFR amplification and poorer survival [59] as well as poorer response to anti-angiogenic therapy [60]. However older studies show a lack of consensus between EGFR amplification and clinical outcomes, and it has been suggested that this may be a result of IDH and MGMT not being accounted for, and data from an era before widespread TMZ use [61].

2.7.5 p53 pathway

The tumour suppressor protein p53 is implicated in almost every cancer. Deletion of p53 can occur but the pathway is more often modulated by a number of upstream regulators and downstream effectors [58]. Various stresses as well as anti-tumour therapies can activate p53 by increasing its stability, which then acts as a transcriptional regulator of its downstream genes [62]. Mutations within the p53 pathway are seen in 78% of glioblastoma however IDH-mutant glioblastoma more often shows direct mutations of the p53 gene and alterations in the p53 pathway are thought to promote progression to a high-grade lesion [58]. However, as the p53 pathway is involved in various cellular responses, the prognostic value of this mutation is largely unknown [63].

2.7.6 CDKN2 A/B

The CDKN2 gene encodes for the protein p14ARF which stabilises p53 function for tumour suppression and the deletion is associated with greater proliferation, higher tumour grade and homozygous deletion of CDKN2 A/B is associated with a lower OS and PFS in IDH-wildtype glioblastoma [61].

2.7.7 Loss of ATRX

The ATRX gene has a role in histone deposition, cell cycle regulation and maintaining stability of the genome, and ATRX inactivation can be due to mutations, deletions, gene fusions, or a combination of these [64]. ATRX mutations are markers of astrocytic tumours and generally mutually exclusive with 1p/19q co-deletion [65]. They are seen in 71% of IDH-mutant glioblastoma and rarely in IDH-wildtype glioblastoma [6]. Presence of the mutation confers a better prognosis [66].

2.7.8 TERT

TERT promoter gene alterations are seen in 72% of IDH-wildtype glioblastoma and 26% of IDH-mutant glioblastoma [6], and are usually mutually exclusive with ATRX alterations [67]. They are thought to represent a mechanism by which the tumours perform telomere elongation to achieve limitless replication potential, however there is a varied consensus and the majority of studies to date suggest that TERT mutation is not an independent prognostic factor for IDH-wildtype glioblastoma [61].

2.7.9 Phosphatase and tensin homolog (PTEN)

PTEN, a tumour suppressor gene found in chromosome 10 shows mutations in 24% of IDH-wildtype glioblastoma and rarely in IDH-mutant glioblastoma [6,68]. Studies have shown that PTEN mutations do not provide a prognostic benefit in IDH-wildtype glioblastoma, however PTEN mutation status is a predictor of responsiveness to tumour treating fields (TTF) therapy

with an almost doubling of median post-progression survival from 11.6 months to 22.2 months [69].

2.8 Treatment of glioblastoma

2.8.1 Multi-disciplinary team (MDT) meeting

Within the NHS in the UK and across the world in many other countries, patients are discussed at a specialist neuro-oncology MDT meeting at first radiological diagnosis of a suspected brain tumour [28], which is the primary direct pathway of referral for all new brain tumour diagnoses. The MDT comprises of specialist consultant neuro-oncologists, neurosurgeons, neuroradiologists and neuropathologists. In addition, allied healthcare professionals such as specialist brain tumour nurses, occupational and speech therapists, radiotherapy radiographers and research trial coordinators also attend the meeting.

The role of the MDT meeting is to ensure diagnosis, treatment and care is effectively provided by specialists through multidisciplinary team-working; ensure guidelines are followed; and ensure eligible patients are supported into clinical trials. There is a strong clinical consensus from the UK that effective team working at the MDT results in improved clinical decision making, better coordinated patient care, and higher quality care [70].

Each patient case is presented with clinical assessments, imaging studies and pathology specimens discussed in detail in order to come to an appropriate diagnosis. Appropriate treatment strategies such as surgical approaches and CRT protocols considering the patient's individual circumstances are discussed, and management plan options are created for

discussion with the patient, in a timely manner. The creation of surgeon-led subspecialist clinics involving brain tumour specialist clinical nurse practitioners allow the rapid review of patients to discuss diagnosis and management options [71].

The overarching aim of glioblastoma treatment is to delay tumour progression and increase the patient's OS [32], which is the foundation of discussions at the MDT meeting. However, in patients who are elderly, have a poor performance status or have a tumour which is not amenable to surgical resection, MDT discussions will be around offering a biopsy, unless the risk is considered too high, there is a limited prognosis or patient preference, in which case a course of palliative radiotherapy or best supportive care is offered [27].

2.8.2 Surgery

Surgical intervention is the mainstay of treatment, with the aims of firstly acquiring a diagnosis by obtaining a tissue sample for molecular biomarkers and secondly maximal safe resection [20], which has been shown to improve OS [72,73]. In addition, surgery is crucial for improving quality of life and in some patients for reversing neurological deficit and controlling seizures [7]. The extent of resection is highly dependent upon the tumour location and involvement of eloquent brain regions such as the primary motor, somatosensory, visual or auditory cortices, Broca's area, Wernicke's area, the brainstem or basal ganglia which are less amenable to intervention and resultingly lead to a worse prognosis [7]. In addition, the degree of resection can depend on experience of the neurosurgeon as well as the use of pre-operative and intra-operative techniques [20].

In surgical intervention, preservation of cortical and subcortical structures is important to preserve functional status in glioblastoma resection within eloquent areas, and there are various techniques and approaches to identify pathways involved in motor, sensory, language, memory and cognitive functions, particularly when the tumour may distort normal anatomy and there may be reorganisation of neural networks due to cortical plasticity [32]. Various intraoperative tools have been developed to enhance the neurosurgeon's ability to identify tumour margins and improve resection while simultaneously preserving eloquent brain function [32], which are briefly described below. If surgical resection is not feasible due to location of the tumour in an eloquent area or due to patient factors, a stereotactic biopsy is usually performed and includes multiple samples of different regions within the tumour, as studies have shown intratumoural heterogeneity of MGMT promoter methylation as well as other genetic markers [74,75]. Intra-operative review of cytological specimens is performed to confirm the diagnosis and ensure there is an adequate tissue sample [45].

2.8.3 Pre-operative imaging techniques

A recommendation by NICE is that diffusion tensor imaging (DTI) should be considered in addition to standard neuronavigation techniques to reduce injury to critical tracts during resection of glioblastoma [28]. DTI tractography is a technique to visualise the white matter tracts within the brain, obtained through DWI. These can be superimposed onto conventional MRI sequences, to produce a map of critical white matter tracts for neurosurgical planning and navigation. It illustrates the spatial relationships of tumour to white matter tracts, can be performed pre-operatively and is non-invasive.

A randomised controlled trial has shown that the use of pre-operative DTI tractography compared with resection without DTI tractography led to a significantly higher rate of gross total resection (74.4% vs. 33.3%), a significantly lower rate of post-operative motor deficit (15.3% vs. 32.8%), a significantly higher 6-month Karnofsky Performance Scale score (77 vs. 53), a significantly higher median OS (21.2 vs. 14.0 months), and a 43% reduction in the risk of death [76].

DTI tractography has demonstrated a strong clinical correlation with subcortical stimulation, being able to locate the corticospinal tract location in about 95% of cases [77]. In combination with functional MRI (fMRI), which measures changes in blood oxygen level, reflecting activity of neurons, it has demonstrated to directly influence clinical decisions, surgical approach and extent of resection of glioblastoma, due to localisation of functional cortical areas and subcortical pathways in eloquent regions (Figure 12) [32,78]. Motor mapping fMRI correlates very highly with areas identified by direct cortical mapping with a sensitivity and specificity of 95–100%, and language mapping using fMRI has a sensitivity and specificity between 37–91 and 64–83%, respectively, and is becoming the study of choice for pre-operative assessment of language dominance, as a non-invasive alternative to the Wada test [79].

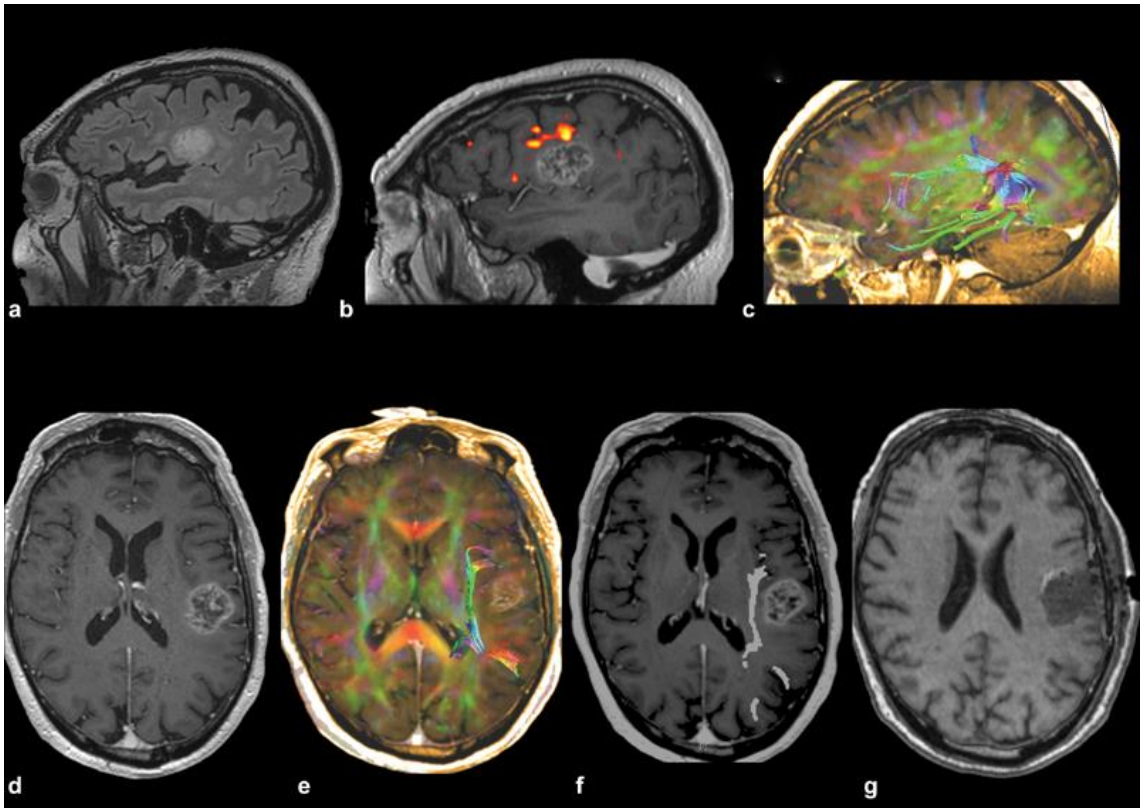

Figure 12. Pre-operative DTI tractography of the arcuate fasciculus to inform planning of awake craniotomy with speech and motor mapping and monitoring in a right-handed man with glioblastoma. (a, d) Pre-operative sagittal and axial CE-T1WI demonstrated an enhancing lesion in the dominant subcentral gyrus extending into the posterior insular. (b) Silent word generation language fMRI showed left-side language dominance. The activated anterior language areas were seen in the inferior and middle frontal gyri, in close proximity to the anterior and superior border of the lesion. (c, e) Left arcuate fasciculus three-dimensional reconstruction to demonstrate relation of the tract to the lesion. (f) Intra-operative neuronavigation MRI with DTI tractography of the arcuate fasciculus. (g) Post-operative CE-T1WI demonstrated greater than 95% extent of resection. Post-operatively there was a transient subtle deterioration in expressive dysphasia that improved to the patient's baseline day 10 post-operatively. (Reprinted from [32], with permission).

Despite limitations of reconstruction variability and a lack of standardised techniques which can generally lead to over-estimation but also under-estimation of tracts, a systematic review correlating with ground truth data has shown that current DTI tractography algorithms

produce tracts containing 90% of ground truth bundles [80]. Protocols for standardised region of interest (ROI) placement can reduce variability and newer techniques and advanced reconstruction methods can also improve tracking particularly where there are crossing fibres [81]. DTI and fMRI should not be used instead of intra-operative mapping techniques; however they are indispensable tools in surgical planning.

2.8.4 Intra-operative techniques

Intra-operative stimulation mapping

Intra-operative cortical and subcortical electrical stimulation mapping performed during awake craniotomy is currently the gold standard [82]. Functional mapping during awake craniotomy allows localisation of language and motor areas as well as position of the white matter tracts associated with the speech and motor functions [32,83]. The recent Cochrane meta-analysis has recommended awake craniotomy as the main method of enabling a maximal safe resection in patients with tumours in eloquent locations [84], and another meta-analysis has shown that resection of high-grade gliomas with intra-operative stimulation mapping during awake craniotomy leads to a more extensive resection, significantly longer OS and fewer post-operative complications compared with craniotomy under general anaesthesia [85], and there are recommendations for its implementation as standard-of-care for glioma surgery [86]. Furthermore, intra-operative stimulation mapping offers the opportunity to rapidly identify motor or language tracts during surgery and reducing the number of subcortical stimulations when combined with DTI fibre tracking [87], as well as

increasing extent of resection and reducing mortality when combined with fluorescent-guided resection [88,89].

Fluorescence-guided surgery

Currently, gross total resection is defined by the lack of residual contrast enhancement on the early post-operative MRI, however the area of contrast enhancement largely reflects areas of breakdown of the blood-brain barrier, and tumour infiltration is present microscopically in the surrounding non-enhancing tumour margins which are an important prognostic factor [90]. One of the most studied technologies is 5-aminolevulinic acid (5-ALA), a prodrug administered orally approximately 2-4 hours before surgery, which leads to accumulation of fluorescent protoporphyrin IX (PPIX) in glioma cells (Figure 13) [32]. Although the underlying mechanisms are unclear, it enables glioma cells to be visualised in real-time intra-operatively using a microscope with appropriate filters and guides resection [91]. Current commercially available systems rely on subjective visual assessment of fluorescence by the neurosurgeon, however more accurate quantitative estimation of PPIX is being developed [32].

A recent systematic review and meta-analysis showed 5-ALA–guided surgery led to a significant increase in gross total resection rate; 26% higher in the 5-ALA group compared to conventional surgery, and a small but significant increase in survival with the use of 5-ALA, although this was less conclusive as an independent outcome [92]. 5-ALA has also been shown to be a useful adjunct in the resection of recurrent glioblastoma and there are recommendations for its use routinely in resection of recurrent disease [93].

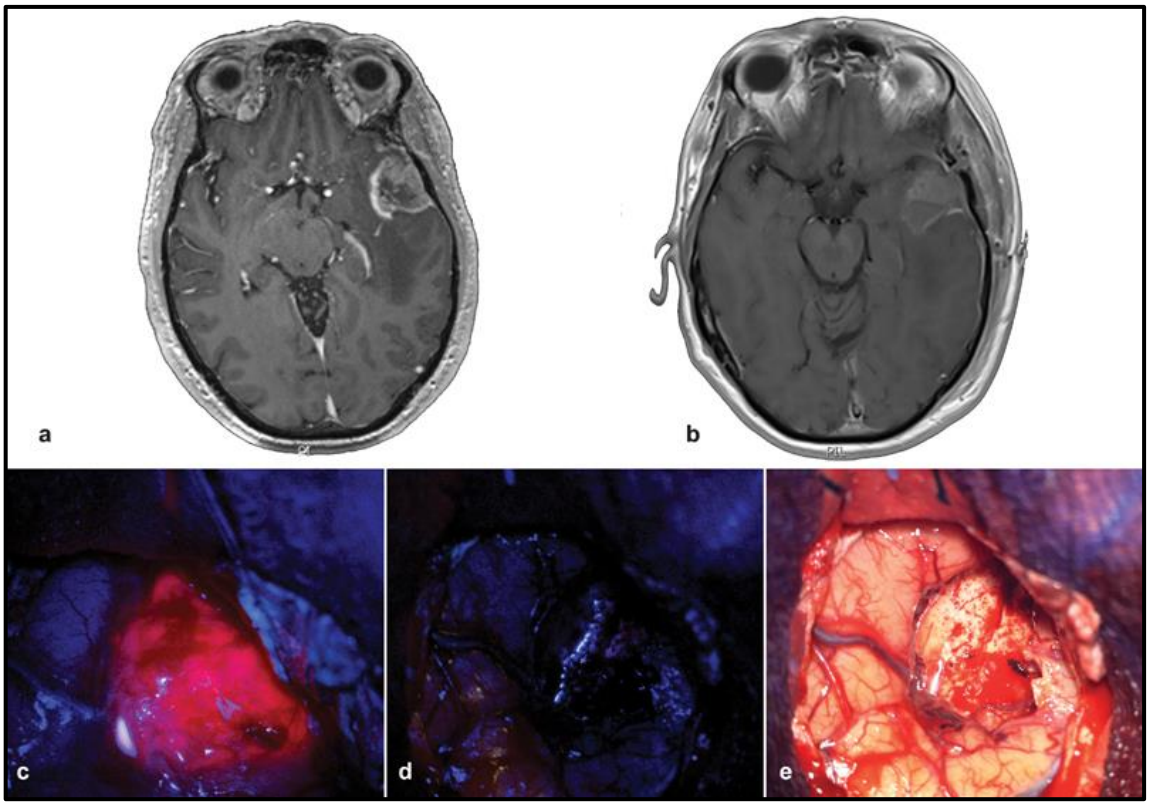

Figure 13. 5-ALA guided resection of glioblastoma. (a) Pre-operative and (b) post-operative axial CE-T1WI demonstrated complete resection of the left temporal glioblastoma. (c) Microscope view under blue light on opening the dura to visualise glioblastoma in coral pink following 5-ALA administration. Microscope view (d) under blue light and (e) under white light showed complete tumour resection. (Reprinted from [32], with permission).

Intra-operative imaging technologies

There have been recent advances in intra-operative imaging technologies, specifically intra-operative MRI (iMRI) and intra-operative ultrasound (iUS) which can provide real-time information about the site of disease as well as nearby structures, providing imaging neuronavigation which can compensate for brain shift during surgery [32]. Both iMRI and iUS are recommended by current NICE guidelines to be considered in helping to achieve maximal surgical resection of glioblastoma [28].

iMRI can provide a three-dimensional view of disease, adjacent structures and interval updates of resection status during surgery for neuronavigation, leading to more accurate resection; however it is not widely available and comes with a high cost and increased time of surgery due to additional imaging time, as well as the extravasation of gadolinium contrast into the resection cavity which can make imaging interpretation difficult [90].

iUS is faster, simpler to use and much more readily available [32]. A recent randomised controlled trial showed that iUS-guided surgery is safe and leads to complete resection of the contrast-enhancing tumour more frequently than standard neurosurgery, without adverse outcomes and can be considered to maximise extent of resection similar to iMRI or 5-ALA-guided surgery, although the detection of tumour is dependent on operator experience, resolution and type of probe used [94]. Advanced ultrasound techniques such as contrast enhanced ultrasound (CEUS), Doppler ultrasound and elastography could improve tumour detection [94].

Many individual studies have demonstrated that the use of intra-operative imaging technologies lead to an increase in the extent of resection and gross total resection rate, although a recent Cochrane review of intra-operative imaging technologies concluded that 5-ALA-guided surgery and iMRI may be beneficial in maximising extent of resection but it is based on low-levels of evidence and the effects of image-guided surgery on OS, PFS and quality of life are unclear [84]. Integrated navigation using information from multiple modalities allows structural and functional information to be co-registered to allow more accurate and safer resection particularly in eloquent areas [32]. A recent systemic review of 5-ALA-guided surgery and iMRI showed no superiority of one technique over the other

regarding outcome, but suggested the combined use of 5-ALA and iMRI, which could be promising for resection beyond the enhancing tumour [95]. Another study suggested that iMRI should only be used in combination with 5-ALA-guided surgery as although 5-ALA fluorescence goes beyond the borders of contrast enhancement, iMRI overcomes the limitations of depth and residual tumour from limited views [90].

Navigated transcranial magnetic stimulation

Navigated transcranial magnetic stimulation (nTMS) is an emerging technology for pre-operative planning and cortical mapping for safe maximal resection of tumours within or close to motor and language areas and can be used during surgery with nTMS-based tractography to also guide intra-operative mapping and resection [96]. A recent meta-analysis has shown its use is associated with fewer post-operative permanent motor deficits and increased gross total resection rate compared to standard surgery without pre-operative nTMS mapping [96]. However, more research is required to provide better evidence for this emerging technology [32].

2.9 Post-operative imaging and treatment

Neuroimaging with MRI is the primary method to evaluate disease status, for treatment response assessment as well as evaluating expected and unexpected tumour and treatment-related changes. Post-treatment imaging includes the immediate post-operative MRI (IP-MRI), a pre-radiotherapy MRI (PR-MRI), a post-radiotherapy treatment baseline MRI (TB-MRI), followed by regular interval imaging during adjuvant TMZ and post-treatment monitoring imaging [97].

The recent WHO brain tumour classification based on an integrated diagnosis including molecular characteristics and advancement in various treatment options has made a direct impact on post-treatment imaging appearances. It has made the interpretation of post-operative/post-treatment imaging more challenging. Accurate assessment of imaging at appropriate time points requires background information of molecular genetics of the tumour, clinical status of the patient and treatment timescales particularly TMZ and radiotherapy treatments.

The response assessment criteria for primary and secondary tumours which were initially produced for clinical trials are making their way into clinical practice. Standardised imaging protocol and multiparametric MRI at appropriate time points and standardised measurements are key factors for post-treatment response assessment.

2.9.1 Immediate post-operative MRI (IP-MRI)

IP-MRI is performed with intravenous (IV) contrast to determine the extent of resection and assess for residual disease. The challenge arises as post-operatively reactive enhancement is present and can mimic residual tumour. There are varied opinions as to the optimal timing of the IP-MRI study, however current practice of imaging within 72 hours of surgery to distinguish between reactive enhancement and residual tumour is based on a very early study [98]. Studies since then have demonstrated post-operative reactive parenchymal, dural and leptomeningeal enhancement is seen in about a third of patients who have IP-MRI within 72 hours [99], and can be seen as early as 17 hours following surgery and increasing with time [100,101]. Thin linear enhancement is more likely but not always associated with reactive change, and thick linear or nodular enhancement has a fairly high specificity for residual tumour [102,103]. More recent studies have proposed that post-operative MRI should be performed as early as possible [104] and at least within 45 hours following surgery [103], and a close analysis of enhancement patterns along with comparison to the pre-operative MRI study is essential to help discriminate between residual tumour and reactive enhancement [99]. iMRI has been shown to be superior to an early post-operative MRI, demonstrating a lower incidence of reactive change and therefore better ability to distinguish residual tumour, however the recommendation is that an additional DWI study is performed in the early post-operative period as ischemic lesions can be overlooked on the iMRI [105].

2.9.2 Pre-radiotherapy MRI (PR-MRI)

CRT treatment involves radiotherapy of 60 Gray in 30 daily fractions over six weeks and typically begins 3-5 weeks following surgery to allow for post-operative recovery [106]. Radiotherapy planning of the gross tumour volume is defined on the planning CT study using the co-registered pre-operative and post-operative CE-T1WI and FLAIR MRI sequences [107]. Due to the time interval between the post-operative MRI and planning CT, shift of normal brain tissue occurs with filling of parts of the resection cavity, leading to inaccurate registration between the post-operative MRI and planning CT study [108], and interval tumour growth or reactive enhancement may occur in the interim and therefore many centres also obtain a repeat MRI at the time of radiotherapy to ensure accurate co-registration of the target volumes. It has been shown that patients with evidence of tumour growth between the IP-MRI and PR-MRI have a shorter survival [109] and the information from the PR-MRI can be useful for the clinical management of patients by reducing the ratio of patients diagnosed with pseudoprogression [110]. Current practice in the UK has shown only 32% of centres reported routinely performing PR-MRI [97]. The issue still remains that glioblastoma infiltration is present diffusely beyond the extent of the visible enhancing lesion on MRI [32]. There is evidence that advanced imaging techniques at the IP-MRI or PR-MRI time point can be useful to identify tumour infiltration and predict recurrence, these include low apparent diffusion coefficient (ADC) on DWI [111,112], high choline (Cho) [113], high lactate to N-acetylaspartate (NAA) ratio on MRS [114], and the use of O-(2-[^{18}F]fluoroethyl-)-L-tyrosine positron emission tomography (^{18}F-FET-PET) [115].

2.9.3 Chemoradiotherapy

The current standard treatment for patients with glioblastoma who have a good performance status (Karnofsky performance status ≥70), and are around the age of 70 years of age and under is maximum safe surgical resection followed by radiotherapy (60 Gray in 30 fractions) with concurrent TMZ [28], which usually commences 3-5 weeks following surgery [106], followed by six months of adjuvant TMZ as per the Stupp protocol [116]. In patients under 70 years of age who do not undergo treatment, the median OS is approximately 3-4.5 months, however treatment with surgery followed by radiotherapy improves median OS to approximately 15-16 months [27]. The role of radiotherapy is to improve local control without inducing neurotoxicity, and the exact timing, dose and radiotherapy schedule is multifactorial, determined by patient age, performance status, volume of residual tumour and prognosis [45].

In older patients with a good performance status, a shortened course of hypofractionated radiotherapy (40 Gray in 15 fractions) with concurrent TMZ followed by adjuvant TMZ for up to 12 months is preferred [27], which has shown to be superior to hypofractionated radiotherapy alone (median OS 9.3 vs. 7.6 months) [117]. Other options for treatment include hypofractionated radiotherapy alone, TMZ alone and best supportive care according to other factors [20]. A summary of the management pathway for patients is shown in Figure 14.

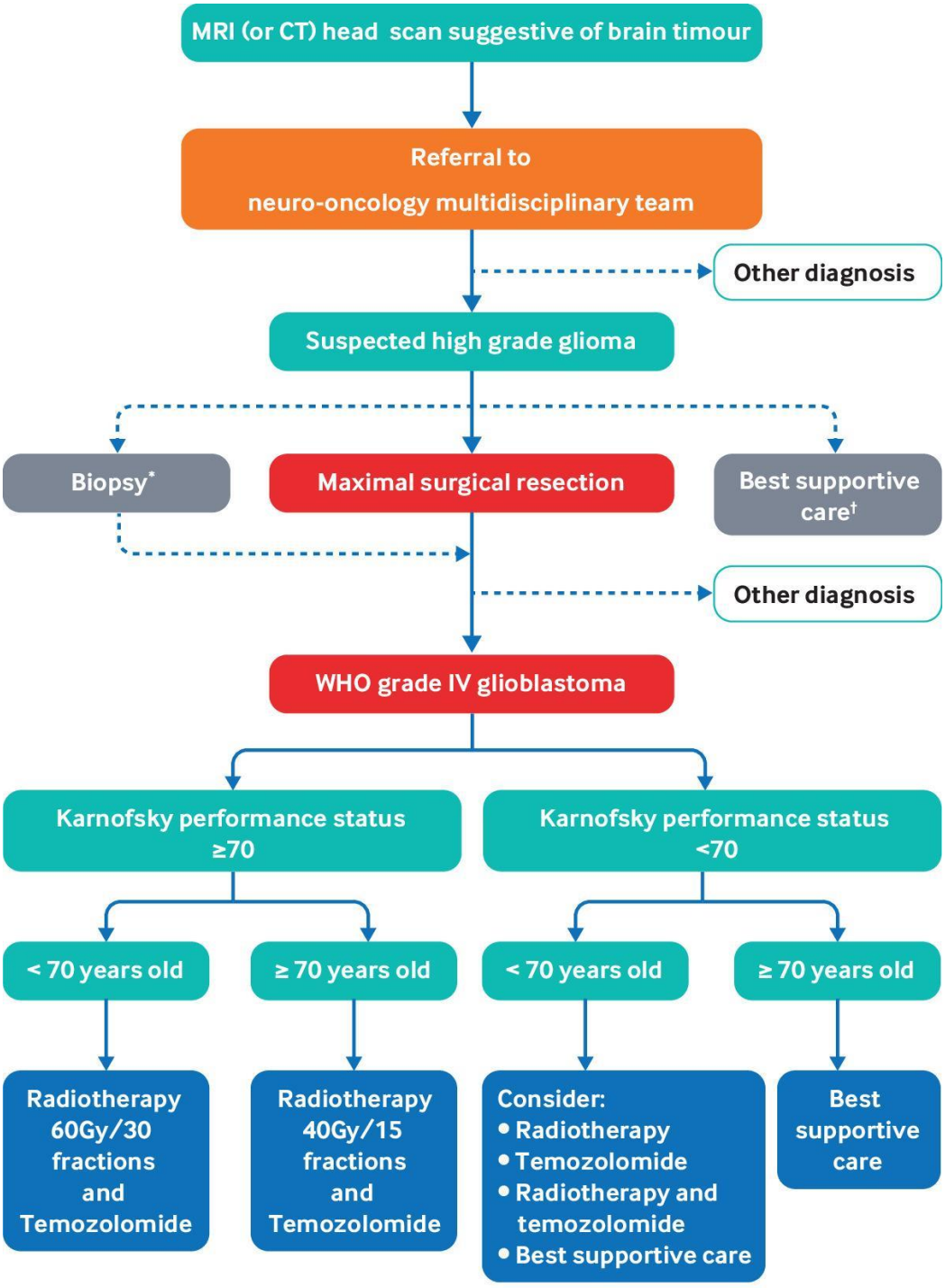

*Consider biopsy if surgical resection not considered possible (for example, poor performance status).
†Consider if histopathological diagnosis cannot be made due to high risk of biopsy or very unfavourable prognosis.[29]

Figure 14. Glioblastoma management pathway, adapted from NICE guideline NG99. (Reprinted from [27], with permission).

In patients who have a tumour with high levels of MGMT promoter methylation, there is a significant increase in survival when treated with CRT compared to those treated with radiotherapy alone; the median OS is 21.7 months versus 15.3 months respectively [52].

2.9.4 Early post-chemoradiotherapy treatment imaging

After completion of radiotherapy and concomitant TMZ chemotherapy, a treatment baseline MRI (TB-MRI) is usually performed at four to six weeks following completion of radiotherapy, which gives an early assessment of the response to treatment [292]. Response to treatment is assessed by changes in the contrast-enhancing lesion from standard MRI using the Response assessment in neuro-oncology criteria (RANO) criteria [293]. Although contrast enhancement is generally a good marker of tumour, in many cases, radiological features of disease progression are observed within the first 3-6 months following radiotherapy treatment, by an increase in enhancing disease [294]. In a proportion of these, increases in oedema, mass effect, and contrast enhancement within the high-dose radiotherapy volume are transient and resolve over time without intervention [295]. This phenomenon is known as pseudoprogression (psPD), and in cases of early enhancing disease, the reported incidence of psPD from a recent meta-analysis is 36% [296], but older studies have shown a variation in incidence from 12-64% according to various criteria used and it is seen more often in patients who show high levels of MGMT promoter methylation [297–301].

Although the pathological process is not clearly understood, histological features associated with psPD are bland necrosis, fibrosis, gliosis, oedema, demyelination and vascular

hyalinisation [302]. Patients with pseudoprogression usually remain clinically asymptomatic and have a longer OS compared with those with true tumour progression (tPD).

In clinical practice, it is difficult to differentiate between tPD and psPD; conventional MRI scans utilising CE-T1WI and T2WI/FLAIR sequences have a low diagnostic accuracy for distinguishing between these two entities at early time points from six weeks to three months post-radiotherapy [118], due to similar imaging appearances as demonstrated in Figure 15. Treatment is therefore continued with short interval imaging (4-6 weeks) and when progression is identified on consecutive imaging, true progression is confirmed. Some patients inevitably continue ineffective treatment, are delayed from receiving alternative treatments, or face potential exclusion from entering clinical trials as a result of deterioration in clinical status. More early and accurate diagnosis between true progression and pseudoprogression is essential to optimise treatment strategies and improve outcome, therefore imaging techniques that act as biomarkers of treatment effectiveness are required [119–121].

A meta-analysis from 2017 has shown the sensitivity and specificity of anatomical MRI to be 68% and 77% respectively from five studies, for treatment response evaluation of high-grade glioma [122]. Early radiographic indicators of true progression on standard CE-T1WI have shown to be enhancement involving the corpus callosum, multiple lesions, subependymal spread, solid enhancement with distinct margins, a spreading wave front of enhancement and enhancing nodules, although these features have a large overlap with psPD and can be influenced by corticosteroid use and MGMT promotor methylation status [123]. On standard T2WI/FLAIR, the increase in volume of signal change shows limited ability to distinguish

between the entities, however a reduction of FLAIR signal at the post-CRT imaging time point can occur in a minority of cases of psPD, but is not seen in tPD [124]. The signal intensity within the resection cavity on FLAIR imaging when hyperintense is associated with higher rates of progression at six and 12 months, and also poor outcomes, thought to be related to leakage of protein and blood products secondary to increased vessel permeability in tumour, within the resection cavity [125].

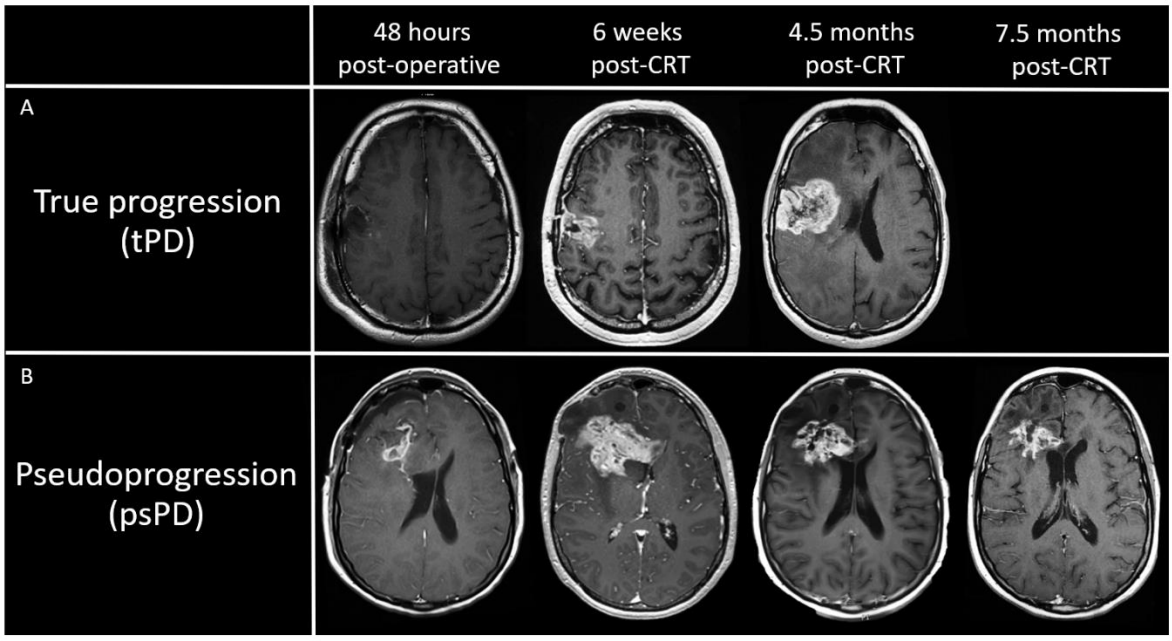

Figure 15. True progression and pseudoprogression in glioblastoma. (A) A case of tPD in glioblastoma. 48 hours post-operative CE-T1WI showed post-surgical changes in the right posterior frontal lobe. Six weeks post-CRT CE-T1WI showed enhancing disease at the site of surgery. 4.5 months post-CRT CE-T1WI showed a significant increase in enhancing disease, suggesting tPD. (B) A case of psPD. 48 hours post-operative CE-T1WI showed a small amount of residual enhancing disease in the right frontal lobe. 6 weeks post-CRT CE-T1WI showed an increase in enhancing disease at the site of surgery. 4.5 months post-CRT CE-T1WI showed a significant decrease in enhancing disease. 7.5 months post-CRT CE-T1WI showed further decrease in enhancing disease, suggesting psPD.

2.9.5 Role of advanced imaging techniques in post-treatment imaging

A recent review article has shown that advanced MRI techniques that can assess physiological and metabolic properties of tissue have shown to be useful, these include ADC from DWI, fractional anisotropy from diffusion tensor imaging (DTI), dynamic susceptibility contrast (DSC) perfusion, dynamic contrast-enhanced (DCE) perfusion, arterial spin labelling (ASL), MRS, ferumoxytol relative cerebral blood volume (rCBV), amide proton transfer (APT) weighted imaging, parametric response mapping (PRM) and perfusion MRI-fractional tumour burden (pMRI-FTB) [123]. Combining advanced MRI techniques in a multiparametric protocol have shown to provide a higher degree of confidence in assessing glioblastoma treatment response (**Figure 16** and **Figure 17**) [113,126–128], which is investigated in **Chapter 6**.

Positron emission tomography (PET) is another imaging modality that can be used to distinguish between true progression and pseudoprogression. The most widely used tracer, fluorodeoxyglucose (FDG), has a limited role however has a higher accuracy in combination with advanced MRI techniques [129]. Other tracers with low background brain activity have shown to be more useful than FDG-PET, such as ^{11}C-methyl-methionine-PET (MET-PET), FET-PET or 3,4-dihydroxy-6-[^{18}F]-fluoro-L-phenylalanine (FDOPA-PET) [123], but are less available.

Many studies have shown that radiomics in combination with machine learning is promising [130–136], which is investigated in **Chapter 7**.

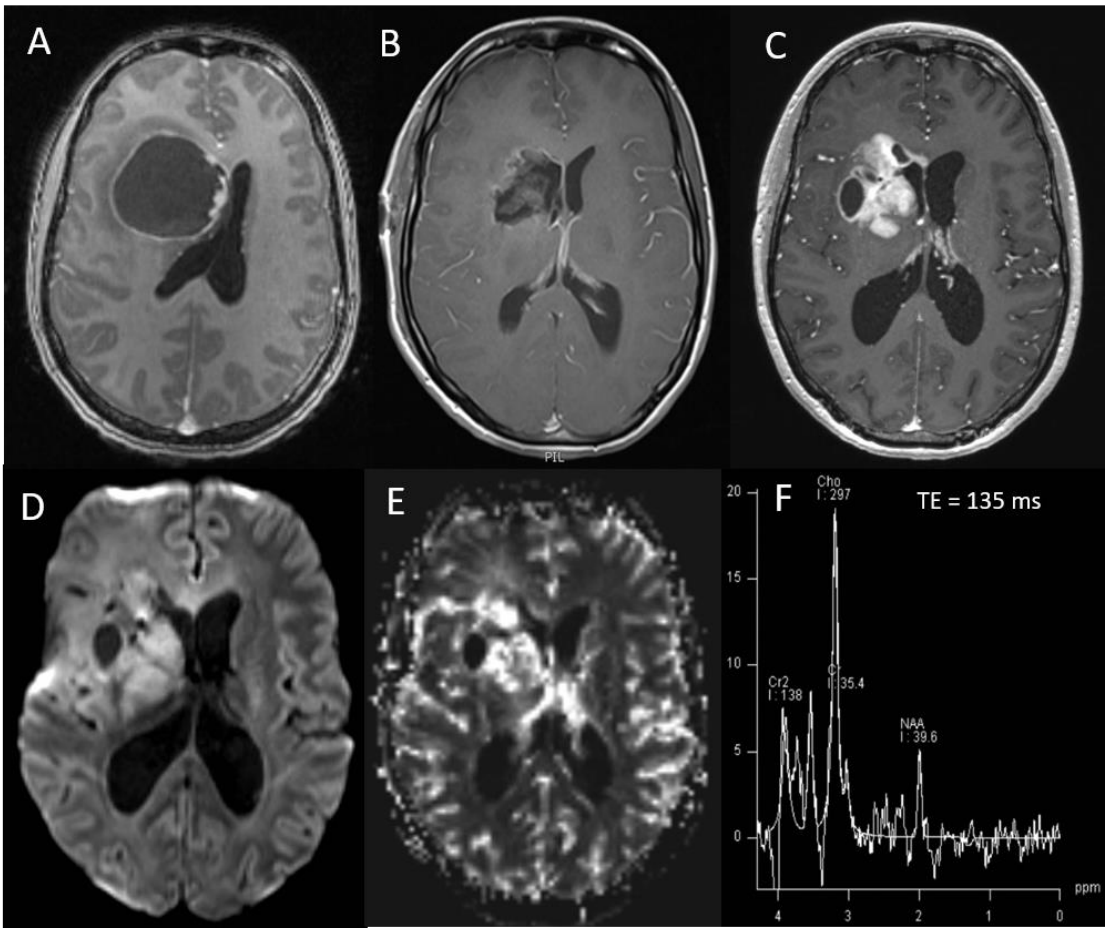

Figure 16. True progression in post-treatment glioblastoma with low MGMT promoter methylation (<10%). (A) Pre-operative CE-T1WI. (B) IP-MRI CE-T1WI showed resection of the right frontal glioblastoma. (C) Early post-CRT CE-T1WI at six weeks showed a significant increase in contrast enhancement. Multiparametric MRI at this time point demonstrated: (D) areas of restricted diffusion on DWI and ADC (<1000), (E) a high rCBV ratio on PWI (>2.0), (F) a very high choline/creatine (Cho/Cr) ratio (3.8), high Cho/NAA ratio on MRS. All parameters suggested a poor response and disease progression.

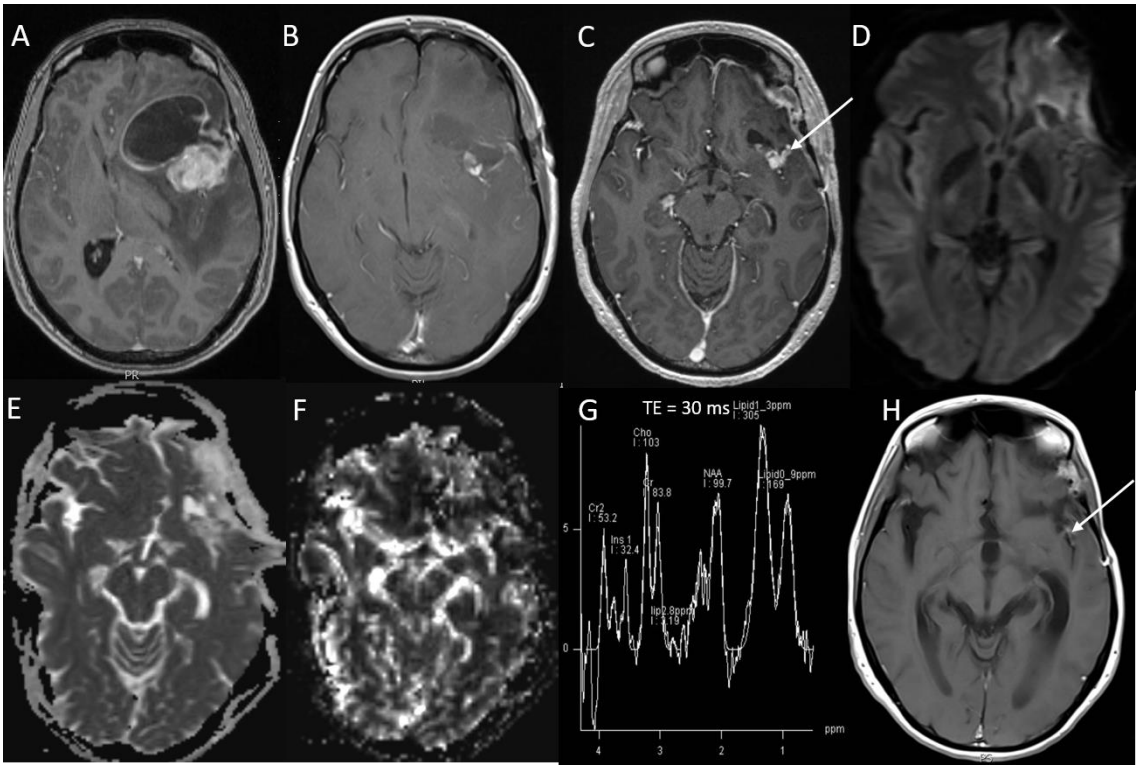

Figure 17. Pseudoprogression in post-treatment glioblastoma. (A) Pre-operative CE-T1WI. (b) Post-operative CE-T1WI showed resection of the left frontal glioblastoma. (C) Early post-CRT CE-T1WI at four weeks showed an increase in contrast enhancement (arrow). Multiparametric MRI at this time point demonstrated (D,E) areas of free diffusion on DWI and ADC, (F) a low rCBV ratio on PWI, (G) a low Cho/Cr ratio, a low Cho/NAA ratio and presence of lipid and lactate on MRS. All these parameters suggested features of pseudoprogression. (H) Follow-up CE-T1WI at 12 months showed a further decrease in enhancement (arrow) confirming pseudoprogression.

2.9.6 Treatment response assessment criteria

Imaging of glioblastoma as well as other high-grade glial tumours during the adjuvant chemotherapy and post-treatment monitoring period, should be assessed by the RANO criteria. This takes account of the size of the contrast-enhancing lesion and non-contrast-enhancing surrounding T2WI/FLAIR signal change on imaging compared to the pre-treatment baseline imaging and uses the smallest lesion size following treatment for determining

progression, as well as incorporating clinical status and use of corticosteroids [137]. Outcome is determined as complete response (CR), partial response (PR), stable disease (SD), or progressive disease (PD). The criteria acknowledges the issue of psPD, specifying that within the first 12 weeks following completion of radiotherapy, tPD can only be attributed if there is new contrast enhancement outside the radiation field or if there is histological confirmation of tumour progression [138]. The inclusion of T2WI/FLAIR disease criteria is important as up to 40% of patients treated with bevacizumab show an increase in non-enhancing disease despite contrast-enhancing disease remaining stable [139]. The working group have discussed issues surrounding pseudoresponse after treatment with anti-angiogenic therapies, where apparent response is due to normalisation of abnormally permeable tumour vessels rather than a true treatment response, and therefore imaging responses should persist for at least four weeks before they are considered as true responses. In 2016, the immunotherapy response assessment in neuro-oncology (iRANO) guidelines were developed to further address this issue, with the key addition of guidelines to continue immunotherapy treatment for three months if immunotherapy treatment was initiated within six months, as long as there is no significant clinical decline. On repeat imaging, if patients have subsequent PD they can be classified as having tPD, which is back dated to the date of initial radiographic PD [140]. If imaging findings at the three month follow up study meet the criteria for SD, PR or CR according to RANO criteria, compared to the previous MRI study meeting the criteria for PD, and there is no clinical decline, patients should be considered as responding to immunotherapy treatment.

2.9.7 Limitations of RANO and future perspective

Although the RANO criteria is the current response assessment criteria for glioblastoma, it has its limitations. The use of bidimensional measurements of the contrasting-enhancing lesion can overestimate disease volume, the thresholds to define PR and PD are relatively arbitrary, the use of percentage change thresholds causes bias in smaller lesions, and the evaluation of non-enhancing T2WI/FLAIR signal change is thought to be more complex than originally thought [137]. Modified treatment response criteria based on volumetric assessment may provide more accurate measurements of lesions, and the use T1 subtraction maps may be able to identify enhancing lesions more clearly. Although the current updated RANO criteria acknowledge the issue of psPD and iRANO considers pseudoresponse, they do not fully address the underlying issues of accurate treatment response and heterogeneity of the tumour, which will require advanced imaging biomarkers to address. There is increasing evidence of advanced MRI techniques such as DWI, PWI and MRS for more accurately assessing treatment response in glioblastoma, and calls for their inclusion, however these techniques have not yet been included in the response assessment criteria.

2.9.8 Imaging during adjuvant TMZ and post-treatment monitoring

Glioblastoma is a very invasive lesion that cannot be removed completely by surgery due to microscopic infiltration, and recurrence of disease occurs in approximately 80% of patients and is usually seen within 2-3 cm of the previously resected disease [7], occurring at a median time of nine months [125]. Clinical assessment and contrast-enhanced MRI forms the basis of glioblastoma follow-up to identify recurrence. MRI should be performed every 3 months

following radiotherapy, or earlier if there is evidence of clinical progression, and ideally on similar MRI equipment and scanner field strength to limit variability [141]. In cases of confirmed tPD, management involves second line treatments or supportive care depending on the patient's prior treatment, performance status and risk.

In contrast to psPD which is generally observed within the first 3-6 months following radiotherapy, radiation necrosis is a later process, seen mostly between 6-24 months after radiotherapy but can occur up to several years later [58]. This is a severe tissue reaction to radiotherapy, more progressive and the proposed mechanism is thought to be related to vascular endothelial injury, glial and white matter damage and changes to the fibrinolytic enzyme system, leading to perivascular coagulative necrosis [143]. Advanced MRI techniques have shown to be useful to distinguish between radiation necrosis and recurrent tumour, however studies have shown that multimodal combination or multiparametric MRI have the best diagnostic accuracies [144,145].

When disease recurrence is identified, further options for treatment are discussed at the neuro-oncology MDT, taking account of tumour phenotype, location of disease, time since previous treatment, patient preference and the patient's performance status [27]. Options may include surgical resection of focal recurrence, further radiotherapy, second-line chemotherapy such as lomustine or combination chemotherapy such as PCV or an active palliative care approach [27]. Where re-operation is feasible, maximal safe resection of recurrent disease has shown to provide a significant benefit to prognosis especially in cases of gross total resection on imaging, irrespective of the extent of resection originally [146].

2.9.9 Recurrence

Treatment options for recurrent glioblastoma should be discussed at the MDT and take account of the patient's personal preferences, performance status, previous treatment and time from last treatment, as well as molecular marker status [28]. In the UK, second-line chemotherapy is usually combination therapy with procarbazine, lomustine, and vincristine (PCV), or lomustine alone, and for focal disease recurrence further surgery or radiotherapy are also options. Compared to the initial management of glioblastoma, the management of recurrence is less standardised and a variety of approaches may be considered. Adequate selection of patients is required for second-line treatments and it is recommended that patients are treated at high-volume specialist centres and clinical trials should also be considered [147].

2.10 Treatment-related complications

2.10.1 Surgery-related complications

An understanding of the commonly encountered post-operative complications on imaging is essential for appropriate management. Post-operative restricted diffusion is seen surrounding the resection cavity in 64% of patients following tumour resection [148], as a result of direct surgical trauma, vascular injury, and tumour devascularisation and is reversible in most cases. However, in 1% of cases post-operative cytotoxic oedema indicating stroke can be seen which shows contrast enhancement in the subacute phase and evolves on serial imaging as encephalomalacia develops. Therefore, it is important to correlate new enhancement with

the immediate post-operative DWI to not mistakenly diagnose tumour recurrence for post-operative infarct [149]. Other complications post-resection include intracranial haemorrhage with an incidence of 1.6% [149]. Post-resection infection is a less common complication typically seen in patients who are immunocompromised and can be seen as bone flap infection, subdural empyema, cerebritis, abscess and meningitis (**Figure 18**) [149].

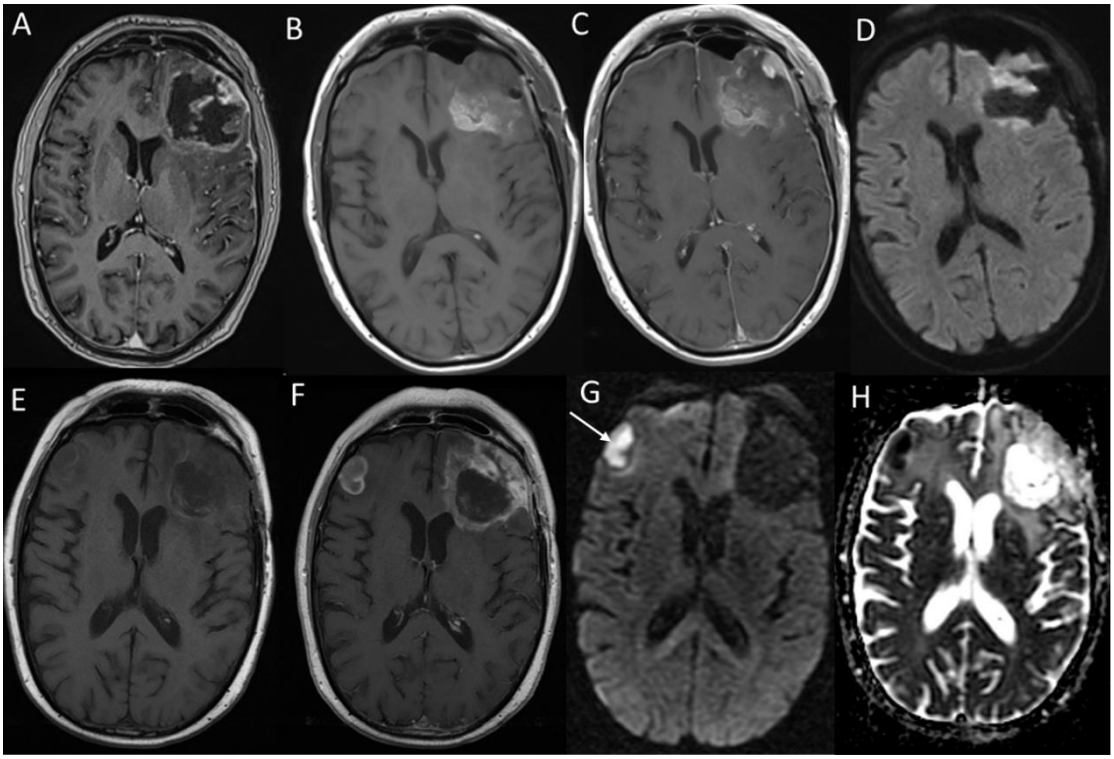

Figure 18. Post-operative complications following debulking of left frontal glioblastoma in a patient on steroids. (A) Pre-operative CE-T1WI. (B,C) IP-MRI pre-contrast and CE-T1WI within 48 hours showing small residual tumour and haematoma within the resection cavity and a shallow right frontal collection, (D) DWI shows resection-related reversible ischaemic changes surrounding the cavity in the left frontal lobe. (E,F) Pre-contrast and CE-T1WI three weeks later shows progression of residual tumour. In addition, there is a new lesion in the right frontal lobe, (G,H) showing strong restricted diffusion (arrow) and low ADC signal in keeping with right frontal lobe abscess formation.

2.10.2 Radiation-related complications

Radiation-related injury is often categorised into acute (days to weeks), early delayed (weeks to months), and late delayed (months to years) complications. Acute and early delayed injury is a result of changes in vessel permeability and blood-brain barrier disruption, resulting in oedema, and is usually reversible resolving spontaneously. On imaging, acute radiation-related injury can be difficult to identify as the oedema is often indistinguishable from tumoural vasogenic oedema. In the early delayed period, there is transient demyelination that demonstrates enhancement usually in the radiation field, however this also can be indistinguishable from tumour on imaging. The issues surrounding this are discussed later in more detail.

Radiation necrosis or radionecrosis is a serious late delayed complication following radiation therapy resulting in an irreversible and progressive necrotic mass lesion and can be seen years following radiation therapy. The true rate is difficult to establish given that appearances can mimic tumour recurrence on MRI, but is estimated to be between 5% and 25% [150]. The proposed pathophysiology of radiation necrosis is thought to be due to vascular injury and damage to glial cells resulting in demyelination and neo-angiogenesis with abnormal leaky vasculature. An increase in enhancing disease and perilesional oedema alone is not specific to diagnose either tumour recurrence or radiation necrosis. Patterns of enhancement have previously been described in the literature to describe radiation necrosis such as “Swiss cheese”, “soap bubble” or “cut green pepper” however these have shown to have a positive predictive value of only 25% [151]. The low predictive value of conventional MRI has led to the use of advanced techniques such as PWI, MRS and PET to help distinguish between

radiation necrosis and tumour recurrence (Figure 19). Using DSC-PWI, with an rCBV cut-off 2.1 has shown to give a high diagnostic accuracy to distinguish between the two entities [152]. Raised Cho levels on MRS have shown to be a useful imaging parameter [153], as have NOE_{MTR} and $Amide_{MTR}$ parameters obtained from chemical exchange saturation transfer (CEST) imaging [154].

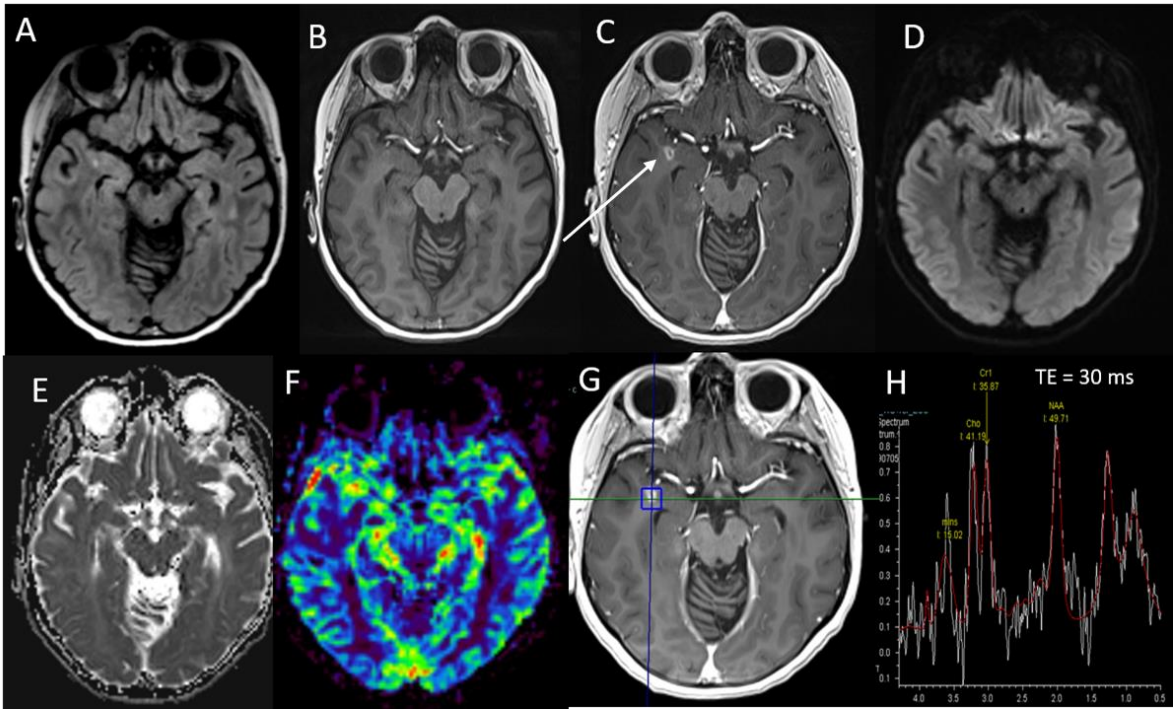

Figure 19. A case of radiation necrosis in a patient with previous craniospinal radiotherapy for medulloblastoma. (A,B,C) FLAIR, pre-contrast and CE-T1WI showing a ring-enhancing lesion in the right anterior temporal lobe (arrow). Multiparametric MRI: (D,E,F) DWI, ADC and rCBV maps show no restricted diffusion or significantly raised perfusion. (G,H) Single-voxel spectroscopy shows mild elevation of Cho/Cr and raised lipid and lactate levels. Findings are consistent with radiation necrosis.

Vascular injury is another late delayed radiation-related complication, and is categorised into three main appearances: radiation-induced vasculopathy, radiation-induced vascular

proliferative lesions, and radiation-induced mineralising microangiopathy [149]. Radiation-induced vasculopathy is the proliferation of vessel walls resulting in stenosis or occlusion, mainly affecting large basal cerebral arteries and as a result, patients are at increased risk for ischaemia and infarcts. Radiation-induced vascular proliferative lesions include capillary telangiectasia and cavernous malformations as a result of microvasculature injury and neoangiogenesis. Radiation-induced mineralising microangiopathy is the formation of dystrophic microcalcifications within the brain parenchyma due to calcium deposition in damaged vessel walls and necrotic brain tissue, typically in the basal ganglia and subcortical white matter [149].

Radiation-induced leukoencephalopathy refers to white matter injury usually without necrosis, thought to be related to direct axonal injury or secondary injury from vascular compromise, appearing as progressive, symmetrical, confluent T2WI/FLAIR hyperintensity involving predominantly the periventricular white matter (Figure 20). The incidence is unclear, but has been reported in 34% of patients receiving whole-brain radiation treatment after six months of follow-up [155]. Patients may be asymptomatic or present with neurocognitive decline and there is a poor correlation between imaging and symptoms. It is important to be aware that some patients may be on immunosuppressive treatments and therefore can develop progressive multifocal leukoencephalopathy (PML), which is generally more asymmetrical and affects the subcortical U fibres, and it is important to be able to distinguish between the two entities [149].

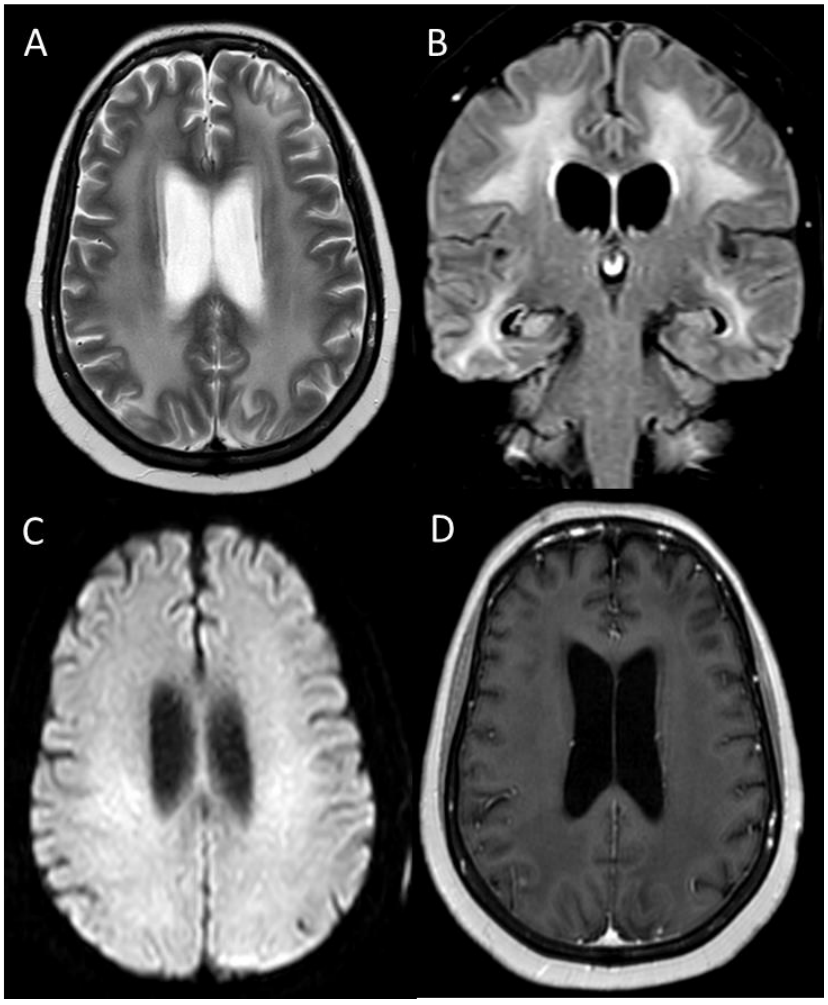

Figure 20. Leukoencephalopathy following whole brain radiotherapy for brain metastases. (A,B) Axial T2WI and coronal FLAIR showing extensive, confluent and symmetrical white matter T2WI/FLAIR signal hyperintensity. (C,D) DWI and CE-T1WI shows no restricted diffusion or contrast enhancement.

Another late delayed phenomenon is stroke-like migraine attacks after radiation therapy (SMART) syndrome consisting of migraine-like symptoms in patients who have had previous radiotherapy treatment. It is proposed to be related to reversible vascular dysregulation resulting in disruption, typically affecting the posterior cerebral hemispheres or cerebellum with gyriform T2WI/FLAIR hyperintensity and enhancement with some cases also showing diffusion restriction (Figure 21) [156], and usually improves or resolves on follow-up imaging.

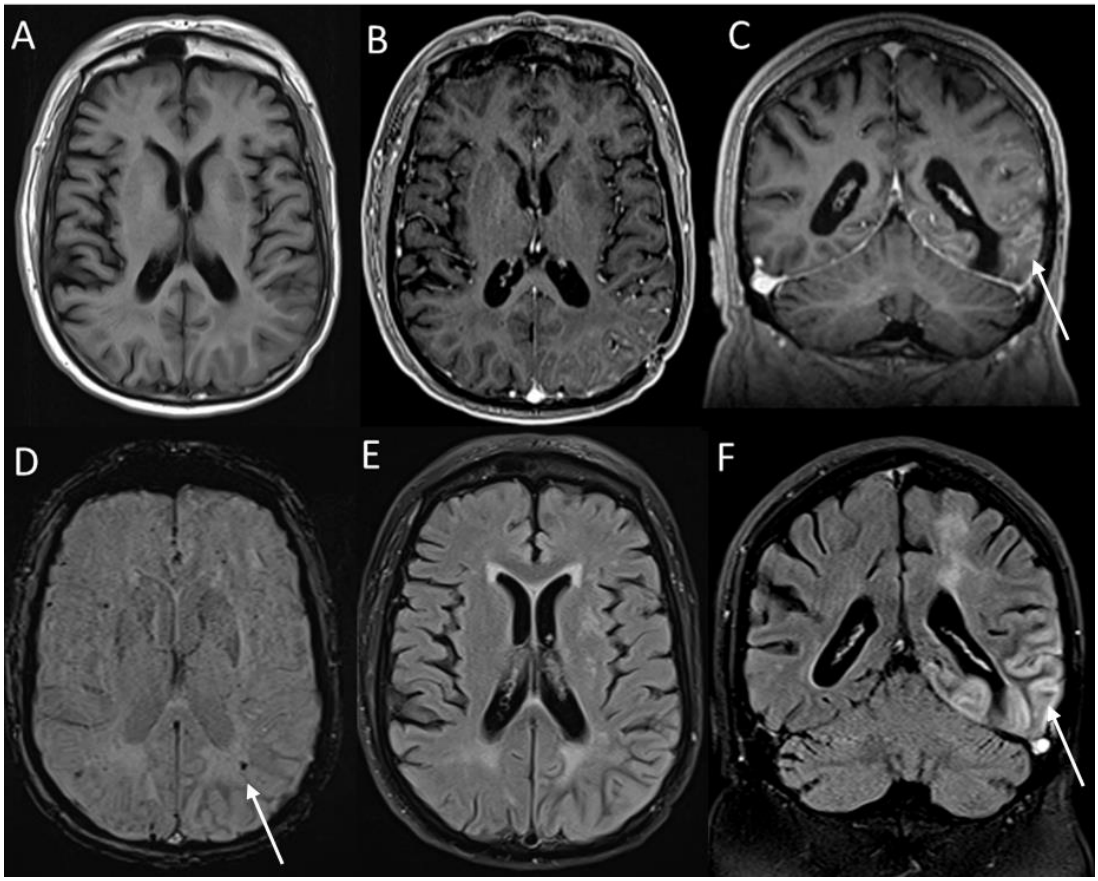

Figure 21. Case of a left parieto-occipital diffuse glioma which was resected and treated with CRT 19 years ago with ongoing surveillance imaging since then. Most recent imaging (A) Pre-contrast T1WI, (B,C) axial and coronal CE-T1WI, (E,F) axial and coronal FLAIR, shows new thickened cortex with FLAIR signal hyperintensity (arrow), as well as cortical and leptomeningeal enhancement in the irradiated area (arrow), in keeping with SMART syndrome. (D) SWI shows foci of susceptibility changes indicating post-radiotherapy cavernoma formation.

Finally, radiation-induced tumours are an uncommon but serious complication and can occur decades following radiation therapy (Figure 22). These can be low-grade or high-grade, with meningioma the most common radiation-induced tumour [157].

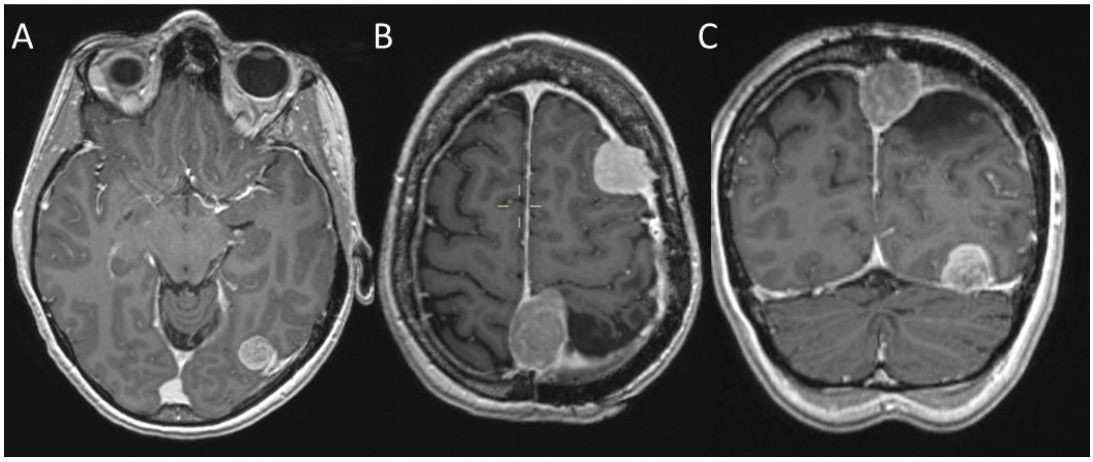

Figure 22. Multiple radiation induced meningiomas. (A,B) Axial and (C) coronal CE-T1WI demonstrating multiple radiation-induced intracranial meningiomas (parasagittal, left tentorial and left frontal) in a patient who had cranial radiotherapy decades previously for leukaemia as a child.

2.10.3 Chemotherapy-related complications

Chemotherapy agents can result in toxicity to various structures in the CNS, with the structure, type and extent of involvement varying according to the agent and dose administered. White matter is particularly vulnerable to chemotherapy-related injury, most commonly resulting in a toxic leukoencephalopathy and many chemotherapy agents can potentiate the effects of radiation-related brain injury. On imaging, the appearances are typically of T2WI/FLAIR hyperintensity in the fronto-parietal white matter and on DWI there may be focal or diffuse areas of reversible restricted diffusion, which improve over time after stopping the causative chemotherapy agent [158].

2.11 Other treatment strategies and experimental approaches

2.11.1 Tumour treating fields (TTF)

TTF delivers low-intensity, intermediate-frequency alternating electric fields via the scalp which selectively disrupting division of glioblastoma cells [159]. A significant survival benefit has been observed by adding TTF therapy to maintenance TMZ therapy, increasing median OS from 16.0 months to 20.9 months and increasing five-year survival from 5% to 13% [159]. The treatment is fairly well tolerated with no increase in systemic side effects, however about a half of patients experience mild to moderate local skin reaction and about 2% of patients develop severe skin reactions [159]. Although TTF is currently used in the United States and in some countries within Europe, it is currently not offered as a treatment in the UK, due to its limited cost-effectiveness.

2.11.2 Anti-angiogenic therapies

These primarily focus on binding to and blocking the vascular endothelial growth factor (VEGF) receptor and have shown to be beneficial in a number of solid tumours as well as in pre-clinical and early clinical glioblastoma trials. Anti-angiogenic therapy appears to improve PFS and possibly improve quality of life, but randomised controlled trials so far have not shown any improvement in OS for patients with glioblastoma [160,161].

2.11.3 Immunotherapy

Immunotherapy treatments for glioblastoma such as immune checkpoint inhibitors, vaccine therapy and adoptive T-cell therapy are undergoing extensive research and clinical trials, however to date, phase III clinical trials for immunotherapy treatments have been disappointing, thought to be due to tumour heterogeneity and the marked immunosuppressive microenvironment induced by glioblastoma [162–164]. Further work is ongoing to try to bypass resistance mechanisms, sensitise glioblastoma to therapy and increase efficacy of the treatments.

2.11.4 Ribonucleic acid (RNA) targeted therapies

RNA targeted therapies have evolved rapidly over the past few years and has the potential for therapeutic targets in glioblastoma, through the use of biodegradable nanoparticles delivery. These can be through liposomes, polymeric nanoparticles, bacterial toxins, stem cell derived exosomes or viral vectors, delivering interference RNA molecules to the tumour and have shown benefit in cell lines and mouse models [165]. This however does not accurately represent a real model due to tumour microenvironment and the presence of the blood-brain barrier (BBB). Although the BBB is disrupted in glioblastoma, it remains a rate-limiting factor for the delivery and therapeutic potential of RNA nanotechnology [166]. Delivery via intrathecal, intraventricular, or intranasal routes to bypass the BBB and techniques to disrupt the BBB such as focussed ultrasound are therefore being investigated. MRI-guided focused ultrasound in combination with cavitating microbubbles can be used to disrupt the BBB and has had extensive research in animal models, showing improved delivery of chemotherapy to

glioblastoma, and is currently being trialled as a promising tool to increase glioblastoma exposure to therapy and reduce systemic toxicity [167].

2.11.5 Convection enhanced delivery (CED)

CED is a method to target therapies such as chemotherapy or conjugated toxins to the CNS and tumour by stereotactic placement of catheters that provide positive-pressure infusion of agents to the target tissue, bypassing the BBB and limiting systemic toxicity [168]. CED has shown to be safe and effective in pre-clinical and clinical studies, however phase III randomised controlled trials have shown no overall benefit and further improvements in CED devices and therapeutic agents is required for this promising tool for the treatment of glioblastoma [168].

2.11.6 Tumour heterogeneity

Recently, an increasing number of studies have reported that worse clinical outcomes are associated with increasing levels of tumour heterogeneity at histological and genetic levels [169]. The heterogeneity is thought to be associated with differences in tumour microenvironment, particularly the pH and oxygen levels in the extracellular environment, as well as glucose and lactate components, which support glioblastoma growth, invasion and infiltration, limiting effectiveness of treatments [170]. Tissue sampling obtained through biopsy can show some information about glioblastoma heterogeneity at the sample site, however, is not able to provide in vivo spatial information about the entire tumour. Furthermore, in the case of tumour recurrence, there is a need to visualise heterogeneity in

vivo. With imaging, phenotypic heterogeneity of the entire tumour is apparent in vivo, through several techniques, which have the advantage of being non-invasive, avoiding the need and risks of biopsy, and assessing heterogeneity more comprehensively. Firstly, advanced techniques that assess and quantitively measure properties of the tissue and tumour microenvironment are able to assess intra- and inter-tumour heterogeneity, discussed further in Chapters 3 and 6. Secondly, macroscopically reflected texture observed on imaging can be used to detect patterns and assess glioblastoma heterogeneity [171], discussed further in Chapters 4, 5 and 7.

2.12 Summary

Glioblastoma is the most common malignant primary brain tumour, and despite significant efforts in diagnostics and treatment strategies, the prognosis for patients is poor, with only a small improvement over the years. Recent updates to the WHO classification of brain tumours have led to major changes, with a much more significant role of molecular markers in the integrated diagnosis and management options for patients with gliomas. In order to improve prognosis and quality of life further for patients with glioblastoma, there is the need for validated biomarkers for earlier diagnosis, better diagnostic techniques for improving the degree of resection of infiltrative non-enhancing disease at surgery and more effective targeted therapies. In addition, interpretation of post-treatment imaging is challenging, and more sensitive and specific biomarkers of treatment response are required to improve patient outcomes.

3. ADVANCED IMAGING IN THE DIAGNOSIS OF GLIOBLASTOMA

Parts of this chapter are adapted from [113], previously published by *Insights into Imaging*.

3.1 Introduction

MRI plays a major role in the diagnosis, grading, treatment planning and treatment response assessment of glioblastoma, as well as other brain tumours and intracranial lesions. Conventional MRI provides the anatomical and structural details of lesions in the neuraxis, however its specificity is limited. Rim-enhancing lesions that mimic the imaging appearances of glioblastoma have a wide differential diagnosis on conventional MRI, each with different treatment strategies. Even with recent improvements in contrast resolution, higher magnetic field strengths and improved contrast agents, tissue characterisation remains limited using conventional imaging acquisitions. When there is diagnostic uncertainty, patients will usually undergo biopsy of brain lesions, which is not without risk [172]. Adjunct MRI techniques have been developed and are used to quantitatively measure a number of properties of brain tissue in vivo, thus allowing regional changes in the tissue microenvironment to be better characterised.

3.1.1 Advanced MRI techniques

The most commonly used advanced techniques in clinical practice are DWI, PWI and MRS. DWI is based on the random (Brownian) motion of water molecules in tissue, and the magnitude is visualised on an ADC map, providing information about water movement and cellularity, with many clinical applications in neuroimaging [173]. PWI provides information about angiogenesis and vascularity and its use has substantially increased over the past decade [174]. MRS provides information about the composition of various metabolites within the tissue. These quantitative methods together provide more than just structural information; they provide functional information about tumour cellularity, proliferation, vascularity, vessel permeability, and tissue metabolite composition [175].

Changes in physiological processes due to the nature of the underlying lesion are reflected in the information obtained from DWI, PWI and MRS. There have been a number of studies demonstrating that these techniques can help improve differentiation of neoplastic from non-neoplastic lesions [176–179] and the grading of brain tumours [180]. The clinical application of advanced imaging for the diagnosis of glioblastoma is detailed later in this chapter, and its role in assessing treatment response is detailed further Chapter 6.

3.1.2 Combining techniques

Over time, there has been development of these adjunct advanced MRI techniques in isolation, beginning with MRS, DWI and then PWI. In clinical practice and throughout the literature usually these techniques were compared with each other, however recent studies show that the information gained from each of these techniques are substantial and

complementary, and there is scarcity of studies investigating the combined approach and this is urgently needed [181]. In this chapter, the combined use of advanced MRI techniques consisting of DWI, PWI and MRS is presented in helping to establish the diagnosis of glioblastoma from similar appearing lesions on imaging.

3.2 Methods

3.2.1 Study design

This was a retrospective review of patients who underwent conventional and multiparametric MRI between June 2014 to March 2021 as part of routine clinical care. The decision to undergo multiparametric MRI was determined at the Queen Elizabeth Hospital Birmingham Neuro-Oncology MDT by uncertainty at the meeting regarding intracranial lesion diagnosis on imaging, which would directly impact upon patient management. Multiparametric MRI was recommended with the aim of providing additional diagnostic information and narrowing the differential diagnosis. A selection of cases highlighting the most common differential diagnoses of glioblastoma on conventional imaging were selected and the utility of multiparametric MRI discussed. Diagnostic outcomes were established from histological, imaging, or clinical follow-up. Approvals for this study were obtained from the University Hospitals Birmingham Research Governance Office.

3.2.2 MRI acquisition

Routine-of-care multiparametric MRI studies were performed on a 3 Tesla scanner (Magnetom Verio; Siemens, Erlangen, Germany) with a 32-channel phased-array head coil.

Standard brain MRI sequences included T2WI and 3D-FLAIR. Echo-planar imaging (EPI) DWI was acquired at *b*-values of 50 and 1000 s/mm^2 with echo time (TE) 100 ms, repetition time (TR) 7000 ms, in-plane resolution of 1 mm and slice thickness of 4 mm. This was followed by DSC perfusion imaging using gradient-echo EPI during the first pass of a standard dose (7.5 mmol) bolus of gadolinium-based contrast agent (Gadovist 0.1 mmol/ml, Bayer plc) administered intravenously at a flow rate of 6 ml/s. A total of 80 imaging volumes were acquired at a temporal resolution of 2.1 seconds with the bolus typically arriving between the 10th and 15th volumes. TE was 30 ms, TR was 2100 ms, in-plane resolution was 1.5 mm and slice thickness was 4 mm. This was followed by a 3D-CE-T1WI magnetisation-prepared rapid acquisition with gradient echo (MPRAGE) sequence acquired in the axial plane (1 mm voxels) with sagittal and coronal reformats. MRS was performed using a combination of multi-voxel (for tumoural and peritumoural regions) and single-voxel point resolved spectroscopy (PRESS) sequences with short echo (TE 30 ms) and intermediate echo (TE 135 ms). TE 135 ms was usually performed to show lactate inversion at 1.3 ppm (J-coupling effect). Typically, 2D or 3D MR spectroscopic imaging (MRSI) was first performed in the axial plane choosing a slice or slab with the largest contrast-enhancing lesion area (or on FLAIR in the case of a non-enhancing lesion), area with restricted diffusion, or high perfusion. This was followed by 10 mm isotropic single-voxel MRS, with placement of the volume-of-interest further guided by the metabolic profiles estimated by MRSI. The single voxel method was used to maximise diagnostic yield by combining information from contrast-enhancement, DWI, DSC-PWI and MRSI to sample the most relevant part of the lesion likely to provide the highest quality spectra.

3.2.3 MRI post-processing and analysis

ADC maps were calculated from the DWI on the MRI scanner software (Magnetom VB17; Siemens, Erlangen, Germany). DSC data were post-processed on a Siemens Leonardo workstation (software version VB17; Siemens, Erlangen, Germany) using a global arterial input function (AIF) without leakage correction, producing maps of rCBV and relative cerebral blood flow (rCBF). MRS data were processed and fitted using the MRI scanner software (Magnetom VB17; Siemens, Erlangen, Germany) to include peak integral values for NAA, Cho, creatine (Cr), myo-inositol (mI), glycine (Gly), glutamine and glutamate (Glx), lactate and lipids. Imaging was visually examined for the areas of lowest ADC values and highest rCBV values (relative to contralateral normal appearing brain) and then measured using a 3 mm ROI. MRS was used to determine the maximum observed ratio of Cho/Cr in the ROI as well as presence or absence of other key metabolites.

3.2.4 Normative and cut-off values

Normal brain ADC values for cortical grey and white matter are 833 x $10^{-6}mm^2s^{-1}$ and 701 x $10^{-6}mm^2s^{-1}$ respectively [182]. Mean ADC values in high-grade neoplastic lesions such as glioblastoma, anaplastic astrocytoma and metastases have shown to be 700-780 x $10^{-6}mm^2s^{-1}$, lymphoma has shown to be 510 x $10^{-6}mm^2s^{-1}$, and low-grade tumours have shown to be 1090 x $10^{-6}mm^2s^{-1}$ [183]. The mean rCBV ratios in high-grade neoplastic lesions have shown to be 1.9, compared to 1.3 in low-grade neoplastic lesions [184]. Normative values for Cho/Cr at TE 135 ms range from 0.7–1.0 in grey matter and 1.2–1.4 in white matter, with slightly higher values seen in the brainstem and cerebellum [185]. Short TE (30 ms) shows more metabolites

and is primarily used for assessing tumoural and non-tumoural lesions. Normal Cho/Cr ratios using short TE MRS are 0.6 in grey matter and 1.0 in white matter [186]. High-grade neoplastic lesions have shown to demonstrate a mean Cho/Cr ratio of 2.4 on short TE MRS, compared with a mean Cho/Cr ratio of 1.5 for low-grade neoplastic lesions [187]. Histopathological correlation has demonstrated that high Cho is suggestive of tumour and lactate is often observed in glioblastoma, thought to represent anaerobic glycolysis in the enhancing rim [116].

As there is a wide variability of cut-off values for each parameter in the literature, based on the results of a number of studies the definition of high-grade neoplastic lesions were deemed to have cut-off values of: ADC $<1000 \times 10^{-6} mm^2 s^{-1}$, rCBV ratio >2.0 and Cho/Cr ratio >1.8 [187–190]. These parameters were used semi-quantitatively by identifying the lowest ADC value, highest rCBV value and highest Cho/Cr ratio within the lesion. This information was read in combination with conventional imaging, clinical findings, and other investigations.

3.3 Neoplastic lesions

As glioblastoma typically presents as a single rim-enhancing, centrally necrotic lesion, the neoplastic differential diagnoses would include a single cerebral metastasis, primary CNS lymphoma in an immunocompromised patient and other primary neoplastic lesions. In the case of multifocal or multicentric glioblastoma, multiple metastases or secondary CNS lymphoma would remain differential diagnoses. As glioblastoma can also present as a non-enhancing lesion, patients who present with a low-grade appearing lesion on conventional imaging should have non-enhancing glioblastoma as a suspected differential diagnosis.

3.3.1 Metastasis

Intracranial metastasis has a similar conventional imaging appearance to glioblastoma. In the presence of normal body imaging and no source of primary neoplastic disease, it can be challenging to distinguish between the two. Metastases usually present as smaller lesions, generally located near the grey-white matter junction, and with proportionally more extensive surrounding vasogenic oedema compared to the size of the lesion than glioblastoma, although these are not entirely reliable methods to distinguish between the entities. However, as glioblastoma infiltrates the brain parenchyma surrounding the enhancing lesion, there are expected to be differences in this region, as opposed to metastases in which there is no invasion of the surrounding parenchyma. Conventional imaging show no discernible differences in the perilesional oedema, however a number of advanced MRI techniques have shown to be able to discriminate between glioblastoma and metastasis based on the perilesional environment due to diffuse tumour infiltration beyond

the enhancing margins in glioblastoma [191]. On MRS, the abnormal perilesional ratios of NAA/Cr >1.5, Cho/Cr >1.4 and Cho/NAA >1.1, as well as rCBV >1.7 have shown to be able to differentiate glioblastoma from metastases with a high sensitivity, with the Cho/Cr ratio performing best at 89%, however the intratumoural values for these metrics did not show any significant differences between the two pathologies [192]. In the case of metastases, the peritumoural region showed values which were closer to the contralateral normal appearing parenchyma. A case of metastasis demonstrating a normal perilesional environment on MRS is shown in **Figure 23**.

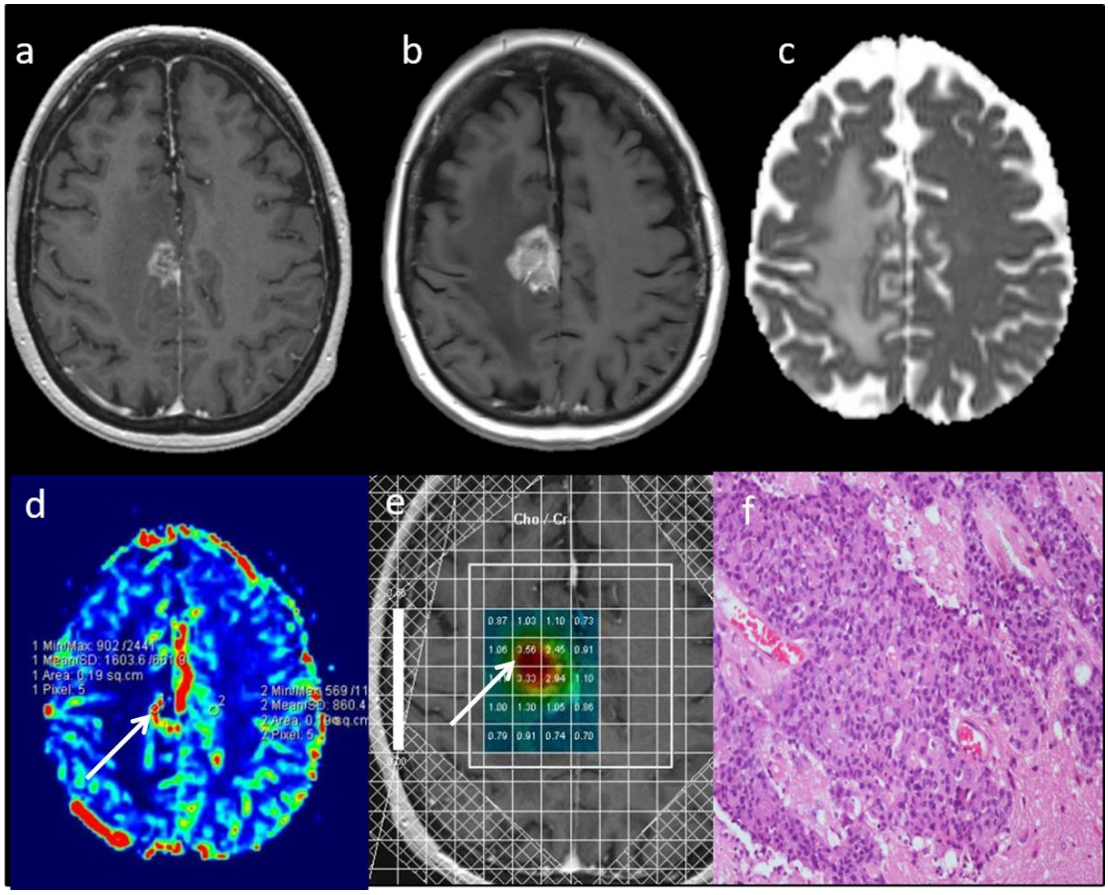

Figure 23. Brain metastasis from breast carcinoma. (a) CE-T1WI showed a lesion in the motor area of the right mesial frontal lobe. (b) Follow-up imaging demonstrated increase in the lesion size with oedema. Multiparametric MRI demonstrated: (c) a low ADC (999 x10^{-6}

mm^2/sec), (d) a borderline rCBV ratio (1.9, arrow) on PWI, and (e) high Cho/Cr ratio (3.6, arrow) on multi-voxel MRS (TE=30 ms). The perilesional parenchyma showed a low Cho/Cr ratio, reflecting vasogenic oedema as opposed to tumour infiltration. (f) Histopathology demonstrated poorly differentiated metastatic adenocarcinoma with discernible focal ductal structures and tumour well demarcated from adjacent brain tissue.

In comparison to metastasis which demonstrates a normal metabolic profile in the peritumoural region, a case of glioblastoma mimicking a haemorrhagic metastasis is shown in Figure 24; in this case the perilesional environment demonstrates an abnormally raised Cho/Cr ratio, indicative of glioblastoma tumour infiltration. Two types of patterns on the MRS spectrum have previously been observed in glioblastoma; the first, seen in the majority of cases is a high Cho and lactate-dominant peak which is associated with lesions that homogeneously enhance or cystic lesions, and the second is a high Cho and a lipid-dominant peak which is seen in ring-enhancing masses with irregular margins on imaging [193].

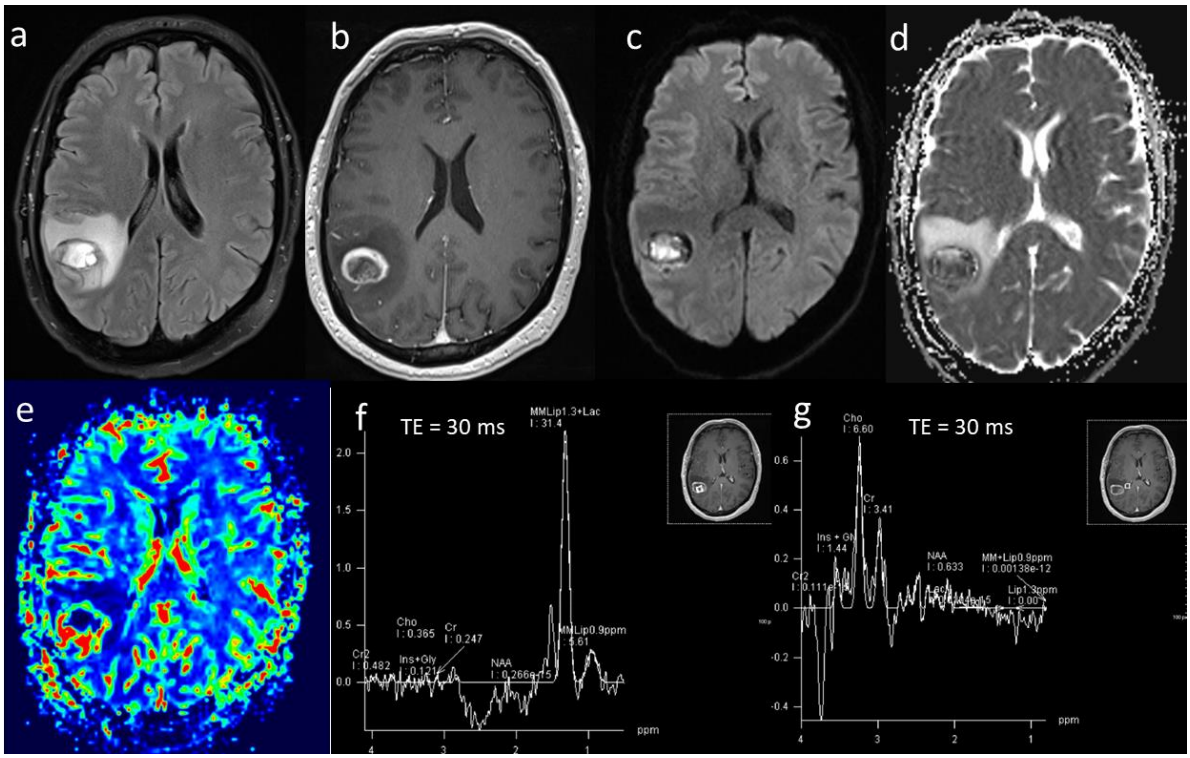

Figure 24. Glioblastoma mimicking a haemorrhagic metastasis. Conventional MRI: (a, b) Axial FLAIR and CE-T1WI, showed a haemorrhagic thick-rimmed enhancing space-occupying mass lesion in the right temporo-parietal region with perilesional oedema. Multiparametric MRI: (c, d) DWI and ADC map demonstrated susceptibility artefact due to haemorrhage within the lesion. (e) PWI showed high perfusion along the enhancing posterolateral aspect of the lesion. (f) MRS within the centre of the lesion demonstrated susceptibility artefact due to the presence of haemorrhage, however a high level of necrosis was demonstrated by the high lipid peak. (g) MRS from perilesional oedema showed a high Cho/Cr ratio (>2), suggesting an abnormal microenvironment. The very high rCBV and high Cho/Cr ratio were consistent with a high-grade glioma containing internal haemorrhage rather than simple haemorrhage, metastasis, lymphoma, granuloma or abscess. The lesion was resected and histopathology confirmed IDH-wildtype glioblastoma.

Other metrics that have been investigated include mean diffusivity (MD) from DTI, which is higher in peritumoural vasogenic oedema from metastases compared to infiltrative oedema in glioblastoma [194]. Using rCBV >3.14 and MD <143 x $10^{-6}mm^2s^{-1}$, the diagnostic accuracy of differentiating glioblastoma from metastasis was 98% [195]. Recently, neurite orientation

dispersion and density imaging (NODDI) of the perilesional oedema has also shown to be useful to discriminate between the two lesions [196]. This is an emerging advanced DWI method that has been developed to evaluate dendrite and axonal microstructure based on a non-Gaussian diffusion model, demonstrating a good agreement of fibre density with histological validation [197]. NODDI has shown to outperform DWI, DTI and diffusion kurtosis imaging (DKI) in differentiating between the lesions [198], although these were small studies. The use of radiomics and machine learning for this clinical issue is further discussed in Chapter 4.

3.3.2 Lymphoma

Primary CNS lymphoma (PCNSL) is a form of extranodal non-Hodgkin's Lymphoma and unlike other brain neoplasms, resection of PCNSL rarely provides benefit, instead chemotherapy and radiotherapy are preferred treatment choices [199]. Hence, it is important to differentiate lymphoma from glioblastoma. Typical conventional imaging appearances of PCNSL are an avidly homogenously enhancing mass, which is hypointense on T1WI and iso- to hypointense on T2WI. There is little mass effect for size and limited surrounding vasogenic oedema. Multiparametric MRI in PCNSL demonstrates a very low ADC indicating dense cellular packing, lower perfusion due to lack of angiogenesis (rCBV <2.18) [200], very high Cho/Cr ratio due to high membrane turnover, high lipid peak at 1.3 ppm due to infiltration by macrophages even without necrosis [201], and very low NAA levels [202]. Imaging features of typical PCNSL is demonstrated in Figure 25.

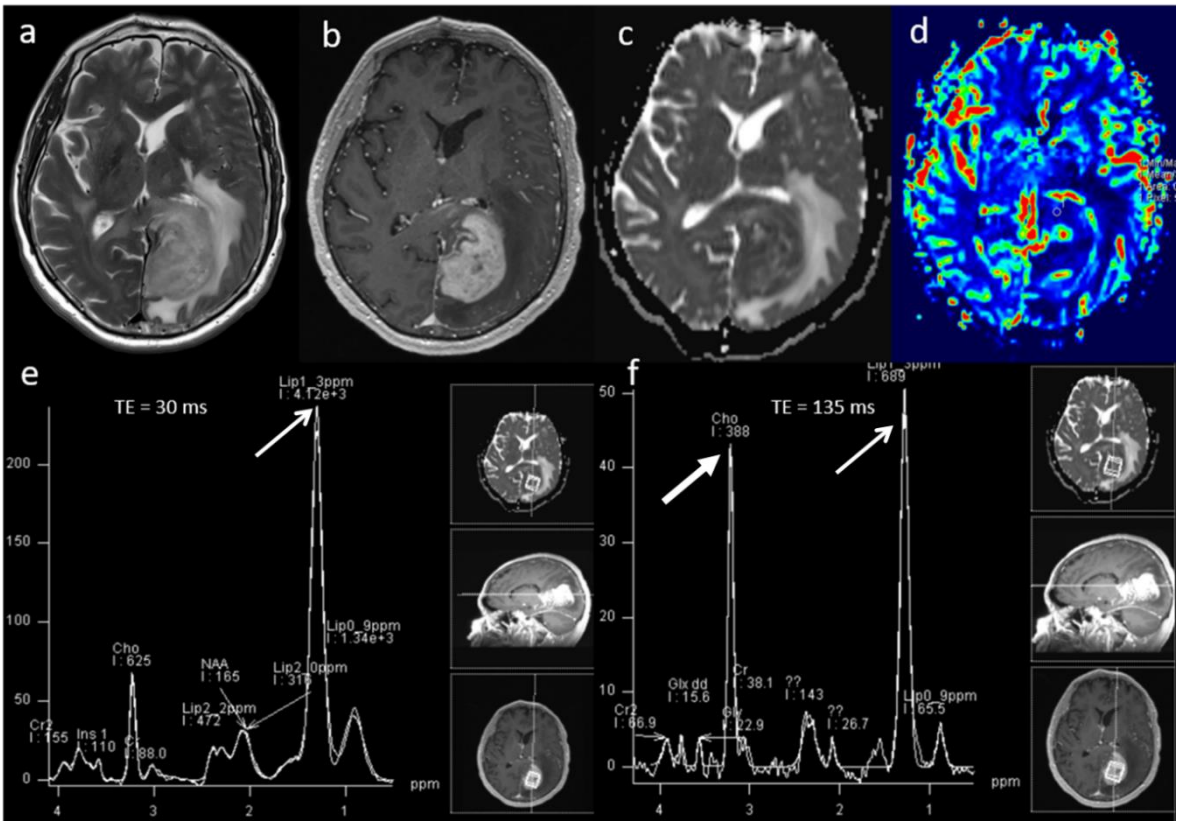

Figure 25. Primary CNS lymphoma. Conventional MRI Findings: (a, b) Axial T2W and post-contrast T1W sequences showed a large homogenously enhancing lesion in the left occipital lobe. (c) ADC map showed very low ADC (<600 x $10^{-6}mm^2s^{-1}$) throughout the lesion. (d) PWI showed low perfusion throughout the lesion compared to normal-appearing contralateral white matter. (e, f) MRS showed a very high Cho/Cr ratio (>6, thick arrow) and very high lipid peaks in a non-necrotic appearing lesion (TE 30 ms and 135 ms, thin arrows). The low perfusion, very low ADC, very high lipid peak in a non-necrotic appearing lesion and high choline peak were characteristic of lymphoma. Histopathology confirmed a diffuse large B-cell PCNSL.

The atypical imaging appearances of PCNSL are necrosis, irregular or peripheral enhancement and haemorrhage, closely mimicking glioblastoma on conventional imaging (Figure 26). It is generally seen in Epstein Barr Virus (EBV)-positive PCNSL as well as patients who are immunocompromised, such as patients with human immunodeficiency virus (HIV), chronic alcohol misuse, and certain collagen vascular diseases, however there is also some evidence

that immunological deterioration due to normal ageing can also lead to these atypical appearances of PCNSL [203].

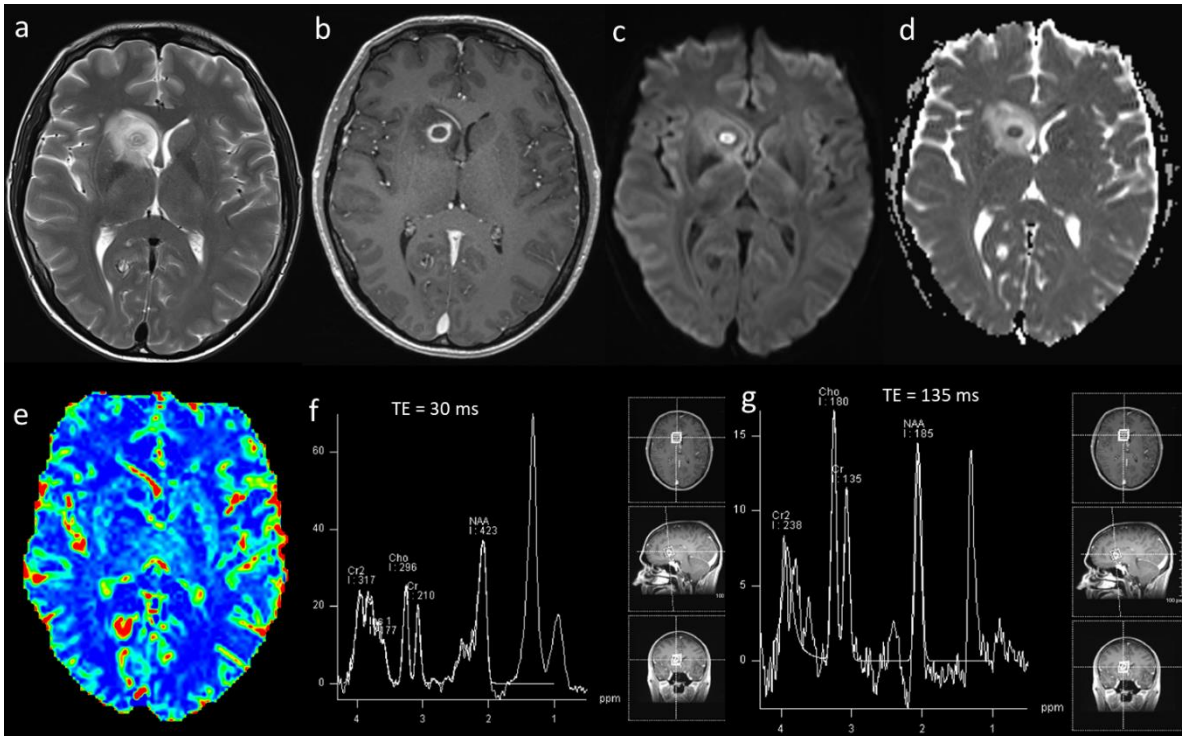

Figure 26. Atypical appearances of lymphoma. Conventional MRI Findings: (a, b) Axial T2WI and CE-T1WI showed a rim-enhancing space-occupying lesion in the right caudate nucleus with surrounding oedema. (c, d) DWI and ADC map showed very low ADC within the central area of necrosis. (e) PWI showed low perfusion throughout the lesion compared to normal-appearing contralateral white matter. (f, g) MRS showed slightly raised Cho/Cr ratio and the presence of lipid at 1.3 and 0.9 ppm. No amino or organic acid peaks were present to suggest abscess. The low perfusion, low ADC, high lipid peak and only slightly raised choline favoured an atypical/necrotic-appearing lymphoma over a high-grade glioma. Histopathology confirmed a diffuse B-cell non-Hodgkin lymphoma.

Haemorrhage within PCNSL is a rare, but can occur as an atypical presentation [204]. A confirmed case of haemorrhagic glioblastoma mimicking lymphoma on conventional MRI as well as DWI and MRS is shown in **Figure 27**. In this case, the raised rCBV on PWI was the

distinguishing factor for glioblastoma rather than lymphoma, despite the typical PCNSL appearances of markedly low ADC on DWI and very high Cho/Cr ratio and lipid peaks on MRS.

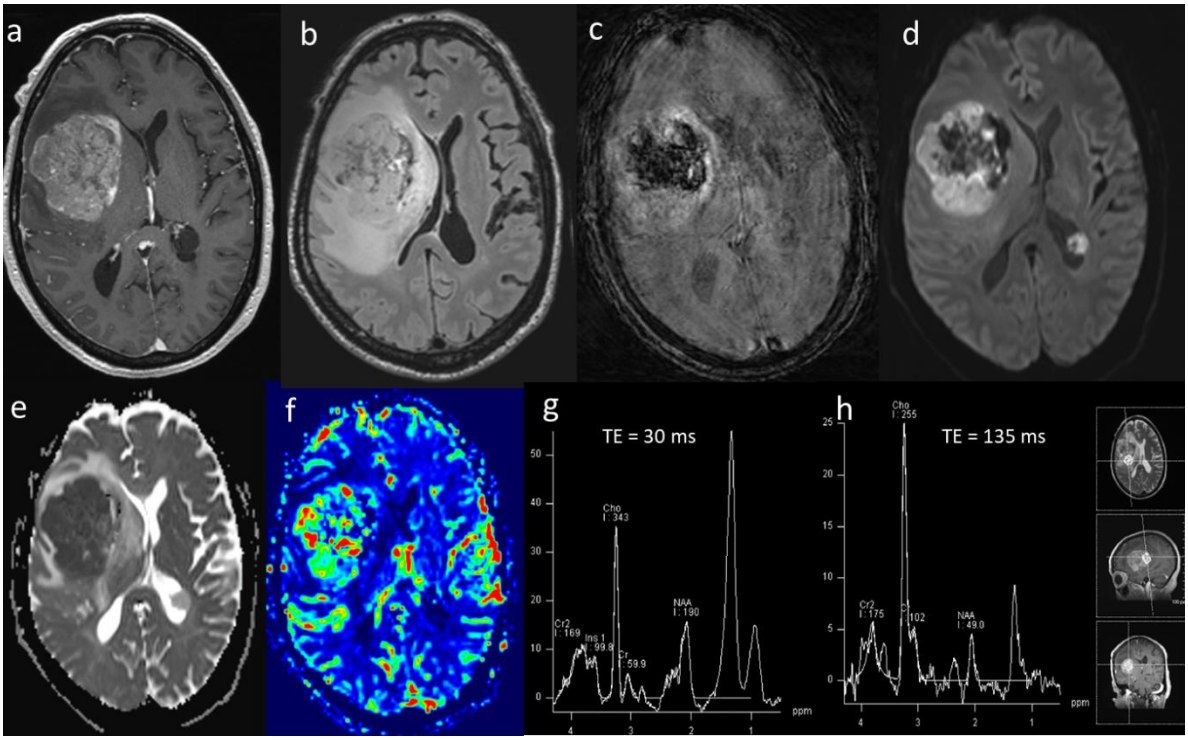

Figure 27. Glioblastoma mimicking haemorrhagic lymphoma. Conventional MRI: (a, b) Axial CE-T1WI and FLAIR sequences, showed a large heterogeneous solid space-occupying mass lesion in the right insular lobe extending into the frontal operculum with perilesional oedema. (c) SWI showed susceptibility artefact indicating internal haemorrhage. Multiparametric MRI: (d, e) DWI and ADC map demonstrated restricted diffusion in the non-haemorrhagic areas of the enhancing lesion. (f) PWI showed high perfusion within the enhancing component. (g, h) MRS from the non-haemorrhagic enhancing component showed a very high Cho/Cr ratio and a very high lipid peak. Resection of the lesion confirmed a diagnosis of IDH-wildtype glioblastoma.

A meta-analysis of 22 studies to evaluate the diagnostic performance of advanced MRI techniques to differentiate between PCNSL from glioblastoma showed a high diagnostic performance, with PWI techniques of DSC or ASL showing the highest performance [205]. A

number of recent studies have investigated machine learning techniques to distinguish between glioblastoma and PCNSL, resulting in a moderate to high model performance with an area under the receiver operating characteristic curve (AUC) of 0.77-0.98 across all studies and also superior to radiologists in some [206–210].

3.3.3 Transforming low grade glioma and non-enhancing glioblastoma

Low-grade gliomas are primary neoplasms of the brain which are generally slow-growing and are typically diagnosed in young adults between the ages of 20-45 years [211,212], but most will transform to a high-grade lesion, with the median time being 56 months for grade 2 gliomas [213]. Low-grade gliomas are usually detected incidentally and appear as an area of focal signal abnormality with no enhancement on conventional MRI. Multiparametric MRI features of a low-grade glioma are a relatively high ADC (>1000 x $10^{-6}mm^2s^{-1}$), low rCBV (<2), low Cho/Cr ratio (<1.8), high NAA and absence of lactate and lipids on MRS [214,215]. Imaging features of a typical low-grade glioma is demonstrated in **Figure 28**.

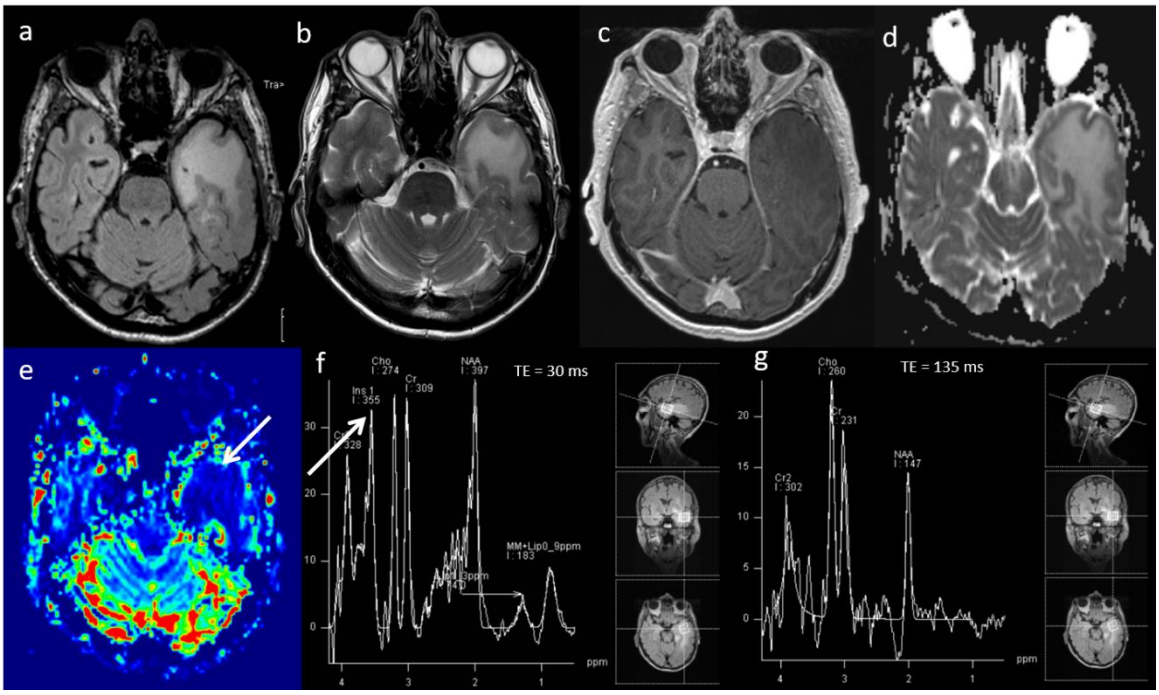

Figure 28. Low-grade glioma. Conventional MRI: (a) FLAIR, (b) T2WI and (c) CE-T1WI showed a diffuse abnormality in the left temporal lobe without contrast enhancement. (d) ADC map showed high ADC throughout the lesion (1300 x $10^{-6}mm^2s^{-1}$), (e) PWI showed low perfusion throughout the lesion (arrow) compared to normal-appearing white matter, and (f, g) MRS (TE 30 ms) showed slightly raised Cho/Cr ratio (1.0), slightly low NAA/Cr (1.1) and a very high mI/Cr ratio (0.9, arrow). Lipid or lactate peaks were not significantly elevated. Multiparametric MRI appearances suggested no evidence of dedifferentiation. Stable appearances were seen on follow-up imaging for over five years, confirming the lesion's low-grade nature.

The presence of contrast enhancement in a diffuse glioma is often regarded as a sign of a high-grade lesion, however non-enhancing diffuse gliomas are high-grade (Grade 3/4) in approximately one third of cases [31]. This has an impact upon treatment, patient outcome and OS, as conventional MRI has limitations for the grading of lesions. Non-enhancing glioblastoma and transforming low-grade gliomas can show changes in multiparametric MRI metrics before contrast enhancement is seen on conventional imaging. In the case of perfusion imaging, a significant increase in rCBV can be seen up to 12 months before

transformation is seen on conventional imaging [216]. Multiparametric MRI features of a non-enhancing high-grade glioma or transforming low-grade glioma are focal low ADC (<1000 x $10^{-6}mm^2s^{-1}$), high rCBV (>2), high Cho/Cr ratio (>1.8), low NAA and presence of lactate and lipids on MRS [214,215,217], and the use of these advanced techniques are recommended in the current NICE guidelines for assessing potential of high-grade transformation in a tumour appearing to be low-grade on conventional MRI [28]. The typical multiparametric MRI features of a non-enhancing glioblastoma are demonstrated in **Figure 29**. In the early stages of malignant transformation, only one or two of the above parameters may be abnormal focally within the tumour, and any longitudinal changes in multiparametric information can suggest a transforming tumour.

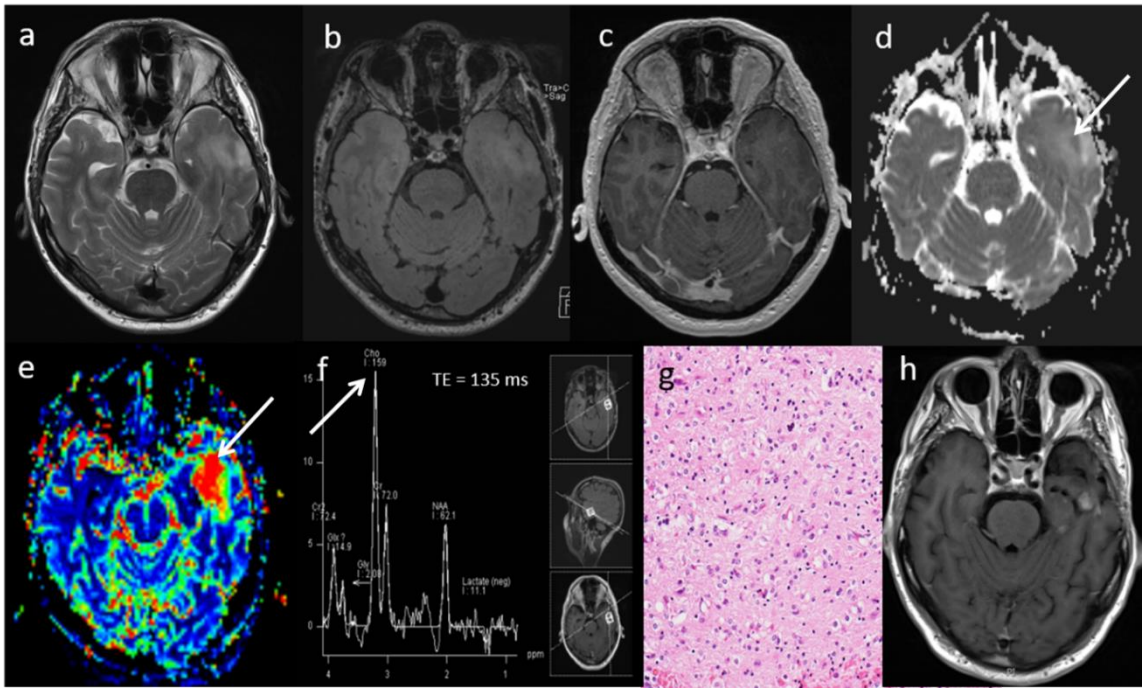

Figure 29. Non-enhancing glioblastoma. (a-c) T2WI, FLAIR and CE-T1WI sequences demonstrated a non-enhancing signal abnormality in the left temporal lobe. Multiparametric MRI: (d) Heterogeneous ADC values throughout the lesion with focal areas of low ADC (lowest observed 940 x $10^{-6}mm^2s^{-1}$, arrow). (e) High rCBV throughout the lesion (arrow) compared to

normal-appearing white matter (3.5). (f) Single-voxel spectroscopy showed very high Cho/Cr (2.3, arrow) and Cho/NAA ratios (3.1). (g) Histopathology from biopsy of the lesion showed low grade diffuse astrocytoma with mild to moderately pleomorphic astrocytic cells in a fibrillary background. There was discrepancy of histological and genetic classification with morphological features of a low-grade glial neoplasm, but a convincing genetic profile of glioblastoma, overriding the morphological appearances. (h) Follow-up imaging 6 months later showed contrast enhancement on conventional MRI.

In non-enhancing tumours, there is risk of inaccuracy in stereotactic biopsy leading to under-grading of WHO grade 3 tumours, reported in 28% of cases [218]. Successful stereotactic biopsy diagnosis rate utilising multiparametric MRI techniques has shown to be more than 93% [219]. To obtain a better biopsy yield and to avoid sampling error for non-enhancing tumours, the target of biopsy can be selected from a high Cho, high rCBV or low ADC location. A case demonstrating high-grade transformation of a diffuse glioma and the use of Cho mapping for choosing the highest Cho peak to target biopsy in a non-enhancing tumour is shown in Figure 30. Early detection of non-enhancing glioblastoma and malignant transformation, before contrast enhancement is seen on conventional MRI will allow early initiation of appropriate treatment, which will ultimately have an effect on improving the patient's OS.

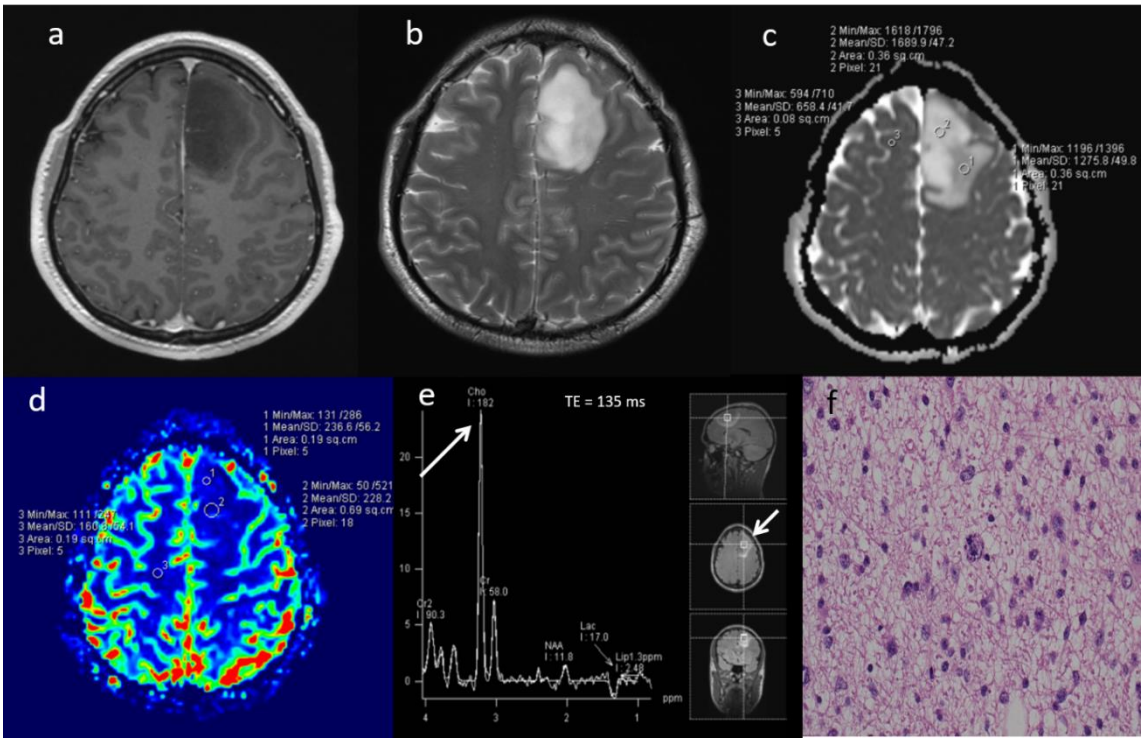

Figure 30. High-grade transformation of a non-enhancing diffuse glioma and targeting biopsy using multiparametric MRI. Conventional MRI: (a, b) CE-T1WI and T2WI demonstrated a large non-enhancing space occupying mass lesion without significant oedema. Multiparametric MRI: (c, d) Heterogeneous ADC and rCBV values throughout the lesion. (e) Multi-voxel MRS clearly showed a focal area of very high Cho/Cr ratio and very small lactate peak. (f) A targeted biopsy was taken from the area of highest choline peak (arrow), and histopathology showed anaplastic astrocytoma with moderately atypical astrocytic cells in a fibrillary background with a few abnormal mitoses (WHO grade 3).

Another advanced imaging technique which has shown promise include magnetic resonance fingerprinting-based relaxometry, which acquires T1 and T2 measurements simultaneously within the lesion and perilesional region. This has shown significant quantitative differences in the perilesional region between glioblastoma and lower grade glioma with mean T1 value of the peritumoural white matter being significantly higher in glioblastoma compared to low-grade glioma (1578 vs. 1066 ms) [220]. In addition, machine learning-based texture radiomics

shows promise and has shown to be able to distinguish between low-grade and high-grade gliomas using DWI and PWI with a high accuracy (>90%) [221].

3.3.4 Gliomatosis cerebri

Gliomatosis cerebri is a rare growth pattern of infiltrative diffuse glioma involving at least 3 lobes of the brain with an incidence of 0.1 per million [222]. Based on the 2016 WHO classification, a recent clinicopathological study identified that the majority of tumours exhibiting this pattern of infiltration were IDH-wildtype diffuse or anaplastic astrocytomas (70%), followed by IDH-mutant diffuse or anaplastic astrocytomas and lastly IDH-wildtype or IDH-mutant glioblastoma (5%) [223]. Due to the extensive involvement, palliative surgery, radiotherapy and chemotherapy have been used to treat patients with gliomatosis cerebri, however there is currently no established treatment guideline [223]. Multiparametric MRI can help in making the diagnosis of a high-grade infiltrative tumour lesion from other non-neoplastic causes and help to identify areas of early transformation and a suitable biopsy target, given the widespread changes [224]. A case of gliomatosis cerebri with focal changes on PWI is shown in **Figure 31**.

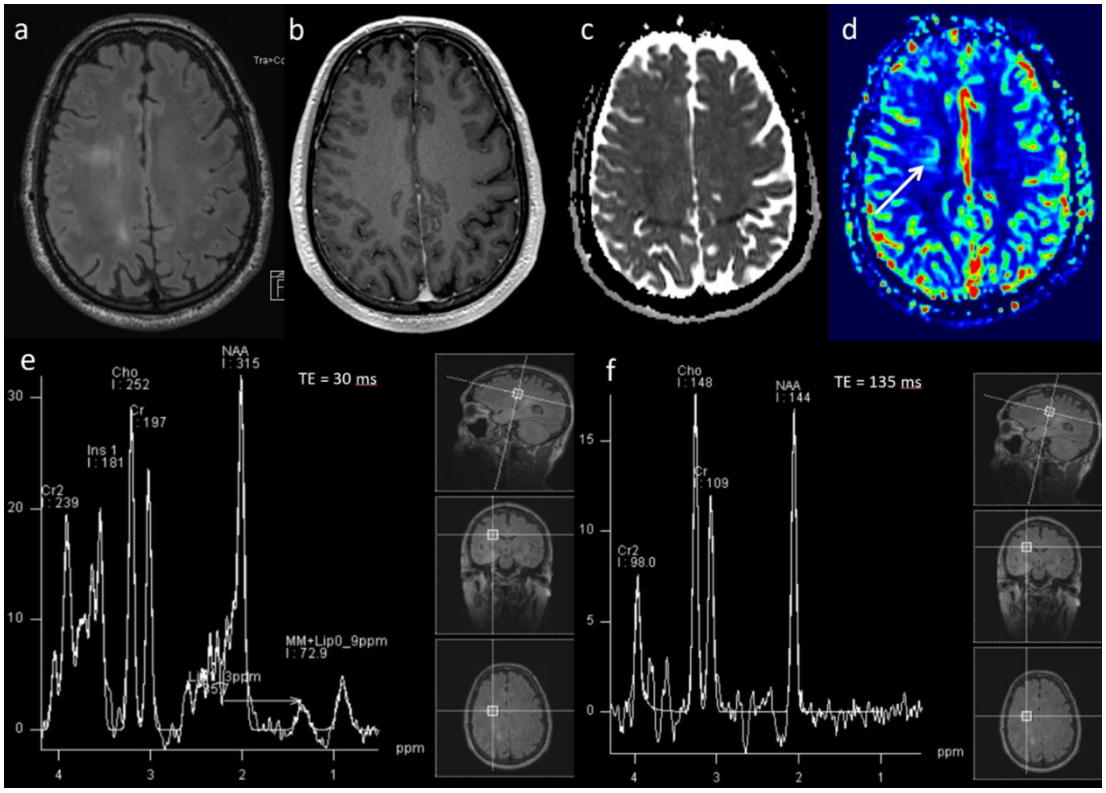

Figure 31. Gliomatosis cerebri pattern of disease. Conventional MRI: (a, b) Axial FLAIR and CE-T1WI showed diffuse non-enhancing multifocal deep white matter infiltrative lesions throughout both cerebral hemispheres. Multiparametric MRI: (c) ADC map demonstrated no areas of low ADC. (d) However, PWI showed a focal area of slightly raised perfusion in the right frontal centrum semiovale (arrow) compared to normal-appearing white matter. (e, f) MRS showed high mI/Cr ratio, slightly raised Cho/Cr ratio (1.2) and slightly low NAA/Cr ratio. Focal raised perfusion and choline area was chosen for the optimal site of a targeted biopsy.

3.3.5 Epidermoid-like lesion of the corpus callosum

The main differential diagnoses for a mass lesion involving the corpus callosum lesion is between glioblastoma and lymphoma. On conventional imaging, it is sometimes difficult to differentiate between these two entities and other less common lesions. In Figure 32, a case of a rare benign epidermoid-like lesion of the corpus callosum is demonstrated. The multiparametric MRI features favoured a benign lesion rather than glioblastoma or lymphoma and this was confirmed on biopsy.

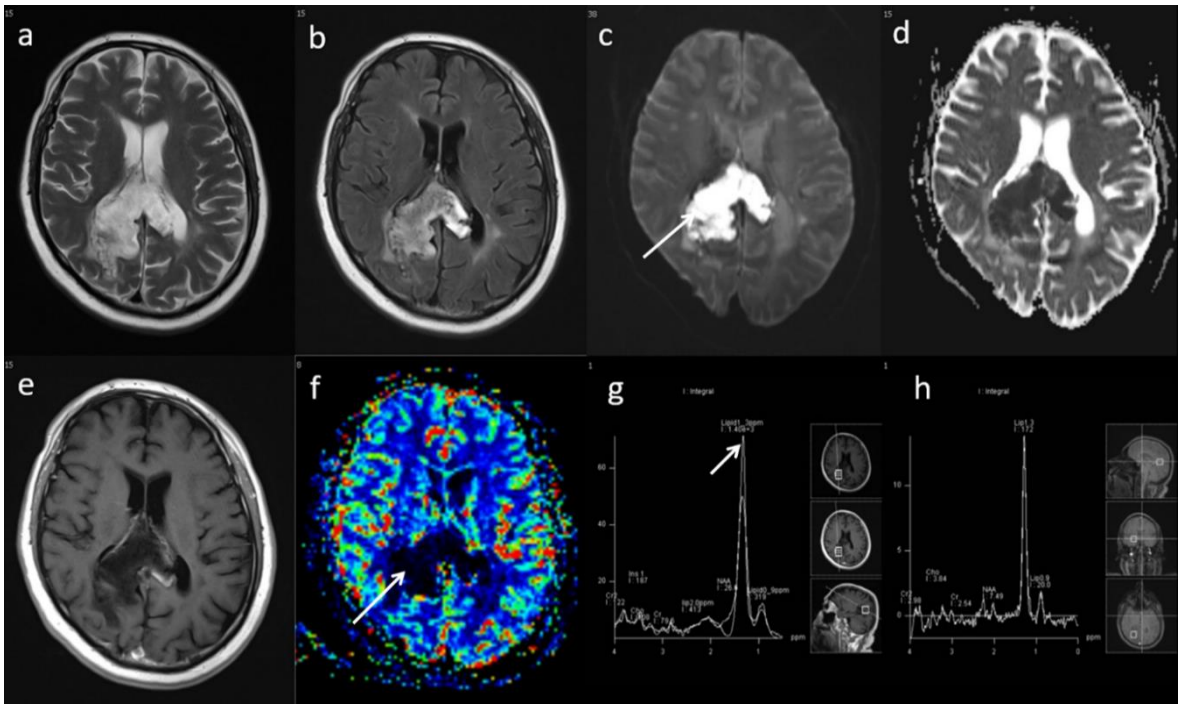

Figure 32. Epidermoid-like lesion of the corpus callosum. Conventional MRI: (a-c) T2WI, FLAIR and CE-T1WI showed a lesion involving the splenium of the corpus callosum and right parietal lobe. Multiparametric MRI: (d, e) DWI and ADC map showed restricted diffusion (arrow). (f) Very low perfusion on PWI (arrow). (g) MRS showed very high lipid (1.3 ppm, arrow), without an increase in Cho. In this case, appearances were not typical for high-grade glioma as there was low perfusion and no significant increase in Cho, and not typical for lymphoma as there was no contrast enhancement or raised Cho. Biopsy was consistent with epidermoid-like lesion with no evidence of malignancy.

3.4 Infective lesions

Similar appearing lesions to glioblastoma on conventional imaging with an infective aetiology most commonly include pyogenic abscess and other less common aetiologies can include tuberculoma, toxoplasmosis, cryptococcoma, neurocysticercosis, aspergillosis as well as other rarer opportunistic infections.

3.4.1 Abscess

Cerebral abscesses account for 1-8% of intracranial mass lesions [225]. Diagnosis can be challenging as abscesses on conventional imaging can mimic primary necrotic tumours and metastases. Multiparametric MRI features of pyogenic abscess are uniformly low ADC due to the higher viscosity of fluid. The ADC values are typically less than $700 \times 10^{-6} mm^2 s^{-1}$ [226], which is lower than expected to be seen in high-grade tumours or metastases ($700\text{-}780 \times 10^{-6} mm^2 s^{-1}$). A case demonstrating haemorrhagic glioblastoma mimicking a pyogenic abscess on conventional and DWI alone is shown in **Figure 33**. In addition, a second similar case is shown in **Figure 34**, in which there was no discernible haemorrhage on CT or MRI except subtle findings on the SWI sequence, highlighting the need for the combined use of advanced imaging and additional parameters to distinguish between glioblastoma and pyogenic abscess.

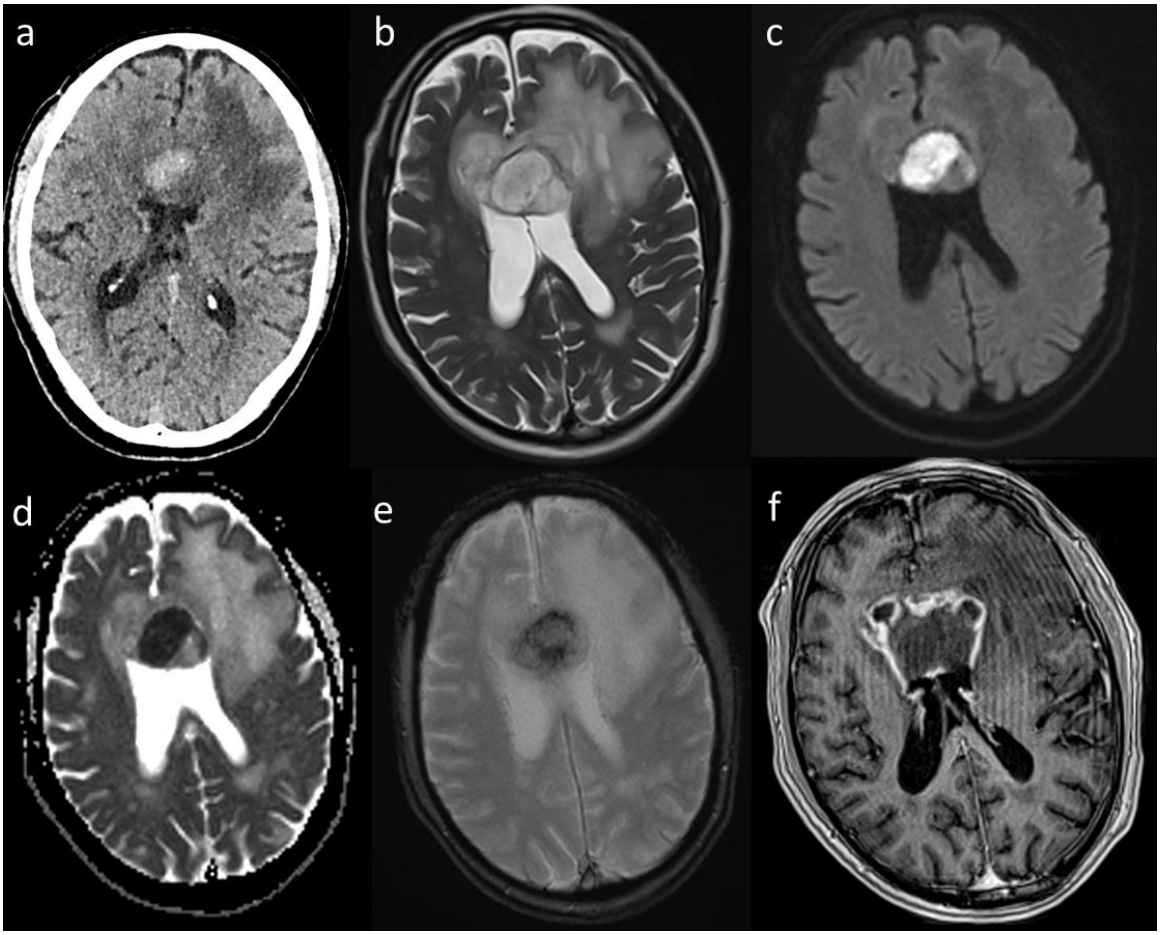

Figure 33. Haemorrhagic glioblastoma mimicking pyogenic abscess. (a) Non-contrast CT showed a hyperdense lesion in the genu of the corpus callosum with extensive surrounding vasogenic oedema. (b) T2WI confirmed a mass lesion with surrounding vasogenic oedema. (c, d) DWI and ADC map showed restricted diffusion with very low ADC within the majority of the lesion. (e) SWI demonstrated faint internal susceptibility artefact. (f) CE-T1WI showed a necrotic appearing mass lesion within the genu of the corpus callosum with thin, irregular peripheral enhancement. The findings on conventional imaging and DWI alone were unable to distinguish between pyogenic abscess and glioblastoma. In this case, follow-up was consistent with glioblastoma. The restricted diffusion is this case was due to haemorrhage, which appeared at least subacute in age, and can be misleading in making the correct diagnosis on imaging.

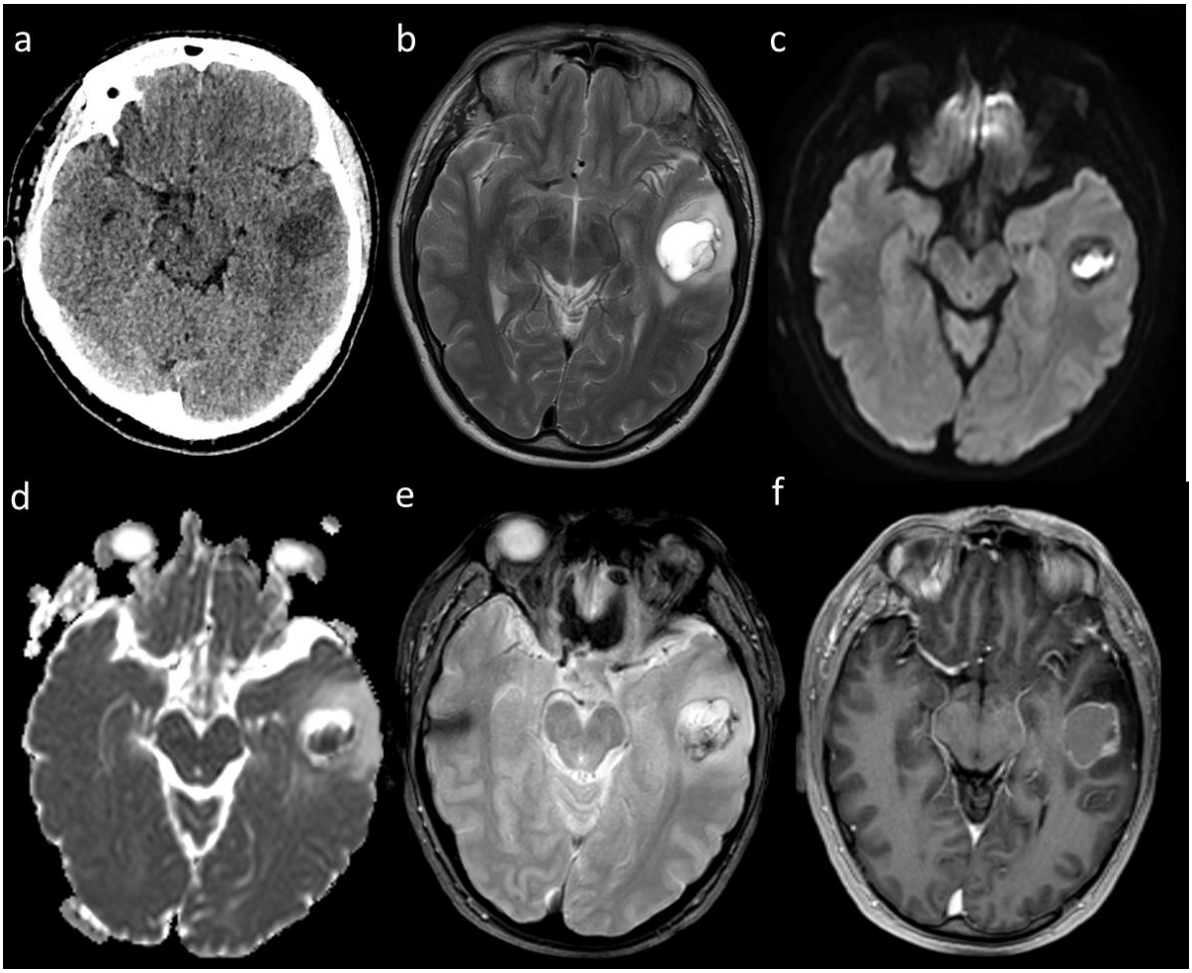

Figure 34. Glioblastoma mimicking pyogenic abscess. (a) Non-contrast CT showed a low attenuation lesion in the left temporal lobe, with no evidence of haemorrhage. (b) T2WI confirmed a cystic mass lesion with surrounding vasogenic oedema. (c, d) DWI and ADC map showed discrete areas of internal restricted and non-restricted diffusion. (e) SWI demonstrated faint internal susceptibility artefact posteriorly. (f) CE-T1WI showed a cystic lesion with thin, irregular rim enhancement. The findings on conventional imaging and DWI alone were unable to confidently distinguish between pyogenic abscess and glioblastoma. Histology was consistent with glioblastoma. The internal restricted diffusion is this case is due to haemorrhage, not appreciable on CT or other conventional sequences, and can be misleading if not identified on SWI or if not combined with other multiparametric imaging.

Given that conventional imaging and DWI alone have a limited ability to distinguish between glioblastoma and abscess, PWI and MRS have shown to be useful to make the distinction.

Perfusion, specifically rCBV is significantly lower in pyogenic abscess compared to

glioblastoma (1.91 vs. 2.76) [227]. MRS features of abscess are different from tumours and show the presence of lactate as well as amino and organic acids such as valine, alanine (0.9 and 1.5 ppm), acetate (1.9 ppm) and pyruvate (2.4 ppm) within the necrotic cavity, which is characteristic for the diagnosis of an abscess [193]. By using MRS and DWI, the sensitivity and specificity for diagnosis is up to 100% [228,229]. Typical multiparametric appearances of a pyogenic abscess are shown in Figure 35.

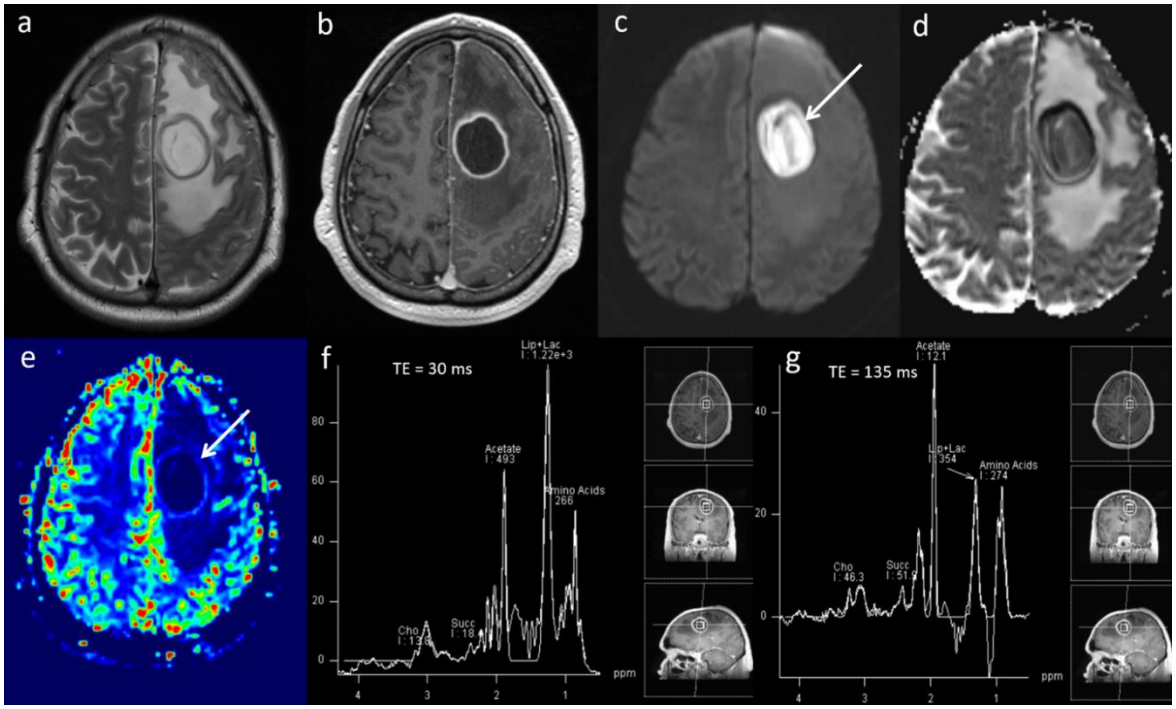

Figure 35. Pyogenic abscess. Conventional MRI: (a, b) T2WI and CE-T1WI sequences demonstrated a ring-enhancing mass lesion in the left frontal lobe with surrounding oedema. (c, d) DWI and ADC sequences showed low ADC (600 × $10^{-6}$$mm^2s^{-1}$, arrow) throughout the lesion. (e) PWI demonstrated significantly lower perfusion (arrow) than the contralateral white matter. (f, g) MRS showed high lipid as well as the presence of amino and organic acid peaks. These characteristic MRS findings in combination with the very low ADC and low perfusion were diagnostic of abscess. Diagnosis was confirmed on aspiration which revealed colonies of gram-positive cocci.

Other techniques that have shown to be able to differentiate between the two pathologies with a high accuracy are DTI metrics. Abscess showed significantly lower MD, higher fractional anisotropy (FA) and higher planar coefficient (CP) compared to necrotic glioblastoma, with a classification model sensitivity and specificity of 91% and 93% respectively [227]. Asphericity values from an ROI of the lesion on CE-T1WI have also shown to be useful, with abscesses being more spherical and a model AUC of 0.98, with the advantage of being simpler than using machine learning-based radiomic models [230]. In addition, SWI has shown to be useful by assessing the degree of intralesional susceptibility signal (ILSS). In glioblastoma, as there is angiogenesis there is associated increased signal loss on SWI indicating tumour microvascularity, which when combined with ADC values had a 100% accuracy for distinguishing between necrotic glioblastoma and pyogenic abscess [231].

3.4.2 Tuberculoma

Intracranial tuberculoma is a rare cause of a space-occupying lesion composed of caseating granuloma from systemic spread of tuberculosis infection, but potentially lethal as it can rupture and cause tuberculous meningitis. Conventional MRI appearances of tuberculoma can mimic glioblastoma due to ring enhancement, but often also shows hypointensity on conventional T2WI. Multiparametric MRI usually demonstrates an intermediate level of ADC, elevated perfusion, and high lipids on MRS, with a normal spectroscopic pattern in the perilesional area. ADC can be variable according to the stage of disease, degree of cellular infiltration and liquefactive necrosis [232]. Elevated rCBV is seen in tuberculoma, secondary to angiogenesis and inflammation. The lipids at 1.3 ppm seen on MRS in tuberculoma reflect the

mycobacterium wall and moderately high Cho is present due to inflammatory activity [233]. Glioblastoma has a higher mean Cho/Cr ratio compared to tuberculoma (2.1 vs. 1.3) on short TE MRS [234]. A case of tuberculoma is shown in Figure 36.

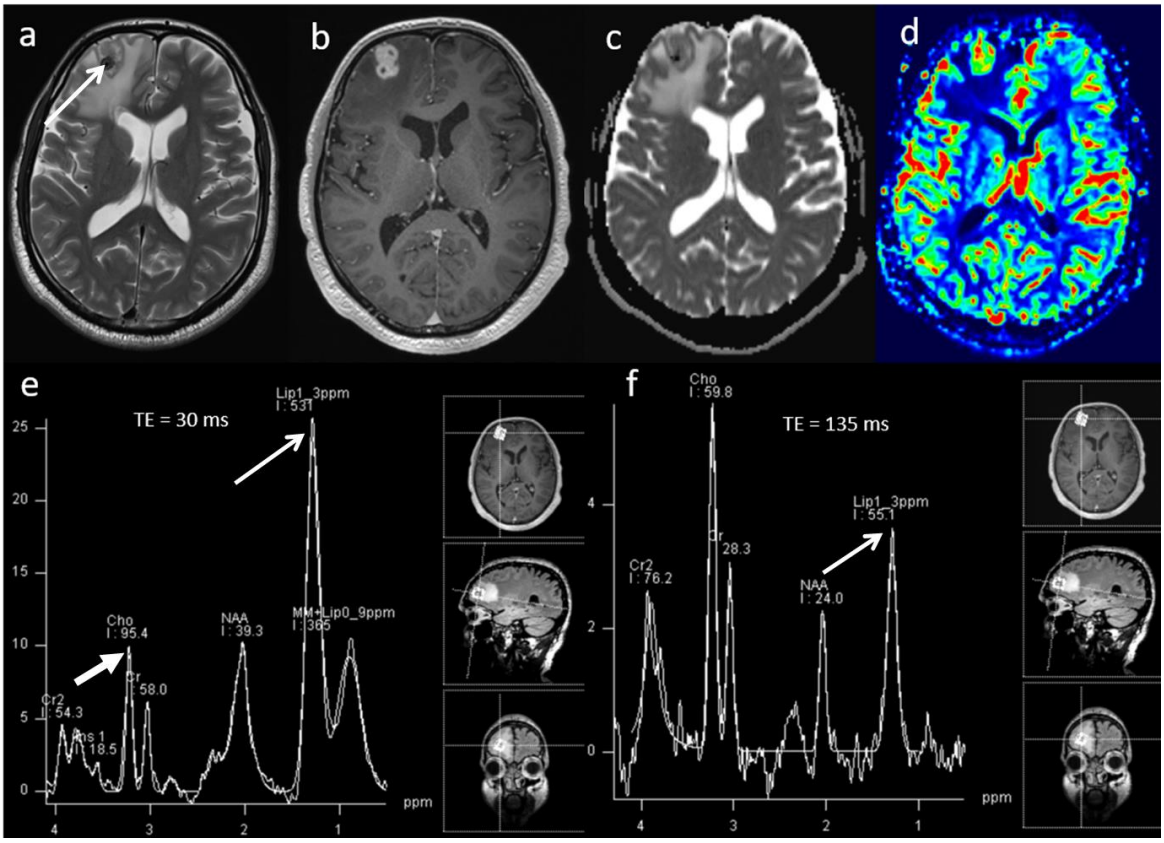

Figure 36. Tuberculoma. Conventional MRI Findings: (a, b) Axial T2WI and CE-T1WI showed hypointense confluent lesions on T2WI in the right frontal lobe with extensive perilesional oedema and enhancement. Multiparametric MRI: (c) ADC map showed intermediate values ($900 \times 10^{-6} mm^2 s^{-1}$), (d) PWI showed perfusion higher than the contralateral white matter, (e, f) MRS showed very high levels of lipid at 1.3 ppm (thin arrows), without any lactate. There was slightly elevated Cho/Cr ratio (1.5) on short TE MRS (thick arrow), moderately low NAA/Cr ratio and absence of mI. In this case of tuberculoma, it was the combination of a hypointense lesion on T2WI, raised rCBV, raised lipids and moderately increased Cho/Cr ratio that helped to make the diagnosis. The patient commenced anti-tuberculosis treatment, and surgical intervention was avoided.

Another useful advanced technique in the diagnosis of tuberculoma include APT-weighted imaging. This generates tissue contrast from mobile amide protons in the tissue's peptides and intracellular proteins and in a small series of patients has shown significantly lower mobile amide protons in the tuberculoma microenvironment as well as raised values in the perilesional parenchyma, reflecting a lower protein content internally and raised protein content in the surrounding parenchyma, compared to glioblastoma [235].

3.4.3 Toxoplasmosis

Cerebral toxoplasmosis is a parasitic infection caused by *Toxoplasma gondii*. It is usually seen in immunocompromised patients and with this background, the differential diagnosis is more extensive and the diagnosis can be difficult to ascertain, however prompt treatment is warranted due to the associated high mortality of up to 65% [236]. Conventional imaging characteristically shows a "target sign" of enhancement, which when eccentric in location is highly specific for toxoplasmosis, although it has a low sensitivity, and another feature is concentric enhancement [237]. However, it may still commonly present as a rim-enhancing lesion without a target sign, depending on the stage of evolution, closely mimicking glioblastoma on conventional imaging, as demonstrated in Figure 37.

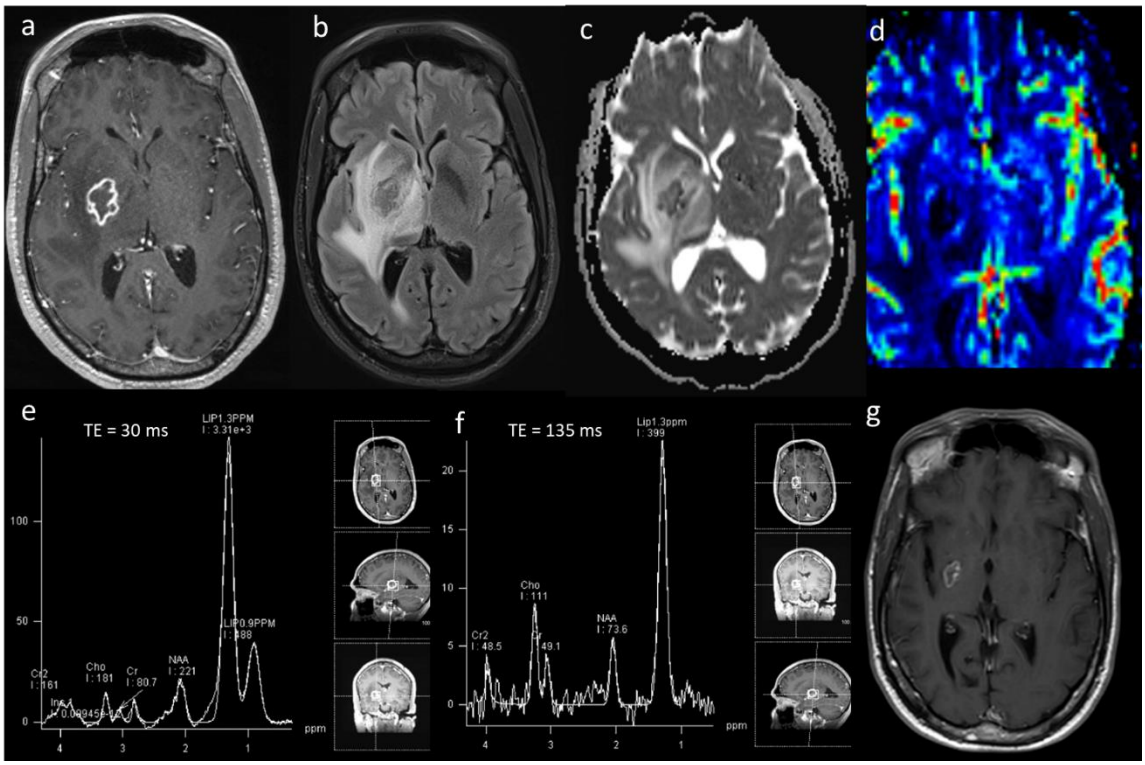

Figure 37. Toxoplasmosis in a HIV positive patient. Conventional MRI Findings: (a, b) Axial CE-T1WI and FLAIR showed a well-defined cystic lesion with a thin enhancing wall in the right lentiform nucleus with extensive perilesional oedema. Multiparametric MRI: (c) ADC map showed a concentric pattern of reduced diffusivity with central cystic change, (d) PWI showed low rCBV, (e, f) MRS showed very high levels of lipid at 1.3 ppm and slightly elevated Cho/Cr ratio. In this case, the combination of multiparametric MRI findings were not consistent with glioblastoma. The differential remained between atypical infection such as toxoplasmosis and lymphoma, however the location was atypical for lymphoma, thus favouring toxoplasmosis. Biopsy of the lesion was non-diagnostic and the patient commenced treatment for toxoplasmosis. (g) Follow up CE-T1WI at 1 month showed reduction in the size of the lesion.

3.4.4 Other CNS infections

Neurocysticercosis is the most common parasitic CNS infection, and a literature review has identified 33 cases of neurocysticercosis lesions than mimicked neoplastic lesions, with a high rate of misdiagnosis particularly when there is a solitary lesion [238]. MRS has shown to be a useful tool to identify succinate in neurocysticercosis [239], and recently the combined use of MRS, DTI and PWI has shown to be able to establish the diagnosis of a solitary neurocysticercosis lesion from other neoplastic lesions by the succinate peak on MRS, high MD, low FA and low rCBV values compared to contralateral normal appearing brain parenchyma [240]. Cryptococcosis is an invasive fungal disease which can infiltrate the CNS leading to encapsulated cystic cryptococcomas which mimic glioblastoma, usually in immunocompromised patients [241], but has also been reported in immunocompetent patients [242,243]. In addition, cerebral aspergillosis is a rare fungal infection of the CNS in which clinical as well as conventional imaging is relatively non-specific, mimicking a neoplastic lesion usually in patients who are immunocompromised [244], but again has also been reported in those who are immunocompetent [245]. MRS of cerebral fungal lesions has shown to be useful as it demonstrates peaks of succinate, alanine, lactate, and lipid as well as multiple peaks between 3.6 and 3.8 ppm which represent trehalose [246,247].

3.5 Inflammatory lesions

3.5.1 Tumefactive demyelinating lesions

Tumefactive demyelinating lesion (TDL) is the term given to demyelinating lesions that present clinically and radiologically indistinguishable from those of a neoplastic mass lesion, and often lead to biopsy [248]. This is estimated to occur in about 1-2 out of every 1000 cases of multiple sclerosis, but also occurs in patients with no history of demyelinating disease [249]. An acute TDL can have ill-defined borders, mass effect, surrounding oedema, central necrosis and contrast enhancement, which mimic glioblastoma [250]. They usually demonstrate central high ADC, a thin rim of low ADC (representing the active zone of demyelination), generally low rCBV, high Cho/Cr ratio, high glutamate and glutamine and presence of lipid and lactate. Raised glutamate and/or glutamine peaks are thought to represent neuroglial breakdown and the astrocytic response secondary to inflammation, even if the conventional imaging pattern is more consistent with a tumour [117]. The metabolic profile from the adjacent perilesional area usually shows a similarly abnormal spectral pattern. MRS should not be read in isolation as it can mimic tumoural spectrum, however the combination of parameters will lead to the correct diagnosis of a TDL. A case of TDL is shown in Figure 38.

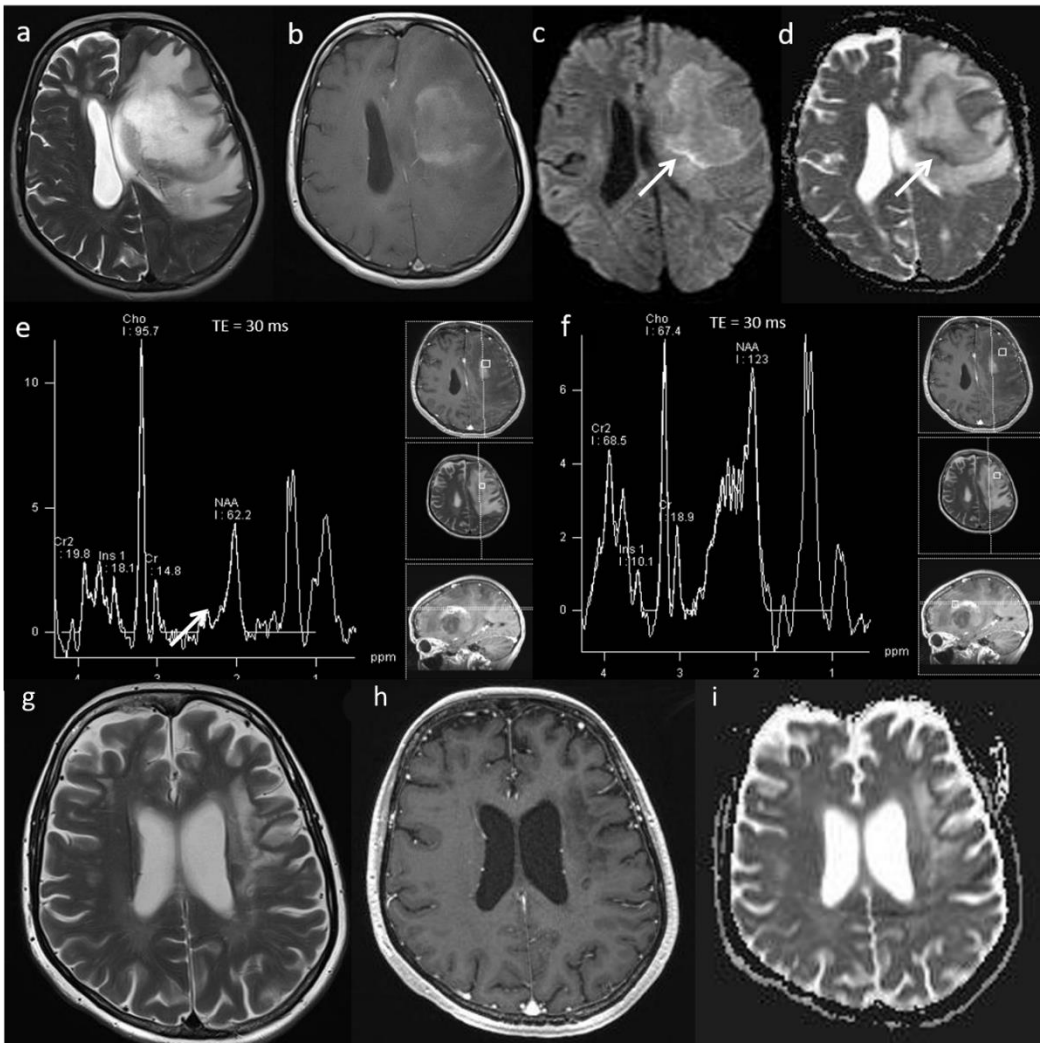

Figure 38. Tumefactive demyelinating lesion. Conventional MRI: (a, b) T2WI and CE-T1WI revealed a large heterogeneous space occupying mass lesion and diffuse pattern of enhancement. Multiparametric MRI: (c, d) DWI and ADC images showed high ADC centrally (>1000 × $10^{-6}$$mm^2s^{-1}$) and a thin rim of low ADC reflecting an advancing edge of demyelination (arrow). (e) MRS showed a high Cho/Cr ratio (6.4), near normal NAA/Cr ratio, high glutamate and glutamine (arrow), low mI/Cr ratio, and the presence of lipid and lactate at 0.9 ppm and 1.3 ppm respectively. (f) The metabolic profile from the adjacent perilesional area also showed a similarly abnormal spectral pattern. PWI (not shown) demonstrated a low rCBV except in the anterior-superior component. The striking presence of glutamine and glutamate on MRS, the enhancement pattern and generally low perfusion favoured an inflammatory lesion, as opposed to high-grade glioma or lymphoma. The patient made a recovery on methylprednisolone and avoided biopsy. One-month follow-up imaging: (g) Axial T2WI, (h) CE-T1WI and (i) ADC map showed significant improvement in mass effect, midline shift and overall volume of the lesion.

Acute disseminated encephalomyelitis (ADEM) is an immune-mediated inflammatory demyelinating condition which can also present as a TDL following infection or vaccination, mostly in children but also seen in adults [251]. MRI typically show large ill-defined T2WI/FLAIR hyperintense lesions which are bilateral and asymmetrical, affecting the white and grey matter, with variable contrast enhancement (approximately in 30% of cases), depending on the stage of the disease, and treatment is with high-dose IV corticosteroids [252]. Contrast-enhancing ADEM can mimic glioblastoma and vice versa, as demonstrated in a recently published case report in which a case of glioblastoma was misinterpreted as ADEM following COVID-19 vaccination based on conventional imaging [253]. Advanced imaging features of tumefactive ADEM are similar to that described previously, with areas of low ADC, low rCBV, an increased Cho/Cr ratio, presence of lipid and lactate as well as elevation of glutamine and glutamate peaks [254].

3.5.2 Neurosarcoidosis

Sarcoidosis is an idiopathic systemic disease with non-caseating granuloma. It typically presents as multiple enhancing parenchymal and/or meningeal lesions and can be extremely difficult to differentiate from glioblastoma. A case of neurosarcoidosis is demonstrated in Figure 39 and follow-up MRI shows near complete resolution of the lesion. A response to steroid treatment is usually helpful in making diagnosis. In this case, multiparametric MRI showed focal areas of low ADC, low perfusion, moderately high Cho/Cr ratio, presence of glutamate and glutamine peak at 2.4-2.6 ppm, large lipid peaks at 0.9 and 1.3 ppm with an absence of a lactate peak suggesting necrosis. There is very little literature on advanced

imaging in neurosarcoidosis, with a recent single case report showing non-specific findings except for slight NAA/Cr ratio reduction on MRS [255].

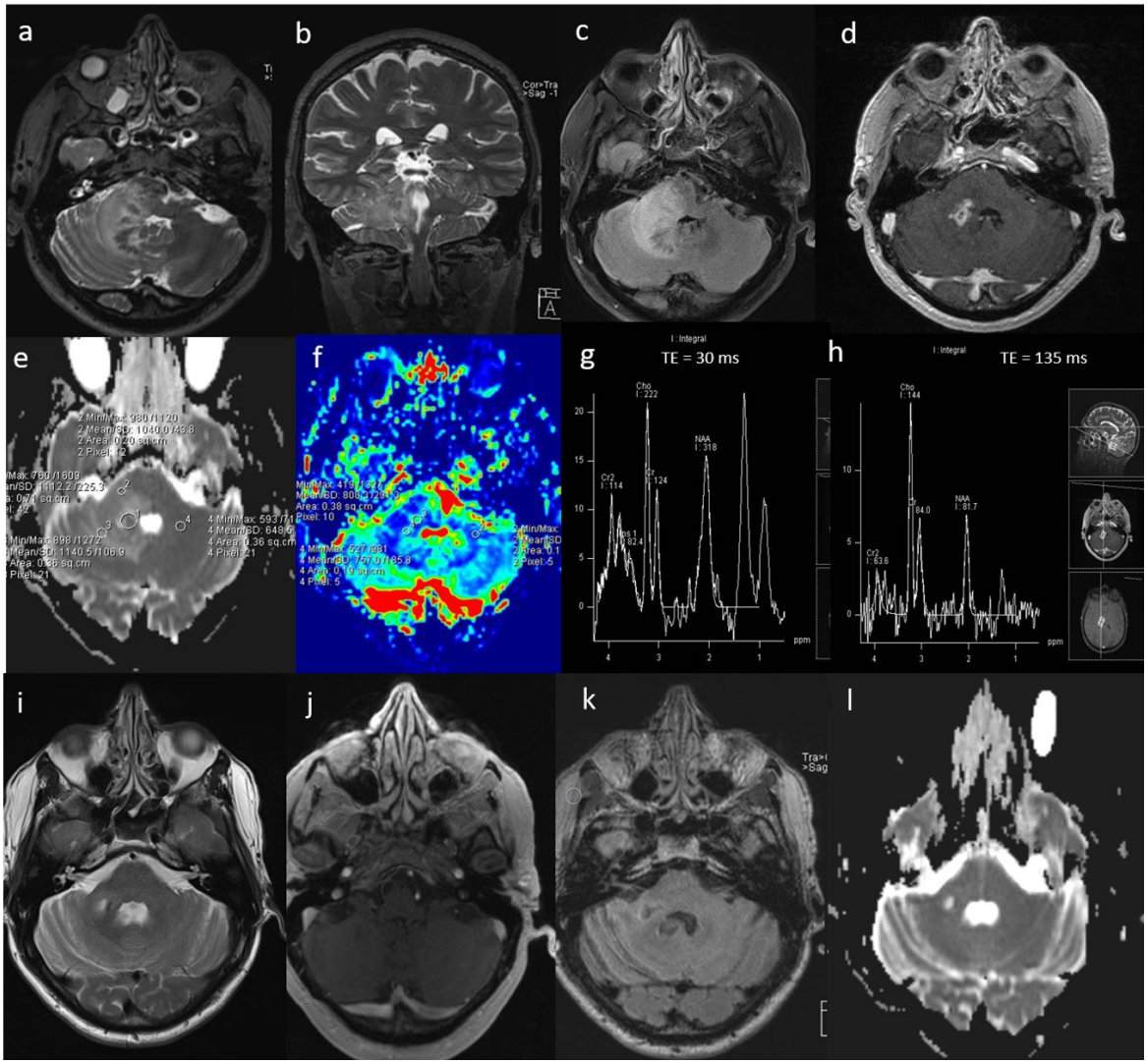

Figure 39. Neurosarcoidosis in a known case of systemic sarcoidosis. Conventional MRI Findings: (a, b) Axial and coronal T2WI, (c) axial FLAIR, and (d) CE-T1WI, showed a diffuse infiltrative lesion with enhancing foci in the right cerebellar peduncle extending to the brainstem, mimicking a neoplastic lesion. Multiparametric MRI: (e) DWI showed focal areas of low ADC (<1000 × $10^{-6}$$mm^2$$s^{-1}$). (f) PWI showed low perfusion in comparison to the contralateral side. (g) MRS with a short TE (30 ms) showed moderately high Cho/Cr ratio (<2), near normal NAA/Cr and mI/Cr, presence of glutamate and glutamine at 2.4-2.6 ppm and large lipid peaks at 0.9 and 1.3 ppm suggesting necrosis. (h) MRS with a TE 135 ms showed slightly low NAA/creatine ratio and absence of lactate. In this case, the findings of low

perfusion (<2), absence of a lactate peak and presence of glutamine and glutamate favoured an inflammatory aetiology such as neurosarcoidosis rather than a high-grade glioma. A tapering dose of an oral corticosteroid was commenced, during which neurological symptoms improved. Three-month follow-up MRI; (i) axial T2WI, (j) CE-T1WI, (k) FLAIR and (l) ADC sequences showed near complete resolution of the lesion.

In comparison, a similar appearing and located lesion on conventional imaging is shown in Figure 40; this showed abnormal multiparametric MRI features suggestive of a high-grade glioma. Again sited in the brainstem, a difficult location for biopsy to obtain a tissue diagnosis. Biopsy of this lesion was inconclusive, however multiparametric MRI demonstrated features of a high-grade neoplastic lesion rather than a non-neoplastic lesion, which had significant implications for changing the course of patient management.

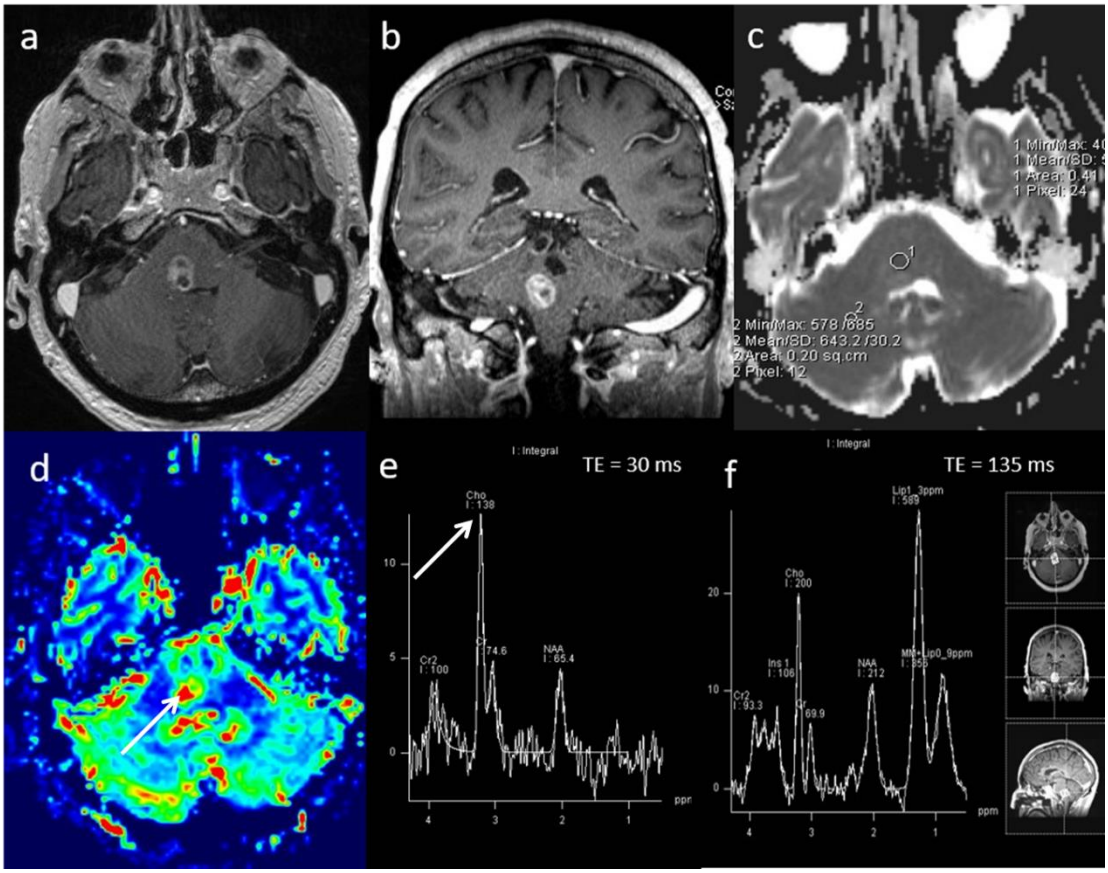

Figure 40. High-grade glioma. Conventional MRI: (a, b) Axial and coronal CE-T1WI, showed a well-defined lesion at the ponto-medullary junction. Multiparametric MRI: (c) ADC map demonstrated low ADC (590 x $10^{-6}mm^2s^{-1}$). (d) PWI showed high perfusion (rCBV 2.8, arrow). (e, f) MRS showed a high Cho/Cr ratio (2.9, arrow), low NAA/Cr ratio, and presence of lipid peaks. MRI findings of a low ADC (<1000 x $10^{-6}mm^2s^{-1}$), high rCBV (>2) and high Cho/Cr ratio (>1.8) were consistent with a high-grade glioma rather than a granuloma or abscess. The presence of high Cho levels in the perilesional area (not shown) favoured high-grade glioma over a metastatic lesion. In this patient, an initial biopsy was inconclusive and as a result of the multiparametric MRI findings, a decision to undergo further biopsy was overturned. The patient underwent radiotherapy for presumed glioblastoma.

3.5.3 Encephalitis

Bickerstaff's Brainstem Encephalitis is a rare disorder characterised by acute ophthalmoplegia, ataxia and altered sensorium [256]. It is now increasingly being recognized as anti-GQ1b syndrome or spectrum disorder [257]. Brainstem signal abnormality has a wide differential of imaging appearances on conventional MRI and may mimic a glial neoplastic lesion. The treatments options of these entities vary significantly. A case of Bickerstaff brainstem encephalitis is shown in **Figure 41**. In this case, the lack of enhancement, low rCBV, high ADC, normal Cho as well as presence of glutamine and glutamate at 2.3 and 2.4 ppm excluded glioma. Following treatment with IV methylprednisolone, follow-up MRI shows complete resolution.

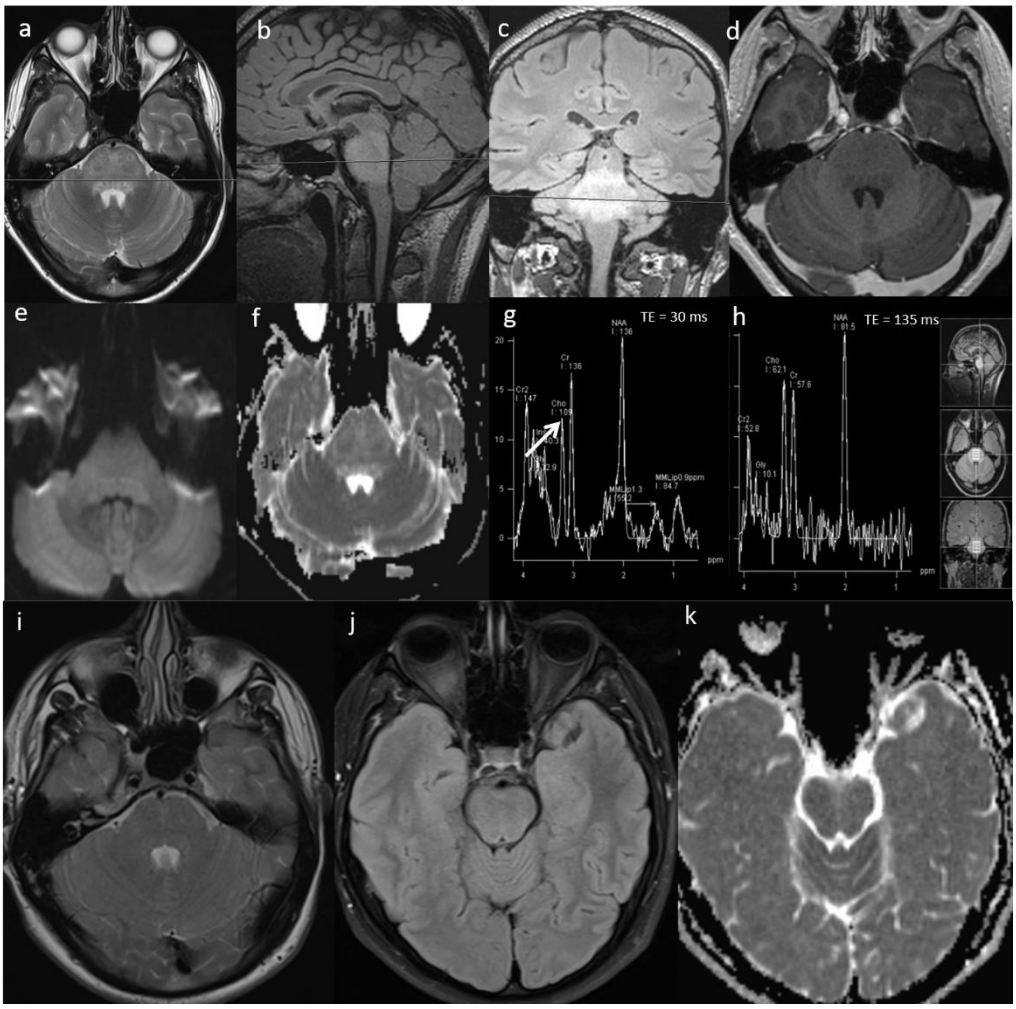

Figure 41. Bickerstaff brainstem encephalitis. Conventional MRI Findings: (a) Axial T2WI, (b, c) sagittal and coronal FLAIR, and (d) axial CE-T1WI, showed a diffuse high signal lesion in the pons with no enhancement post-contrast. Multiparametric MRI: (e, f) DWI showed high ADC throughout the lesion (>1000 × $10^{-6}$$mm^2s^{-1}$). (g, h) MRS showed normal mI/Cr, normal Cho/Cr (arrow), and normal NAA/Cr ratios and minimally increased glutamine and glutamate peaks (2.3 and 2.4 ppm). PWI (not shown) had low rCBV compared to normal-appearing white matter. The lack of enhancement, low rCBV, high ADC and normal Cho excluded glioma. These multiparametric MRI features in conjunction with an acute presentation favoured an inflammatory lesion. Two-month follow-up imaging: (i) Axial T2WI, (j) FLAIR and (k) ADC map showed lesion regression and normalisation of diffusion. In this case, CSF analysis revealed antiganglioside antibodies consistent with a diagnosis of Bickerstaff brainstem encephalitis.

3.6 Vascular-related lesions

3.6.1 Infarct

Cerebral infarcts within the subacute phase demonstrate enhancement and can be mistaken for a neoplastic mass lesion (**Figure 42**). Recent case reports have highlighted this issue, for example a case of cerebellar infarct which was mistakenly diagnosed as glioblastoma on conventional imaging and underwent resection [258]. Conversely even though the clinical presentation and history is generally extremely useful to making the diagnosis, it can be misleading and cases have also been reported of patients presenting clinically and on conventional imaging and DWI with acute stroke due to typical vascular territory location and acute symptoms, but subsequently diagnosed as glioblastoma [259,260]. A case from the current study is also presented in which there was a similar dilemma (**Figure 43**).

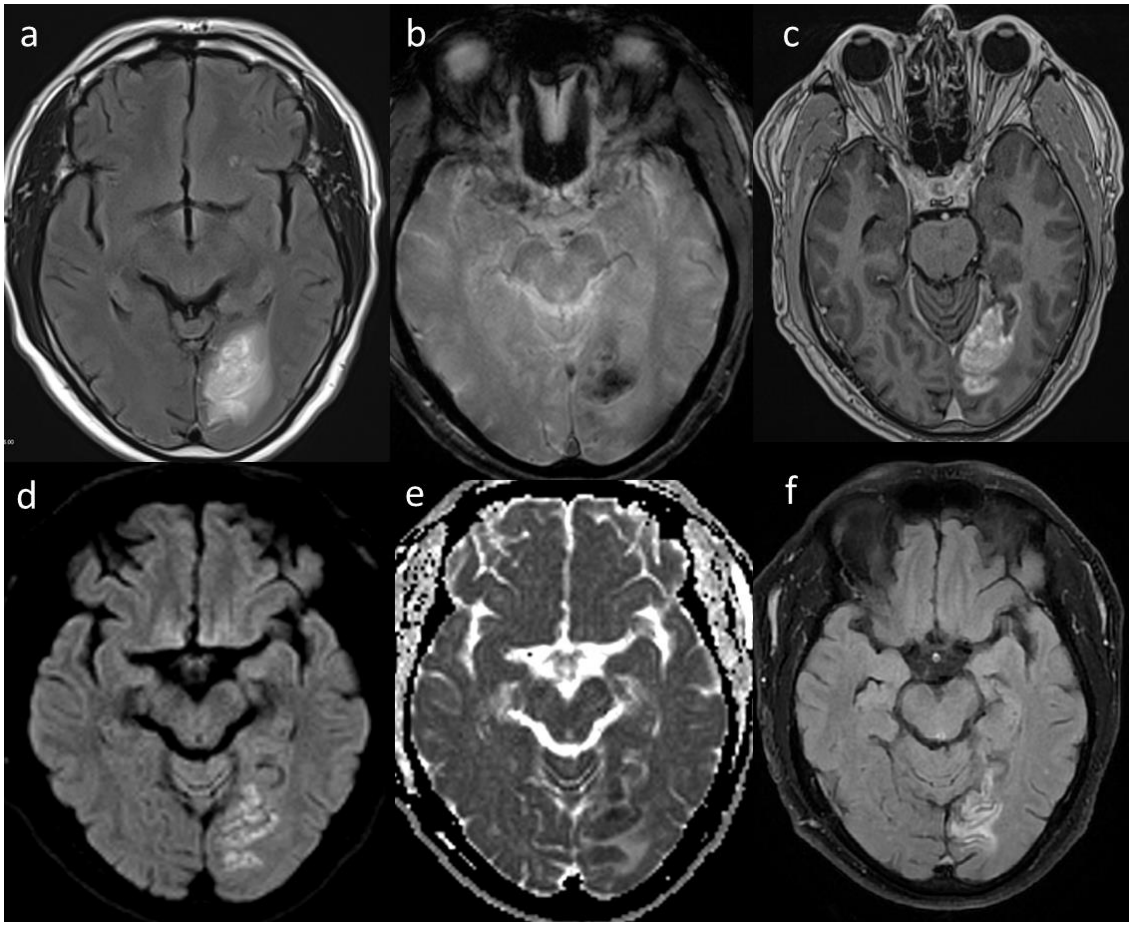

Figure 42. Left posterior cerebral artery (PCA) territory infarct mimicking glioblastoma on conventional imaging. (a) FLAIR, (b) SWI and (c) CE-T1WI showed signal change in the medial left occipital lobe with haemorrhagic change and mass-like enhancement. (d, e) DWI and ADC showed predominately subcortical gyriform restricted diffusion. (f) FLAIR four months later showed a reduction in the degree of signal change, confirming a diagnosis of infarct rather than a neoplastic lesion. The findings on conventional imaging alone were unable to confidently distinguish between glioblastoma and subacute infarct. DWI provided additional information in this case to establish the diagnosis of subacute infarct.

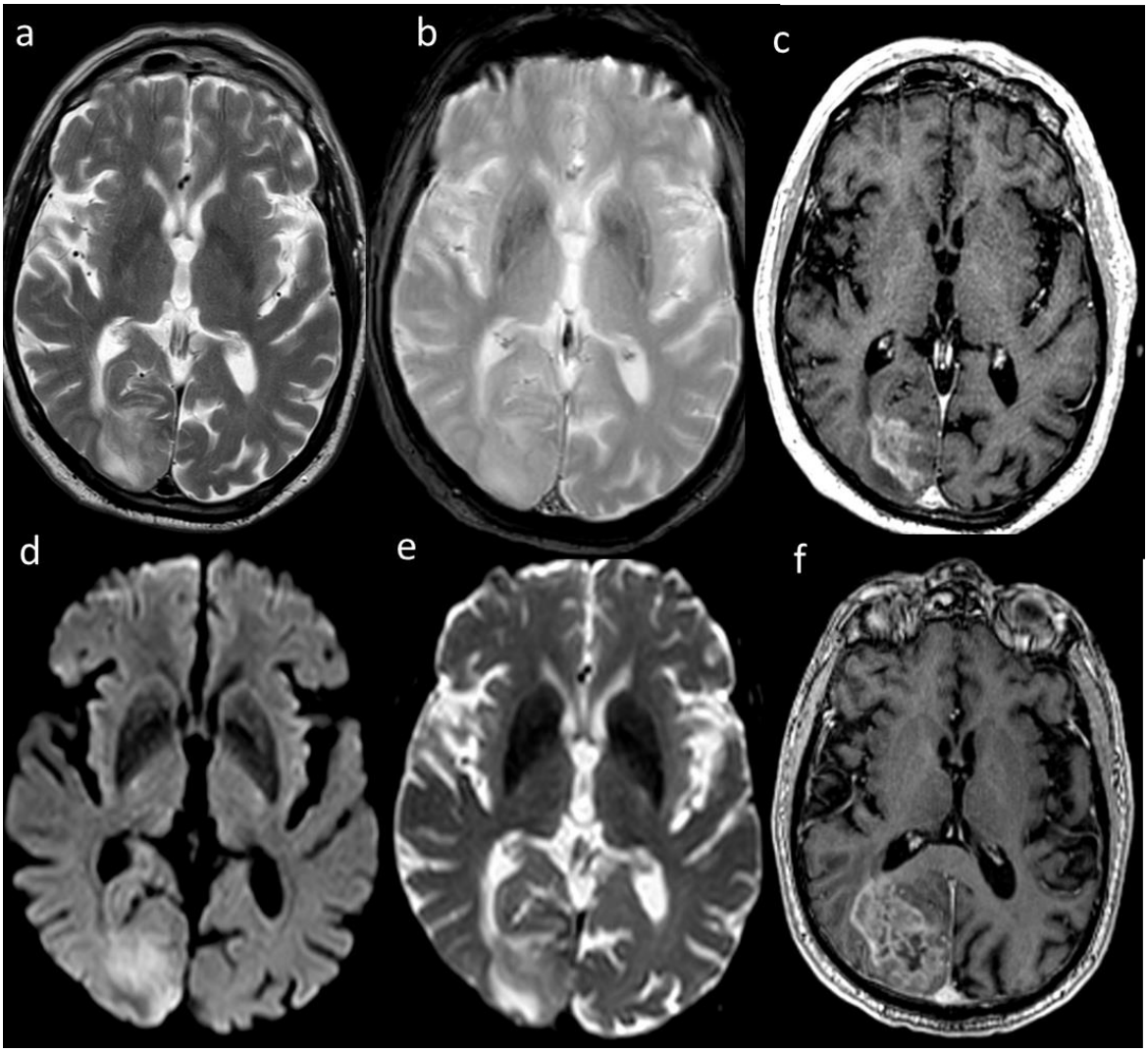

Figure 43. Presumed glioblastoma mimicking subacute infarct on conventional imaging and DWI. (a) T2WI, (b) SWI and (c) CE-T1WI showed signal change in the right occipital lobe without haemorrhagic change and presence of subcortical enhancement. (d, e) DWI and ADC showed a wedge-shaped area of restricted diffusion. (f) CE-T1WI at one (not shown) and two months later showed a progressive significant increase the degree of enhancement and mass effect, confirming a diagnosis of a high-grade neoplastic lesion rather than infarct. The findings on conventional imaging as well as DWI were more consistent with a subacute infarct. However, without additional multiparametric MRI, high-grade neoplasm remained in the differential diagnosis as the clinical history did not provide additional information towards the diagnosis.

The recommendation has been to use additional advanced imaging techniques such as PWI and MRS to help distinguish between infarct and high-grade neoplastic lesions [258]. In infarct, PWI will generally be much lower than glioblastoma and MRS typically shows a high NAA/Cr ratio, low Cho/Cr ratio and lipid-dominant peak in contrast to what is seen in glioblastoma, although occasionally there may be an overlap of some MRS features in the late subacute phase at six weeks post-infarct and therefore the multiparametric approach is essential [193,261,262].

3.6.2 Haemorrhage

Glioblastoma diagnosis has shown to be delayed in patients where the initial presentation of the tumour is through intracerebral haemorrhage, given that underlying malignancy accounts for only 2.3% of cases of intracerebral haemorrhage [24,263], as demonstrated in the case shown in Figure 44. The majority of patients therefore go on to have imaging to identify a vascular abnormality, usually CT angiography, but this cannot reliably identify an underlying tumour, and a post-contrast MRI is suggested as the investigation of choice. This is more able to pick up the pathological enhancement of underlying malignancy, however, it is still confounded by peripherally enhancing haematoma if performed in the subacute stage and therefore should be performed at approximately six weeks following the acute event. In the case of pathological enhancement at this six-week time point, multiparametric MRI can be useful to confirm the presence of a neoplastic process.

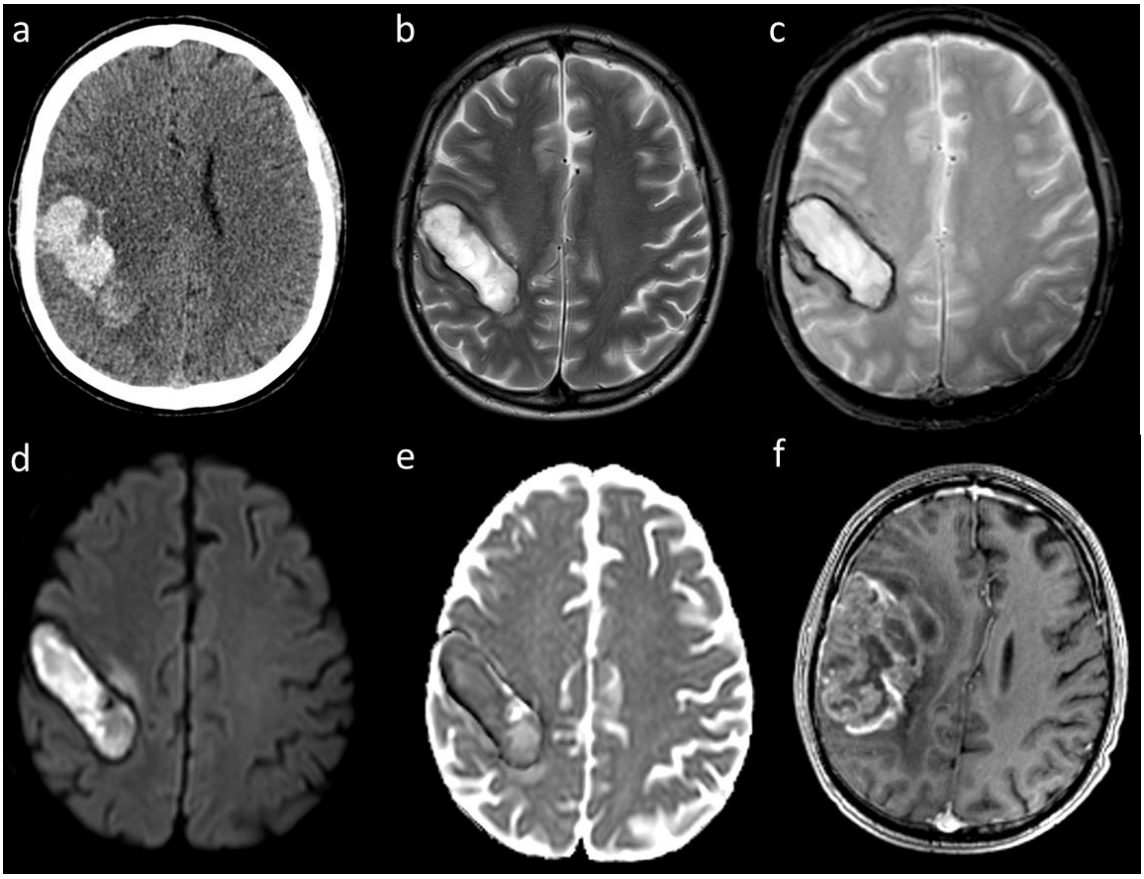

Figure 44. Glioblastoma presenting as intracerebral haemorrhage. (a) Non-contrast CT showed acute right fronto-parietal intracerebral haemorrhage. Follow up MRI at six weeks: (b) T2WI, (c) SWI and (d, e) DWI and ADC confirmed the presence of haematoma contraction and evolution, with peripheral haemosiderin susceptibility artefact. (f) CE-T1WI at 12 months showed a large enhancing necrotic mass lesion, at the site of prior haemorrhage, consistent with an IDH-wildtype glioblastoma on histology. In this case, post-contrast MRI at the six-week time point may have been useful to detect abnormal enhancement and if present, additional multiparametric MRI of the enhancing disease could have provided information pointing towards the diagnosis of a high-grade neoplasm rather than simple haemorrhage, potentially avoiding a delay in the diagnosis and enabling earlier commencement of treatment.

3.6.3 Vasculitis

Primary angiitis of the CNS (PACNS), also known as primary CNS vasculitis is a rare form of vasculitis caused by idiopathic cerebrovascular granulomatous inflammation. Tumour-like

mass lesion is a rare presentation of PACNS, seen in approximately 5% of cases and is extremely difficult to distinguish from neoplastic lesions on conventional imaging, frequently misdiagnosed as glioblastoma and leads to surgical intervention rather than aggressive immunosuppression and steroid treatment [264,265]. MRS is recommended and has shown to be one of the key imaging methods to be able to distinguish between glioblastoma and a tumour-like mass lesion of PACNS through the marked elevation of the glutamate and glutamine peaks which is associated with inflammatory processes and not consistent with glioblastoma [264,266,267]. The degree of Cho, NAA, lipid and lactate levels were found to be less specific to distinguish between the entities [264]. High-resolution vessel wall MRI (VW-MRI) is a newer technique more frequently being used to detect abnormalities within and surrounding cerebral vasculature, which is more specific for a diagnosis of vasculitis and not often seen in neoplastic disorders, although VW-MRI requires further studies to establish imaging biomarkers to distinguish between the various causes of vasculitis [264,268].

3.7 Limitations and future direction

There are some inherent challenges for adoption of multiparametric MRI techniques in routine clinical practice, such as brain regions affected by susceptibility, small lesions and non-enhancing lesions. However, the adoption and widespread clinical use of multiparametric MRI protocols is improving with the use of higher magnetic field strength magnets, specialised coils and readily available vendor post-processing tools. There has been improvement in the standardisation of acquisition techniques over time, particularly with the publication of white papers on imaging [175,269]. However, the cross-site and cross-vendor standardisation is still difficult to address, as there is some variability of threshold values and limited understanding of combining the parametric information. This is expected to improve further with training of specialists in the field, development of consensus guidelines and the routine incorporation of these techniques into clinical practice providing larger datasets and scope for multi-centre and prospective studies [270].

It is imperative that functional multiparametric information from DWI, PWI and MRS is read in combination with structural MRI sequences, such as T1WI, T2WI, FLAIR, SWI, CE-T1WI to further characterise lesions. These semi-quantitative multiparametric parameters of ADC, rCBV and Cho/Cr should be evaluated comprehensively and in conjunction with each other, rather than in isolation to narrow the differential diagnosis. Integrating these techniques with other more advanced MRI methods, other imaging modalities such as PET, as well as quantitative machine learning-based techniques such as radiomics and deep learning is expected to even further improve the diagnostic accuracy of imaging, but requires further work and validation [271,272].

3.8 Conclusion

This study has demonstrated through a variety of clinical cases that glioblastoma is mimicked by various other neoplastic, infective, inflammatory, and vascular-related disease processes on conventional MRI and can be frequently misdiagnosed. Combining conventional imaging with advanced MRI techniques that assess the lesion and perilesional microenvironment are crucial and have shown to make a positive difference for individual patient management and more informed decisions at the MDT meeting. Their use is strongly recommended by numerous studies and guidelines to improve the diagnostic accuracy of imaging and thus reducing uncertainty, unnecessary invasive procedures in the case of non-neoplastic lesions, as well as being able to commence definitive treatment earlier with the aim of improving patient outcomes.

4. MACHINE LEARNING-BASED RADIOMIC ANALYSIS FOR DISTINGUISHING BETWEEN GLIOBLASTOMA AND METASTASIS

4.1 Introduction

There are approximately 2,500 new cases of glioblastoma in England every year [4], and it has been estimated that there are 16,000 patients diagnosed with brain metastasis in the UK every year [273], affecting approximately 30-40% of patients with extracranial primary cancer [274,275], although there is difficulty in establishing the true incidence [276]. As previously discussed in Section 3.3.1, brain metastases have a similar appearance to glioblastoma on conventional imaging, and particularly when presenting as a solitary or single lesion it can be difficult to distinguish from glioblastoma. Each of the pathologies have different treatment strategies and considerations, such as the pre-operative administration of 5-ALA for fluorescence guided resection to ensure maximal safe resection of glioblastoma, en bloc resection of metastases compared to piecemeal resection in glioblastoma, and option of non-surgical treatments such systemic therapies or stereotactic radiosurgery for certain brain metastases [277].

The diagnosis of metastasis or glioblastoma is currently based on histopathological appearances of the lesion, from samples obtained through biopsy or resection, which is not

without risk particularly when lesions are sited in eloquent areas or in high-risk patients. An accurate method for differentiating between glioblastoma and solitary metastasis non-invasively using imaging is required to help plan patient management options. Although advanced MRI techniques have shown the ability to distinguish between the two pathologies, they are not routinely performed for this indication in clinical practice within the UK and therefore techniques that utilise conventional imaging sequences would be more clinically utilisable. Radiomic studies involve the extraction of numerous quantitative features from images and in combination with an AI technique such as machine learning, diagnostic or prediction models can be created. The aim of this study was to investigate the accuracy of radiomics and machine learning for distinguishing between glioblastoma and brain metastasis, using routinely-acquired pre-treatment MRI studies.

4.2 Background

AI is a broad term encompassing several branches of computer science that involve creating systems to perform tasks that usually require human intelligence, such as machine learning and deep learning. Machine learning involves training computers to perform tasks without explicit programming, usually using human engineered features to distinguish patterns of data, whereas in deep learning the computer learns features in order to classify data and these are compositional or hierarchical [278]. Machine learning and deep learning have been used in many applications outside of imaging and medicine with success, and only recently over the last few years have these been used in medical imaging. Although the techniques have been used for decades, three key factors have allowed these techniques to be used

more widely: (a) large quantities of labelled data, (b) more powerful and less expensive parallel computing hardware, and (c) improvements in training techniques [278]. There are various steps involved as described below.

4.2.1 Image acquisition and pre-processing

Standardised image acquisition and pre-processing steps are essential for machine and deep learning. For optimum results, radiological studies should be standardised as much as possible. They should ideally be acquired using the same protocol (resolution, field of view, slice thickness, cut angles, contrast washout time) and images should be acquired from the same scanner and without artefact. The use of volumetric imaging is superior to thick slices as there is limited loss of information or the need to create information by interpolating or re-slicing. The use of multiple conventional MRI sequences and multiparametric information provides additional data for use in machine and deep learning but will make analysis timelier and more complex. As with all studies, larger number of cases will give more power and can compensate for heterogeneity in the dataset, from the use of different scanners, different protocols, or imaging from different institutions. Pre-processing usually involves image intensity normalisation, applying magnetic field inhomogeneity correction and re-slicing if required. Multiple sequences from each case should also be co-registered to allow application of the mask for segmentation, and feature extraction in machine learning or feature definition in deep learning.

4.2.2 Segmentation

Segmentation of the lesion is usually a pre-requisite for machine and deep learning studies, although depending on the application, some deep learning studies may involve input of the entire image or image stack without delineation of a particular ROI. Usually the ROI is a tumour or lesion but can also include its subcomponents or the perilesional environment; an example shown in **Figure 45**.

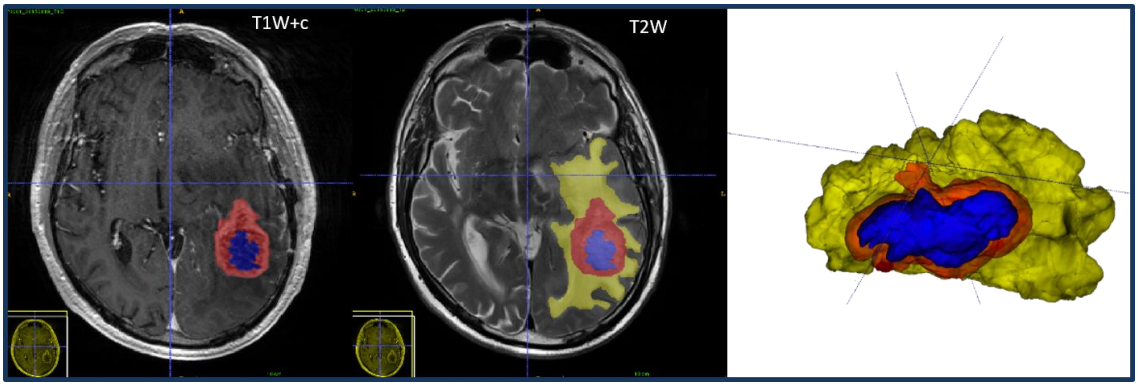

Figure 45. Example of glioblastoma segmentation. Left: Enhancing disease (red) and necrosis (blue) components segmented on post-contrast T1-weighted imaging. Middle: In addition peritumoural oedema (yellow) is segmented on T2-weighted imaging. Right: Volumes of interest created in three dimensions.

The ROI can be two-dimensional in the form of a segmentation mask on a single image or on a single slice of a series, or it can be a three-dimensional mask spanning over a number of slices, in the form of a volume of interest (VOI). Segmentation can be performed manually, semi-automatically or automatically, and there are various tools available. The manual technique, if performed by a radiologist is generally the most accurate and considered to be gold-standard or ground truth but is subjective and there may be interobserver variability. Manual segmentation is considered the most time-consuming, especially when there are

large lesions which span over a number of slices, in combination with thin slice volumetric imaging. Semi-automatic methods are preferred to reduce segmentation time and involve automatic computer-aided segmentation methods, most commonly edge-based detection methods in combination with a manually-placed seed point, followed by manual adjustments. Fully automatic methods can be used, although these methods usually require multiple MRI sequences for tumour segmentation and may not be accurate where there are complex lesions, and close proximity or attachments to surrounding structures.

4.2.3 Feature extraction

Machine learning can be used to recognise patterns in imaging, by converting medical images into higher-dimensional data [279,280]. Large numbers of quantitative radiological features, termed “radiomic features” can be extracted from the image ROI or VOI; the features are usually mathematical descriptions of the visual properties of an image. Radiomic feature extraction is performed using dedicated software packages or custom-built applications for specific features. Features consist of shape and size, first-order statistics (histogram-based techniques of voxel values), second-order statistics (textural features defining correlations between voxels) and higher-order methods (such as the use of filter grids) [281]. Human-defined imaging features, clinical and patient features, laboratory results, and molecular markers can also be integrated as additional features into the machine learning algorithm and combined with imaging as inputs into deep learning algorithms.

For deep learning, features are not defined, rather the computer encodes features using artificial neural networks which consists of connected nodes, based on the structure of

biological neural networks [278]. For processing imaging data, the dominant architecture is the convolutional neural network (CNN), which has neurons arranged to produce a convolution of a small part of the image (kernel), which subsequently moves across the image and outputs its location and value, producing a set of values that pass through various hidden layers to amplify important features [282].

4.2.4 Feature selection and classification

In machine learning, the algorithm computes the radiomic features and additional features, and ranks them according to importance in making the defined outcome prediction, known as supervised learning, as the data is labelled. The outcome can be a histological diagnosis, correlation with a molecular or genomic marker (termed "radiogenomics"), a dichotomous clinical outcome, or prognostic outcome. The algorithm then identifies the best combination of features for classification. There are various classifiers that can be used; the most popular include support vector machine (SVM), random forest, *k*-nearest neighbour (*k*-NN), Naïve Bayes and logistic regression. A final model is produced combining the most predictive features and their weightings.

For deep learning, the input is a set of values representing features, each multiplied by a corresponding weight. The CNN determines the important features as a part of its search process and therefore the bias of testing only features that a human believes to be important as well as the bias of selecting important features, is removed. The CNN is trained by adjusting weights and biases of each node, via an optimisation algorithm and the performance of the CNN is re-assessed by measuring the inaccuracy of the prediction and

parameters are incrementally adjusted [278]. Unsupervised learning approaches for CNN remains difficult in practice, as data is not labelled therefore the classifier clusters images based on the algorithm results, hence semi-supervised learning approaches are preferred, combining unlabelled and labelled data [278]. There are many different types of CNN architecture, with varying numbers of layers and layer sizes, and they appear to perform differently for different given problems, and selecting the best one is still a trial-and-error process [282]. Compared to machine learning studies, deep learning studies require many more samples to provide adequate results.

4.3 Methods

4.3.1 Study design

The study involved retrospective analysis of consecutive patients at the Queen Elizabeth Hospital Birmingham who had pre-operative imaging and subsequently newly diagnosed with IDH-wildtype glioblastoma, as well as patients who had imaging prior to a diagnosis of brain metastases. Approvals for this study were obtained from the University Hospitals Birmingham Research Governance Office.

4.3.2 Inclusion and exclusion criteria

Inclusion criteria for glioblastoma cases were: (a) pathology-confirmed IDH-wildtype glioblastoma according to the WHO Criteria, and (b) pre-operative volumetric CE-T1WI MRI sequence. Inclusion criteria for brain metastases cases were: (a) pathology-confirmed primary

malignancy elsewhere with imaging confirmation of one or more brain metastasis, and (b) volumetric CE-T1WI MRI sequence. Exclusion criteria were: (a) biopsy, surgical resection or radiotherapy treatment of the brain lesion prior to the MRI; (b) significant imaging artefact; (c) ambiguous tumour margins resulting in unsuitability for segmentation; and (d) enhancing lesions measuring less than 10 mm in diameter in at least one dimension.

In total, 228 lesions across 55 patients with brain metastases were assessed for suitability from which 53 lesions across 37 patients were included in the study from those who had imaging over a 4-month period between August and November 2018. Of the 175 excluded lesions, 171 were excluded due to size less than 10 mm and 4 were excluded due to previous treatment or biopsy. In total 101 cases of glioblastoma were assessed for eligibility over a 17-month period between June 2016 and November 2017, and the same number of corresponding glioblastoma lesions were included in the study (53 cases). Of the 48 excluded patients, 28 patients did not have a confirmed IDH status or had a glioblastoma variant, 8 patients had IDH-mutant glioblastoma, and 12 patients did not have volumetric CE-T1WI performed, or imaging contained significant artefact. The mean age (and standard deviation (SD)) of patients in the glioblastoma group (n=53) was 55.6 years (11.6) and in the brain metastasis group (n=37) it was 63.2 years (10.9). In the glioblastoma group, 23/53 (43%) were female and in the brain metastasis group, 20/37 (54%) were female. A flowchart of patients is shown in Figure 46.

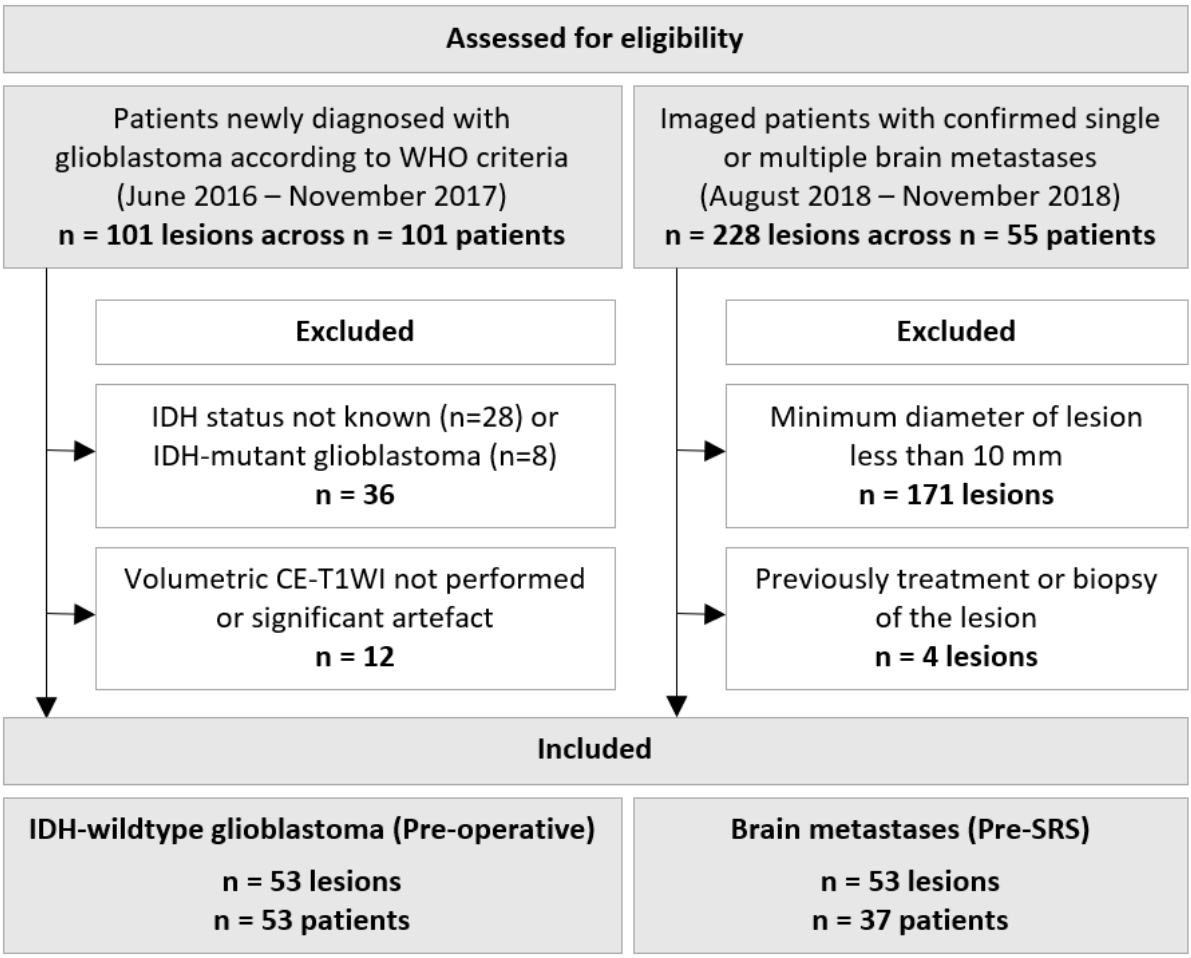

Figure 46. Flowchart of patient inclusion and exclusion criteria.

4.3.3 MRI acquisition

All volumetric CE-T1WI was acquired with a maximum in-plane voxel size of 1.0 x 1.0 mm^2 and the maximum slice thickness was 1 mm. For patients with glioblastoma, standard-of-care clinical imaging data was acquired from various MRI scanners: Siemens and GE 1.5 Tesla (45 studies), Siemens 3.0 Tesla (8 studies) scanners (Siemens Healthcare, Erlangen, Germany and GE, Milwaukee, USA) with 32-channel phased-array head coils, across several sites with TR = 540-690 ms and TE = 3-17 ms at 1.5 Tesla, TR = 1480-2350 ms and TE = 3-10 ms at 3.0 Tesla.

For patients with brain metastases, standard-of-care clinical imaging data was acquired from two Siemens 3.0 Tesla MRI scanners (Siemens Healthcare, Erlangen, Germany) with 32-channel phased-array head coils, TR = 1480-1700 ms and TE = 2.6-3.2 ms. IV gadolinium contrast (Dotarem; Guerbet, Villepinte, France) was administered as a bolus of 10-15 ml (10 ml if weight <70 kg, 15 ml if weight ≥70 kg).

4.3.4 Segmentation

A three-dimensional mask was created for each lesion based on the CE-T1WI. The entire enhancing lesion including non-enhancing tumour core, was manually segmented in the Microsoft Radiomics App (Microsoft Research, Cambridge, UK), as shown in **Figure 47**. For glioblastoma cases, manual adjustments were made on each slice through the consensus of two neuroradiologists (>20 and 5 years' experience). For brain metastases cases, the radiotherapy masks used for delivering SRS were used from routine clinical care, which was contoured by a consultant neuroradiologist and verified for accuracy by another neuroradiologist (>20 years' experience).

Figure 47. Tumour segmentation environment in the Microsoft Radiomics App.

4.3.5 Image pre-processing pipeline

Image resampling and intensity normalisation was performed using PyRadiomics (version 3.0) pipeline modules [283]. Image voxel size was normalised by performing image resampling according to the lowest acquisition resolution to avoiding upsampling (1.0 x 1.0 x 1.0 mm). Image intensity normalisation was applied based on the entire image and centred at the mean with SD. Hyperintensity artifact was corrected for by removing outlier voxel intensities greater than the 99.9^{th} percentile for each image.

4.3.6 Radiomic feature data extraction and models

Radiomic feature data extraction was performed using PyRadiomics (version 3.0) [283]. Numerical values were obtained for a total of 107 features from the segmentation mask for each patient. Features included 14 shape-based features, 18 first order and 75 second order features. Second-order features consisted of 24 gray-level co-occurrence matrix (GLCM) features 14 gray-level dependence matrix (GLDM) features, 16 gray-level run-length matrix (GLRLM) features, 16 gray-level size-zone matrix (GLSZM) features and five neighbourhood gray-tone difference matrix (NGTDM) features. Feature groups, families and individual features are listed in **Figure 48**. Features were normalised and standardised by centring the mean at zero and scaling the variance at one prior to machine learning. Two feature set models were constructed which subsequently underwent feature selection and classification: (i) 14 shape-based radiomic features from the tumour mass segmentation mask; and (ii) 93 first order and second order radiomic features extracted from the tumour mass segmentation mask.

Shape-based features		First order features	
Elongation	Maximum 3D diameter	10^{th} percentile	Median
Flatness	Mesh volume	90^{th} percentile	Minimum
Least axis length	Minor axis length	Energy	Range
Major axis length	Sphericity	Entropy	Robust mean absolute deviation
Maximum 2D diameter column	Surface area	Interquartile range	Root mean squared
Maximum 2D diameter row	Surface area to volume ratio	Kurtosis	Skewness
Maximum 2D diameter slice	Voxel volume	Maximum	Total energy
		Mean absolute deviation	Uniformity
		Mean	Variance

Second order features		
Gray-level co-occurrence matrix (GLCM)	**Gray-level dependence matrix (GLDM)**	**Gray-level size-zone matrix (GLSZM)**
Autocorrelation	Dependence entropy	Gray level non-uniformity
Cluster prominence	Dependence non-uniformity	Gray level non-uniformity normalized
Cluster shade	Dependence non-uniformity normalized	Gray level variance
Cluster tendency	Dependence variance	High gray level zone emphasis
Contrast	Gray level non-uniformity	Large area emphasis
Correlation	Gray level variance	Large area high gray level emphasis
Difference average	High gray level emphasis	Large area low gray level emphasis
Difference entropy	Large dependence emphasis	Low gray level zone emphasis
Difference variance	Large dependence high gray level emphasis	Size zone non-uniformity
Inverse difference	Large dependence low gray level emphasis	Size zone non-uniformity normalized
Inverse difference moment	Low gray level emphasis	Small area emphasis
Inverse difference moment normalized	Small dependence emphasis	Small area high gray level emphasis
Inverse difference normalized	Small dependence high gray level emphasis	Small area low gray level emphasis
Informational measure of correlation 1	Small dependence low gray level emphasis	Zone entropy
Informational measure of correlation 2		Zone percentage
Inverse variance	**Gray-level run-length matrix (GLRLM)**	Zone variance
Joint average		
Joint energy	Gray level non-uniformity	**Neighbourhood gray-tone difference matrix (NGTDM)**
Joint entropy	Gray level non-uniformity normalized	
Maximal correlation coefficient	Gray level variance	
Maximum probability	High gray level run emphasis	Busyness
Sum average	Long run emphasis	Coarseness
Sum entropy	Long run high gray level emphasis	Complexity
Sum squares	Long run low gray level emphasis	Contrast
	Low gray level run emphasis	Strength
	Run entropy	
	Run length non-uniformity	
	Run length non-uniformity normalized	
	Run percentage	
	Run variance	
	Short run emphasis	
	Short run high gray level emphasis	
	Short run low gray level emphasis	

Figure 48. List of the shape-based, first order and second order radiomic features used.

4.3.7 Feature selection and classification

The entire dataset was split into five folds using stratified random sampling, to carry out variable selection within nested cross-validation [284], as shown conceptually in **Figure 49**. The outer loop of nested cross-validation comprised of the five folds, each containing 80% training data and 20% testing data. The inner loop of each of the five training folds were used to identify the most predictive features in each model using a multi-step pipeline. Clusters of highly correlated features were identified using the Pearson correlation coefficient matrix (Python pandas environment, version 1.0.1 [285]) and the most representative features were kept from the clusters ($R^2 > 0.8$) and remaining features removed. Cross-validated 10-fold recursive feature elimination with a random forest classifier considering Gini impurity measures was then used to further reduce and select the most predictive features (Python scikit-learn environment, version 0.22.1 [286]). Classification in the outer loop was performed using a Naïve Bayes classifier in Orange (version 3.24) [287]. Only features that appeared in all five folds of the outer loop were selected to produce the final feature set. The AUC, sensitivity, specificity, positive predictive value (PPV), negative predictive value (NPV) and accuracy of the model was calculated.

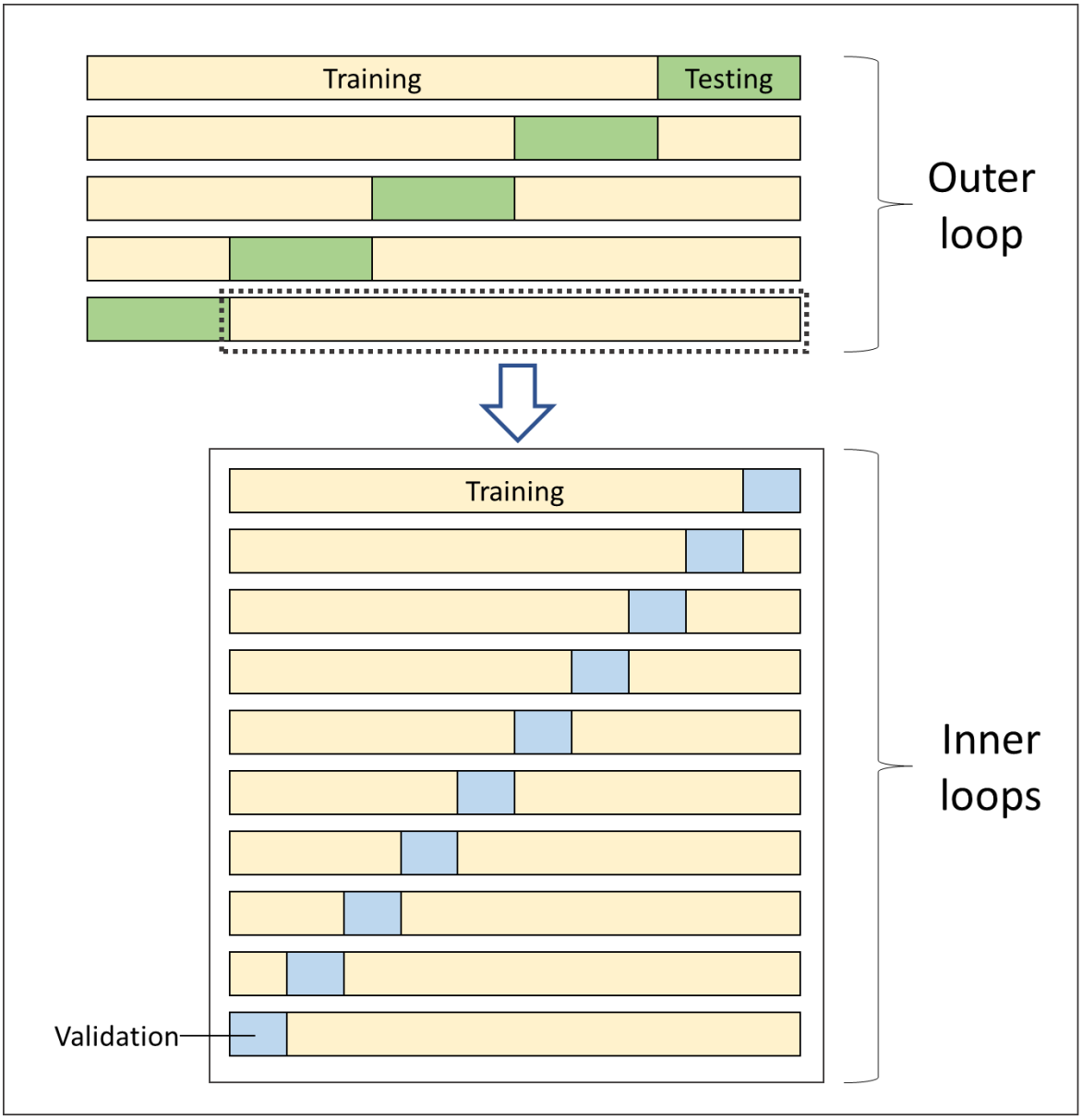

Figure 49. Conceptual overview of the nested-cross validation technique used.

4.4 Results

4.4.1 Predictive features

The most predictive features for each of the five folds, as well as the top common features across all folds of the two models along with the average AUC are shown in the tables below. The average AUC for the shape-based radiomic feature model was 0.97 (Table 4), with *least axis length* and s*phericity* features being common across all folds. The average AUC for the first and second order radiomic feature model was 0.92 (Table 5), with the first order feature of *energy* being common across all folds.

Fold	1	2	3	4	5	Common features and average AUC across all folds
Top features	Least axis-length Sphericity	Least axis-length Sphericity Elongation	Least axis length Sphericity	Least axis-length Sphericity Elongation	Least axis-length Sphericity	Least axis-length Sphericity
AUC	0.97	0.98	0.98	0.92	0.99	0.97

Table 4. Most predictive shape-based radiomic feature sets across each fold.

Fold	1	2	3	4	5	Common features and average AUC across all folds
Top features	Energy (FO) LAHGLE (GLSZM) LAE (GLSZM) DE (GLDM) 10th percentile (FO) Range (FO) SRE (GLRLM) Minimum (FO)	RLNU (GLRLM) LAE (GLSZM) Energy (FO) LALGLE (GLSZM) DE (GLDM) LRLGLE (GLRLM) 10th percentile (FO) Minimum (FO) SRE (GLRLM)	LAHGLE (GLSZM) Energy (FO) LAE (GLSZM) Minimum (FO) DE (GLDM) 10th percentile (FO) SDE (GLDM) GLNU (GLSZM) SRE (GLRLM)	RLNU (GLRLM) Energy (FO)	Energy (FO) LAHGLE (GLSZM) LAE (GLSZM) DE (GLDM) LRLGLE (GLRLM) SRLGLE (GLRLM) Minimum (FO) Range (FO) 10th percentile (FO)	Energy (FO)
AUC	0.95	0.86	0.98	0.92	0.89	0.92

DE = dependence entropy, *FO* = first-order, *GLDM* = gray-level dependence matrix, *GLNU* = gray-level non-uniformity, *GLRLM* = gray-level run-length matrix, *GLSZM* = gray-level size-zone matrix, *LAE* = large area emphasis, *LAHGLE* = large area high gray level emphasis, *LALGLE* = large area low gray level emphasis, *LRLGLE* = long run low gray level emphasis, *RLNU* = run length non-uniformity, *SDE* = small dependence emphasis, *SRE* = short run emphasis, *SRLGLE* = short run low gray level emphasis.

Table 5. Most predictive first and second order radiomic feature sets across each fold.

4.4.2 Final feature set model

For the final feature set model, the most predictive features that appeared in all folds of both models were combined. Two features were obtained from the shape-based radiomic features (*least axis length* and s*phericity*) and one feature was obtained from the first and second order radiomic features model (first order *energy*). Definitions of the individual radiomic features within the final radiomic signature are shown in **Table 6**.

Feature Name	Feature Category	Feature Definition
Least axis length	Shape-based	$4\sqrt{\lambda_{least}}$
Sphericity	Shape-based	$\frac{2\pi R}{P} = \frac{2\sqrt{\pi A}}{P}$
Energy	First-order	$\sum_{i=1}^{N_p}(X(i)+c)^2$
A = surface area of the mesh in mm^2, c = optional value which shifts the intensities to prevent negative values in X, N_p = the number of pixels included in the ROI, P = perimeter of the mesh in mm, R = radius of circle with the same surface as the region of interest, X = a set of N_p voxels included in the region of interest, λ_{least} = smallest axis length.		

Table 6. Definitions for the most predictive radiomic features in the final feature set for differentiating between glioblastoma and brain metastasis.

Comparison of the final radiomic feature set mean values between the glioblastoma and brain metastasis groups showed significant difference, which are shown as box plots in **Figure 50**. In the glioblastoma groups there were significantly higher values of *least axis length*, significantly lower values of *sphericity*, and significantly higher values of *energy* (p<0.001).

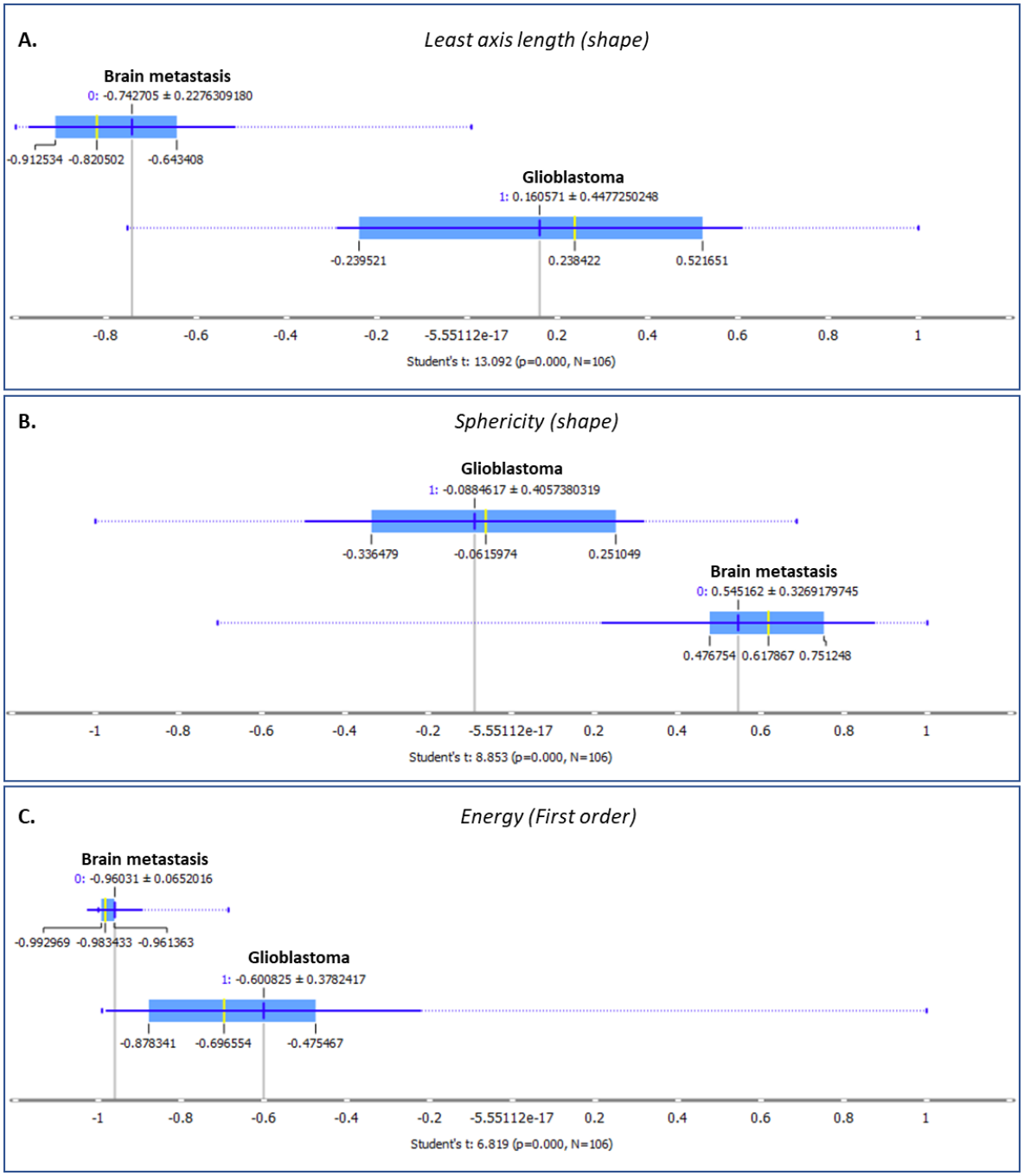

Figure 50. Box plots of the final model radiomic feature values, comparing the glioblastoma and brain metastasis groups. (A) *Least axis length*, (B) *sphericity*, and (C) *energy*.

The performance of the final model combining these three features demonstrated an AUC of 0.97, with an accuracy and confidence interval (CI) of 88.7% (81.1-94.0), sensitivity 88.7% (77.0-95.7), specificity 88.7% (77.0-95.7), PPV 88.7% (78.6-94.4) and NPV 88.7% (78.6-94.4). Results of each fold from the final model are shown in Table 7 and the receiver operating characteristic curve for the final feature set model is shown in Figure 51.

Fold	AUC	Sensitivity, %	Specificity, %	PPV, %	NPV, %	Accuracy, %
1	0.97	81.8	100.0	100.0	84.6	90.9
2	0.97	90.9	90.0	90.1	90.8	90.5
3	0.98	100.0	90.0	90.9	100.0	95.0
4	0.96	100.0	81.8	84.6	100.0	90.9
5	0.96	90.0	81.8	83.2	89.1	85.9
Average	0.97	88.7 (77.0-95.7)	88.7 (77.0-95.7)	88.7 (78.6-94.4)	88.7 (78.6-94.4)	88.7 (81.1-94.0)

Table 7. Diagnostic performance of the combined final radiomic signature model.

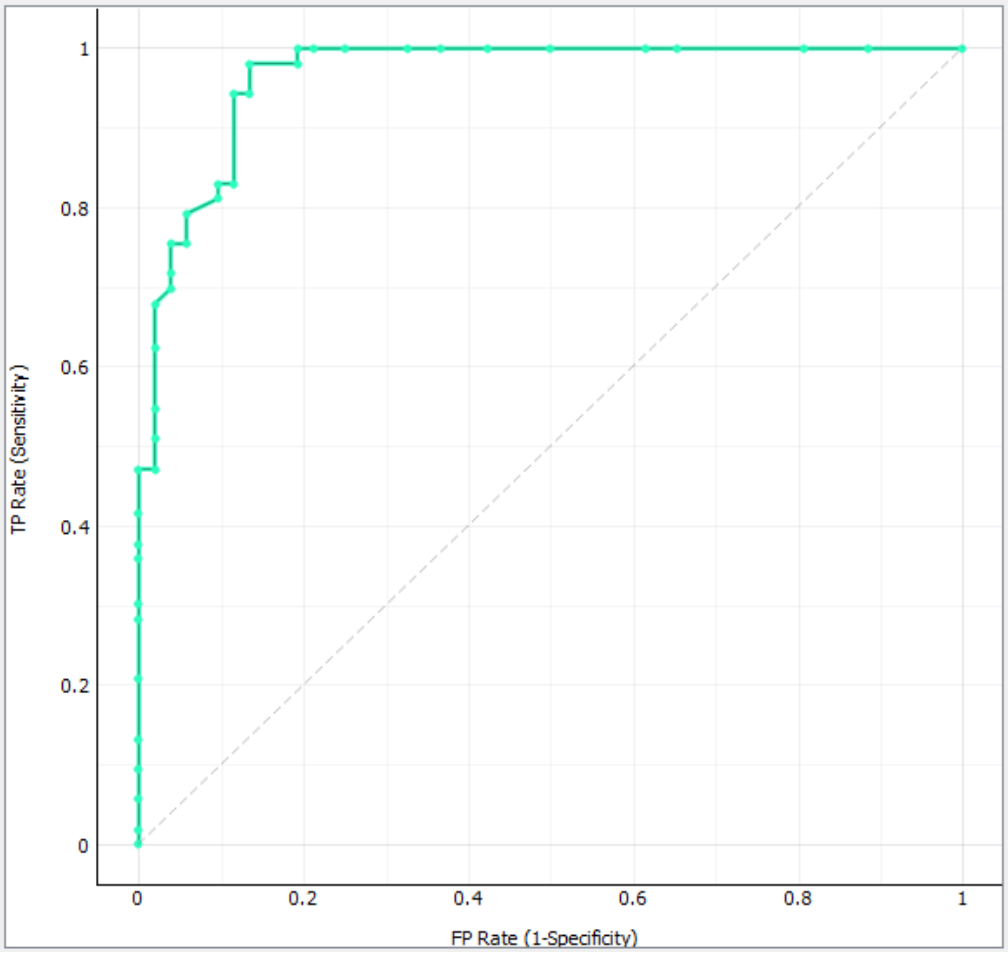

Figure 51. Receiver operating characteristic (ROC) curve for the final feature set model.

4.5 Discussion

Brain metastasis and glioblastoma have overlapping conventional imaging features and it can be difficult to differentiate between the two, which can have a direct impact upon patient management options. One study of patients with brain metastases has shown that the presence of a "solitary" brain metastasis in which there is a controlled primary tumour and no other metastases is 45.6%, "single" brain metastases in seen in 26.5% of cases and the remainder of patients had two or more brain metastases [288]. Two other studies have

shown that a single brain metastasis is seen at presentation in 53-58% of cases [289,290], although they do not differentiate between solitary and single metastasis. Therefore, the issue of distinguishing between glioblastoma and solitary or single brain metastasis is a frequently encountered scenario. There are different treatment approaches for both pathologies, including method of surgical resection and guidance, as well as the option of non-surgical treatments such systemic therapies or radiotherapy for certain metastases. A misdiagnosis of glioblastoma instead of a solitary or single metastasis on imaging prior to surgical resection may lead to unnecessary surgery and associated risks if non-surgical treatments are preferred options. Conversely a pre-operative misdiagnosis of metastasis instead of glioblastoma can lead to suboptimal extent of resection of the infiltrative disease within the surrounding brain parenchyma, which impacts upon OS for the patient.

The results of the current study have demonstrated that a machine learning-based radiomics model using shape-based and first order features from a single mask on the pre-treatment volumetric CE-T1WI can differentiate between IDH-wildtype glioblastoma and metastasis with an accuracy of 89%. The imaging in this study reflects standard-of-care practice acquired across field strengths and with varying acquisition parameters as per clinical care, followed by standardisation to account for heterogeneity. A moderate-sized dataset of 53 cases of glioblastoma and 53 cases of metastases were analysed compared to the currently published similar studies. The use of a single volumetric CE-T1WI sequence for analysis provides more clinical applicability. Methods included cross-validation within feature selection, rather than external to feature selection, which provides more reliable results by reducing selection bias [284].

There have been a small number of studies to date investigating machine learning-based radiomics to differentiate between glioblastoma and brain metastases. As with the current study, a few have utilised only CE-T1WI. Artzi *et al.* evaluated one of the largest number of patients to date, which included 212 glioblastoma cases and 227 brain metastasis cases, utilising a single volumetric CE-T1WI sequence acquired across both 1.5 and 3 Tesla with varying acquisition parameters for a robust approach [291]. In addition, clinical information and tumour location were used in the study as features in combination with radiomic features, but these were only extracted from three slices at the centre of the lesion rather than the whole lesion volume to reduce segmentation time. Final model performance was 85% to differentiate between glioblastoma and metastasis, and results showed it was also possible to distinguish between brain metastasis subtypes. Chen *et al.* also utilised volumetric CE-T1WI, acquired from a single 3T scanner and used the whole tumour mask across 76 cases of glioblastoma and 58 cases of brain metastases, and achieved an accuracy of 78% [292]. Qian *et al.* utilised datasets from a hospital site as well as The Cancer Genome Atlas (TCGA) publicly available dataset to produce a relatively large dataset, however these were thick slices of 5 mm rather than volumetric studies with 1 mm slice thickness [293]. The results from this study showed the clinical performance of the best models were superior to neuroradiologists.

Three previous studies have utilised masks on multiple sequences; one small study which utilised T2WI and SWI with volumetric CE-T1WI sequences [294] and another moderate-sized study which combined T2WI and ADC with volumetric CE-T1WI features, which showed the machine learning method was superior to univariate analysis and clinical performance was

comparable to that of radiologists [295]. The third study utilised both a traditional machine learning and radiomics-based deep learning approach incorporating T2WI with volumetric CE-T1WI in a relatively large dataset [296]. The diagnostic performance of the model was 89%, and top radiomic features included shape, first order and second order features.

Of the three top radiomic features from the final model in the current study, two were shape-based features (*least axis length* and *sphericity*) and one was a first order feature (*energy*). The *least axis length* feature is based on the length of the smallest axis of the volume of interest, with higher values representing larger lengths, the *sphericity* feature measures roundness of the volume of interest with higher values representing a more circle-like shape, and the first order *energy* feature is a measure of the magnitude of voxel values in the lesion with larger values representing a greater sum of the squares of these values [283]. Significantly higher *least axis length*, lower *sphericity*, and higher *energy* values were observed in IDH-wildtype glioblastoma compared to brain metastases, suggesting that glioblastoma lesions were larger in short axis measurements, were less round in shape and had overall higher signal intensity on CE-T1WI throughout the entire lesion. Shape and first order radiomic features have been demonstrated as useful and top features in models in several previous studies [291,294–296]. Morphological differences in size and sphericity have previously been demonstrated between the two pathologies, with metastases reported being smaller and more spherical compared to glioblastoma [297,298], which is in agreement with the results and top radiomics features in the current study. The first order feature of *energy* is reflective of greater enhancing disease and solid components within the lesion in glioblastoma compared to metastases which appeared to be more cystic and contain a lower

proportion of enhancing disease. This is demonstrated in Figure 52, which shows cases to highlight the extreme differences visually in the degree of solid enhancing disease as a proportion of the lesion and corresponding *energy* values.

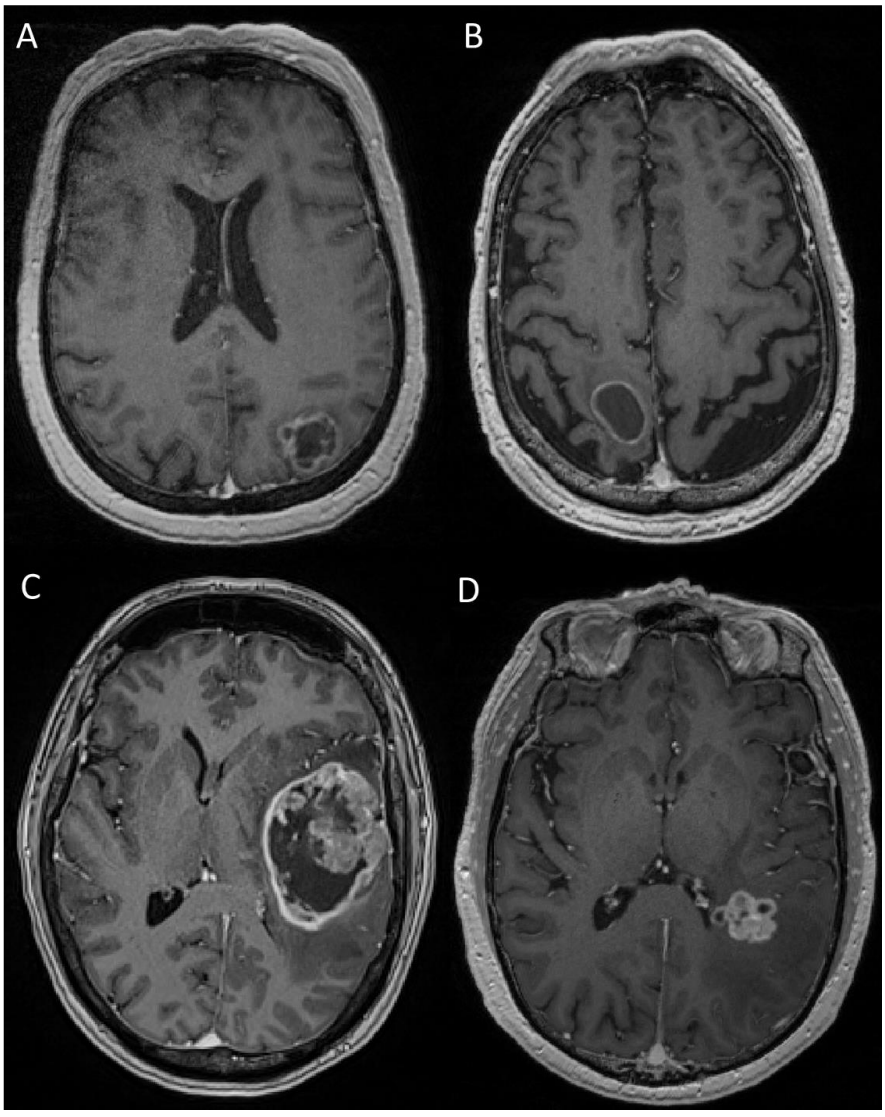

Figure 52. Images to reflect differences in *energy* between brain metastasis and glioblastoma on CE-T1WI. (A) Left parietal brain metastasis, with a very low standardised *energy* value of -0.98. (B) Right parietal brain metastasis, with a very low standardised *energy* value of -0.98. (C) Left insula glioblastoma with a relatively high standardised *energy* value of -0.47. (D) Left peri-trigonal glioblastoma with a much higher standardised *energy* value of -0.07.

4.6 Limitations and future work

One of the main limitations of this study is the selection bias from utilising cases of glioblastoma and metastases that were at different stages of disease and therefore different sizes. Brain metastases usually present as smaller lesions due to early and greater extent of vasogenic oedema, as well as the other systemic metastases leading to systemic symptoms and earlier imaging. Glioblastoma will usually present with a larger lesion size and therefore although this represents clinical practice, it would be ideal to size-match cases for the purpose of this study. This would significantly reduce the available dataset size as very large metastatic lesions would be fewer in number. However, on further analysis of the data in this study, the predictive power of each individual features in the final model were analysed and the AUC for each were: *least axis length* 0.93, *sphericity* 0.86, and *energy* 0.89. Although the size feature of *least axis length* had the highest performance, when this was removed from the model to assess the degree of selection bias, *sphericity* and *energy* features combined demonstrated an AUC of 0.94, which only slightly less compared to result of the final model including the size feature of *least axis length* with an AUC 0.97. This indicated that there was a difference in the model performance without size-matching lesions, but the difference was small and reflected routine clinical practice. It would also be useful to include human reading accuracy by a neuroradiologist for comparison. In addition, imaging studies with confirmed glioblastoma were reviewed from an earlier time period compared to metastases, at which point there were more studies performed on 1.5 Tesla compared to 3.0 Tesla, and this may have increased heterogeneity in results, but this was partially accounted for during the intensity normalisation process.

The study only used radiomic features from a single mask of the entire lesion on a single CE-T1WI sequence, however the use of clinical features or radiologist defined semantic features in combination with multiple sequences may help improve the diagnostic accuracy of models further. With additional sequences, segmentation of the peritumoural oedema is also possible on T2WI or FLAIR. Radiomic texture analysis of the perilesional environment has also shown to be useful to distinguish between metastasis and glioblastoma with a high accuracy, reflecting the heterogeneity of peritumoural oedema on imaging in glioblastoma [277], and also found to have a model performance comparable to that of radiologists [295].

In addition, advanced MRI techniques have shown to be useful for this issue but may not be clinically applicable for some centres as they are not routinely performed, require longer examination times and experienced neuroradiologists for interpretation. With more complex examinations, naturally datasets will be smaller in size, and machine learning studies favour large datasets from multiple centres, ideally with a prospective cohort to ensure robust validation. A small study of nine glioblastoma cases and nine metastases cases in which machine learning combined with multiple diffusion and perfusion parameters were able to distinguish between the pathologies with a highest accuracy of 83% [209].

In this study, various histologically distinct metastases were included in the same group, which inherently leads to heterogeneity and can lead to reduced accuracy of models and may be the reason for the lack of second order texture features in the final model. Separately analysing histologically similar metastatic lesions would enable greater performance of radiomic models but would require a larger sample size. The current study incorporated 53 lesions in each group, however further increasing the number of cases will also help to reduce

the chance of overfitting in the machine learning analysis and give more accurate results. Future work should include differentiating primary tumour type of a metastasis from imaging, and molecular subtyping of glioblastoma and metastases using radiomics, through the acquisition of larger datasets and using deep neural networks on handcrafted radiomic features, which has shown a higher performance than traditional machine learning methods [296]. The use of deep learning-based metabolic fingerprints from MRS data have also shown potential to differentiate between glioblastoma and metastasis with a high accuracy [299], and should be investigated further in combination with other MRI parameters.

4.7 Conclusion

This study has demonstrated that a machine learning-based radiomics model using shape-based and first order features from a single whole tumour segmentation mask on the pre-treatment volumetric CE-T1WI can differentiate between IDH-wildtype glioblastoma and metastasis with a moderately high accuracy. Future work should aim to integrate additional sequences and advanced MRI techniques to analyse the peritumoural region which may provide even greater diagnostic accuracy, as well as larger studies to provide greater diagnostic information about tissue diagnosis and molecular markers from imaging.

5. MACHINE LEARNING-BASED RADIOMIC EVALUATION OF PRE-OPERATIVE IMAGING FOR PREDICTION OF MGMT METHYLATION PROMOTER STATUS AND OVERALL SURVIVAL

This chapter is adapted from [300], previously published by *Magnetic Resonance Imaging*.

5.1 Introduction

It has been shown that the level of MGMT promoter methylation alters the effectiveness of alkylating agents, for example TMZ, which is the most common chemotherapy agent used for glioblastoma [301]. Therefore, epigenetic silencing of MGMT promoter expression, has been used as an important molecular marker in clinical practice [302,303]. Glioblastoma patients with a high level of MGMT promoter methylation tend to be more sensitive to TMZ and have a better OS as opposed to patients with a low level of methylation [304,305]. MGMT promoter methylation level is obtained through analysis of tumour DNA from biopsy or surgical resection [306]. It is currently used as a prognostic and predictive marker, however intra-tumoural heterogeneity of MGMT promoter methylation can pose difficulties in whole-tumour characterisation, leading to variable results with survival outcome [74].

MRI is an essential non-invasive imaging modality in clinical practice for assessing the three-dimensional characteristics of tumours and surrounding brain structures. Radiomics, as an emerging field, is the extraction of numerous quantitative imaging features for data-mining, to establish potential associations between imaging and biological markers non-invasively [307,308]. Recent studies have reported the usefulness of imaging parameters to predict MGMT promoter methylation status, however, there still remains debate whether radiomics could be used to accurately reflect tumour MGMT promoter methylation and which part of the lesion (enhancing solid part, necrotic/cystic part or whole tumour mass) contributes most to this correlation [304,309–316]. Semantic imaging features using Visually Accessible Rembrandt Images (VASARI) feature scoring system have been shown to improve survival prognostication in glioblastoma [317], and there are a few recent studies to investigate whether radiomic features and MGMT promoter methylation could be used to predict the OS of patients with glioblastoma [318–323].

The aim of this study was to determine how accurately sub-regional MRI radiomic models based on pre-operative CE-T1WI could accurately assess MGMT promoter methylation status and whether machine learning-based models using MGMT methylation, radiomic and clinical features could be improved with the addition of semantic features to predict OS in newly-diagnosed glioblastoma patients from pre-operative imaging.

5.2 Methods

5.2.1 Study design

The study involved retrospective analysis of consecutive patients who were newly diagnosed with glioblastoma and referred to the Queen Elizabeth Hospital Birmingham over a 3.5-year period between June 2014 and December 2017 as part of routine clinical care. Approvals for this study were obtained from the University Hospitals Birmingham Research Governance Office.

5.2.2 Inclusion and exclusion criteria

Inclusion criteria were: (a) pathology-confirmed glioblastoma according to the WHO Criteria; (b) pre-operative volumetric CE-T1WI MRI sequence; (c) MGMT promoter methylation status available; and (d) follow-up until death or May 2019. Exclusion criteria were: (a) treatment or biopsy of the tumour prior to the pre-operative MRI (n=0); (b) significant imaging artefact (n=13); (c) presence of another significant intracranial lesion (n=0); (d) ambiguous tumour margins resulting in unsuitability for segmentation (n=8); and (e) incomplete clinical data (n=13). 215 patients were assessed for suitability and 181 were included in the study.

5.2.3 Clinical and MGMT promoter methylation profiles

MGMT promoter methylation status was detected based on methylation-specific polymerase chain reaction and recorded in the form of a percentage, reported by a consultant neuro-histopathologist. Clinical information that was recorded included patient age, gender,

resection extent, post-operative chemo-radiotherapy treatment and OS until May 2019. Resection extent was categorised as complete macroscopic resection, near complete resection (>90%), debulking or biopsy, based on the post-operative MRI reported by a consultant neuroradiologist.

5.2.4 MRI acquisition

Standard-of-care clinical imaging data was acquired from various MRI scanners: Siemens 1.5 Tesla (130 studies), Siemens 3.0 Tesla (29 studies) and GE 1.5 Tesla (22 studies) scanners (Siemens Healthcare, Erlangen, Germany and GE, Milwaukee, USA) with 32-channel phased-array head coils, across several sites. Volumetric CE-T1WI was acquired with a maximum in-plane voxel size of 1.0 x 1.0 mm^2 and the maximum slice thickness was 1 mm. Field of view was 240 x 240 mm, matrix size was 256 x 256, TR = 540-690 ms and TE = 3-17 ms at 1.5 Tesla, TR = 1480-2350 ms and TE = 3-10 ms at 3.0 Tesla. IV gadolinium contrast (Dotarem; Guerbet, Villepinte, France) was administered as a hand-injected bolus of 10-15 ml (10 ml if weight <70 kg, 15 ml if weight ≥70 kg).

5.2.5 Image pre-processing and segmentation

Image signal intensity normalisation was performed using Cancer Imaging Phenomics Toolkit (CaPTk) software (version 1.3.0) [324]. Three 3D masks were segmented from each volumetric CE-T1WI study. Tumour mass (TM), defined as the entire enhancing lesion including non-enhancing tumour core, was manually segmented in the Microsoft Radiomics App (Microsoft Research, Cambridge, UK). Following this, the TM sub-component masks of

enhancing disease (ENH) and necrosis (NEC), the latter defined as non-enhancing tumour core, were semi-automatically segmented using ITK-SNAP (version 3.6.0) [325]. Manual adjustments were made on each slice through the consensus of two neuroradiologists (>20 and 5 years' experience), who were blind to clinical data and outcome.

5.2.6 Radiomic feature extraction

Radiomic features were extracted from TM, ENH and NEC from the volumetric CE-T1WI using PyRadiomics (version 1.2.0) [283]. A total of 111 features were extracted from each VOI, which included 18 shape-based features, 18 first-order features, and 75 second-order features made up of: 24 GLCM, 14 GLDM, 16 GLRLM, 16 GLSZM and five NGTDM features, resulting in 333 radiomic features from each patient. Semantic features were assessed using VASARI feature scoring system for gliomas [326]. The scoring system involved 16 semantic descriptors of imaging features that could be assessed on the single CE-T1WI. These included: location, side of lesion centre, eloquent location, degree of enhancement, presence of cyst, multifocality, enhancing margin thickness, definition of the enhancing margin, oedema proportion, presence of pial invasion, ependymal extension, cortical involvement, deep white matter involvement, non-contrast-enhancing tumour crossing midline, contrast-enhancing tumour crossing midline and satellite lesions. A consensus was obtained for each feature score between the two blinded neuroradiologists.

5.2.7 Feature selection, machine learning and statistics analysis

Cases were randomly assigned into training and testing groups (ratio 7:3). Feature selection and machine learning was performed on the training dataset to ensure an independent testing dataset. MGMT promotor methylation cut-off value was determined based on low and high survival groups using the "*surv_cutpoint*" function from the "*survminer*" package in R software, version 3.2.4 (R Foundation for Statistical Computing, Vienna, Austria) and all-relevant feature selection package "*boruta*" was used to determine the best feature set. SVM, *k*-NN, decision tree, random forest, gradient boosted trees and deep learning models were used in RapidMiner Studio (version 9.2.001) to build classification models, with 10-fold cross validation to tune the hyperparameters. The hold-out testing dataset was used to predict performance of each model.

Random survival forest (RSF) analysis was performed for survival prediction in R software. Features were ranked by positive importance and used in the variable-hunting algorithm through the "*randomForestSRC*" package. RSF models were built based on each set of features using 10-fold cross validation. Testing data was used to validate the performance of the model with predicted risk. The time-dependent cumulative case/dynamic control receiver operative curve (ROC) was analysed according to the predicted risk of each RSF model at the time point of every half month from 80 to 1325 days using the "*survivalROC*" package. The concordance probability (C-index) was also calculated to reflect the discrimination power of RSF models. Furthermore, the prediction risks were dichotomised into low and high-risk groups to find whether the models could be used to stratify the cases based on OS by using the log-rank test.

Various sets of features were built, consisting of one-layered set (radiomic, clinical, VASARI features and methylation separately), two-layered (a combination of any two categories of features), three-layered (a combination of any three categories of features) and four-layered (all feature sets combined). Continuous parameters were expressed as the means and SD, and compared using a Student's two-sided, unpaired *t*-test and one-way ANOVA. Discontinuous variables were reported as numbers and percentages and difference between groups were tested by Fisher's exact probability test, with $p<0.05$ to indicate a significant statistical difference. The entire workflow is demonstrated in Figure 53.

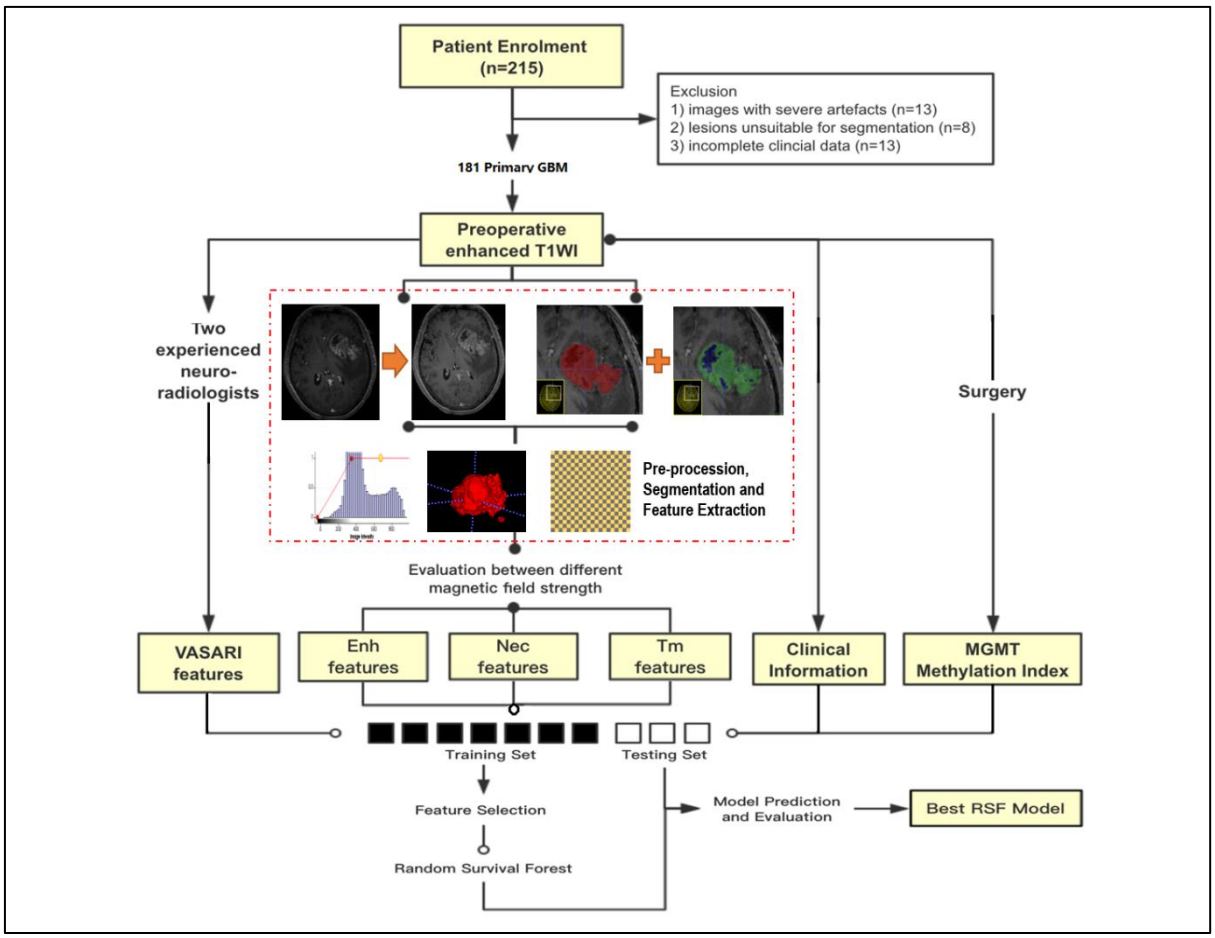

Figure 53. Overview of the study workflow.

5.3 Results

5.3.1 Patients

A total of 181 patients were included in this study (mean age 58.0±12.8 years, 68 (38%) female and 113 (62%) male). The median OS was 431 days (range 7 to 2426 days). There were no significant differences in age, gender, VASARI features, MGMT promoter methylation index or OS following random allocation into training and testing sets (Table 8).

		Training set (n=127)	Testing set (n=54)	*P* value
Age (years)		57.19 ±12.72	59.75 ±12.91	0.22
Gender (F/M)		49/78	19/35	0.79
Methylation (%)		16.71 ±17.24	18.53 ±19.59	0.55
Location	Brainstem	4	1	0.43
	Frontal lobe	44	13	
	Insular	4	0	
	Occipital lobe	9	6	
	Parietal lobe	17	8	
	Temporal lobe	49	26	
Side of lesion centre	Left/Middle/Right	62/3/62	29/0/25	0.47
Eloquent location	Motor	2	2	0.86
	Speech-Motor	17	6	
	Speech-Reception	7	4	
	Vision	10	5	
	None	91	37	
Enhancement	Marked/Mild/None	111/15/1	45/9/0	0.56
Cyst	Yes/No	96/31	37/17	0.42
Multifocal	Multicentric/Multifocal/None	4/13/110	0/8/46	0.30
Enhancing margin thickness	<3mm	31	14	0.61
	>3mm	89	35	
	Solid	7	5	
Enhancing margin	Well-/Poor-defined	46/81	24/30	0.38
Oedema proportion	None/ <33% />33%	9/62/52	6/24/24	0.52
Pial invasion	Yes/No	67/60	23/31	0.68
Ependymal extension	Yes/No	34/92	15/39	1.00
Cortical involvement	Yes/No	107/20	43/11	0.59
Deep white matter involvement	Yes/No	59/68	24/30	0.93
Non-contrast-enhancing tumour crossing midline	Yes/No	10/114	3/54	1.00
Contrast-enhancing tumour crossing midline	Yes/No	15/112	4/50	0.54
Satellites	Yes/No	29/98	12/42	1.00
Surgery:	Complete macroscopic resection	22	9	1.00
	Near complete resection	23	9	
	Debulking	77	36	
	Biopsy	3	0	
	Not available	2	0	
Chemotherapy:	Yes/No/Not available	98/28/1	37/16/1	1.00
Radiotherapy:	Yes/No/Not available	115/11/1	47/6/1	1.00
Survival Status:	Alive/Died	19/108	9/45	0.95
Overall survival (days)		502.21 ±354.14	485.44 ±356.10	0.78

Table 8. Baseline clinical information and VASARI features for patients in the training and testing cohorts.

5.3.2 Differences in radiomic features across magnetic field strengths

111 radiomic features were extracted from each of the components of ENH/NEC/TM for each patient. Of these, nine features demonstrated significant differences between 1.5 Tesla and 3.0 Tesla scanner magnetic field strengths. All features had higher values at 3.0 Tesla, these were: *firstorder.10Percent*, *ClusterShade*, *lmc1*, *lmc2*, *ClusterProminence*, *MCC* (from ENH mask), *firstorder.10Percent* (from NEC mask) and *LargeDependenceHighGrayLevel*, *MCC*, *Correlation* (from TM mask). All these radiomic features were excluded from further analysis.

5.3.3 Radiomic features to reflect MGMT methylation

MGMT promoter methylation in the cohort could be used to predict OS, with the best cut-off value being 12.75%, therefore this was chosen as the threshold for classification into high-methylation and low-methylation groups (Figure 54). There were significant differences in values of 42 radiomic features between high and low-methylation groups. The majority demonstrated higher values in the low-methylation group, especially in the first-order features. Following all-relevant feature selection, six features were deemed to be important and five more deemed equivocal. Therefore, these 11 features were used to build machine learning models, which showed accuracies of between 45-67% to predict MGMT promoter methylation status (Table 9).

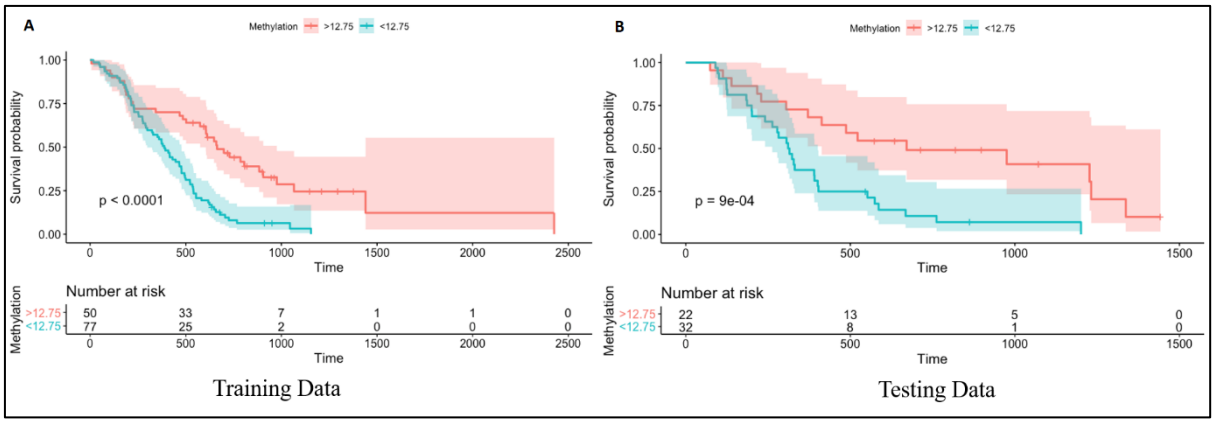

Figure 54. Kaplan-Meier plots of training (A) and testing (B) groups based on MGMT promoter methylation index.

Feature Layers	*k*-NN	SVM	Decision forest	Decision tree	Gradient boosted tree	Deep learning
Radiomic features	52.31%/ 60.00%	60.26%/ 60.00%	61.92%/ 61.82%	57.12%/ 58.18%	55.58%/ 61.82%	45.58%/ 47.27%
Radiomic features Clinical information	52.31%/ 58.18%	60.26%/ 60.00%	56.35%/ 60.00%	57.82%/ 58.18%	56.47%/ 60.00%	46.15%/ 49.09%
Radiomic features VASARI features	58.53%/ 56.36%	60.26%/ 60.00%	48.46%/ 67.27%	53.91%/ 60.00%	53.72%/ 62.27%	49.29%/ 54.55%
Radiomic features Clinical information VASARI features	58.53%/ 56.36%	60.26%/ 60.00%	60.90%/ 52.73%	63.40%/ 54.55%	58.65%/ 52.73%	49.81%/ 45.45%

Table 9. Performance of machine learning models and deep learning for prediction of MGMT promoter methylation status, according to feature set in the training/testing groups.

5.3.4 RSF models to predict OS

Across all features, age and MGMT promoter methylation index were the most important for predicting OS in the RSF models (**Figure 55**). Using variable importance and the variable-hunting algorithm, five ENH, two NEC and four TM radiomic features were selected to build

RSF models with cross-validation. The importance of these features and their cut-off values to separate the high- and low-survival groups are listed in **Table 10**. Four layers of RSF models were built and the discriminative performances were demonstrated via C-index and integrated AUC (iAUC) values at each 15-day time point by cumulative case/dynamic control ROC, which was taken at 82 points between days 15 to 1230. The average iAUC and C-index values in the testing set are listed in **Table 11**.

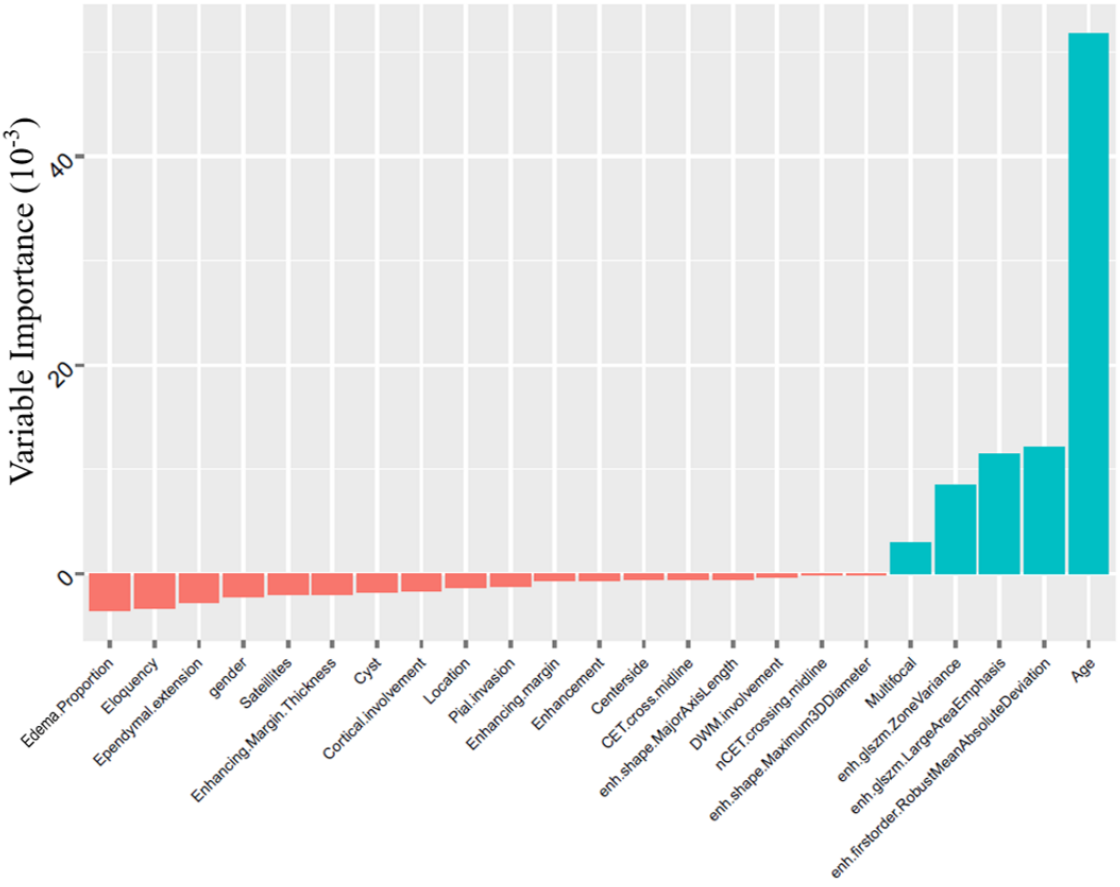

Figure 55. Variable importance in the best RSF model.

Features	Importance ($x10^{-3}$)	Cut-off value	High Survival Group (value, N)	Low Survival Group (value, N)	*P* value
Enhancing mask					
Enh.glszm.LargeArea-Emphasis	38.26	23021.35	169470.20 ±26710.76 (31)	4113.88 ±5721.11 (150)	0.02
Enh.glszm.ZoneVariance	32.99	22870.60	169058.10 ±26649.24 (31)	4071.05 ±5687.17 (150)	0.02
Enh.firstorder.Robust-MeanAbsoluteDeviation	20.05	34.23	27.06 ±4.85 (39)	58.24 ±14.58 (142)	<0.01
Enh.shape.MajorAxis-Length	12.71	48.32	63.39 ±12.65 (101)	35.06 ±8.38 (80)	0.03
Enh.shape.Maximum3D Diameter	10.23	62.74	76.19 ±12.73 (72)	44.69 ±11.84 (109)	0.01
Necrosis mask					
Nec.Image.original.-Mean	9.87	79.74	93.54 ±9.47 (144)	74.73 ±3.67 (37)	0.14
Nec.firstorder.-RootMeanSquared	7.48	182.94	141.94 ±33.50 (75)	232.13 ±46.71 (106)	<0.01
Tumour mass mask					
Tm.glrlm.shortRunLow-GrayLevelEmphasis	44.51	$1.06x10^{-2}$	$2.12 \pm 1.39x10^{-2}$ (115)	$0.76 \pm 0.18x10^{-2}$ (66)	<0.01
Tm.shape.Maximum3D Diameter	26.15	53.46	71.76 ±14.40 (112)	39.89 ±8.91 (69)	0.03
Tm.ngtdm.Busyness	17.54	11.68	24.44 ±22.00 (72)	5.69 ±3.23 (109)	0.01
Tm.shape.SurfaceArea	17.24	3752.96	10233.89 ±4083.43 (140)	2567.8 5±889.92 (41)	0.02

Enh = Contrast-enhancing region, *glrlm* = gray-level run length matrix, *glszm* = gray-level size zone matrix, *nec* = necrotic region, *ngtdm* = neighbourhood gray-tone difference matrix, *tm* = tumour mass mask, *3D* = three-dimensional.

Table 10. Selected radiomic features using the variable hunting function in RSF models.

Feature layer	Feature set	iAUC (RSF Model)	C-index (RSF Model)
1 layer	Clinical	80.78±6.15	75.56±0.18
	VASARI	90.66±3.31	84.16±0.21
	Methylation	81.62±12.80	69.76±0.22
	Radiomics-ENH	83.21±11.18	67.44±0.33
	Radiomics-NEC	82.63±6.17	71.28±0.28
	Radiomics-TM	87.96±4.85	84.05±0.29
2 layer	Clinical+VASARI	92.51±2.07	84.92±0.35
	Clinical+Rad(ENH)	83.77±5.96	74.47±0.42
	Clinical+Rad(NEC)	84.07±3.41	78.10±0.32
	Clinical+Rad(TM)	88.19±3.91	83.68±0.29
	VASARI+Rad(ENH)	94.34±2.22	88.07±0.35
	VASARI+Rad(NEC)	89.91±3.48	83.10±0.42
	VASARI+Rad(TM)	94.09±1.82	89.81±0.30
	Methylation+Clinical	85.25±16.27	76.07±0.25
	Methylation+VASARI	90.57±10.82	81.58±0.24
	Methylation+Rad(ENH)	86.03±10.81	74.91±0.20
	Methylation+Rad(NEC)	85.36±13.58	73.10±0.35
	Methylation+Rad(TM)	93.46±5.35	83.61±0.23
3 layer	Clinical+VASARI+Rad(ENH)	96.34±1.76	90.00±0.24
	Clinical+VASARI+Rad(NEC)	95.80±1.56	90.79±0.31
	Clinical+VASARI+Rad(TM)	92.21±3.39	85.35±0.31
	Clinical+VASARI+Methylation	93.74±8.41	86.00±0.32
	VASARI+Methylation+Rad(ENH)	92.97±6.58	82.02±0.37
	VASARI+Methylation+Rad(NEC)	89.25±10.42	80.86±0.38
	VASARI+Methylation+Rad(TM)	92.82±6.62	83.25±0.21
4 layer	Clinical+VASARI+Rad(ENH)+Methylation	95.12±5.85	87.31±0.27
	Clinical+VASARI+Rad(NEC)+Methylation	91.69±10.58	83.97±0.30
	Clinical+VASARI+Rad(TM)+Methylation	90.79±11.32	81.65±0.31

ENH = contrast-enhancing mask, *C-index* = index of concordance, *iAUC* = integrated AUC. *Rad* = Radiomic features, *NEC* = necrosis mask, *TM* = tumour mass mask, *VASARI* = Visually Accessible Rembrandt Images.

Table 11. Performance of the different RSF models with various feature layers.

VASARI features extracted from CE-T1WI provided the best performing RSF model among the six single-layer models. The highest performing model overall was the 3-layer model combining selected radiomic features, clinical information and VASARI features, with an iAUC

of 96.2±1.7 and C-index of 90.0±0.3. Feature distribution heatmap from this model is provided in **Figure 56** and the AUC performance at each time point from the highest performing model in each layer is shown (**Figure 57**). Kaplan-Meier survival plot and prediction values of each case in the best RSF model are presented, with linear regression used to calculate OS prediction with an R^2 of 0.67 (**Figure 58** and **Figure 59**). Typical cases are presented in **Figure 60**.

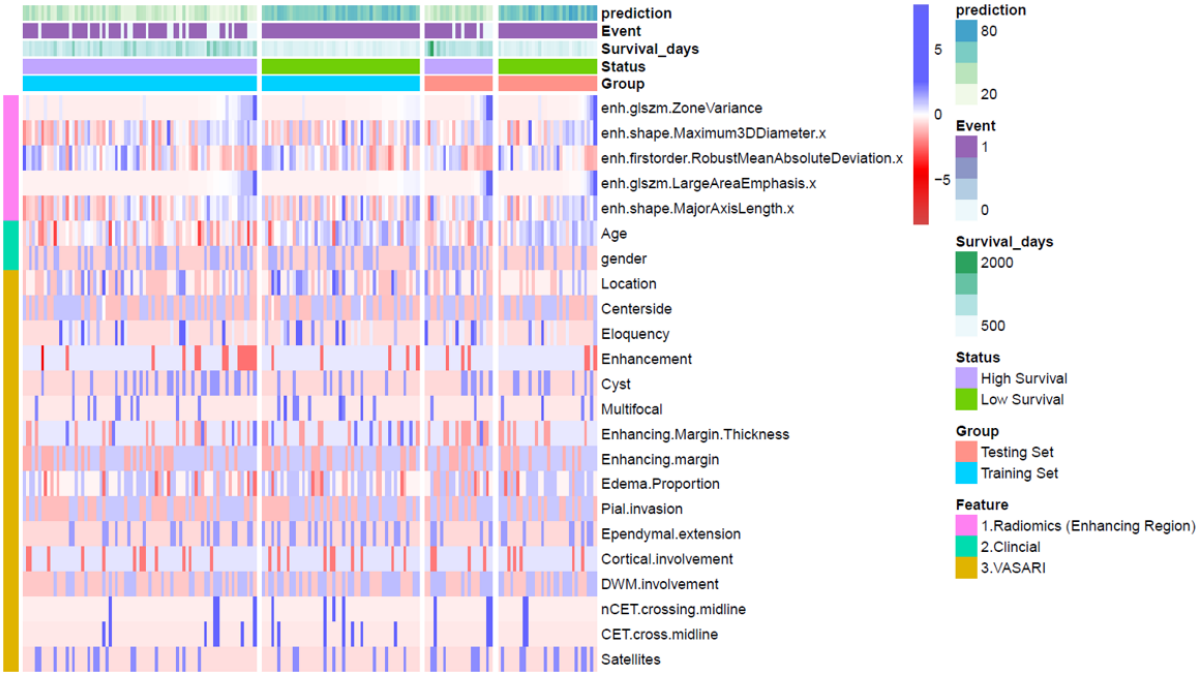

Figure 56. Heatmap of features used in the best RSF model. The cut-off prediction value was 48. For the high survival group, the median survival duration was 648 days while the median value was 214 days in the low survival group.

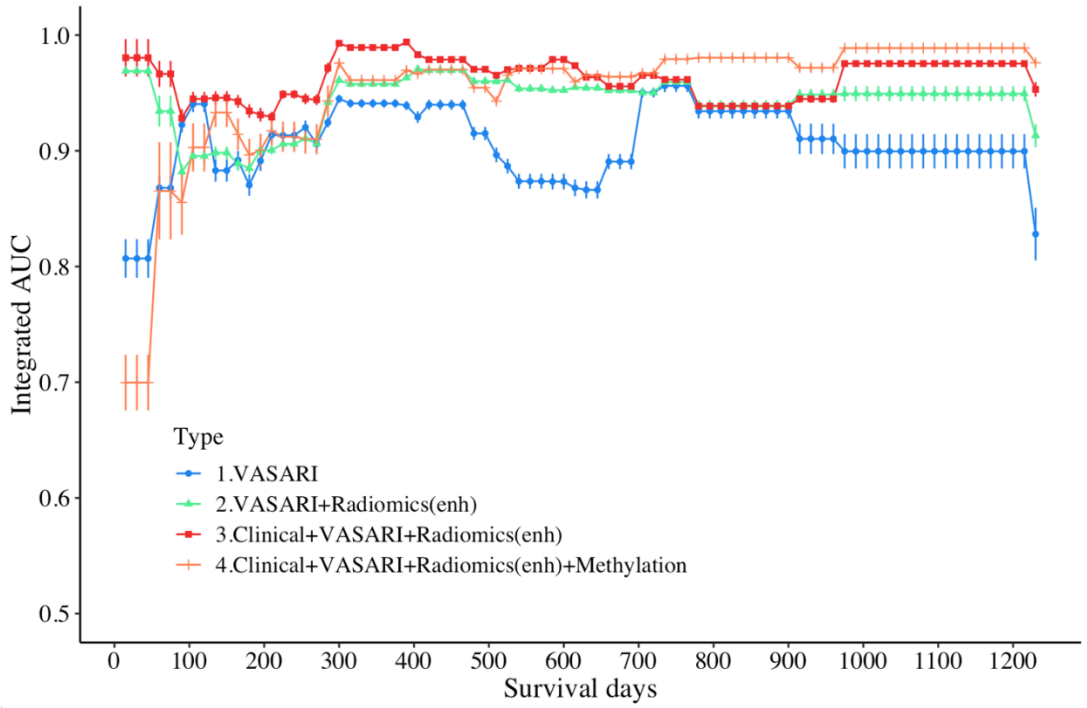

Figure 57. Performance of the best RSF models based on 1-, 2-, 3- and 4-layer features.

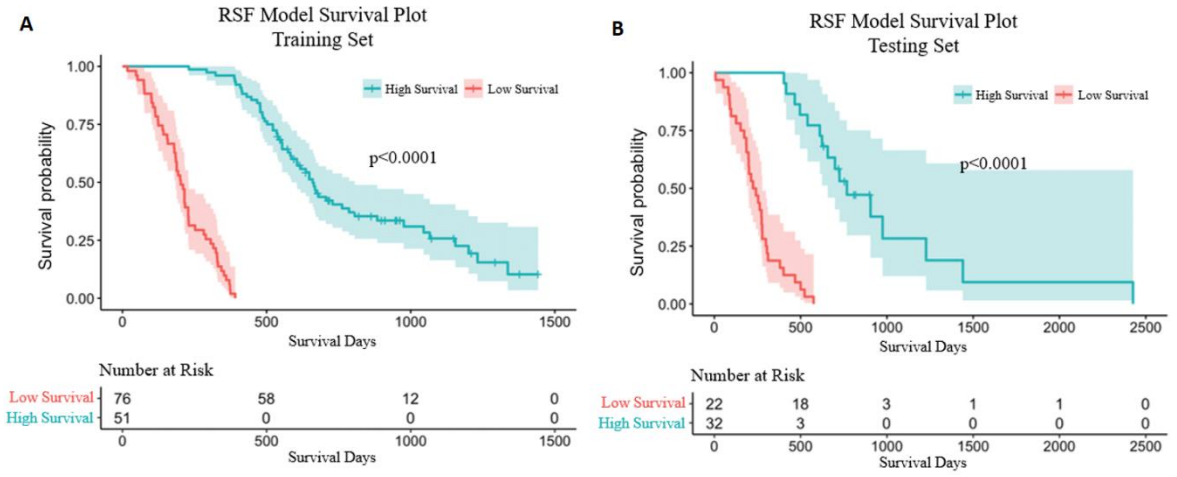

Figure 58. The Kaplan-Meier survival plot of the RSF model in the training (A) and testing (B) groups.

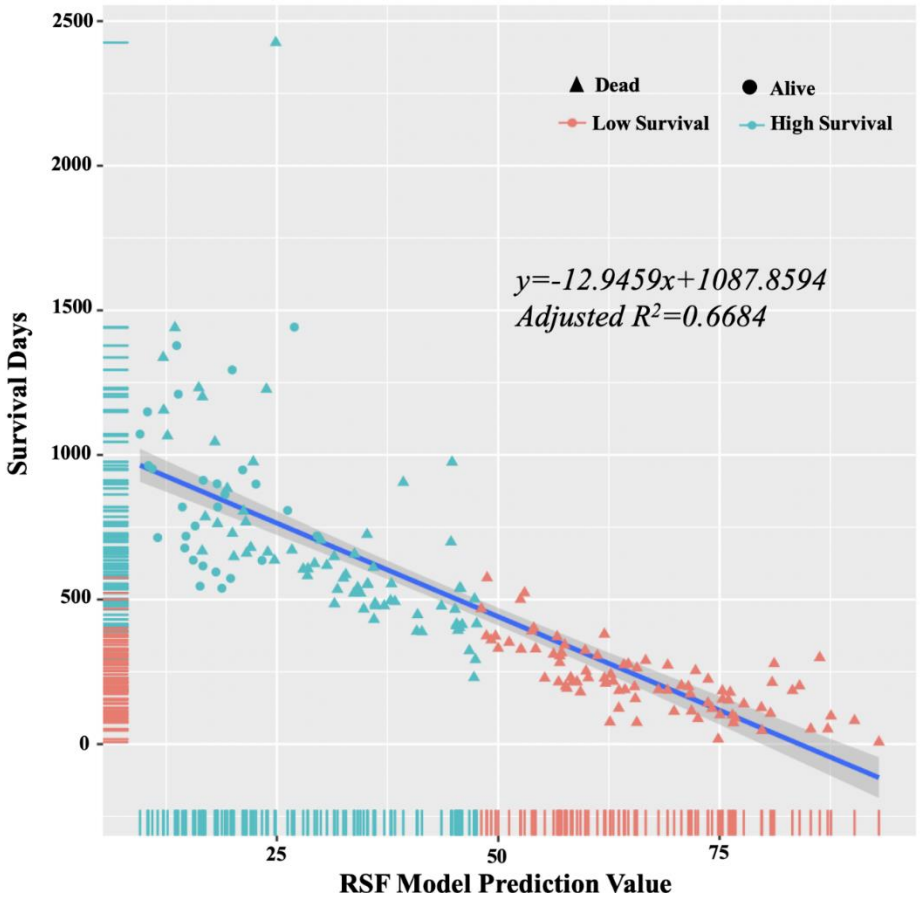

Figure 59. Scatter plot and fitted linear regression based on the prediction value of the best RSF model.

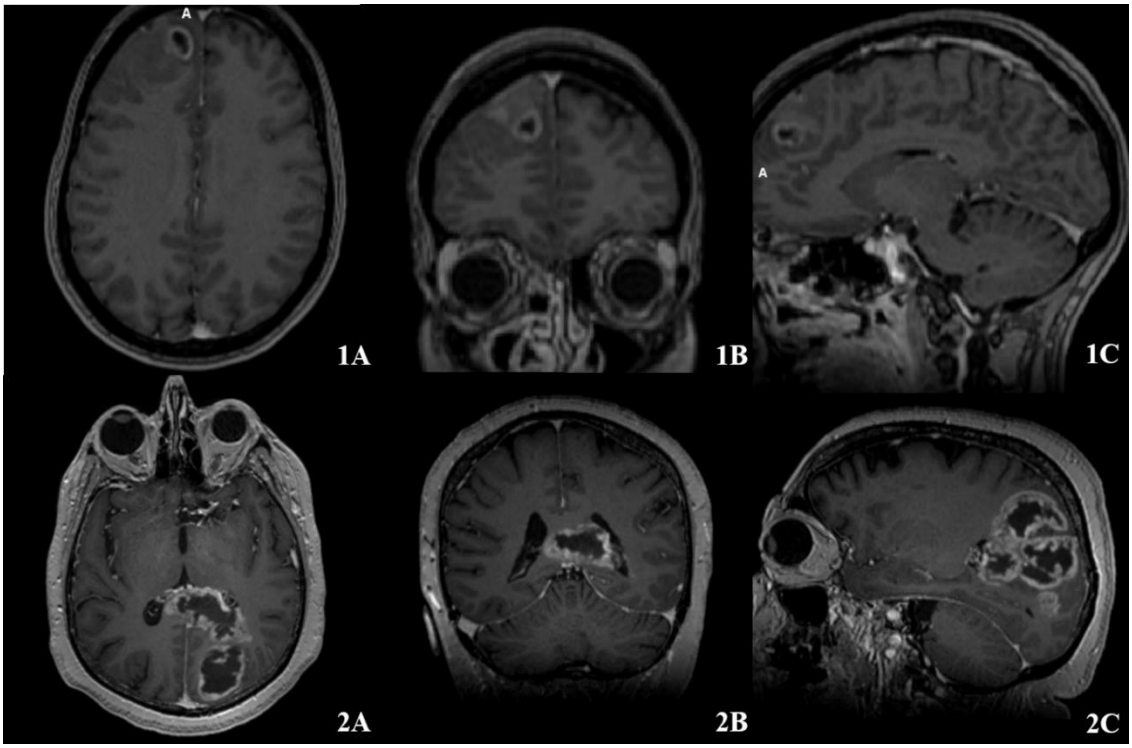

Figure 60. Typical glioblastoma cases in the high and low survival groups. (1A-1C) Single glioblastoma lesion in the right frontal lobe with no invasion of surrounding structures. All selected radiomic feature values were relatively low and indicated a small-size and homogeneously enhancing component. The model's prediction value for this patient was 29.7, classified as low risk. MGMT promoter methylation index was 43.5% and the patient's OS was 1440 days. (2A-2C) Glioblastoma with multifocal lesions and ependymal and pial invasion. Lesions crossed the midline and satellite lesions were present. All selected radiomic feature values were relatively high, indicating a larger and heterogeneously enhancing component. The model's prediction value for this patient was 76.4, classified as high risk. The MGMT promoter methylation index was 2% and the patient's OS was 100 days.

5.4 Discussion

Radiomic features derived from conventional MRI, provides additional information beyond the scope of human visual perception, which is emerging to be valuable in prediction of glioblastoma OS and PFS, and there is relatively limited literature on this topic [314,315,318–322]. There are several strengths to this study; firstly, the amalgamation of clinical features, radiomic features, MGMT promoter methylation index and semantic VASARI features for glioblastoma OS prediction, to date has not been investigated in combination.

VASARI morphological features, assessed by neuroradiologists, were deemed to be very important in the survival models and the best performing one-layer RSF model. According to variable importance, multifocality was the most important VASARI feature for OS prediction. Regarding radiomic features, a total of five ENH, two NEC and four TM features were selected via variable hunting. Shape-related and first-order features accounted for 64% (7/11) which meant the size and enhancing signal intensity appeared to be important for OS. These in combination with the other second-order selected features including ENH-GLSZM *zone variance*, ENH-GLSZM *large area emphasis*, ENH-GLRLM *short run low gray level emphasis* and TM-NGTDM *busyness*, reflected that glioblastoma with longer OS presented as a larger tumour along with weaker and more heterogenous enhancement. ENH features contained more useful information to predict OS than NEC or TM features. The best performing RSF model for OS prediction was based on clinical, VASARI and selected ENH radiomic features, achieving an iAUC of 96.20±1.73 and C-index of 90.00±0.34, indicating that it was possible to accurately predict OS from pre-operative imaging. Furthermore, the relationship between model prediction and actual OS of the cases showed a linear relationship with R^2=0.67. It

should also be noted that although ENH radiomic features were important, the performance of the model based on clinical, VASARI and selected TM features also achieved an iAUC value of 92.21±3.39 and C-index of 85.35±0.31, similar to those from the RSF model aforementioned. This model would be less time-consuming and more practical as it may easier for a radiologist or segmentation algorithm to produce a mask from the entire tumour as opposed to the subcomponent of contrast-enhancing area alone.

The second strength of this study is that it has a comparatively large sample size and used imaging from multiple MRI scanners across a number of hospital sites at different field strengths, reflecting heterogeneity of clinical practice. The majority of previous studies utilise imaging from either a single institution, single magnetic field strength or publicly available imaging datasets, which limits wider clinical applicability. In this study, after gray-scale normalisation, the few significantly different features between field strengths were excluded, to analyse radiomic features from 1.5 Tesla and 3.0 Tesla together for a more utilisable and clinically applicable model. Few researchers have combined imaging studies across magnetic field strengths for radiomic studies in feature selection and model-building, however, the use of and combining studies from different scanners and field strengths is an important practical issue that radiologists encounter in clinical practice. In addition, this study has utilised the single pre-operative volumetric CE-T1WI, used for neurosurgical navigation, which is more practical than analysis of multiple sequences which recent studies have employed. Producing models based on volumetric imaging is also ideal going forward as imaging protocols with thick slices are being replaced with thin-slice volumetric imaging.

MGMT promoter methylation index proved to be important for OS prediction with the optimal cut-off value of 12.75% in this cohort. A total of 42 radiomic features exhibited significant differences between the low- and high-methylated groups. Six of these showed a weak but significant relationship with MGMT promoter methylation index value (Pearson coefficient range: -0.22 to -0.19). First-order ENH radiomic features of *mean*, *root mean squared* and *median* exhibited the greatest negative correlation with MGMT methylation (Figure 61). This indicates that higher MGMT promoter methylation is associated with lower normalised signal intensity from contrast-enhancing glioblastoma, which might be explained by higher protein concentration or less BBB impairment in the highly methylated group, which requires further laboratory studies for confirmation. Although several popular models were used, accuracies of model performance for MGMT promotor methylation prediction appeared to be low, at 45-67%. This is similar to previously published work, which showed an accuracy of 67% [313]. Other research using features extracted from multiple sequences and thick-sliced imaging have demonstrated slightly higher performance [314,315], and therefore the limited model performance might be caused by the use of a single volumetric CE-T1WI protocol, with thin-slices.

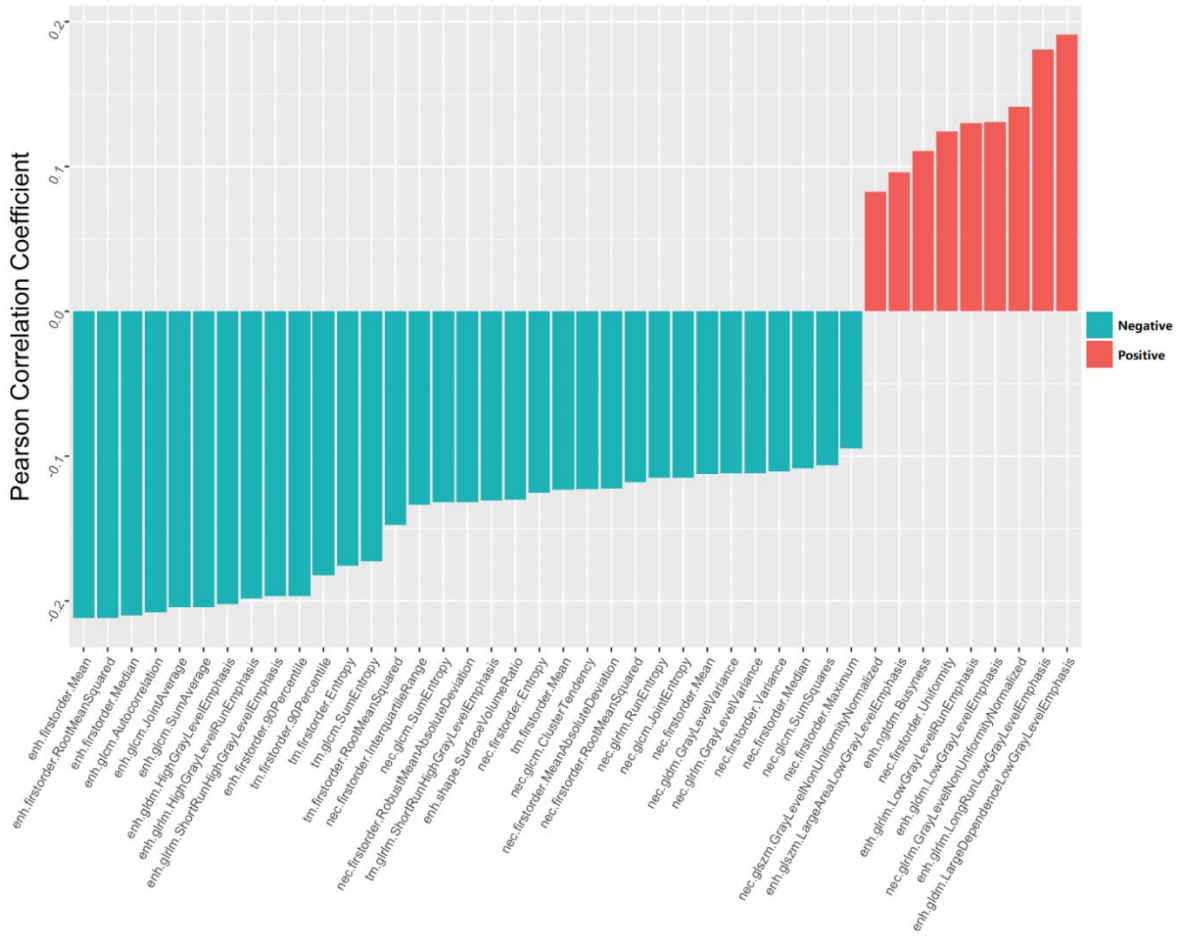

Figure 61. An illustration of Pearson correlation coefficient between the selected 42 radiomic features and MGMT promoter methylation index.

5.5 Limitations and future direction

The limitations of this study include the lack of multiple imaging sequences. The use of additional conventional imaging sequences, the component of oedema, as well as advanced multiparametric imaging such as DWI, PWI and MRS can provide additional information and is expected to improve model performance. However, there is a practical and health economic impact for the use of these additional imaging sequences pre-operatively, which needs to be

weighed up, as currently the single CE-T1WI is the only essential sequence required for operative planning. A recent study using radiomic features derived from conventional and multiparametric MRI consisting of PWI and DTI parameters identified three distinct imaging subtypes of glioblastoma which could risk-stratify patients and identify phenotypic heterogeneity in vivo [327], highlighting the potential of combining advanced imaging into machine learning models. Secondly, all genetic molecular marker information was not available for this study, such as IDH, EGFR, ATRX, p53, etc. which may be important factors in OS prediction. Future work should be focussed on improving models for prediction of MGMT promotor methylation status as well as other molecular markers. In fact, recent radiomic studies have shown the potential to predict other molecular markers such as TERT promoter mutation from combining conventional imaging and DWI, although further work is required to improve these models [328]. Advancing imaging such as MRS can be used for the oncometabolite 2HG to specifically identify IDH-1 mutations in vivo with a high positive predictive value [329,330], but it is recommended that other metabolites and structural imaging is included in the analysis [331], which could form the basis of future machine learning models. Unsupervised deep learning-based techniques using CNN on the publicly available dataset from The Cancer Imaging Archive (TCIA) have shown the potential to be able to classify IDH-1 mutation, 1p19q co-deletion and MGMT promoter methylation status with a high accuracy as well as showing that each genetic category was associated with distinctive morphologic imaging features [332]. Lastly, although this study utilised data from a number of hospital sites, this was a retrospective study performed on routinely collected clinical data. Going forward, larger prospective studies are required with external cross-validation cohorts. The larger studies will also favour the use of deep learning models, which have shown the

potential to outperform supervised radiomic model approaches for this particular question of imaging-based molecular marker prediction.

5.6 Conclusion

This study presents the usefulness of radiomic and VASARI features from pre-operative volumetric CE-T1WI in patients with glioblastoma. MGMT promoter methylation index demonstrated a significant relationship with a number of first order radiomic features from enhancing disease, however models only gave a modest level of accuracy for its prediction and further work is required to improve its accuracy. Models using semantic VASARI and radiomic features in combination with clinical information showed promise for predicting OS with a high level of accuracy.

6. ADVANCED MRI TECHNIQUES FOR EARLY PREDICTION OF TREATMENT RESPONSE

Parts of this chapter are adapted from [113], previously published by *Insights into Imaging*.

6.1 Introduction

Alternative imaging techniques that are clinically applicable and can more accurately assess early treatment response are required to optimise treatment strategies, improve patient outcomes and maximise quality of life for patients. Multiparametric MRI methods that can monitor physiological and metabolic properties of tumour are being employed and investigated to address this question. The most commonly used techniques include DWI, PWI and MRS. There is increasing data supporting the utility of each of these methods, although limitations remain such that no method is currently validated as yielding the definitive MRI parameter of choice to distinguish between tPD and psPD. Nevertheless, combining these three techniques in a multiparametric MRI protocol may provide a higher degree of confidence in assessing glioblastoma treatment response [127,128]. The aim of this study was to evaluate the clinical utility of multiparametric MRI through DWI, PWI and MRS for differentiating between tPD and psPD in patients undergoing treatment for glioblastoma.

6.2 Methods

6.2.1 Study design

The study involved retrospective analysis of patients who were treated for glioblastoma at Queen Elizabeth Hospital Birmingham over a two-year period (June 2014 to May 2016). Approvals for this study were obtained from the University Hospitals Birmingham Research Governance Office.

6.2.2 Inclusion and exclusion criteria

Inclusion criteria were: (a) pathology-confirmed glioblastoma according to the World Health Organisation Criteria; (b) surgery followed by standard CRT treatment of radiotherapy and concurrent TMZ followed by adjuvant TMZ [4]; (c) presence of and measurable increase in contrast-enhancing disease on the post-CRT baseline MRI study at 4-8 weeks, compared to the immediate post-operative MRI study; and (d) multiparametric MRI with DWI, PWI and MRS performed between 4-8 weeks post-CRT. Exclusion criteria were: (a) patient lost to follow-up within six months of CRT treatment; and (b) incomplete post-CRT imaging or presence of significant imaging artefact. The flowchart of patient inclusion and exclusion is shown in Figure 62. In total, 220 patients underwent surgery for glioblastoma at Queen Elizabeth Hospital Birmingham between June 2014 to May 2016 and were assessed for eligibility. Of these, 45 patients had new or an increase in enhancing disease of at least 25% on the post-CRT baseline MRI study and had clinical and imaging follow-up until at least six months, in order to determine outcome. Nine of the 45 patients subsequently had

multiparametric MRI within 4-8 weeks following CRT. Overall survival was assessed until August 2020 (75 months).

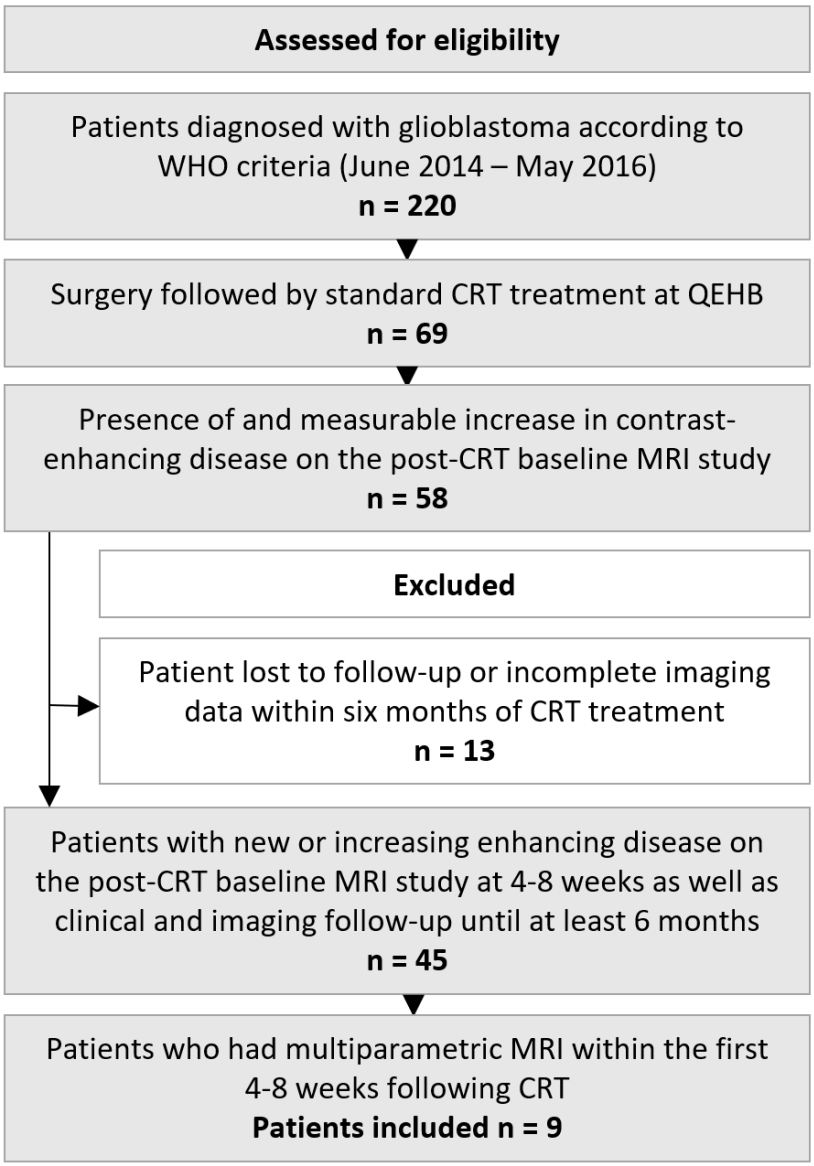

Figure 62. Flowchart of patient inclusion and exclusion criteria.

6.2.3 Reference standard

Standard-of-care MRI reports and clinical oncology noting within the six months following CRT were reviewed in order to ascertain the outcome of tPD or psPD. Patients were deemed to have tPD if there was radiological or clinical progression according to RANO criteria, or death within six months. Patients were deemed to have psPD if there was no further radiological or clinical progression according to RANO criteria, within the six months following CRT. Imaging was re-reviewed by a consultant neuroradiologist where there was outcome discrepancy or uncertainty.

6.2.4 MRI acquisition, post-processing and analysis

Imaging acquisition was performed as previously described in Section 3.2.2; post-processing and analysis of imaging was performed as described in Section 3.2.3. Multiparametric MRI parameters of ADC, rCBV, Cho/Cr ratios at 30 ms and 135 ms, Cho/NAA ratio at 135 ms and presence or absence of lipid/lactate were recorded, compared to cut-off values and correlated with subsequent clinico-radiological treatment response outcome. Interpretation of multiparametric MRI to distinguish tPD from psPD was undertaken using optimal threshold values, based on previous literature and local expertise, as follows: ADC<1000x$10^{-6}$$mm^2$$s^{-1}$ [341,342], rCBV>2.1 [127,343,344], Cho/Cr ratio≥1.8 [345,346], and Cho/NAA≥1.9 [153,346]. Results from the case series are presented and discussed.

6.3 Results

6.3.1 Patients

There were 45 patients who had new or an increase in enhancing disease on the early post-CRT MRI study, which was performed at a mean of five weeks following treatment; all these patients had clinical and imaging follow-up until at least six months or death if this was earlier. In this cohort, 23 (51%) were deemed to have tPD (mean age 53.7 years, 30% female, mean MGMT promoter methylation 10.3%), 18 (40%) were deemed to have psPD (mean age 49.5 years, 33% female, mean MGMT promoter methylation 14.5%), and 4 (9%) were deemed to have an equivocal outcome (mean age 67.6 years, 25% female, mean MGMT promoter methylation 22.5%). The mean OS from the end of CRT treatment was 13.5 months (range 1.3-53.8) for those with tPD, 23.7 months (range 6.6-57.4) for those with psPD and 9.6 months (range 4.5-17.6) for those with an equivocal outcome. Of the 45 patients, 9 subsequently had multiparametric MRI within 4-8 weeks following CRT as part of routine clinical care.

6.3.2 Multiparametric MRI parameters

Results from the individual parameters acquired from multiparametric MRI, multiparametric MRI outcome, clinico-radiological outcome, MGMT promotor methylation and OS for all cases are presented in Table 12.

Case	MGMT promoter methylation (%)	DWI	PWI	MRS				Multiparametric MRI outcome (time of scan, months)	Radiological follow-up and RANO outcome at each timepoint	Overall survival from CRT (months)	Overall outcome (according to RANO)
		ADC (x 10^{-6} mm^2/s)	rCBV ratio	Cho/Cr ratio (135ms)	Cho/Cr ratio (30ms)	Cho/NAA ratio (135ms)	Lipid/ Lactate (30ms)				
1	5.50	914	3.8	2.0	2.4	2.2	Present	tPD (1.0)	3-month MRI: SD	6	tPD
2	2.00	903	3.0	1.8	2.3	3.1	Present	tPD (1.0)	3-month MRI: SD 6-month MRI: PD	9	tPD
3	2.25	504	10.5	3.0	2.7	1.9	Present	tPD (1.0)	3-month MRI: SD 6-month MRI: PD	6	tPD
4	3.00	863	5.4	4.4	4.0	3.8	Present	tPD (1.8)	None	2	tPD
5	3.75	673	9.1	1.9	1.8	2.0	Present	tPD (1.2)	4-month MRI: PD 10-month MRI: PD	20	tPD
6	51.75	1186	1.4	1.2	1.4	1.4	Present	psPD (0.9)	3-month MRI: SD 5-month MRI: SD	52+	psPD
7	4.25	1497	1.5	1.7	1.4	1.8	Absent	psPD (1.0)	3-month MRI: SD 6-month MRI: SD	37	psPD
8	18.00	951	4.2	2.6	2.2	4.1	Present	tPD (1.9)	4-month MRI: SD 7-month MRI: PR	36	psPD
9	6.75	1281	8.1	2.3	1.8	2.3	Present	tPD (0.9)	4-month MRI: PD 7-month MRI: PD	34	tPD

Table 12. Multiparametric MRI findings [diffusion (ADC), perfusion (rCBV ratio), spectroscopy (Cho/Cr ratio, Cho/NAA ratio and presence of lipid/lactate)] and patient outcome.

6.3.3 True progression

Six patients (cases 1-5 and 9) were correctly deemed to have tPD from multiparametric MRI evaluation within the first 4-8 weeks post-CRT. Cases 1-5 showed similar multiparametric findings across all parameters with a low ADC, high rCBV, high Cho/Cr ratio and high Cho/NAA ratio consistent with expectations for tPD (**Figure 63**). All patients had clinico-radiological confirmation of tPD. One patient (case 5) had debulking surgery at 7-months due to tPD and received second line chemotherapy between 11-15 months, likely contributing to the survival time of 20 months.

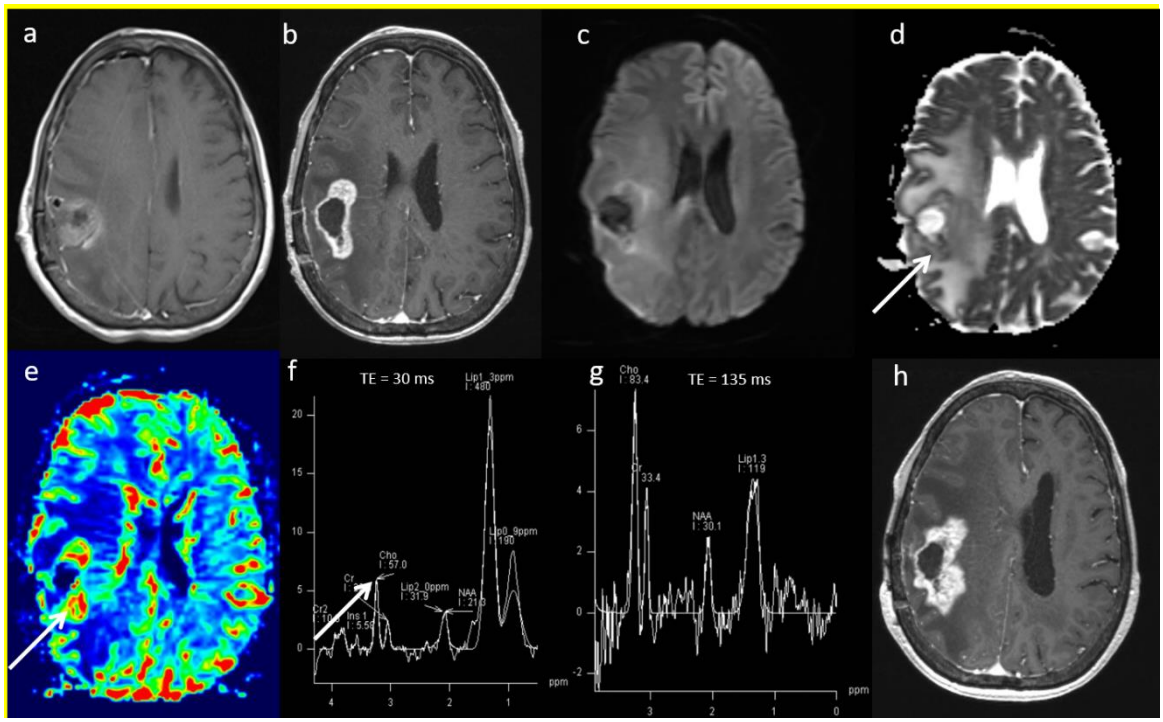

Figure 63. Case 2: True progression. (a) Immediate post-operative CE-T1WI following resection of a right fronto-parietal glioblastoma. (b) Conventional CE-T1WI four weeks post-CRT treatment demonstrated an increase in the enhancing lesion size with surrounding perilesional oedema. Multiparametric MRI at this time point demonstrated: (c, d) areas of low ADC (903 x $10^{-6}$$mm^2s^{-1}$, arrow), (e) a high rCBV ratio (3.1, arrow) on PWI, (f, g) a high Cho/Cr ratio (2.3, arrow), high Cho/NAA ratio and presence of lipid/lactate on MRS. All parameters

suggested a poor response and disease progression. (h) Six-month follow-up conventional CE-T1WI confirmed an increase in enhancing disease, indicating tPD.

The remaining patient (case 9) also demonstrated features of tPD on initial multiparametric MRI (Figure 64), with two of the three parameters (PWI and MRS) consistent with tPD. PD was confirmed on imaging at 4 months and as a result of confirmed progression, chemotherapy was changed. The 7-month follow-up MRI scan showed continued PD, confirming tPD according to RANO criteria, and treatment stopped. No further imaging was performed until 19 months, which revealed a stable treated lesion, but a new separate lesion. There was further PD at 32 months and death at 34 months.

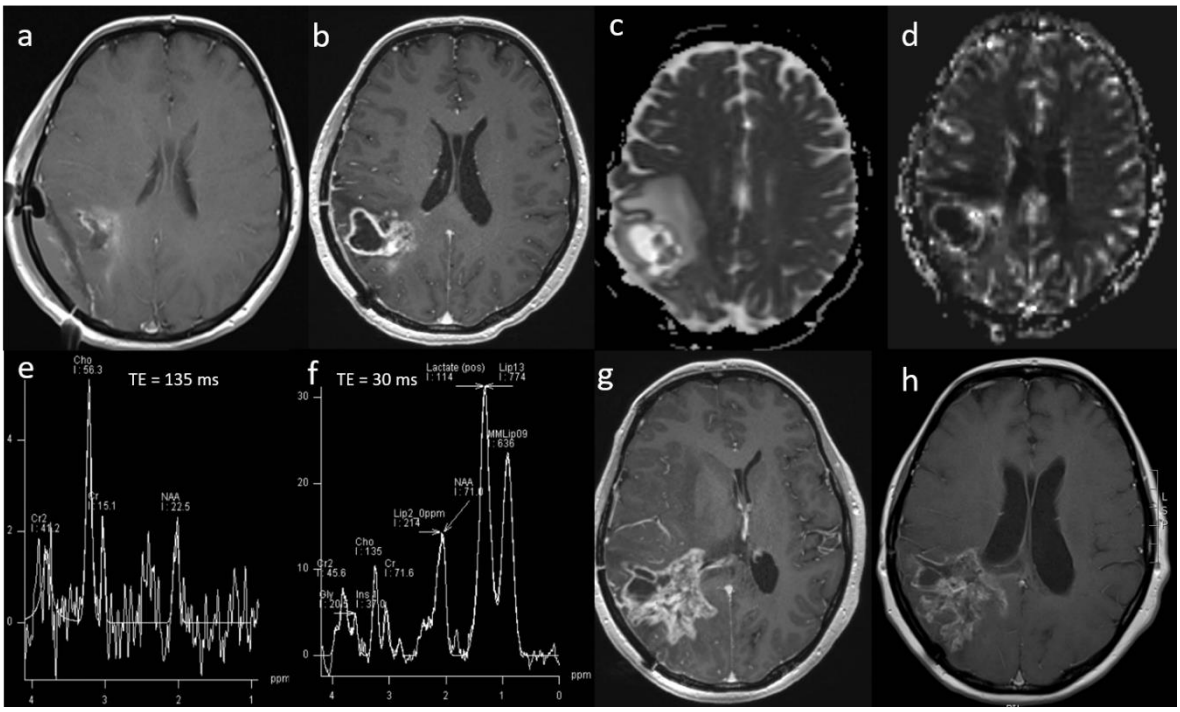

Figure 64. Case 9. (a) Post-operative CE-T1WI following resection of a right parietal glioblastoma. (b) CE-T1WI post-CRT demonstrated a significant increase in enhancement. Multiparametric MRI demonstrated: (c) free diffusion with a high ADC (1281 x $10^{-6}mm^2s^{-1}$), (d) high rCBV (8.1), (e,f) high Cho/Cr (2.3) and Cho/NAA ratios with the presence of lipid/lactate. Two of the three (PWI and MRS) parameters suggested a poor response. (g) 7-month imaging confirmed tPD according to RANO. (h) The 19-month scan showed overall stable appearances of the treated lesion and a new separate lesion.

6.3.4 Pseudoprogression

Two patients (cases 6 and 7) were correctly deemed to have psPD from multiparametric MRI. Both cases showed high ADC, low rCBV, Cho/Cr and Cho/NAA ratios consistent with psPD, despite one patient demonstrating a low MGMT promoter methylation status (4.25%), and the other patient demonstrating a high methylation status (**Figure 65**). Both of these patients survived more than three years following CRT.

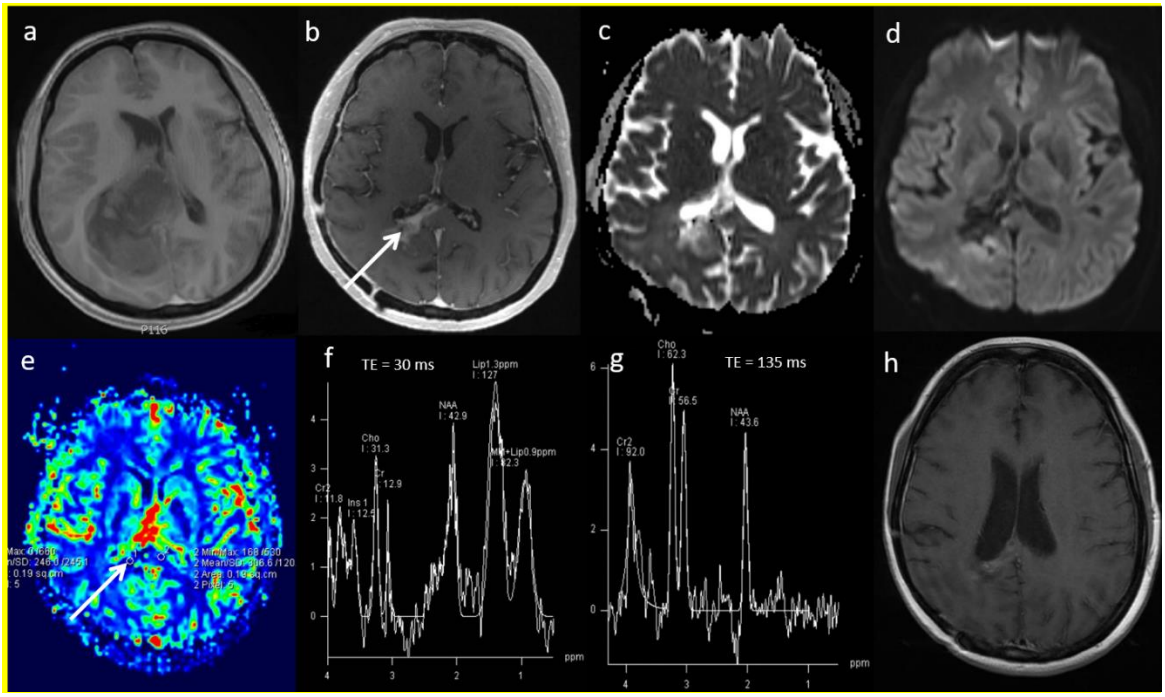

Figure 65. Case 6: Pseudoprogression. (a) Pre-operative CE-T1WI showed a right deep parietal region glioblastoma. (b) Conventional CE-T1WI four weeks after CRT treatment demonstrated a significant increase in the contrast-enhancing area (arrow). Multiparametric MRI at this time point demonstrated: (c, d) areas of high ADC (1186 x $10^{-6}mm^2s^{-1}$) , (e) a low rCBV ratio (1.4, arrow) on PWI, (f, g) a low Cho/Cr ratio (1.4), a low Cho/NAA ratio and presence of lipid and lactate on MRS. The combination of parameters suggested psPD. (h) Follow-up conventional CE-T1WI at six months showed a reduction in the amount of enhancing disease, which confirmed psPD.

The remaining patient (case 8) showed an initial increase in enhancing disease on the baseline MRI study at 1-month and on the multiparametric MRI at 2-months post-CRT there was a low ADC (951 x $10^{-6}mm^2s^{-1}$), high rCBV (4.2), and raised Cho/Cr (2.2) and Cho/NAA ratios (**Figure 66**). All three parameters of DWI, PWI and MRS were suggestive of a poor response and tPD on multiparametric MRI. The patient then showed SD on conventional imaging at 4-months and PR on conventional imaging at 7-months, surviving for 36 months, indicating psPD according to RANO.

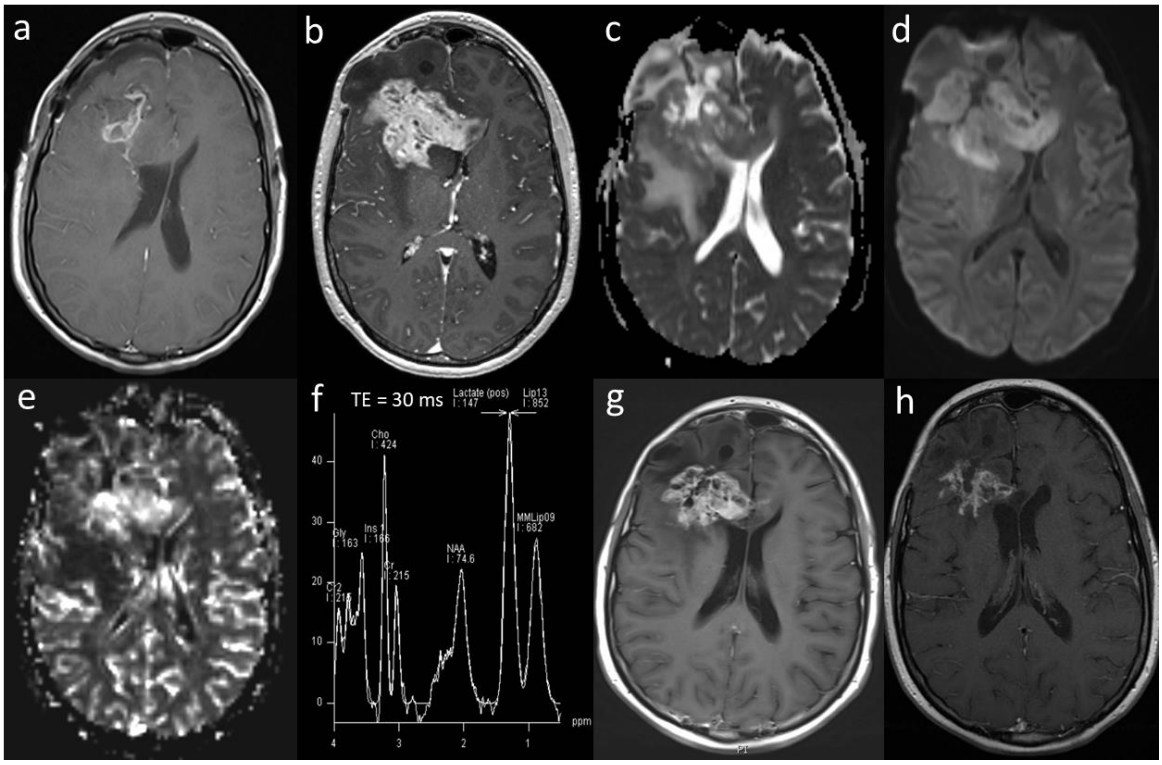

Figure 66. Case 8. (a) Post-operative CE-T1WI showed partial resection of a right frontal glioblastoma. (b) Conventional CE-T1WI four weeks after CRT treatment demonstrated a significant increase in contrast enhancement. Multiparametric MRI at this time point demonstrated: (c, d) areas of low ADC (951 x $10^{-6}mm^2s^{-1}$) , (e) a high rCBV ratio (4.2) on PWI, (f) a high Cho/Cr ratio (2.2), a high Cho/NAA ratio and presence of lipid and lactate on MRS. All parameters suggested tPD. (g) Follow-up conventional CE-T1WI at four months, and (g) seven months showed a reduction in the amount of enhancing disease, which confirmed psPD according to RANO criteria.

6.4 Discussion

The phenomenon of psPD, which mimics tPD on conventional MRI during glioblastoma treatment, is widely recognised as a significant problem. Whilst the underlying mechanisms of psPD are not fully understood, it has been suggested that radiotherapy in combination with TMZ chemotherapy causes a higher degree of tumour-cell and endothelial-cell damage [334].

This increased cell damage likely leads to secondary reactions, such as oedema, abnormal vessel permeability and necrosis in the tumour area [121], visualised as enhancement on conventional imaging, mimicking the appearances of disease progression. Clinically, it can be difficult to distinguish between the two and therefore treatment is usually continued, despite the possibility that it may be ineffective and short interval imaging is performed until disease progression is identified on consecutive imaging. Many patients will inevitably continue treatment that is not effective for weeks or months and can be delayed or excluded from receiving second-line CRT treatments, surgery, or entering clinical trials as a result of deterioration in clinical status from disease progression. Therefore, addressing the uncertainty around tPD and psPD on imaging is a key clinical issue which can directly impact upon patient outcomes.

Given the differing mechanisms of treatment effect, response and progression, techniques probing the physiological and metabolic characteristics would be expected to provide a more accurate assessment of changes following treatment than conventional MRI alone. ADC derived from DWI measures the mobility of water molecules in tissue and is inversely correlated with cellularity [347]. Mean ADC values in high-grade tumours such as glioblastoma are low, with a value typically of $700 \times 10^{-6} mm^2 s^{-1}$ [183], consequently, mean ADC values have shown to be significantly lower in tPD compared to psPD through numerous studies [129,341,342,344,348–354]. There is variability in the literature regarding cut-off values, generally ranging from 900-1300 x $10^{-6} mm^2 s^{-1}$, and a meta-analysis has shown the sensitivity and specificity of ADC to be 71% and 87% respectively across seven studies for treatment response assessment [122]. Assessments of the microvasculature using PWI to

estimate rCBV, a biomarker for neoangiogenesis, have also been shown to differentiate treatment response, with a significantly higher rCBV ratio in tPD compared to psPD [127,129,342–344,350,355–366]. There is again variation in optimal cut-off values for rCBV in each study, typically ranging from 1.7-2.4, and a meta-analysis has shown the sensitivity and specificity of DSC-PWI to be 87% and 86% respectively across five studies [122]. In addition, non-invasive measurements of metabolite levels using MRS have been shown to be useful for characterising brain lesions. Elevated Cho, a biomarker of cellular proliferation, relative to NAA, a marker of neuronal integrity as well as to Cr have shown to indicate tPD whilst high lipids (due to necrosis) combined with low Cho/Cr and Cho/NAA ratios are features of radiation damage or psPD [127,129,153,344,346,348,349,354,361,367–372]. A meta-analysis has shown the sensitivity and specificity of MRS to be 91% and 95% respectively across nine studies [292]. It has been suggested that the Cho/Cr and Cho/NAA ratios are the most useful measures for discerning glioblastoma treatment response [127,346], and a Cho/Cr threshold ratio >1.79 was suggestive of tumour recurrence, but spectral patterns were less definitive when there was a mixed response [345]. In the current study, the Cho/Cr ratios from both the intermediate (TE=135ms) and short (TE=30ms) echo times provided similar trends to classify treatment response, and an additional parameter for greater confidence.

Although numerous studies have shown to be useful for this clinical issue, the multiparametric approach adds relevant and important information alongside conventional MRI findings in distinguishing tPD from psPD in post-treatment glioblastoma. It is a better assessment of the structural, physiological and metabolic environment of the tumour, compared to the single parameter approach. Combining techniques has shown benefit and

could significantly improve diagnostic accuracy. Combining ADC and MRS has shown a sensitivity and specificity of 91.5% and 100% respectively, and a reported accuracy of 97.2% [363]. Combining PWI and MRS has shown to improve diagnostic accuracy from 82.5% for perfusion alone, to 90% with both parameters [341]. Combining ADC, rCBV and MRS has shown to produce a diagnostic accuracy of 93.3%, compared to the single parameter approach which yielded accuracies between 84.6% to 86.7% [127]. Another study has shown that the accuracy of correctly classifying cases was between 62.1% to 79.3% for single parameter techniques, however when the three parameter of DWI, PWI and MRS were combined, the accuracy of correct classification between recurrent tumour and radiation injury improved to 96.6% [128].

In this study, combining a high rCBV (>2.1), high Cho/Cr ratio (≥1.8), high Cho/NAA ratio (≥1.9) and low ADC (≤1000 x $10^{-6}mm^2s^{-1}$) correctly identified tPD in all six cases of tPD according to RANO criteria. In one of these patients (case 9), there were multiparametric features of tPD at the early time point. Following a second multiparametric and conventional MRI assessment at the 4-month follow-up time point which again showed PD, TMZ was changed to second-line treatment and there was further PD at 7-months. At 19-months and 32-months there was PD. In this case, according to RANO, PD at multiple time points until after the 6-month time point would be consistent with tPD, which was determined at the earliest time point by multiparametric MRI. In addition, this patient's MGMT promoter methylation was low, indicating that true progression was more likely [336]. This case suggests that there may have been foci of tumour on initial imaging, detected by the areas of highest rCBV and Cho/Cr ratio. Despite the multiparametric findings being consistent with RANO criteria of tPD in the

initial 7-month period, there could have been a good response to treatment after the initial 7-month period leading to stability of disease and a prolonged OS until further progression at 19 months.

Combining a low rCBV (≤2.1), low Cho/Cr (<1.8), low Cho/NAA (<1.9) and high ADC (>1000 x $10^{-6}mm^2s^{-1}$) correctly identified psPD in two of the three cases according to RANO. One of these patients had a low level of MGMT promoter methylation, which is more often associated with tPD [336]. In the final patient (case 8), multiparametric MRI features at eight weeks post-CRT suggested a picture of tumour recurrence in residual disease from surgery. The patient subsequently went on to show psPD according to conventional imaging, with an overall survival of 36 months. MGMT promoter methylation was 18%, suggesting both tPD and psPD were clinical possibilities. In this case, there may have been a mixed pattern of tumour recurrence and treatment-related changes, and as the methods used identify the area of lowest ADC, highest rCBV and highest Cho/Cr ratio to represent tumour activity, it is likely that the focal residual tumour is what was detected within predominant treatment-related changes. This bias in the methodology of the current study for using multiparametric MRI to identify the area of tumour activity, which is used to inform clinical management, could inevitably lead to false positive reports of tPD in patients with and mixed response or in patients with residual tumour and psPD. Therefore, careful comparison with the post-operative MRI study to assess the degree of resection and serial multiparametric MRI following treatment to assess for change in parameters to reflect the shift in the disease process would be more useful and help overcome this problem, rather than multiparametric imaging at one time point. Both case 8 and 9 highlight the issue of mixed response patterns

and the limitations of utilising current RANO criteria as the reference standard for this clinical issue.

The current RANO guidelines [138], as well as many studies support the consideration of multiparametric MRI to address the unsolved problem of pseudoprogression in glioblastoma [119–121,127,333,363,372–376]. This small study and evidence from the literature suggests that combining advanced MRI techniques are promising for increasing the accuracy of treatment response assessment in glioblastoma.

6.5 Future direction

Over the past decade, there has been an increasing validation of quantitative advanced imaging biomarkers for treatment response assessment in glioblastoma. Individual studies and institutions show good accuracies and clinical benefit in utilising these individual advanced techniques, but there remains a lack of standardisation across institutions due to differing acquisition parameters and techniques and differing levels of expertise and training [377]. The majority of studies so far have investigated individual parameters independently, have had limited subject numbers, and have been retrospectively performed at single centres. Systematic prospective evaluation using standardised analysis across multiple centres is required to validate multiparametric MRI biomarkers in routine clinical practice, to identify optimal combination of parameters and optimum thresholds. This will inevitably take time, but until this can be established, it is clear that combining the data from multiple advanced parameters assessing metabolic, functional, haemodynamic and cellular information increases accuracy and can significantly improve assessment of treatment response

compared to single parameters and conventional imaging [378], giving greater confidence to neuroradiologists and clinicians. This will be even more relevant in the era of emerging and targeted therapies, in which treatment response assessment may be even more complex and advanced MRI parameters such as DWI, PWI and MRS have already shown the potential to be useful [379–381]. Additional imaging parameters and techniques that have shown to be useful in treatment response assessment but require larger studies and more evidence include DTI, delayed contrast extravasation [382], ferumoxytol iron oxide nanoparticle MRI contrast [364,383], APT-weighted MRI [384], and PET has also shown to be a useful modality for this clinical issue [385]. Better methodologies of assessment are also required to address the issues of a mixed response or residual disease, and volumetric analysis of the entire lesion using advanced parameters or histograms may help with this issue. Machine learning techniques have great potential, for example in conjunction with radiomic texture features extracted from conventional or advanced imaging parameter maps, or unsupervised deep learning-based techniques for predicting treatment response [307,386,387], and should be explored further, particularly in combination with multiparametric MRI, as will be discussed further in Chapter 7.

6.6 Conclusion

Advanced MRI parameters are powerful tools in the assessment of treatment response in patients with glioblastoma, particularly as treatments evolve and assessment becomes more complex. A multiparametric approach using DWI, PWI and MRS is feasible in the clinical setting and provides greater accuracy compared with techniques used in isolation. Further prospective evaluation and large multi-centre trials are required for validation, with the aim of producing accurate quantitative multiparametric MRI biomarkers.

7. MACHINE LEARNING-BASED RADIOMIC EVALUATION OF EARLY TREATMENT RESPONSE PREDICTION

This chapter is adapted from [130], previously published by *Clinical Radiology*.

7.1 Introduction

Treatment response assessment is an important clinical issue, which is complicated by psPD mimicking the appearances of tPD on CE-T1WI. Conventional MRI has a low diagnostic accuracy for distinguishing between the two entities at early time points and this can lead to delays in patient management. Radiomics allows the conversion of standard medical imaging into higher-dimensional data through the extraction of mathematical-based features [279,280], and can be combined with machine learning to create models for outcome prediction.

The aim of this study was to investigate the accuracy of radiomics and machine learning for distinguishing between early tPD and psPD in post-treatment glioblastoma, using routinely acquired MRI sequences in combination with clinical information and MGMT promoter methylation status.

7.2 Methods

7.2.1 Study design

The study involved retrospective analysis of consecutive patients who had surgery for newly diagnosed glioblastoma at the Queen Elizabeth Hospital Birmingham over a 3.5-year period between June 2014 and December 2017 as part of routine clinical care. Approvals for this study were obtained from the University Hospitals Birmingham Research Governance Office.

7.2.2 Inclusion and exclusion criteria

Inclusion criteria were: (a) pathology-confirmed glioblastoma according to the WHO Criteria; (b) surgery followed by standard CRT treatment [116]; and (c) presence of and measurable increase in contrast-enhancing disease on the post-CRT baseline MRI study at 4-6 weeks, compared to the immediate post-operative MRI study. Exclusion criteria were: (a) absence of baseline MRI study at University Hospitals Birmingham (performed at another centre); (b) incomplete post-CRT baseline MRI study, which did not include CE-T1WI, T2WI and ADC sequences or presence of significant imaging artefact; (c) mixed response or difficulty categorising outcome; (d) patient lost to follow-up within six months of CRT treatment; and (e) baseline MRI performed at field strength other than 1.5 Tesla. In total, 76 patients (mean age 55 years, range 18-76 years, 39% female) were included in the study (**Figure 67**). Baseline demographics and clinical characteristics were collected, which included patient sex, age at diagnosis, extent of surgical resection of the tumour (biopsy, debulking, near total resection, complete resection) based on post-operative MRI, Eastern Cooperative Oncology Group

(ECOG) performance status, radiotherapy dose, number of radiotherapy fractions and MGMT promoter methylation status, from the tumour tissue sample obtained at surgery.

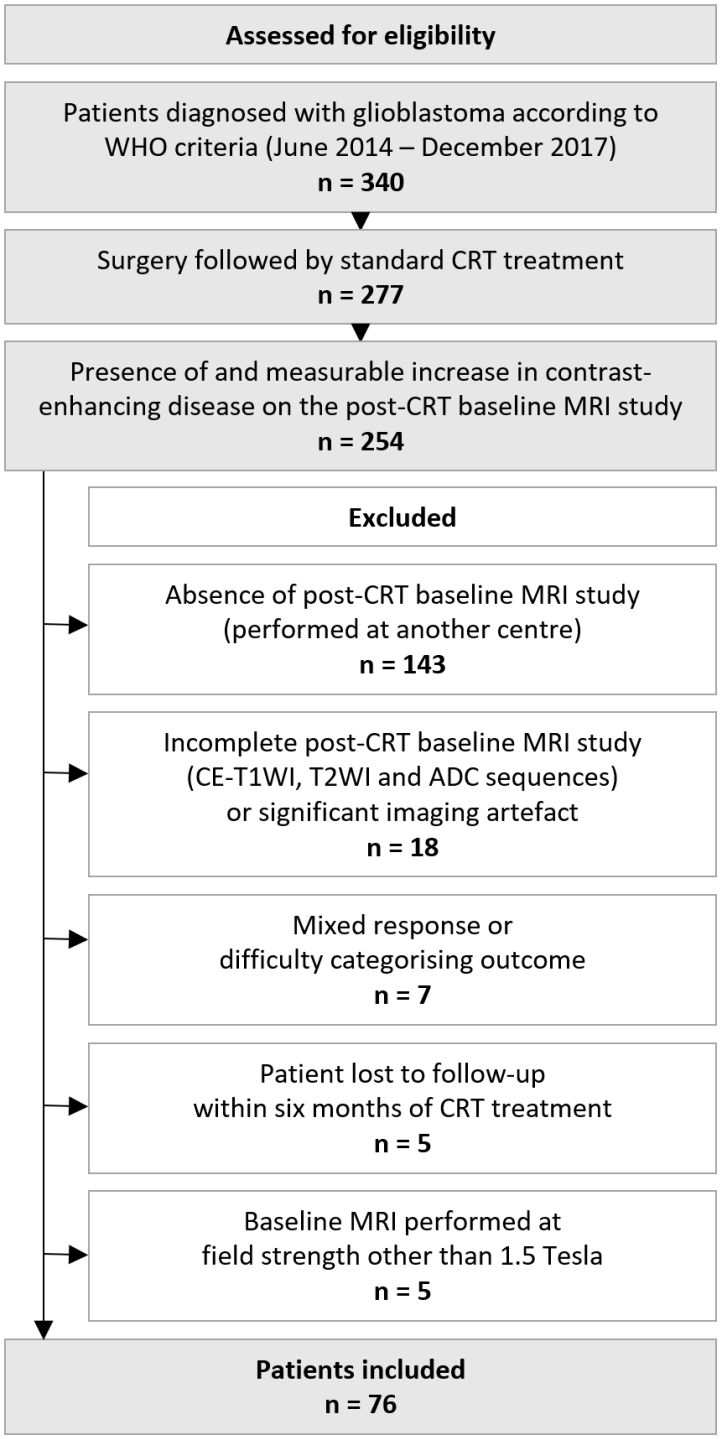

Figure 67. Flowchart of patient inclusion and exclusion criteria.

7.2.3 Reference standard

Clinical radiology reports written by consultant neuroradiologists were reviewed to obtain the final diagnosis of tPD or psPD. Studies were labelled as tPD if there was radiological or clinical progression according to RANO criteria, or death within six months. A label of psPD was given if there was no further radiological or clinical progression according to RANO criteria, within the six months following CRT. Imaging was also reviewed and where there was discrepancy of outcome, consensus was obtained by two consultant neuroradiologists. Of the 76 patients, 46 demonstrated tPD and 30 demonstrated psPD. There were seven additional cases which showed a mixed response within the six-month period following CRT and a clear outcome was not established, therefore these patients were excluded from the study.

7.2.4 MRI acquisition

MRI was performed on 1.5 Tesla scanners with 32-channel phased-array head coils. Various scanner manufacturers and parameters were used for image acquisition, reflecting the heterogeneity of standard-of-care imaging in clinical practice. The imaging protocol included axial T2WI, axial DWI with *b*-values 0 and 1000 s/mm^2, and axial spin-echo CE-T1WI of the whole-brain. Gadolinium contrast agent (Dotarem; Guerbet, Villepinte, France) was administered intravenously 4-6 minutes prior to acquisition of the CE-T1WI as a hand-injected bolus of 10-15 ml (10 ml if weight <70 kg, 15 ml if weight ≥70 kg). Acquisition parameters for T2WI were: TR = 2800-3050 ms and TE = 95-111 ms; and for CE-T1WI: TR = 540-640 ms and TE = 10-17 ms. Maximum in-plane voxel sizes were 0.7 x 0.7 mm^2 for T2WI, 1.0 x 1.0 mm^2 for CE-T1WI and 1.56 x 1.56 mm^2 for DWI. Maximum slice thickness for all acquisitions were 5

mm with a maximum interslice gap of 2.5 mm. An ADC map was calculated for each patient with a *b*-value of 1000 s/mm^2.

7.2.5 Image pre-processing pipeline

Image resampling and intensity normalisation was performed using PyRadiomics (version 3.0) pipeline modules [283]. Image voxel size was normalised by performing image resampling according to the lowest acquisition resolution to avoiding upsampling. Therefore, re-sectioned images contained the maximum voxel sizes for each sequence across all patients. Image intensity normalisation was applied to CE-T1WI and T2WI based on the entire image and centred at the mean with standard deviation. Hyperintensity artifact was corrected for by removing outlier voxel intensities greater than the 99.9th percentile for each image. CE-T1WI, ADC and T2WI were imported into and co-registered in ITK-SNAP (version 3.6.0), using the automatic rigid transformation model and mutual information similarity metric [325], to aid segmentation of masks.

7.2.6 Segmentation

Three-dimensional masks were created for enhancing disease and perilesional oedema, based on CE-T1WI and T2WI respectively. A semi-automatic method was used for each set of imaging studies using the ITK-SNAP machine learning-based tissue classification pre-segmentation technique [325]. Mask registration was verified, and accuracy was visually inspected by a neuroradiologist with over 20 years of experience, blind to clinical data and outcome, with manual adjustments made to masks on each slice of the image if required.

7.2.7 Radiomic feature extraction

Radiomic features were extracted using the defined masks on the baseline MRI using PyRadiomics (version 3.0) [283]. A total of 307 features were extracted for each patient. There were 14 shape-based features extracted from each mask. Remaining features were extracted from three sets of mask-imaging pairs: the enhancing disease mask on CE-T1WI and ADC map, as well as from the perilesional oedema mask on T2WI. From each pair, there were 18 first-order features and 75 second-order features. Second-order features consisted of 24 GLCM features 14 GLDM features, 16 GLRLM features, 16 GLSZM features and five NGTDM features. A full list of the feature groups, feature families and individual features are shown in Figure 68.

Clinical and Molecular	Shape-based features		First order features	
Age ECOG performance status Extent of surgical resection Radiotherapy dose Radiotherapy fractions Sex MGMT promoter methylation status	Elongation Flatness Least axis length Major axis length Maximum 2D diameter column Maximum 2D diameter row Maximum 2D diameter slice	Maximum 3D diameter Mesh volume Minor axis length Sphericity Surface area Surface area to volume ratio Voxel volume	10^{th} percentile 90^{th} percentile Energy Entropy Interquartile range Kurtosis Maximum Mean absolute deviation Mean	Median Minimum Range Robust mean absolute deviation Root mean squared Skewness Total energy Uniformity Variance

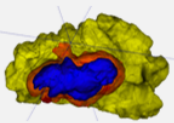

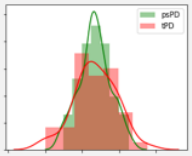

Second order features				
Gray-level co-occurrence matrix (GLCM)	**Gray-level dependence matrix (GLDM)**	**Gray-level run-length matrix (GLRLM)**	**Gray-level size-zone matrix (GLSZM)**	**Neighbourhood gray-tone difference matrix (NGTDM)**
Autocorrelation Cluster prominence Cluster shade Cluster tendency Contrast Correlation Difference average Difference entropy Difference variance Inverse difference Inverse difference moment Inverse difference moment normalized Inverse difference normalized Informational measure of correlation 1 Informational measure of correlation 2 Inverse variance Joint average Joint energy Joint entropy Maximal correlation coefficient Maximum probability Sum average Sum entropy Sum squares	Dependence entropy Dependence non-uniformity Dependence non-uniformity normalized Dependence variance Gray level non-uniformity Gray level variance High gray level emphasis Large dependence emphasis Large dependence high gray level emphasis Large dependence low gray level emphasis Low gray level emphasis Small dependence emphasis Small dependence high gray level emphasis Small dependence low gray level emphasis	Gray level non-uniformity Gray level non-uniformity normalized Gray level variance High gray level run emphasis Long run emphasis Long run high gray level emphasis Long run low gray level emphasis Low gray level run emphasis Run entropy Run length non-uniformity Run length non-uniformity normalized Run percentage Run variance Short run emphasis Short run high gray level emphasis Short run low gray level emphasis	Gray level non-uniformity Gray level non-uniformity normalized Gray level variance High gray level zone emphasis Large area emphasis Large area high gray level emphasis Large area low gray level emphasis Low gray level zone emphasis Size zone non-uniformity Size zone non-uniformity normalized Small area emphasis Small area high gray level emphasis Small area low gray level emphasis Zone entropy Zone percentage Zone variance	Busyness Coarseness Complexity Contrast Strength

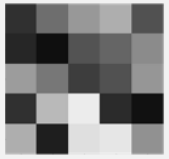

Figure 68. List of the clinical, molecular and radiomic features used.

7.2.8 Models

Six feature set models were constructed which subsequently underwent feature selection and classification: (i) Clinical and molecular features including the six clinical features of patient sex, age at diagnosis, extent of surgical resection of the tumour, ECOG performance status, radiotherapy dose, and number of radiotherapy fractions, as well as MGMT promoter methylation status; (ii) 14 shape-based radiomic features from the enhancing disease mask; (iii) 14 shape-based radiomic features from the perilesional oedema mask; (iv) 93 first- and second-order radiomic features extracted from CE-T1WI using the enhancing disease mask; (v) 93 first- and second-order radiomic features extracted from the ADC map using the enhancing disease mask; and (vi) 93 first- and second-order radiomic features extracted from T2WI using the perilesional oedema mask.

7.2.9 Feature selection

The entire dataset was split into five folds using stratified random sampling, to carry out variable selection within nested cross-validation [284], conceptually demonstrated in **Figure 49**. Therefore, there were five total datasets, each comprising of 80% of the data for training and the remaining 20% of the data for validation. The most predictive features were identified in each model using a multi-step pipeline. Firstly, within each training set clusters of highly correlated features were identified using the Pearson correlation coefficient matrix (Python pandas environment, version 1.0.1 [285]). The most representative feature was kept from the highly correlated clusters ($R^2 > 0.8$) and remaining features removed. Cross-validated (k=10) recursive feature elimination with a random forest classifier was then used to

further reduce and select the most predictive features (Python scikit-learn environment, version 0.22.1 [286]). A 10-fold bootstrapped cross-validation approach was used considering Gini impurity measures.

7.2.10 Statistical analysis and classification

T-test and chi-squared test were used to calculate differences between clinical features and baseline demographics of the tPD and psPD groups, using RStudio software, version 1.2.5033 (RStudio: Integrated Development for R. RStudio, Inc., Boston, MA, USA). Statistical significance was determined at a *P*-value of less than 0.05. Classification using a Naïve Bayes classifier was performed in Orange (version 3.24) [287]. Test data across each of the five folds were used to evaluate the performance of each model, with overall model performance determined by the mean across the folds. A combined clinico-radiomic signature was generated based on the top selected features present in all five folds of each model. The AUC, sensitivity, specificity, PPV, NPV and accuracy of the model was calculated. A summary of the workflow is shown in Figure 69.

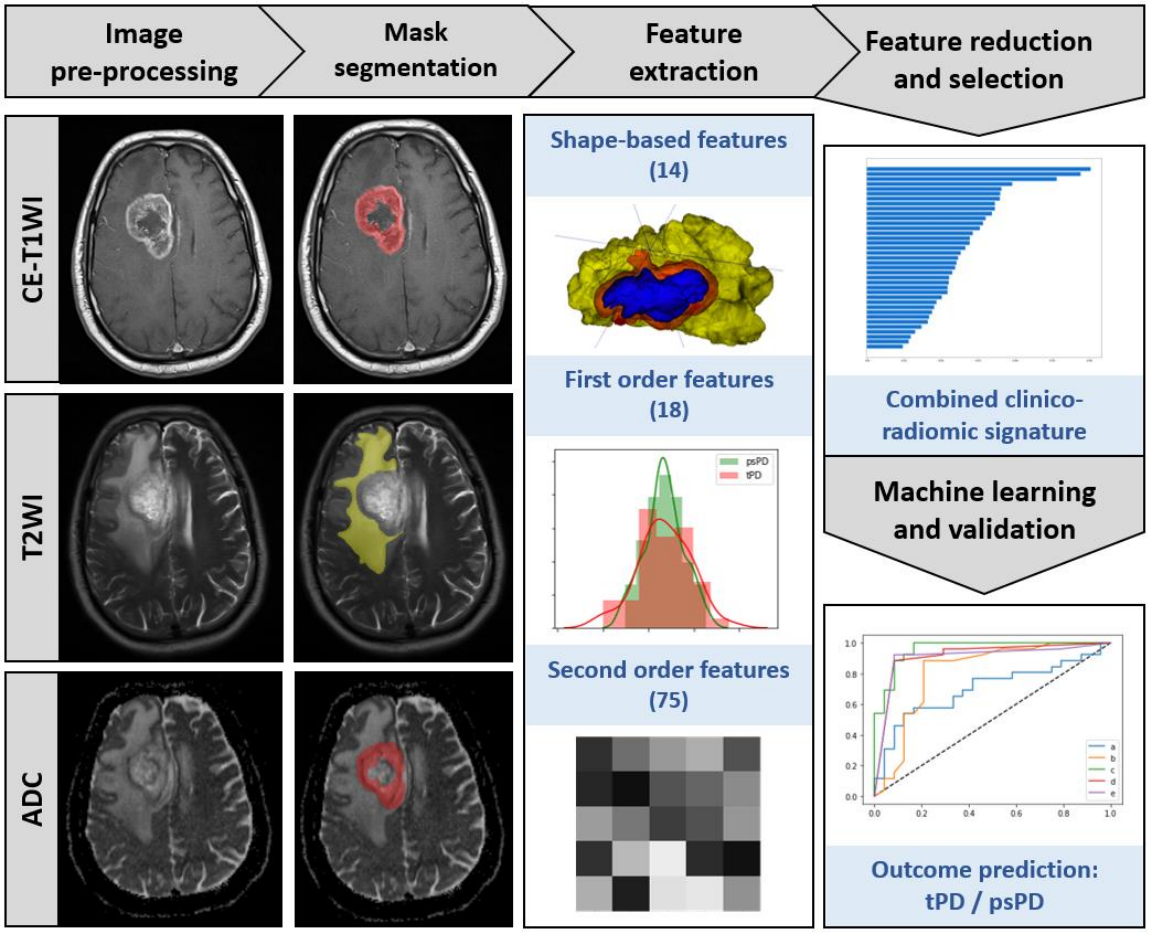

Figure 69. Conceptual overview of the radiomics-based study workflow.

7.3 Results

7.3.1 Patient demographics

Patient demographics are summarised in Table 13. Of the 76 patients included in the study, within six months of CRT, clinico-radiological follow-up in 46 (60.5%) demonstrated tPD, and 30 (39.5%) demonstrated psPD. Patients in the psPD group had a significantly higher overall survival (21.8 vs. 11.8 months), significantly higher MGMT promotor methylation level (22.1% vs. 10.1%) and were significantly younger (50.8 vs. 57.2 years). There were no significant

differences observed between the two groups with regard to sex, surgical resection, baseline ECOG performance status, radiotherapy dose or fractions.

	True progression (n=46)	Pseudoprogression (n=30)	
Age, years (SD)	57.2 (10.2)	50.8 (12.9)	*p*=0.03*
Sex, female, n	18 (39%)	12 (40%)	*p*=0.87
Surgical resection, n			*p*=0.34
Biopsy	2 (4%)	0 (0%)	
Debulking	24 (52%)	21 (70%)	
Near total	9 (20%)	5 (17%)	
Complete	11 (24%)	4 (13%)	
ECOG performance status, n			*p*=0.98
0	25 (54%)	16 (53%)	
1	17 (37%)	11 (37%)	
2	4 (9%)	3 (10%)	
Radiotherapy dose, Gray (SD)	58 (5.7)	57 (6.6)	*p*=0.60
Radiotherapy fractions, n (SD)	29 (4.2)	29 (4.1)	*p*=0.72
MGMT methylation, % (SD)	10.1 (14.0)	22.1 (17.4)	*p*<0.01*
Overall survival, months (SD)	11.8 (5.8)	21.8 (7.3)	*p*<0.01*

Table 13. Patient demographics and clinical characteristics.

7.3.2 Neuroradiologist assessment

Clinical neuroradiologist prediction of treatment response assessment was based on standard-of-care reports from the post-CRT baseline MRI study at 4-6 weeks and classified as

a dichotomous outcome (tPD or psPD), with an equivocal conclusion categorised as misclassification. At this early time point the accuracy of neuroradiologists to distinguish tPD from psPD on standard-of-care imaging was 32.9%, with a sensitivity of 52.2% (95% CI 37.0-67.1), specificity of 3.3% (0.1-17.2), positive predictive value of 45.3% (38.8-52.9) and negative predictive value of 4.3% (0.6-23.9).

7.3.3 Feature set models

The top features in each fold of each of the six models were selected by Pearson correlation coefficient redundant feature removal, recursive feature elimination and bootstrapped cross-validation. Selected features for each fold and the top common features across all folds of the models are shown in the tables below. The average AUC was calculated for each model using results from each fold. The AUC for the clinical and molecular model was 0.66 (**Table 14**), imaging shape-based radiomics (enhancing disease) was 0.62 (**Table 15**), imaging shape-based radiomics (perilesional oedema) was 0.46 (**Table 16**), imaging CE-T1WI radiomics (enhancing disease) was 0.56 (**Table 17**), imaging ADC radiomics (enhancing disease) was 0.69 (**Table 18**), and imaging T2WI radiomics (perilesional oedema) was 0.58 (**Table 19**).

Fold	1	2	3	4	5	Common features and average AUC across all folds
Top features	MGMT Age	MGMT Age Resection ECOG Sex	MGMT Age	MGMT Age Resection	MGMT Age	MGMT Age
AUC	0.77	0.68	0.61	0.50	0.72	0.66

Table 14. Performance of top-ranking clinical and molecular feature sets across each fold and the common feature set.

Fold	1	2	3	4	5	Common features and average AUC across all folds
Top features	Elongation SAVR Sphericity	Elongation SAVR Sphericity Flatness	Sphericity Elongation	SAVR Elongation Flatness Sphericity	Elongation M2DDC Sphericity Flatness	Elongation Sphericity
AUC	0.73	0.42	0.64	0.83	0.50	0.62
M2DDC = maximum 2D diameter column, *SAVR* = surface area to volume ratio.						

Table 15. Performance of top-ranking imaging related feature sets across each fold and the common feature set for shape-based radiomics using the enhancing disease mask.

Fold	1	2	3	4	5	Common features and average AUC across all folds
Top features	Flatness Major axis length	Flatness	Flatness SAVR Elongation M2DDC Least axis length	Flatness SAVR Sphericity M2DDC Elongation Least axis length	Major axis length SAVR Sphericity Elongation M2DDC	None
AUC	0.55	0.31	0.50	0.50	0.46	0.46
M2DDC = maximum 2D diameter column, *SAVR* = surface area to volume ratio.						

Table 16. Performance of top-ranking imaging related feature sets across each fold and the common feature set for shape-based radiomics using the perilesional oedema mask.

Fold	1	2	3	4	5	Common features and average AUC across all folds
Top features	Maximum (FO) DE (GLDM) DN (GLDM) Kurtosis (FO) 90th percentile (FO) Energy (FO) LDLGLE (GLDM)	DV (GLDM) RE (GLRLM) DE (GLDM) LDLGLE (GLDM) Skewness (FO) SDHGLE (GLDM)	DV (GLDM) Energy (FO) Minimum (FO) RE (GLRLM) LALGLE (GLSZM) SDHGLE (GLDM) Kurtosis (FO)	SAE (GLSZM) Skewness (FO) Energy (FO) DV (GLDM) SDLGLE (GLDM) 90th percentile (FO) SDE (GLDM)	DV (GLDM)	None
AUC	0.65	0.50	0.57	0.65	0.41	0.56
DE = dependence entropy, *DV* = dependence variance, *FO* = first-order, *GLDM* = gray-level dependence matrix, *GLRLM* = gray-level run-length matrix, *GLSZM* = gray-level size-zone matrix, *LALGLE* = large area low gray level emphasis, *LDLGLE* = large dependence low gray level emphasis, *RE* = run entropy, *SAE* = small area emphasis, *SDE* = small dependence emphasis, *SDHGLE* = small dependence high gray level emphasis, *SDLGLE* = small dependence low gray level emphasis.						

Table 17. Performance of top-ranking imaging-based feature sets across each fold and the common feature set for CE-T1WI radiomics using the enhancing disease mask.

Fold	1	2	3	4	5	Common features and average AUC across all folds
Top features	IMC1 (GLCM) LDLGLE (GLDM) Contrast (NGTDM) Kurtosis (FO) Busyness (NGTDM) Correlation (GLCM) Energy (FO)	Correlation (GLCM) Kurtosis (FO) IDM (GLCM) CS (GLCM) Energy (FO) 10th percentile (FO) Contrast (NGTDM)	Correlation (GLCM) Contrast (NGTDM) Kurtosis (FO) Busyness (NGTDM) IMC1 (GLCM) IMC2 (GLCM) IDMN (GLCM)	Correlation (GLCM) Kurtosis (FO) IDMN (GLCM) 10th percentile (FO) Energy (FO) Contrast (NGTDM) Busyness (NGTDM)	Kurtosis (FO) 10th percentile (FO) LDLGLE (GLDM) Correlation (GLCM) Energy (FO) IDMN (GLCM) Contrast (NGTDM)	Kurtosis (FO) Correlation (GLCM) Contrast (NGTDM)
AUC	0.58	0.82	0.64	0.79	0.61	0.69

CS = cluster shade, *FO* = first-order, *GLCM* = gray-level co-occurrence matrix, *GLDM* = gray-level dependence matrix, *IDM* = inverse difference moment, *IDMN* = inverse difference moment normalized, *IMC1* = informational measure of correlation 1, *IMC2* = informational measure of correlation 2, *LDLGLE* = large dependence low gray level emphasis, *NGTDM* = neighbourhood gray-tone difference matrix.

Table 18. Performance of top-ranking imaging-based feature sets across each fold and the common feature set for ADC radiomics using the enhancing disease mask.

Fold	1	2	3	4	5	Common features and average AUC across all folds
Top features	LDLGLE (GLDM) Skewness (FO) Maximum (FO) 10th percentile (FO) 90th percentile (FO) Minimum (FO) Energy (FO) DE (GLDM)	Maximum (FO) LDLGLE (GLDM) DE (GLDM) Minimum (FO) IR (FO) 10th percentile (FO)	Minimum (FO) DE (GLDM) 90th percentile (FO) LDLGLE (GLDM) Maximum (FO) 10th percentile (FO) SAE (GLSZM) IR (FO)	Skewness (FO) LDLGLE (GLDM) DE (GLDM) DV (GLDM) Minimum (FO)	10th percentile (FO) Maximum (FO) DE (GLDM)	DE (GLDM)
AUC	0.58	0.72	0.48	0.61	0.51	0.58

DE = dependence entropy, *DN* = dependence non-uniformity, *DV* = dependence variance, *FO* = first-order, *GLDM* = gray-level dependence matrix, *IR* = interquartile range, *LDLGLE* = large dependence low gray level emphasis, *SAE* = small area emphasis.

Table 19. Performance of top-ranking imaging-based feature sets across each fold and the common feature set for T2WI radiomics using the perilesional oedema mask.

7.3.4 Combined clinico-radiomic signature

For the combined clinico-radiomic signature, top common features across all folds of each model were combined (**Table 20**). Two features were obtained from the clinical and molecular model (age and MGMT promoter methylation status) and six features were obtained from the imaging radiomics models. Of the imaging features, two were shape-based from the enhancing disease mask (*elongation* and *sphericity*), three were ADC radiomic features from the enhancing disease mask (first-order: *kurtosis*; second-order: *correlation* (GLCM) and *contrast* (NGTDM)), and there was one T2WI radiomic feature from the perilesional oedema mask (*dependence entropy* (GLDM)). Definitions of the individual radiomic features within the combined clinico-radiomic signature are shown in **Table 21**. The performance of the model

with selected clinical and molecular features only (age and MGMT promoter methylation status) demonstrated an AUC of 0.66 (0.62-0.70) and the selected imaging-based radiomic feature model (six features) demonstrated an AUC of 0.63 (0.58-0.67). For the clinical and molecular model, accuracy was 55.3% (44.3-66.3), sensitivity 71.7% (57.0-84.0), specificity 30.0% (14.7-49.4), PPV 61.1% (53.9-67.9) and NPV 40.9% (25.3-58.6). Combining the clinical, molecular and radiomic features improved model performance, with the combined model demonstrating an AUC of 0.80 (0.74-0.86), accuracy of 73.7% (66.5-80.9), sensitivity of 78.2% (70.7-85.7), specificity of 66.7% (50.7-82.7), PPV of 78.1% (70.9-85.3) and NPV of 67.4% (60.6-74.3). Results of each fold from the final model are shown in Table 22, and the ROC curve for the combined clinico-radiomic model is shown in Figure 70.

Feature Name	Feature Type	Feature Category	Imaging Parameter	Image Mask
MGMT methylation	Molecular	-	-	-
Age	Clinical	-	-	-
Elongation	Imaging	Shape-based	CE-T1WI	Enhancing disease
Sphericity	Imaging	Shape-based	CE-T1WI	Enhancing disease
Kurtosis	Imaging	First-order	ADC	Enhancing disease
Correlation	Imaging	Second-order (GLCM)	ADC	Enhancing disease
Contrast	Imaging	Second-order (NGTDM)	ADC	Enhancing disease
Dependence entropy	Imaging	Second-order (GLDM)	T2WI	Perilesional oedema

Table 20. List of top features in the combined clinico-radiomic signature to differentiate between early true progression and pseudoprogression in patients with glioblastoma.

Feature Name	Feature Category	Feature Definition
Elongation	Shape-based	$\sqrt{\frac{\lambda_{minor}}{\lambda_{major}}}$
Sphericity	Shape-based	$\frac{2\pi R}{P} = \frac{2\sqrt{\pi A}}{P}$
Kurtosis	First-order	$\frac{\mu_4}{\sigma_4} = \frac{\frac{1}{N_P}\sum_{i=1}^{N_p}(X(i)-\bar{X})^4}{\left(\frac{1}{N_p}\sum_{i=1}^{N_p}(X(i)-\bar{X})^2\right)^2}$
Correlation	Second-order (GLCM)	$\frac{\sum_{i=1}^{N_g}\sum_{j=1}^{N_g}p(i,j)ij - \mu_x\mu_y}{\sigma_x(i)\sigma_y(j)}$
Contrast	Second-order (NGTDM)	$\left(\frac{1}{N_{g,p}(N_{g,p}-1)}\sum_{i=1}^{N_g}\sum_{j=1}^{N_g}p_i p_j (i-j)^2\right)\left(\frac{1}{N_{v,p}}\sum_{i=1}^{N_g}s_i\right)$
Dependence entropy	Second-order (GLDM)	$\sum_{i=1}^{N_g}\sum_{j=1}^{N_d}p(i,j)\,log_2(p(i,j)+\epsilon)$

A = surface area of the mesh in mm^2, *GLCM* = gray-level co-occurrence matrix, *GLDM* = gray-level dependence matrix, N_d = the number of discreet dependency sizes in the image, N_g = the number of discreet intensity levels in the image, $N_{g,p}$ = the number of gray levels where $p_i \neq 0$, *NGTDM* = neighbourhood gray-tone difference matrix, $N_{v,p}$ = the total number of voxels in $X_{g,l}$, *P* = perimeter of the mesh in mm, p_i = the gray level probability, *p(i,j)* = the normalized dependence matrix, *R* = radius of circle with the same surface as the region of interest, s_i = the sum of absolute differences for gray level *I*, *X* = a set of N_p voxels included in the region of interest, ϵ = an arbitrarily small positive number, μ_4 = the 4th central moment, μ_x = the mean gray level intensity of p_x, μ_y = the mean gray level intensity of p_y, σ_x = the standard deviation of p_x, σ_y = the standard deviation of p_y, λ_{major} = length of largest principle component axis, λ_{minor} = length of second largest principle component axis.

Table 21. Definitions for the radiomic features from the final clinico-radiomic signature [283].

Fold	AUC	Sensitivity, % (CI)	Specificity, % (CI)	PPV, % (CI)	NPV, % (CI)	Accuracy, % (CI)
1	0.77	80.0 (44.3-97.5)	66.7 (22.3-95.7)	80.0 (55.3-92.8)	66.7 (33.9-88.7)	75.0 (47.6-92.7)
2	0.82	77.8 (40.0-97.2)	66.7 (22.3-95.7)	77.8 (51.7-92.0)	66.7 (34.2-88.5)	73.3 (44.9-92.2)
3	0.83	88.9 (51.8-99.7)	66.7 (22.3-95.7)	80.0 (55.8-92.7)	80.0 (36.7-96.5)	80.0 (51.9-95.7)
4	0.76	66.7 (30.0-92.5)	66.7 (22.3-95.7)	75.0 (46.9-91.1)	57.1 (31.1-79.8)	66.7 (38.4-88.2)
5	0.82	77.8 (40.0-97.2)	66.7 (22.3-95.7)	77.8 (51.7-92.0)	66.7 (34.2-88.5)	73.3 (44.9-92.2)
Average	0.80	78.2 (58.9-85.7)	66.7 (47.2-82.7)	78.1 (66.6-85.3)	67.4 (49.1-74.3)	73.7 (59.5-80.9)

Table 22. Diagnostic performance of the combined clinico-radiomic signature model.

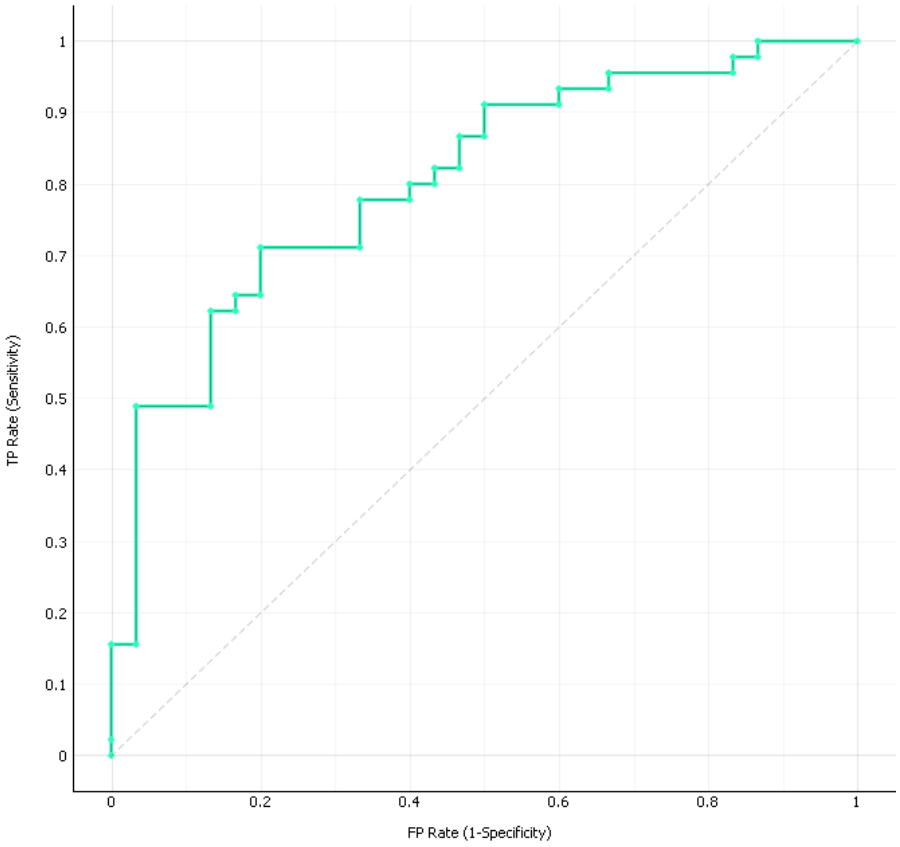

Figure 70. ROC curve for the combined clinico-radiomic signature model.

7.4 Discussion

This study has demonstrated that incorporating a machine learning-based radiomics model in conjunction with clinical features and MGMT promoter methylation status improves early prediction of glioblastoma treatment response. As reflected in the neuroradiologist assessment results, prediction of treatment response assessment at the early time point is extremely difficult in clinical practice based on conventional imaging. The imaging and patient cohort in this study reflects standard practice of glioblastoma patient management across the UK and most of the world. A relatively large single institution dataset was utilised consisting of standard-of-care conventional and ADC imaging from a number of scanners, which will have more clinical relevance [388]. Standardisation of imaging was performed through pre-processing steps to account for heterogeneity from the slightly differing acquisition parameters. To avoid variable selection bias, the methods included cross-validation within feature selection, rather than external to feature selection, which provides more reliable results [284].

There have been a small number of studies using machine learning-based radiomics of conventional imaging, such as on T1WI, T2WI, FLAIR or CE-T1WI, for distinguishing between early tPD and psPD. These have investigated radiomics of the contrast-enhancing lesion [131,132,389], radiomics of perilesional oedema [133], or a combination of both [135,390]. In addition to imaging, in this current study, clinical and molecular marker information has been incorporated. One of these prior imaging studies also included MGMT promotor methylation status within the models, with a combined model accuracy of 79%, and 76% accuracy for imaging alone [135]. Another study had included MGMT promoter methylation status as well

as other clinical information within the models, with a combined model AUC of 0.83, and 0.69 for conventional imaging alone [132]. The results of the current study are broadly in agreement with these prior studies; in addition it incorporates robust cross-validation within feature selection, achieving an overall combined clinico-radiomic model (imaging, clinical features and MGMT) accuracy of 73.7%, AUC 0.80, sensitivity of 78.2% and specificity of 66.7%.

Machine learning-based radiomics of the enhancing tumour on ADC maps have been previously investigated in several studies, however this has always been in conjunction with PWI [363,391–393]. Given the differing mechanisms of treatment effect, response and progression, functional techniques probing the physiological and metabolic characteristics could be expected to provide a more accurate assessment of changes following treatment than conventional MRI alone. Indeed, radiomic evaluation incorporating ADC and rCBV maps from PWI has shown to improve diagnostic performance for identifying psPD from tPD compared to conventional imaging alone [391]. However in clinical practice, the majority of centres in the UK do not perform PWI routinely. In the current study, ADC was specifically chosen to be used in conjunction with conventional imaging, as DWI is routinely performed for glioblastoma follow up at most centres. The inclusion of this commonly used advanced technique has the benefit of improving accuracy as well as making the study results more generalisable and clinically applicable. As would be expected, the ADC radiomic model was the best performing individual model in this study, however, the combined clinico-radiomic signature showed higher performance than the clinical and molecular model or the radiomic model alone. Therefore, incorporating the selected shape-based, ADC enhancing disease and

T2WI perilesional oedema radiomic features in this signature alongside clinical and molecular features provides complementary information, and consequently the best diagnostic performance. Of the three top selected ADC radiomic features, one was a first-order feature (*kurtosis*), and the other two (*correlation* and *contrast*) were second-order features. The top selected feature from T2WI perilesional oedema was a second-order feature (*dependence entropy*).

First-order features reflect the distribution of voxel intensities within the ROI and second-order features assess the relationship between neighbouring pixel or voxel grey level values, or texture [394]. Image texture assessed by radiomic characterisation of features such as enhancement, diffusion and K^{trans}, reflects the structure of the lesion and its environment, and provides a measure of lesion heterogeneity. Increasing levels of histological and genetic tumour heterogeneity are associated with adverse clinical outcomes [395]. Higher *kurtosis*, lower *correlation*, and higher *contrast* values were observed in tPD compared to psPD, suggesting greater heterogeneity of ADC values of the enhancing lesion in tPD. Example cases of visible heterogeneity differences between tPD and psPD are presented in Figure 71. Histopathologically there are differences between treatment-related effects and tumour progression; psPD is related to necrosis, oedema and abnormal vascular permeability whilst tPD is associated with tumour cellularity and vascular proliferation [334,396], therefore associated heterogeneity may be detected on imaging. There was a relatively higher *dependence entropy* value within the perilesional oedema on T2WI in tPD compared with psPD, implying a more complex texture to the oedema in tPD [323]. Given that glioblastoma tends to microscopically infiltrate the surrounding tissue [397], there may be variations in

texture in this surrounding region of radiological apparent hyperintensity on T2WI in cases of tPD compared with treatment-related effects where there is expected to be less tumour infiltration of the surrounding tissue.

Results from two selected shape-based features of elongation and sphericity indicated that there are morphological differences in enhancing disease patterns, which has also been seen in treatment response assessment of brain metastases [398]. Furthermore, it is well-established that low levels of MGMT promoter methylation and higher age is associated with tPD, in agreement with the selected features in our model [336,337].

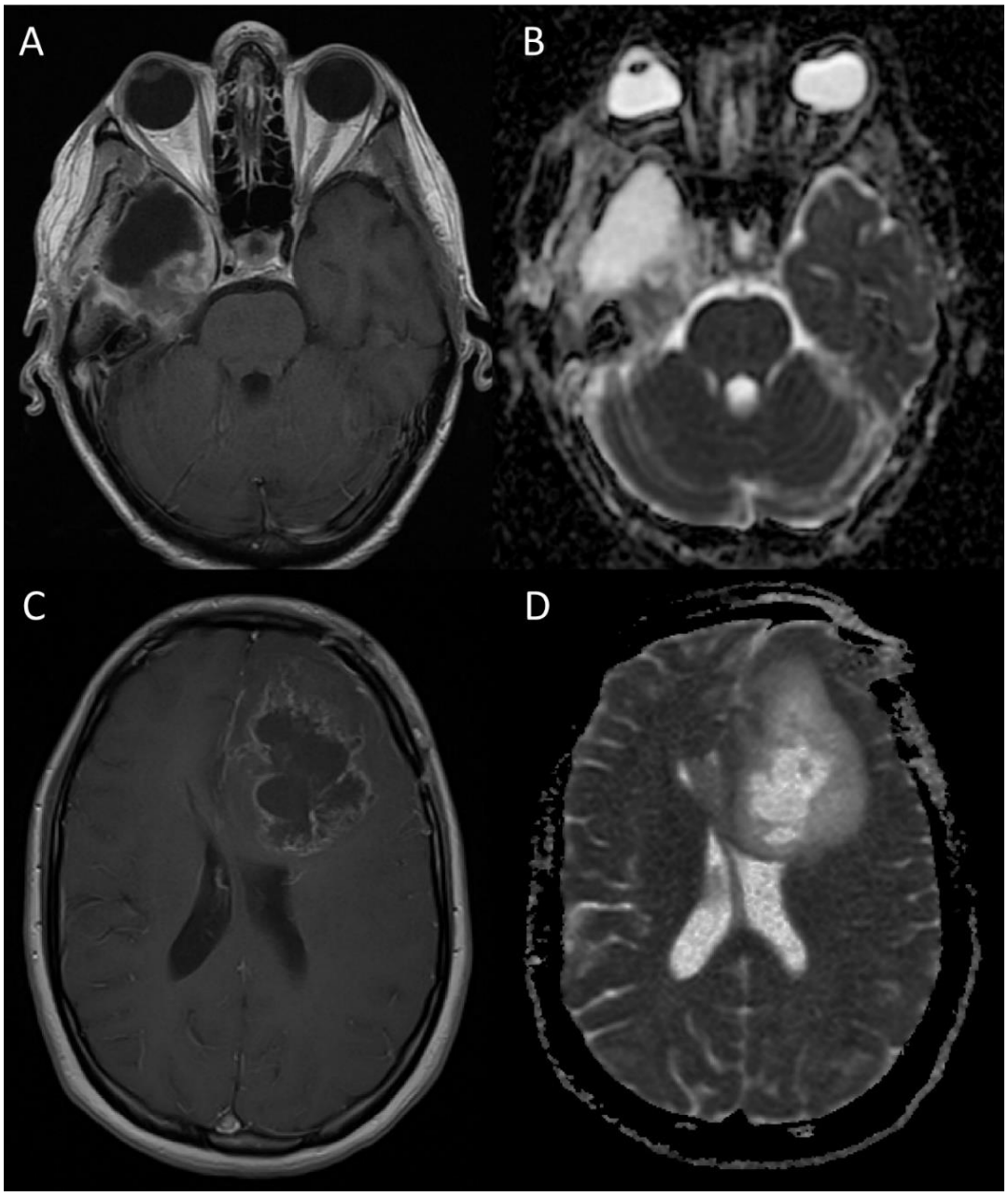

Figure 71. Differences in heterogeneity between tPD and psPD. (A,B) A case of tPD. CE-T1WI and ADC map at six weeks post-CRT shows enhancing disease in the right temporal region with visible heterogeneity in the corresponding region on the ADC map. ADC radiomics showed relatively higher kurtosis, lower correlation and higher contrast values. (C,D) A case of psPD. CE-T1WI and ADC map at six weeks post-CRT shows left frontal enhancing disease with a more homogenous appearance on the corresponding ADC map. ADC radiomics showed relatively lower kurtosis, higher correlation and lower contrast values.

7.5 Limitations and future direction

The RANO criteria was used for outcome classification and although this is the current standard for clinical care and trials, there are several limitations as also discussed previously in Section 1. These include the use of bidimensional measurements of the contrasting-enhancing disease which can overestimate disease volume, the relatively arbitrary thresholds to define response and progression, as well as the use of percentage change thresholds in lesions of different sizes [399]. The biology of post-treatment glioblastoma is also complex and there generally exists a combination of both tumour progression as well as treatment effects within the region of interest [359]. Modified treatment response criteria based on volumetric assessment may provide more accurate classification of ground truth outcome, although does not fully address heterogeneity of tumour response. Volumetric conventional imaging which is becoming more commonplace due to standardised high-resolution imaging protocols, would provide more information, however segmentation can be more time-consuming if performed manually or semi-automatically. Accurate segmentation in complex lesions is likely to be the most time-consuming step in future clinical decision support tools, which may take several minutes of manual adjustment, whereas application of machine learning-based models to imaging takes in order of only a few seconds. Although glioblastoma segmentation at longitudinal follow-up demonstrates high inter-rater agreement [400], automated methods have shown comparable performance for segmentation of enhancing disease and perilesional oedema [401], and these tools would help integrate radiomics into clinical workflows. More consistent scanner acquisition parameters or use of a single scanner

may provide better performance of radiomic models, however, may result in smaller datasets with less generalisable results.

Although this study had a relatively large single-centre dataset for this clinical issue, a number of patients were excluded as they had their baseline MRI study at their regional hospital, despite surgery being performed at Queen Elizabeth Hospital Birmingham. As with all machine learning-based radiomic studies, larger datasets from multiple institutions are more advantageous, and identification of radiomic features which are reliable and robust between scanner manufacturers will help negate some limitations of multicentre studies [387,402].

Advanced techniques, particularly the multiparametric MRI approach utilising DWI, PWI and MRS is expected to improve classification even further [122,367] given the functional assessment of water movement, angiogenesis and cell membrane turnover. However, the multiparametric approach currently is only performed at some large specialist centres and quantitative analysis of PWI and MRS is sensitive to acquisition parameters as well as post-processing, therefore at the current time provides smaller datasets, unless standardisation across centres is achieved. Radiologist-defined semantic imaging features such as the VASARI feature scoring system can also provide an additional source of information and has shown benefit in predicting outcome [403]. Similarly, including additional clinical information and molecular marker information would be expected to improve classification. With the greater availability of additional molecular marker testing, this data should be incorporated into future clinico-radiomic model studies. Information from liquid biopsy of circulating tumour DNA, specifically genetic cargo used for treatment response assessment, which currently used

alone have a low sensitivity, could also be combined with imaging biomarkers in machine learning models [404].

Lastly, there are a number of packages for radiomic feature extraction and it has been demonstrated that reliability of features can vary depending on the package chosen, therefore further work into performance and harmonisation of various packages and features is required [405]. To date, the use of deep learning techniques using implicit features through CNN have not shown superiority to radiomic-based machine learning models for this clinical issue [387], however study numbers are small and further work is required to investigate unsupervised methods in larger studies.

7.6 Conclusion

This study has shown that incorporating a machine learning-based radiomics model utilising conventional and advanced imaging in conjunction with clinical features and MGMT promoter methylation status, has a complementary effect and improves early prediction of glioblastoma treatment response. Future work should aim to integrate additional molecular markers, radiologist-defined semantic imaging features, high-resolution imaging with multiparametric MRI, and modified treatment response criteria. Multi-centre prospective studies are essential to clinically validate glioblastoma treatment response radiomic models, with the aim of being used as clinical decision support tools for personalised treatment decisions and improving the quality of life for patients.

8. CONCLUSIONS

8.1 Summary and clinical relevance

Glioblastoma is the most common aggressive primary brain tumour, and patients have an extremely poor prognosis, despite significant efforts in diagnostics and therapeutics over the years. Conventional MRI has a well-established and vital role in glioblastoma and is the imaging modality of choice; essential for diagnosis, treatment planning, assessing for complications, treatment response assessment and post-treatment monitoring. It is non-invasive, has little risks, easily repeatable and widely available. Despite its key role, conventional MRI has a number of limitations as it generally provides structural information which has a limited ability to inform treatment strategies, which are not without risks and cost.

AI techniques using radiomic features in combination with machine and deep learning can utilise conventional structural imaging sequences and convert them into higher-dimensional data through quantitative imaging features that represent tumour metrics. They provide an objective method to assess the tumour radiophenotype, reflecting pathology and genetics, in a way that is not perceptible to the human eye, showing great potential to be used as imaging biomarkers. Machine and deep learning techniques have the advantage of being able to incorporate multiple clinical features, molecular markers, and radiologist-defined semantic features into complex algorithms which are expected to produce more powerful prediction models. There are already several clinical applications of AI in neuroimaging, and the pace of

research and progress is expected to be rapid over the next few years with better quality, structured and labelled data, advances in training architecture and more powerful computing hardware. The current work has shown that AI techniques applied to routinely acquired imaging for glioblastoma are feasible and can provide an enhanced level of diagnostic and prognostic information compared to current standard-of-care image interpretation. The machine learning models have demonstrated the ability to:

1. Differentiate between IDH-wildtype glioblastoma and metastasis with a moderately-high accuracy from a single pre-treatment conventional imaging sequence.
2. Predict OS in patients with glioblastoma with a high level of accuracy using multiregional segmentations from pre-operative conventional imaging, combined with clinical information and radiologist-defined imaging features.
3. Stratify patients into high- and low-level groups of MGMT promoter methylation from a single pre-operative conventional imaging sequence, with a modest level of accuracy.
4. Predict glioblastoma treatment response outcome at the six-month time point with a moderate level of accuracy, from multi-regional segmentations on conventional imaging and DWI performed at the 4-6 weeks post-CRT imaging time point, combined with clinical features and MGMT promoter methylation status. Results showed a significantly higher accuracy compared to that of standard-of-care neuroradiologist reports at the early imaging time point.

Secondly, functional and dynamic advanced MRI techniques have shown to provide a wealth of additional information from the tumour and peritumoural microenvironment. These can

better assess tumour heterogeneity, be used as tools for clinical problem-solving, provide greater diagnostic certainty, avoid unnecessary invasive procedures, and allow therapies to be commenced sooner for better patient outcomes. These techniques are currently being used in clinical practice at a few centres, however practice varies, and it is clear that combining multiple parameters in a multiparametric approach is essential for a more reliable assessment and to increase diagnostic accuracy, rather than using parameters in isolation, as each one has its own limitations. The current work into advanced imaging techniques has shown:

1. The ability of multiparametric MRI to diagnose and differentiate between glioblastoma and various other lesions that mimic its appearances on conventional imaging through a series of cases performed in clinical practice, highlighting the real-world benefit of its use.
2. The utility of multiparametric MRI in combination with conventional imaging in the post-treatment assessment of glioblastoma, particularly in treatment response assessment for which it has demonstrated clear clinical benefit.

Both AI and advanced imaging techniques have shown to be much more useful than conventional MRI for non-invasive diagnosis, identifying optimal biopsy targets, assessing disease infiltration, in vivo molecular subtyping, prognosis inference, stratifying patients for treatment, predicting treatment response, and disease monitoring. Furthermore, the use of advanced imaging combined with AI techniques is expected to significantly revolutionise diagnostics further, with the aim of being used as clinical decision support tools.

8.2 Future direction

In order to use radiomic and radiogenomic biomarkers in clinical practice as clinical decision support tools, further work and validation is required as AI in medical imaging is still in the early phases of research. This should include accurate and automated segmentation algorithms, larger higher-quality imaging datasets from multiple institutions, prospective studies with external validation of radiomic biomarkers and models, and the integration of clinical, molecular and multiparametric advanced imaging techniques into machine and deep learning algorithms.

Image segmentation challenges such as the "Brain Tumor Segmentation (BraTS) challenge" are helping to address and improve the quality of higher-quality automated segmentation. The issue of larger datasets and external validation is partially being addressed by the use of publicly available datasets such as TCIA and TCGA, which are a valuable resource that provide imaging, genomic, and some clinical data. There is however a lack of publicly available datasets for the key clinical issue of treatment response assessment, due to complexity of interpretation, outcome assessment and ground truth labelling. This has a subsequent effect on the choice of AI techniques; currently the biggest limitation for the lack of deep learning techniques in neuro-oncology is the small sample sizes, given the relatively smaller numbers of patients diagnosed with glioblastoma compared to other tumours or pathologies. The available datasets are further reduced for post-treatment imaging issues including treatment response assessment, therefore standardised acquisitions and combining datasets from multiple institutions and publicly available datasets will be essential for future deep learning studies. There is also lack of publicly available datasets of advanced MRI techniques due to

limited use in practice by only a few specialist centres with experienced neuroradiologists. Guidelines, standards and training in the use of these techniques is essential, for neuroradiologists and higher specialty registrars training in neuroradiology. As advanced techniques continue to evolve, these should be used and investigated in parallel with and in combination with AI techniques in the future.

Given the major shift in WHO classification of gliomas in 2021, with a greater emphasis on molecular markers towards an integrated diagnosis, further work in radiogenomics is required. AI and advanced imaging techniques that can reflect tumour genomic phenotype non-invasively through a "virtual biopsy" will be a significant achievement towards assessment of tumours and personalised treatments. As already discussed, there are studies that show promise towards this aim, however there is a broad array of molecular and genomic markers that have complex interactions between them and the radiophenotype, which will require further understanding and investigation.

The overarching aim is to produce clinical decision support tools that will assist neuroradiologists in assessing the tumour and provide greater confidence in decision-making. This will be achieved through correlating the patient's clinical features, genomic and molecular markers, combined with radiophenotypes from conventional and quantitative advanced imaging. Clinical trial platforms such as the recently announced Tessa Jowell BRAIN MATRIX in the UK, will be crucial to accelerate research and develop more sensitive diagnostic and prognostic biomarkers in glioblastoma. Through this, infrastructure is being developed to create a linked network of specialist brain tumour hubs, with central repositories for clinical, molecular, pathology and imaging data collection. Standardised protocols for data collection

across the centres, and central specialist evaluation of imaging studies will provide large numbers of cases and robust data quality for clinical studies. The wealth of clinical, molecular and pathological data will be extremely valuable for correlation with imaging through radiogenomic studies. Furthermore, through the network of clinical trial units, the accuracy of imaging biomarkers that have been developed or identified can be evaluated, and validation performed with statistically robust analyses in large cohorts of participants in prospective studies across the platform.

9. LIST OF REFERENCES

1. Sawlani V, Patel M. Role of post-operative imaging in neuro-oncology. *Int J Neurooncol*. 2021;4(3):30.
2. Office for National Statistics. *Cancer Registration Statistics 2017, England*. 2019. Available at: https://www.ons.gov.uk/peoplepopulationandcommunity/healthandsocialcare/conditionsanddiseases/datasets/cancerregistrationstatisticscancerregistrationstatisticsengland (Accessed 29-07-2020).
3. Greenberg D, Winters T, Brodbelt A, Williams M. Incidence and outcomes for cerebral glioblastoma in England. *NHS National Cancer Intelligence Networks*. 2014. Available at: www.ncin.org.uk/view?rid=2662 (Accessed 29-07-2020).
4. Brodbelt A, Greenberg D, Winters T, Williams M, Vernon S, Collins VP. Glioblastoma in England: 2007-2011. *Eur J Cancer*. 2015;51(4):533–42.
5. Philips A, Henshaw DL, Lamburn G, O'Carroll MJ. Brain tumours: Rise in glioblastoma multiforme incidence in England 1995-2015 Suggests an Adverse Environmental or Lifestyle Factor. *J Environ Public Health*. 2018;2018:7910754.
6. Louis DN, Perry A, Reifenberger G, et al. The 2016 World Health Organization Classification of Tumors of the Central Nervous System: a summary. *Acta Neuropathol*. 2016;131(6):803–20.
7. Hanif F, Muzaffar K, Perveen K, Malhi SM, Simjee SU. Glioblastoma multiforme: A review of its epidemiology and pathogenesis through clinical presentation and treatment. *Asian Pacific J Cancer Prev*. 2017;18(1):3-9.
8. Ostrom QT, Bauchet L, Davis FG, et al. The epidemiology of glioma in adults: a 'state of the science' review. *Neuro Oncol*. 2014;16(7):896–913.
9. Andersen ZJ, Pedersen M, Weinmayr G, et al. Long-term exposure to ambient air pollution and incidence of brain tumor: the European Study of Cohorts for Air Pollution Effects (ESCAPE). *Neuro Oncol*. 2017;20(3):420-432.
10. Philips A, Henshaw DL, Lamburn G, O'Carroll MJ. Authors' Comment on "brain Tumours: Rise in Glioblastoma Multiforme Incidence in England 1995-2015 Suggests an Adverse Environmental or Lifestyle Factor." *J Environ Public Health*. 2018; 2170208.
11. Bräuner E V., Andersen ZJ, Andersen CE, et al. Residential Radon and Brain Tumour Incidence in a Danish Cohort. He C, ed. *PLoS One*. 2013;8(9):e74435.
12. World Health Organization. IARC classifies radiofrequency electromagnetic fields as possibly carcinogenic to humans. *Press release N° 208*. 2011;1-6. Available at: https://www.iarc.who.int/wp-content/uploads/2018/07/pr208_E.pdf (Accessed 14-10-2021).

13. Jargin S V. Radiofrequency radiation: carcinogenic and other potential risks. *J Radiat Oncol*. 2020;9(1):81-91.

14. Carlberg M, Koppel T, Ahonen M, Hardell L. Case-control study on occupational exposure to extremely low-frequency electromagnetic fields and glioma risk. *Am J Ind Med*. 2017;60(5):494-503.

15. Joseph GP, McDermott R, Baryshnikova MA, Cobbs CS, Ulasov I V. Cytomegalovirus as an oncomodulatory agent in the progression of glioma. *Cancer Lett*. 2017;384:79-85.

16. Rahman M, Dastmalchi F, Karachi A, Mitchell D. The role of CMV in glioblastoma and implications for immunotherapeutic strategies. *Oncoimmunology*. 2019;8(1).

17. Linos E, Raine T, Alonso A, Michaud D. Atopy and Risk of Brain Tumors: A Meta-analysis. *JNCI J Natl Cancer Inst*. 2007;99(20):1544-1550.

18. Tamimi A, Juweid M. Epidemiology and Outcome of Glioblastoma. In: *Glioblastoma*. Codon Publications; 2017:143-153.

19. Thomas RP, Xu LW, Lober RM, Li G, Nagpal S. The incidence and significance of multiple lesions in glioblastoma. *J Neurooncol*. 2013;112(1):91-97.

20. Lapointe S, Perry A, Butowski NA. Primary brain tumours in adults. *Lancet*. 2018;392(10145):432-446.

21. Dührsen L, Sauvigny T, Ricklefs FL, et al. Seizures as presenting symptom in patients with glioblastoma. *Epilepsia*. 2019;60(1):149-154.

22. Alexander BM, Cloughesy TF. Adult glioblastoma. *J Clin Oncol*. 2017;35(21):2402-2409.

23. Wirsching HG, Galanis E, Weller M. Glioblastoma. In: *Handbook of Clinical Neurology*. Vol 134. Elsevier; 2016:381-397.

24. Joseph DM, O'Neill AH, Chandra R V., Lai LT. Glioblastoma presenting as spontaneous intracranial haemorrhage: Case report and review of the literature. *J Clin Neurosci*. 2017;40:1-5.

25. Perkins A, Liu G. Primary Brain Tumors in Adults: Diagnosis and Treatment. *Am Fam Physician*. 2016;93(3):211-217.

26. Kernick DP, Ahmed F, Bahra A, et al. Imaging patients with suspected brain tumour: Guidance for primary care. *Br J Gen Pract*. 2008;58(557):880-885.

27. McKinnon C, Nandhabalan M, Murray SA, Plaha P. Glioblastoma: Clinical presentation, diagnosis, and management. *BMJ*. 2021;374:n1560.

28. National Institute for Health and Care Excellence. NICE guidelines: Brain tumours (primary) and brain metastases in adults (NG99). *National Institute for Health and Care Excellence*. 2018. Available at: https://www.nice.org.uk/guidance/ng99/resources/brain-tumours-primary-and-brain-metastases-in-adults-pdf-1837763558341 (Accessed 08-08-2021).

29. Ideguchi M, Kajiwara K, Goto H, et al. MRI findings and pathological features in early-stage glioblastoma. *J Neurooncol*. 2015;123(2):289-297.

30. Toh CH, Wei KC, Chang CN, et al. Differentiation of pyogenic brain abscesses from necrotic glioblastomas with use of susceptibility-weighted imaging. *Am J Neuroradiol*. 2012;33(8):1534-1538.

31. Scott JN, Brasher PMA, Sevick RJ, Rewcastle NB, Forsyth PA. How often are nonenhancing supratentorial gliomas malignant? A population study. *Neurology*. 2002;59(6):947-949.

32. Wykes V, Zisakis A, Irimia M, Ughratdar I, Sawlani V, Watts C. Importance and Evidence of Extent of Resection in Glioblastoma. *J Neurol Surgery, Part A Cent Eur Neurosurg*. 2021;82(1):75-86.

33. Le Rhun E, Seoane J, Salzet M, Soffietti R, Weller M. Liquid biopsies for diagnosing and monitoring primary tumors of the central nervous system. *Cancer Lett*. 2020;480:24-28.

34. Simonelli M, Dipasquale A, Orzan F, et al. Cerebrospinal fluid tumor DNA for liquid biopsy in glioma patients' management: Close to the clinic? *Crit Rev Oncol Hematol*. 2020;146:102879.

35. Nassiri F, Chakravarthy A, Feng S, et al. Detection and discrimination of intracranial tumors using plasma cell-free DNA methylomes. *Nat Med*. 2020;26(7):1044-1047.

36. Gatto L, Franceschi E, Nunno V Di, Tosoni A, Lodi R, Brandes AA. Liquid Biopsy in Glioblastoma Management: From Current Research to Future Perspectives. *Oncologist*. 2021;26(10):865-878.

37. NHS England. NHS to pilot potentially revolutionary blood test that detects more than 50 cancers. Nov 2020. Available at: https://www.england.nhs.uk/2020/11/nhs-to-pilot-potentially-revolutionary-blood-test/ (Accessed 10-10-2021).

38. Duffy MJ, Diamandis EP, Crown J. Circulating tumor DNA (ctDNA) as a pan-cancer screening test: is it finally on the horizon? *Clin Chem Lab Med*. 2021;59(8):1353-1361.

39. Johnson DR, Guerin JB, Giannini C, Morris JM, Eckel LJ, Kaufmann TJ. 2016 updates to the WHO brain tumor classification system: What the radiologist needs to know. *Radiographics*. 2017;37(7):2164-2180.

40. Louis DN, Wesseling P, Aldape K, et al. cIMPACT-NOW update 6: new entity and diagnostic principle recommendations of the cIMPACT-Utrecht meeting on future CNS tumor classification and grading. *Brain Pathol*. 2020;30(4):844-856.

41. WHO Classification of Tumours Editorial Board. WHO Classification of Tumours: Central Nervous System Tumours. vol. 1. 5th ed. *International Agency for Research on Cancer*; 2022.

42. Louis DN, Perry A, Wesseling P, et al. The 2021 WHO Classification of Tumors of the Central Nervous System: a summary. *Neuro Oncol*. 2021;23:1231–51.

43. Parker NR, Khong P, Parkinson JF, Howell VM, Wheeler HR. Molecular heterogeneity in glioblastoma: Potential clinical implications. *Front Oncol*. 2015;5(FEB):55.

44. Sturm D, Witt H, Hovestadt V, et al. Hotspot Mutations in H3F3A and IDH1 Define Distinct Epigenetic and Biological Subgroups of Glioblastoma. *Cancer Cell*. 2012;22(4):425-437.

45. Weller M, van den Bent M, Preusser M, et al. EANO guidelines on the diagnosis and treatment of diffuse gliomas of adulthood. *Nat Rev Clin Oncol*. 2020;18(3):170-186.

46. Burnet NG, Jefferies SJ, Benson RJ, Hunt DP, Treasure FP. Years of life lost (YLL) from cancer is an important measure of population burden - And should be considered when allocating research funds. *Br J Cancer*. 2005;92(2):241-245.

47. Aldape K, Brindle KM, Chesler L, et al. Challenges to curing primary brain tumours. *Nat Rev Clin Oncol*. 2019;16(8):509-520.

48. Chen X, Yan Y, Zhou J, et al. Clinical prognostic value of isocitrate dehydrogenase mutation, O-6-methylguanine-DNA methyltransferase promoter methylation, and 1p19q co-deletion in glioma patients. *Ann Transl Med*. 2019;7(20):541-541.

49. Dang L, White DW, Gross S, et al. Cancer-associated IDH1 mutations produce 2-hydroxyglutarate. *Nature*. 2009;462(7274):739-744.

50. Yan H, Parsons DW, Jin G, et al. IDH1 and IDH2 Mutations in Gliomas. *N Engl J Med*. 2009;360(8):765-773.

51. Han S, Liu Y, Cai SJ, et al. IDH mutation in glioma: molecular mechanisms and potential therapeutic targets. *Br J Cancer*. 2020;122(11):1580-1589.

52. Hegi ME, Diserens A-C, Gorlia T, et al. MGMT Gene Silencing and Benefit from Temozolomide in Glioblastoma . *N Engl J Med*. 2005;352(10):997-1003.

53. Cohen AL, Colman H. Glioma biology and molecular markers. *Cancer Treat Res*. 2015;163:15-30.

54. Gurrieri L, De Carlo E, Gerratana L, et al. MGMT pyrosequencing-based cut-off methylation level and clinical outcome in patients with glioblastoma multiforme. *Futur Oncol*. 2018;14(8):699-707.

55. Riemenschneider MJ, Jeuken JWM, Wesseling P, Reifenberger G. Molecular diagnostics of gliomas: state of the art. *Acta Neuropathol*. 2010;120(5):567-584.

56. Smith JS, Perry A, Borell TJ, et al. Alterations of chromosome arms 1p and 19q as predictors of survival in oligodendrogliomas, astrocytomas, and mixed oligoastrocytomas. *J Clin Oncol*. 2000;18(3):636-645.

57. Saadeh FS, Mahfouz R, Assi HI. Egfr as a clinical marker in glioblastomas and other gliomas. *Int J Biol Markers*. 2018;33(1):22-32.

58. Ludwig K, Kornblum HI. Molecular markers in glioma. *J Neurooncol*. 2017;134(3):505-512.

59. Muñoz-Hidalgo L, San-Miguel T, Megías J, et al. Somatic copy number alterations are associated with EGFR amplification and shortened survival in patients with primary glioblastoma. *Neoplasia (United States)*. 2020;22(1):10-21.

60. Hovinga KE, McCrea HJ, Brennan C, et al. EGFR amplification and classical subtype are associated with a poor response to bevacizumab in recurrent glioblastoma. *J Neuro-Oncology*. 2019;142(2):337-345.

61. Ma S, Rudra S, Campian JL, et al. Prognostic impact of CDKN2A/B deletion, TERT mutation, and EGFR amplification on histological and molecular IDH-wildtype glioblastoma. *Neuro-Oncology Adv*. 2020;2(1):1-11.

62. Ham SW, Jeon HY, Jin X, et al. TP53 gain-of-function mutation promotes inflammation in glioblastoma. *Cell Death Differ*. 2019;26(3):409-425.

63. Karsy M, Neil JA, Guan J, Mahan MA, Colman H, Jensen RL. A practical review of prognostic correlations of molecular biomarkers in glioblastoma. *Neurosurg Focus*. 2015;38(3):E4.

64. Nandakumar P, Mansouri A, Das S. The role of ATRX in glioma biology. *Front Oncol*. 2017;7(SEP):236.

65. Jiao Y, Killela PJ, Reitman ZJ, et al. Frequent ATRX, CIC, FUBP1 and IDH1 mutations refine the classification of malignant gliomas. *Oncotarget*. 2012;3(7):709-722.

66. Wiestler B, Capper D, Holland-Letz T, et al. ATRX loss refines the classification of anaplastic gliomas and identifies a subgroup of IDH mutant astrocytic tumors with better prognosis. *Acta Neuropathol*. 2013;126(3):443-451.

67. Eckel-Passow JE, Lachance DH, Molinaro AM, et al. Glioma Groups Based on 1p/19q, IDH , and TERT Promoter Mutations in Tumors . *N Engl J Med*. 2015;372(26):2499-2508.

68. Hou S-Q, Ouyang M, Brandmaier A, Hao H, Shen WH. PTEN in the maintenance of genome integrity: From DNA replication to chromosome segregation. *BioEssays*. 2017;39(10):1700082.

69. Dono A, Mitra S, Shah M, et al. PTEN mutations predict benefit from tumor treating fields (TTFields) therapy in patients with recurrent glioblastoma. *J Neurooncol*. 2021;153(1):153-160.

70. Taylor C, Munro AJ, Glynne-Jones R, et al. Multidisciplinary team working in cancer: what is the evidence? *BMJ*. 2010;340(7749):743-745.

71. Guilfoyle MR, Weerakkody RA, Oswal A, et al. Implementation of neuro-oncology service reconfiguration in accordance with NICE guidance provides enhanced clinical care for patients with glioblastoma multiforme. *Br J Cancer*. 2011;104(12):1810-1815.

72. Noorbakhsh A, Tang JA, Marcus LP, et al. Gross-total resection outcomes in an elderly population with glioblastoma: A SEER-based analysis. *J Neurosurg*. 2014;120(1):31-39.

73. Ahmadipour Y, Kaur M, Pierscianek D, et al. Association of Surgical Resection, Disability, and Survival in Patients with Glioblastoma. *J Neurol Surgery, Part A Cent Eur Neurosurg*. 2019;80(4):262-268.

74. Wenger A, Vega SF, Kling T, Bontell TO, Jakola AS, Carén H. Intratumor DNA methylation heterogeneity in glioblastoma: Implications for DNA methylation-based classification. *Neuro Oncol*. 2019;21(5):616-627.

75. Tang C, Guo J, Chen H, et al. Gene mutation profiling of primary glioblastoma through multiple tumor biopsy guided by 1H-magnetic resonance spectroscopy. *Int J Clin Exp Pathol*. 2015;8(5):5327.

76. Wu JS, Zhou LF, Tang WJ, et al. Clinical evaluation and follow-up outcome of diffusion tensor imaging-based functional neuronavigation: A prospective, controlled study in patients with gliomas involving pyramidal tracts. *Neurosurgery*. 2007;61(5):935-948.

77. Umana GE, Scalia G, Graziano F, et al. Navigated transcranial magnetic stimulation motor mapping usefulness in the surgical management of patients affected by brain tumors in eloquent areas: A systematic review and meta-analysis. *Front Neurol*. 2021;12:250.

78. Berntsen EM, Gulati S, Solheim O, et al. Functional magnetic resonance imaging and diffusion tensor tractography incorporated into an intraoperative 3-dimensional ultrasound-based neuronavigation system: Impact on therapeutic strategies, extent of resection, and clinical outcome. *Neurosurgery*. 2010;67(2):251-264.

79. Salama GR, Heier LA, Patel P, Ramakrishna R, Magge R, Tsiouris AJ. Diffusion Weighted/Tensor Imaging, Functional MRI and Perfusion Weighted Imaging in Glioblastoma—Foundations and Future. *Front Neurol*. 2018;0(JAN):660.

80. Maier-Hein KH, Neher PF, Houde J-C, et al. The challenge of mapping the human connectome based on diffusion tractography. *Nat Commun*. 2017;8(1):1-13.

81. Verburg N, de Witt Hamer PC. State-of-the-art imaging for glioma surgery. *Neurosurg Rev*. 2020;44(3):1331-1343.

82. Yamao Y, Matsumoto R, Kikuchi T, Yoshida K, Kunieda T, Miyamoto S. Intraoperative Brain Mapping by Cortico-Cortical Evoked Potential. *Front Hum Neurosci*. 2021;0:55.

83. Saito T, Muragaki Y, Maruyama T, Tamura M, Nitta M, Okada Y. Intraoperative Functional Mapping and Monitoring during Glioma Surgery. *Neurol Med Chir (Tokyo)*. 2015;55(1):1.

84. Fountain DM, Bryant A, Barone DG, et al. Intraoperative imaging technology to maximise extent of resection for glioma: a network meta-analysis. *Cochrane Database Syst Rev*. 2021;2021(1).

85. Gerritsen JKW, Arends L, Klimek M, Dirven CMF, Vincent AJPE. Impact of intraoperative stimulation mapping on high-grade glioma surgery outcome: a meta-analysis. *Acta Neurochir (Wien)*. 2019;161(1):99-107.

86. De Witt Hamer PC, Robles SG, Zwinderman AH, Duffau H, Berger MS. Impact of intraoperative stimulation brain mapping on glioma surgery outcome: A meta-analysis. *J Clin Oncol*. 2012;30(20):2559-2565.

87. Bello L, Gambini A, Castellano A, et al. Motor and language DTI Fiber Tracking combined with intraoperative subcortical mapping for surgical removal of gliomas. *Neuroimage*. 2008;39(1):369-382.

88. Schucht P, Beck J, Abu-Isa J, et al. Gross Total Resection Rates in Contemporary Glioblastoma SurgeryResults of an Institutional Protocol Combining 5-Aminolevulinic Acid Intraoperative Fluorescence Imaging and Brain Mapping. *Neurosurgery*. 2012;71(5):927-936.

89. Schucht P, Seidel K, Beck J, et al. Intraoperative monopolar mapping during 5-ALA-guided resections of glioblastomas adjacent to motor eloquent areas: Evaluation of resection rates and neurological outcome. *Neurosurg Focus*. 2014;37(6).

90. Suero Molina E, Schipmann S, Stummer W. Maximizing safe resections: the roles of 5-aminolevulinic acid and intraoperative MR imaging in glioma surgery—review of the literature. *Neurosurg Rev*. 2019;42(2):197-208.

91. Ma R, Watts C. Selective 5-aminolevulinic acid-induced protoporphyrin IX fluorescence in Gliomas. *Acta Neurochir*. 2016;158(10):1935-1941.

92. Gandhi S, Meybodi AT, Belykh E, et al. Survival outcomes among patients with high-grade glioma treated with 5-aminolevulinic acid–guided surgery: A systematic review and meta-analysis. *Front Oncol*. 2019;9:620.

93. Chohan MO, Berger MS. 5-Aminolevulinic acid fluorescence guided surgery for recurrent high-grade gliomas. *J Neurooncol*. 2019;141(3):517-522.

94. Incekara F, Smits M, Dirven L, et al. Intraoperative B-Mode Ultrasound Guided Surgery and the Extent of Glioblastoma Resection: A Randomized Controlled Trial. *Front Oncol*. 2021;11:1480.

95. Coburger J, Wirtz CR. Fluorescence guided surgery by 5-ALA and intraoperative MRI in high grade glioma: a systematic review. *J Neurooncol*. 2019;141(3):533-546.

96. Raffa G, Scibilia A, Conti A, et al. The role of navigated transcranial magnetic stimulation for surgery of motor-eloquent brain tumors: a systematic review and meta-analysis. *Clin Neurol Neurosurg*. 2019;180:7-17.

97. Booth TC, Luis A, Brazil L, et al. Glioblastoma post-operative imaging in neuro-oncology: current UK practice (GIN CUP study). *Eur Radiol*. 2020;31(5):2933-2943.

98. Albert FK, Forsting M, Sartor K, Adams HP, Kunze S. Early postoperative magnetic resonance imaging after resection of malignant glioma: Objective evaluation of residual tumor and its influence on regrowth and prognosis. *Neurosurgery*. 1994;34(1):45-61.

99. Lescher S, Schniewindt S, Jurcoane A, Senft C, Hattingen E. Time window for postoperative reactive enhancement after resection of brain tumors: Less than 72 hours. *Neurosurg Focus*. 2014;37(6).

100. Henegar MM, Moran CJ, Silbergeld DL. Early postoperative magnetic resonance imaging following nonneoplastic cortical resection. *J Neurosurg*. 1996;84(2):174-179.

101. Sato N, Bronen RA, Sze G, et al. Postoperative changes in the brain: MR imaging findings in patients without neoplasms. *Radiology*. 1997;204(3):839-846.

102. Ekinci G, Akpinar IN, Baltacioğlu F, et al. Early-postoperative magnetic resonance imaging in glial tumors: Prediction of tumor regrowth and recurrence. *Eur J Radiol*. 2003;45(2):99-107.

103. Bette S, Gempt J, Huber T, et al. Patterns and Time Dependence of Unspecific Enhancement in Postoperative Magnetic Resonance Imaging after Glioblastoma Resection. *World Neurosurg*. 2016;90:440-447.

104. Bukhari SS, Shamim MS, Mubarak F. Timing of postoperative magnetic resonance imaging (MRI) following glioma resection: Shattering the 72 hour window. *J Pak Med Assoc*. 2019;69(8):1224-1225.

105. Masuda Y, Akutsu H, Ishikawa E, et al. Evaluation of the extent of resection and detection of ischemic lesions with intraoperative MRI in glioma surgery: Is intraoperative MRI superior to early postoperative MRI? *J Neurosurg*. 2019;131(1):209-216.

106. Press RH, Shafer SL, Jiang R, et al. Optimal timing of chemoradiotherapy after surgical resection of glioblastoma: Stratification by validated prognostic classification. *Cancer*. 2020;126(14):3255-3264.

107. Niyazi M, Brada M, Chalmers AJ, et al. ESTRO-ACROP guideline "target delineation of glioblastomas." *Radiother Oncol*. 2016;118(1):35-42.

108. Bagri PK, Kapoor A, Singh D, Singhal MK, Narayan S, Kumar HS. Addition of magnetic resonance imaging to computed tomography-based three-dimensional conformal radiotherapy planning for postoperative treatment of astrocytomas: Changes in tumor volume and isocenter shift. *South Asian J Cancer*. 2015;04(01):018-020.

109. Villanueva-Meyer JE, Han SJ, Cha S, Butowski NA. Early tumor growth between initial resection and radiotherapy of glioblastoma: incidence and impact on clinical outcomes. *J Neurooncol*. 2017;134(1):213-219.

110. Majós C, Cos M, Castañer S, et al. Preradiotherapy MR Imaging: A prospective pilot study of the usefulness of performing an MR examination shortly before radiation therapy in patients with glioblastoma. *Am J Neuroradiol*. 2016;37(12):2224-2230.

111. Elson A, Paulson E, Bovi J, Siker M, Schultz C, Laviolette PS. Evaluation of pre-radiotherapy apparent diffusion coefficient (ADC): patterns of recurrence and survival outcomes analysis in patients treated for glioblastoma multiforme. *J Neurooncol*. 2015;123(1):179-188.

112. Qu J, Qin L, Cheng S, et al. Residual low ADC and high FA at the resection margin correlate with poor chemoradiation response and overall survival in high-grade glioma patients. *Eur J Radiol*. 2016;85(3):657-664.

113. Sawlani V, Patel MD, Davies N, et al. Multiparametric MRI: practical approach and pictorial review of a useful tool in the evaluation of brain tumours and tumour-like lesions. *Insights Imaging*. 2020;11(1):84.

114. Deviers A, Ken S, Filleron T, et al. Evaluation of the lactate-to-N-acetyl-aspartate ratio defined with magnetic resonance spectroscopic imaging before radiation therapy as a new predictive marker of the site of relapse in patients with glioblastoma multiforme. *Int J Radiat Oncol Biol Phys*. 2014;90(2):385-393.

115. Harat M, Małkowski B, Makarewicz R. Pre-irradiation tumour volumes defined by MRI and dual time-point FET-PET for the prediction of glioblastoma multiforme recurrence: A prospective study. *Radiother Oncol*. 2016;120(2):241-247.

116. Stupp R, Mason WP, van den Bent MJ, et al. Radiotherapy plus Concomitant and Adjuvant Temozolomide for Glioblastoma. *N Engl J Med*. 2005;352(10):987-996.

117. Perry JR, Laperriere N, O'Callaghan CJ, et al. Short-Course Radiation plus Temozolomide in Elderly Patients with Glioblastoma. *N Engl J Med*. 2017;376(11):1027-1037.

118. Hygino Da Cruz LC, Rodriguez I, Domingues RC, Gasparetto EL, Sorensen AG. Pseudoprogression and pseudoresponse: Imaging challenges in the assessment of posttreatment glioma. *Am J Neuroradiol*. 2011;32(11):1978-1985.

119. Sanghera P, Perry J, Sahgal A, et al. Pseudoprogression following chemoradiotherapy for glioblastoma multiforme. *Can J Neurol Sci*. 2010;37(1):36-42.

120. De Wit MCY, De Bruin HG, Eijkenboom W, Sillevis Smitt PAE, Van Den Bent MJ. Immediate post-radiotherapy changes in malignant glioma can mimic tumor progression. *Neurology*. 2004;63(3):535-537.

121. Chamberlain MC, Glantz MJ, Chalmers L, Van Horn A, Sloan AE. Early necrosis following concurrent Temodar and radiotherapy in patients with glioblastoma. *J Neurooncol*. 2007;82(1):81-83.

122. van Dijken BRJ, van Laar PJ, Holtman GA, van der Hoorn A. Diagnostic accuracy of magnetic resonance imaging techniques for treatment response evaluation in patients with high-grade glioma, a systematic review and meta-analysis. *Eur Radiol*. 2017;27(10):4129-4144.

123. Le Fèvre C, Constans JM, Chambrelant I, et al. Pseudoprogression versus true progression in glioblastoma patients: A multiapproach literature review. Part 2 – Radiological features and metric markers. *Crit Rev Oncol Hematol*. 2021;159:103230.

124. Rowe LS, Butman JA, Mackey M, et al. Differentiating pseudoprogression from true progression: analysis of radiographic, biologic, and clinical clues in GBM. *J Neurooncol*. 2018;139(1):145-152.

125. Gatson NTN, Bross SP, Odia Y, et al. Early imaging marker of progressing glioblastoma: a window of opportunity. *J Neurooncol*. 2020;148(3):629-640.

126. Strauss SB, Meng A, Ebani EJ, Chiang GC. Imaging Glioblastoma Posttreatment: Progression, Pseudoprogression, Pseudoresponse, Radiation Necrosis. *Neuroimaging Clin N Am*. 2021;31(1):103-120.

127. Matsusue E, Fink JR, Rockhill JK, Ogawa T, Maravilla KR. Distinction between glioma progression and post-radiation change by combined physiologic MR imaging. *Neuroradiology*. 2010;52(4):297-306.

128. Di Costanzo A, Scarabino T, Trojsi F, et al. Recurrent glioblastoma multiforme versus radiation injury: a multiparametric 3-T MR approach. *Radiol Med*. 2014;119(8):616-624.

129. Jena A, Taneja S, Jha A, et al. Multiparametric evaluation in differentiating glioma recurrence from treatment-induced necrosis using simultaneous 18F-FDG-PET/MRI: A single-institution retrospective study. *Am J Neuroradiol*. 2017;38(5):899-907.

130. Patel M, Zhan J, Natarajan K, et al. Machine learning-based radiomic evaluation of treatment response prediction in glioblastoma. *Clin Radiol*. 2021;76(8):628.e17-628.e27.

131. Gao XY, Wang Y Da, Wu SM, et al. Differentiation of treatment-related effects from glioma recurrence using machine learning classifiers based upon pre-and post-contrast T1WI and T2 FLAIR subtraction features: A two-center study. *Cancer Manag Res*. 2020;12:3191-3201.

132. Jang BS, Jeon SH, Kim IHIA, Kim IHIA. Prediction of Pseudoprogression versus Progression using Machine Learning Algorithm in Glioblastoma. *Sci Rep*. 2018;8(1):1-9.

133. Booth TC, Larkin TJ, Yuan Y, et al. Analysis of heterogeneity in T2-weighted MR images can differentiate pseudoprogression from progression in glioblastoma. *PLoS One*. 2017;12(5):e0176528.

134. Ismail M, Hill V, Statsevych V, et al. Shape features of the lesion habitat to differentiate brain tumor progression from pseudoprogression on routine multiparametric MRI: A multisite study. *Am J Neuroradiol*. 2018;39(12):2187-2193.

135. Bani-Sadr A, Eker OF, Berner L-P, et al. Conventional MRI radiomics in patients with suspected early- or pseudo-progression. *Neuro-Oncology Adv*. 2019;1(1):1-9.

136. Sun YZ, Yan LF, Han Y, et al. Differentiation of Pseudoprogression from True Progressionin Glioblastoma Patients after Standard Treatment: A Machine Learning Strategy Combinedwith Radiomics Features from T1-weighted Contrast-enhanced Imaging. *BMC Med Imaging*. 2021;21(1):17.

137. Gonçalves FG, Chawla S, Mohan S. Emerging MRI Techniques to Redefine Treatment Response in Patients With Glioblastoma. *J Magn Reson Imaging*. 2020;52(4):978-997.

138. Wen PY, Macdonald DR, Reardon DA, et al. Updated Response Assessment Criteria for High-Grade Gliomas: Response Assessment in Neuro-Oncology Working Group. *J Clin Oncol*. 2010;28(11):1963-1972.

139. Chukwueke UN, Wen PY. Use of the Response Assessment in Neuro-Oncology (RANO) criteria in clinical trials and clinical practice. *CNS Oncol*. 2019;8(1):CNS28.

140. Okada H, Weller M, Huang R, et al. Immunotherapy response assessment in neuro-oncology: A report of the RANO working group. *Lancet Oncol*. 2015;16(15):e534-e542.

141. Martínez-Garcia M, Álvarez-Linera J, Carrato C, et al. SEOM clinical guidelines for diagnosis and treatment of glioblastoma (2017). *Clin Transl Oncol*. 2018;20(1):22-28.

142. Le Fèvre C, Lhermitte B, Ahle G, et al. Pseudoprogression versus true progression in glioblastoma patients: A multiapproach literature review: Part 1 – Molecular, morphological and clinical features. *Crit Rev Oncol Hematol*. 2021;157.

143. Kumar AJ, Leeds NE, Fuller GN, et al. Malignant Gliomas: MR Imaging Spectrum of Radiation Therapy- and Chemotherapy-induced Necrosis of the Brain after Treatment. *Radiology*. 2000;217(2):377-384.

144. Nael K, Bauer AH, Hormigo A, et al. Multiparametric MRI for differentiation of radiation necrosis from recurrent tumor in patients with treated glioblastoma. *Am J Roentgenol*. 2018;210(1):18-23.

145. Hojjati M, Badve C, Garg V, et al. Role of FDG-PET/MRI, FDG-PET/CT, and Dynamic Susceptibility Contrast Perfusion MRI in Differentiating Radiation Necrosis from Tumor Recurrence in Glioblastomas. *J Neuroimaging*. 2018;28(1):118-125.

146. Lu VM, Goyal A, Graffeo CS, et al. Survival Benefit of Maximal Resection for Glioblastoma Reoperation in the Temozolomide Era: A Meta-Analysis. *World Neurosurg*. 2019;127:31-37.

147. Nunno V Di, Franceschi E, Tosoni A, et al. Treatment of recurrent glioblastoma: state-of-the-art and future perspectives. *Expert Rev Anticancer Ther*. 2020;20(9):785-795.

148. Smith JS, Cha S, Mayo MC, et al. Serial diffusion-weighted magnetic resonance imaging in cases of glioma: Distinguishing tumor recurrence from postresection injury. *J Neurosurg*. 2005;103(3):428-438.

149. Kessler AT, Bhatt AA. Brain tumour post-treatment imaging and treatment-related complications. *Insights Imaging*. 2018;9(6):1057-1075.

150. Vellayappan B, Tan CL, Yong C, et al. Diagnosis and Management of Radiation Necrosis in Patients With Brain Metastases. *Front Oncol*. 2018;8:395.

151. Dequesada IM, Quisling RG, Yachnis A, Friedman WA. Can standard magnetic resonance imaging reliably distinguish recurrent tumor from radiation necrosis after radiosurgery for brain metastases? A radiographic-pathological study. *Neurosurgery*. 2008;63(5):898-903.

152. Muto M, Frauenfelder G, Senese R, et al. Dynamic susceptibility contrast (DSC) perfusion MRI in differential diagnosis between radionecrosis and neoangiogenesis in cerebral metastases using rCBV, rCBF and K2. *Radiol Medica*. 2018;123(7):545-552.

153. Anbarloui MR, Ghodsi SM, Khoshnevisan A, et al. Accuracy of magnetic resonance spectroscopy in distinction between radiation necrosis and recurrence of brain tumors. *Iran J Neurol*. 2015;14(1):29-34.

154. Mehrabian H, Desmond KL, Soliman H, Sahgal A, Stanisz GJ. Differentiation between radiation necrosis and tumor progression using chemical exchange saturation transfer. *Clin Cancer Res*. 2017;23(14):3667-3675.

155. Ebi J, Sato H, Nakajima M, Shishido F. Incidence of leukoencephalopathy after whole-brain radiation therapy for brain metastases. *Int J Radiat Oncol Biol Phys*. 2013;85(5):1212-1217.

156. Kerklaan JP, Lycklama Á Nijeholt GJ, Wiggenraad RGJ, Berghuis B, Postma TJ, Taphoorn MJB. SMART syndrome: A late reversible complication after radiation therapy for brain tumours. *J Neurol*. 2011;258(6):1098-1104.

157. Yamanaka R, Hayano A, Kanayama T. Radiation-Induced Meningiomas: An Exhaustive Review of the Literature. *World Neurosurg*. 2017;97:635-644.e8.

158. Sarbu N, Shih RY, Jones R V., Horkayne-Szakaly I, Oleaga L, Smirniotopoulos JG. White matter diseases with radiologic-pathologic correlation. *Radiographics*. 2016;36(5):1426-1447.

159. Stupp R, Taillibert S, Kanner AA, et al. Maintenance therapy with tumor-Treating fields plus temozolomide vs temozolomide alone for glioblastoma a randomized clinical trial. *JAMA - J Am Med Assoc*. 2015;314(23):2535-2543.

160. Wang N, Jain RK, Batchelor TT. New Directions in Anti-Angiogenic Therapy for Glioblastoma. *Neurother*. 2017;14(2):321-332.

161. Funakoshi Y, Hata N, Kuga D, et al. Update on Chemotherapeutic Approaches and Management of Bevacizumab Usage for Glioblastoma. *Pharm*. 2020;13(12):470.

162. Medikonda R, Dunn G, Rahman M, Fecci P, Lim M. A review of glioblastoma immunotherapy. *J Neuro-Oncology*. 2020;151(1):41-53.

163. Weenink B, French PJ, Smitt PAES, Debets R, Geurts M. Immunotherapy in Glioblastoma: Current Shortcomings and Future Perspectives. *Cancers.* 2020;12(3):751.

164. Mende AL, Schulte JD, Okada H, Clarke JL. Current Advances in Immunotherapy for Glioblastoma. *Curr Oncol Reports*. 2021;23(2):1-18.

165. Sharma RK, Calderon C, Vivas-Mejia PE. Targeting Non-coding RNA for Glioblastoma Therapy: The Challenge of Overcomes the Blood-Brain Barrier. *Front Med Technol*. 2021;0:42.

166. Arvanitis CD, Ferraro GB, Jain RK. The blood–brain barrier and blood–tumour barrier in brain tumours and metastases. *Nat Rev Cancer*. 2019;20(1):26-41.

167. Bunevicius A, McDannold NJ, Golby AJ. Focused Ultrasound Strategies for Brain Tumor Therapy. *Oper Neurosurg*. 2020;19(1):9-18.

168. D'Amico RS, Aghi MK, Vogelbaum MA, Bruce JN. Convection-enhanced drug delivery for glioblastoma: a review. *J Neuro-Oncology*. 2021;151(3):415-427.

169. Dagogo-Jack I, Shaw AT. Tumour heterogeneity and resistance to cancer therapies. *Nat Rev Clin Oncol*. 2018;15(2):81-94.

170. Perrin SL, Samuel MS, Koszyca B, et al. Glioblastoma heterogeneity and the tumour microenvironment: Implications for preclinical research and development of new treatments. *Biochem Soc Trans*. 2019;47(2):625-638.

171. Liu Y, Xu X, Yin L, Zhang X, Li L, Lu H. Relationship between glioblastoma heterogeneity and survival time: An MR imaging texture analysis. *Am J Neuroradiol*. 2017;38(9):1695-1701.

172. Hall WA. The safety and efficacy of stereotactic biopsy for intracranial lesions. *Cancer*. 1998;82(9):1749-1755.

173. Drake-Pérez M, Boto J, Fitsiori A, Lovblad K, Vargas MI. Clinical applications of diffusion weighted imaging in neuroradiology. *Insights into Imaging*. 2018;9(4):535-547.

174. Griffith B, Jain R. Perfusion imaging in neuro-oncology: basic techniques and clinical applications. *Radiol Clin North Am*. 2015;53(3):497–511.

175. Öz G, Alger JR, Barker PB, et al. Clinical proton MR spectroscopy in central nervous system disorders. *Radiology*. 2014;270(3):658-679.

176. Hourani R, Brant LJ, Rizk T, Weingart JD, Barker PB, Horská A. Can proton MR spectroscopic and perfusion imaging differentiate between neoplastic and nonneoplastic brain lesions in adults? *Am J Neuroradiol*. 2008;29(2):366-372.

177. Tsitsia V, Svolou P, Kapsalaki E, et al. Multimodality-multiparametric brain tumors evaluation. *Hell J Nucl Med*. 2017;20(1):57-61.

178. Fink JR, Muzi M, Peck M, Krohn KA. Multimodality brain tumor imaging: MR imaging, PET, and PET/MR imaging. *J Nucl Med*. 2015;56(10):1554-1561.

179. Villanueva-Meyer JE, Mabray MC, Cha S. Current Clinical Brain Tumor Imaging. *Neurosurgery*. 2017;81(3):397-415.

180. Vamvakas A, Williams SC, Theodorou K, et al. Imaging biomarker analysis of advanced multiparametric MRI for glioma grading. *Phys Medica*. 2019;60:188-198.

181. Langen K-J, Galldiks N, Hattingen E, Shah NJ. Advances in neuro-oncology imaging. *Nat Rev Neurol*. 2017;13(5):279-289.

182. Grech-Sollars M, Hales PW, Miyazaki K, et al. Multi-centre reproducibility of diffusion MRI parameters for clinical sequences in the brain. *NMR Biomed*. 2015;28(4):468-485.

183. Kitis O, Altay H, Calli C, Yunten N, Akalin T, Yurtseven T. Minimum apparent diffusion coefficients in the evaluation of brain tumors. *Eur J Radiol*. 2005;55(3):393-400.

184. Abrigo JM, Fountain DM, Provenzale JM, et al. Magnetic resonance perfusion for differentiating low-grade from high-grade gliomas at first presentation. *Cochrane Database Syst Rev*. 2018;2018(1).

185. Safriel Y, Pol-Rodriguez MA, Novotny EJ, Rothman DL, Fulbright RK. Reference values for long echo time MR spectroscopy in healthy adults. *Am J Neuroradiol*. 2005;26(6):1439-1445.

186. Krukowski P, Podgórski P, Guziński M, Szewczyk P, Sąsiadek M. Analysis of the brain proton magnetic resonance spectroscopy - differences between normal grey and white matter. *Polish J Radiol*. 2010;75(2):22-26.

187. Usinskiene J, Ulyte A, Bjørnerud A, et al. Optimal differentiation of high- and low-grade glioma and metastasis: a meta-analysis of perfusion, diffusion, and spectroscopy metrics. *Neuroradiology*. 2016;58(4):339-350.

188. Lee EJ, Lee SK, Agid R, Bae JM, Keller A, terBrugge K. Preoperative Grading of Presumptive Low-Grade Astrocytomas on MR Imaging: Diagnostic Value of Minimum Apparent Diffusion Coefficient. *Am J Neuroradiol*. 2008;29(10):1872-1877.

189. Hakyemez B, Erdogan C, Ercan I, Ergin N, Uysal S, Atahan S. High-grade and low-grade gliomas: Differentiation by using perfusion MR imaging. *Clin Radiol*. 2005;60(4):493-502.

190. Murakami R, Hirai T, Sugahara T, et al. Grading Astrocytic Tumors by Using Apparent Diffusion Coefficient Parameters: Superiority of a One-versus Two-Parameter Pilot Method 1. *Radiology*. 2009;251(3):838.

191. Martín-Noguerol T, Mohan S, Santos-Armentia E, Cabrera-Zubizarreta A, Luna A. Advanced MRI assessment of non-enhancing peritumoral signal abnormality in brain lesions. *Eur J Radiol*. 2021;143(0):109900.

192. Kousi E, Tsougos I, Tsolaki E, et al. Spectroscopic evaluation of glioma grading at 3T: The combined role of short and long TE. *Sci World J*. 2012;2012:546171.

193. Kimura T, Sako K, Gotoh T, Tanaka K, Tanaka T. In vivo single-voxel proton MR spectroscopy in brain lesions with ring-like enhancement. *NMR Biomed*. 2001;14(6):339-349.

194. Fordham AJ, Hacherl CC, Patel N, et al. Differentiating glioblastomas from solitary brain metastases: An update on the current literature of advanced imaging modalities. *Cancers (Basel)*. 2021;13(12):2960.

195. Bauer AH, Erly W, Moser FG, Maya M, Nael K. Differentiation of solitary brain metastasis from glioblastoma multiforme: a predictive multiparametric approach using combined MR diffusion and perfusion. *Neuroradiol*. 2015;57(7):697-703.

196. Kadota Y, Hirai T, Azuma M, et al. Differentiation between glioblastoma and solitary brain metastasis using neurite orientation dispersion and density imaging. *J Neuroradiol*. 2020;47(3):197-202.

197. Sone D. Neurite orientation and dispersion density imaging: Clinical utility, efficacy, and role in therapy. *Reports Med Imaging*. 2019;12:17-29.

198. Mao J, Zeng W, Zhang Q, et al. Differentiation between high-grade gliomas and solitary brain metastases: a comparison of five diffusion-weighted MRI models. *BMC Med Imaging*. 2020;20(1):1-11.

199. Batchelor T, Loeffler JS. Primary CNS lymphoma. *J Clin Oncol*. 2006;24(8):1281-1288.

200. Neska-Matuszewska M, Bladowska J, Sąsiadek M, Zimny A. Differentiation of glioblastoma multiforme, metastases and primary central nervous system lymphomas using multiparametric perfusion and diffusion MR imaging of a tumor core and a

peritumoral zone—Searching for a practical approach. *PLoS One*. 2018;13(1):e0191341.

201. Yamasaki F, Takayasu T, Nosaka R, et al. Magnetic resonance spectroscopy detection of high lipid levels in intraaxial tumors without central necrosis: A characteristic of malignant lymphoma. *J Neurosurg*. 2015;122(6):1370-1379.

202. Saini J, Kumar Gupta P, Awasthi A, et al. Multiparametric imaging-based differentiation of lymphoma and glioblastoma: using T1-perfusion, diffusion, and susceptibility-weighted MRI. *Clin Radiol*. 2018;73(11):986.e7-986.e15.

203. Fiester PJ, Soule E, Natter PE, Haymes D, Rao D. Necrotic Primary Central Nervous System Lymphoma in an Immunocompetent Patient: A Case Report and Literature Review. *Cureus*. 2019;11(6).

204. Wu Y-W, Zheng J, Liu L-L, Cai J-H, Yuan H, Ye J. Imaging of hemorrhagic primary central nervous system lymphoma: A case report. *World J Clin Cases*. 2020;8(15):3329.

205. Suh CH, Kim HS, Jung SC, Park JE, Choi CG, Kim SJ. MRI as a diagnostic biomarker for differentiating primary central nervous system lymphoma from glioblastoma: A systematic review and meta-analysis. *J Magn Reson Imaging*. 2019;50(2):560-572.

206. Nguyen A V., Blears EE, Ross E, Lall RR, Ortega-Barnett J. Machine learning applications for the differentiation of primary central nervous system lymphoma from glioblastoma on imaging: A systematic review and meta-analysis. *Neurosurg Focus*. 2018;45(5):E5.

207. Nakagawa M, Nakaura T, Namimoto T, et al. Machine learning based on multi-parametric magnetic resonance imaging to differentiate glioblastoma multiforme from primary cerebral nervous system lymphoma. *Eur J Radiol*. 2018;108:147-154.

208. Kunimatsu A, Kunimatsu N, Yasaka K, et al. Machine Learning-based Texture Analysis of Contrast-enhanced MR Imaging to Differentiate between Glioblastoma and Primary Central Nervous System Lymphoma. *Magn Reson Med Sci*. 2019;18(1):44.

209. Swinburne NC, Schefflein J, Sakai Y, et al. Machine learning for semi-automated classification of glioblastoma, brain metastasis and central nervous system lymphoma using magnetic resonance advanced imaging. *Ann Transl Med*. 2019;7(11):232-232.

210. Bathla G, Priya S, Liu Y, et al. Radiomics-based differentiation between glioblastoma and primary central nervous system lymphoma: a comparison of diagnostic performance across different MRI sequences and machine learning techniques. *Eur Radiol*. Published online April 23, 2021:1-11.

211. Pignatti F, Van den Bent M, Curran D, et al. Prognostic factors for survival in adult patients with cerebral low-grade glioma. *J Clin Oncol*. 2002;20(8):2076-2084.

212. Murphy ES, Leyrer CM, Parsons M, et al. Risk Factors for Malignant Transformation of Low-Grade Glioma. *Int J Radiat Oncol Biol Phys*. 2018;100(4):965-971.

213. Rees J, Watt H, Jäger HR, et al. Volumes and growth rates of untreated adult low-grade gliomas indicate risk of early malignant transformation. *Eur J Radiol*. 2009;72(1):54-64.

214. Hakyemez B, Erdogan C, Ercan I, Ergin N, Uysal S, Atahan S. High-grade and low-grade gliomas: Differentiation by using perfusion MR imaging. *Clin Radiol*. 2005;60(4):493-502.

215. Bulik M, Jancalek R, Vanicek J, Skoch A, Mechl M. Potential of MR spectroscopy for assessment of glioma grading. *Clin Neurol Neurosurg*. 2013;115(2):146-153.

216. Danchaivijitr N, Waldman AD, Tozer DJ, et al. Low-grade gliomas: Do changes in rCBV measurements at longitudinal perfusion-weighted MR imaging predict malignant transformation? *Radiology*. 2008;247(1):170-178.

217. Soares DP, Law M. Magnetic resonance spectroscopy of the brain: review of metabolites and clinical applications. *Clin Radiol*. 2009;64(1):12-21.

218. Muragaki Y, Chernov M, Maruyama T, et al. Low-grade glioma on stereotactic biopsy: How often is the diagnosis accurate? *Minim Invasive Neurosurg*. 2008;51(5):275-279.

219. Jin T, Ren Y, Zhang H, Xie Q, Yao Z, Feng X. Application of MRS- and ASL-guided navigation for biopsy of intracranial tumors. *Acta radiol*. 2019;60(3):374-381.

220. Badve C, Yu A, Dastmalchian S, et al. MR Fingerprinting of Adult Brain Tumors: Initial Experience. *Am J Neuroradiol*. 2017;38(3):492-499.

221. Zhang X, Yan L-F, Hu Y-C, et al. Optimizing a machine learning based glioma grading system using multi-parametric MRI histogram and texture features. *Oncotarget*. 2017;8(29):47816-47830.

222. Georgakis MK, Spinos D, Pourtsidis A, et al. Incidence and survival of gliomatosis cerebri: a population-based cancer registration study. *J Neurooncol*. 2018;138(2):341-349.

223. Kwon MJ, Kang SY, Cho H, Lee J Il, Kim ST, Suh YL. Clinical relevance of molecular subgrouping of gliomatosis cerebri per 2016 WHO classification: a clinicopathological study of 89 cases. *Brain Pathol*. 2020;30(2):235-245.

224. Förster A, Brehmer S, Seiz-Rosenhagen M, et al. Heterogeneity of glioblastoma with gliomatosis cerebri growth pattern on diffusion and perfusion MRI. *J Neurooncol*. 2019;142(1):103-109.

225. Osenbach RK, Loftus CM. Diagnosis and Management of Brain Abscess. *Neurosurg Clin N Am*. 1992;3(2):403-420.

226. Horvath-Rizea D, Surov A, Hoffmann K-T, et al. The value of whole lesion ADC histogram profiling to differentiate between morphologically indistinguishable ring enhancing lesions-comparison of glioblastomas and brain abscesses. *Oncotarget*. 2018;9(26):18148-18159.

227. Chawla S, Wang S, Mohan S, et al. Differentiation of brain infection from necrotic glioblastoma using combined analysis of diffusion and perfusion MRI. *J Magn Reson Imaging*. 2019;49(1):184-194.

228. Hsu SH, Chou MC, Ko CW, et al. Proton MR spectroscopy in patients with pyogenic brain abscess: MR spectroscopic imaging versus single-voxel spectroscopy. *Eur J Radiol*. 2013;82(8):1299-1307.

229. Xu XX, Li B, Yang HF, et al. Can diffusion-weighted imaging be used to differentiate brain abscess from other ring-enhancing brain lesions? A meta-analysis. *Clin Radiol*. 2014;69(9):909-915.

230. Zeng T, Xu Z, Yan J. The value of asphericity derived from T1-weighted MR in differentiating intraparenchymal ring-enhancing lesions–comparison of glioblastomas and brain abscesses. *Neurol Sci 2021*. Published online April 1, 2021:1-5.

231. Lai PH, Chung HW, Chang HC, et al. Susceptibility-weighted imaging provides complementary value to diffusion-weighted imaging in the differentiation between pyogenic brain abscesses, necrotic glioblastomas, and necrotic metastatic brain tumors. *Eur J Radiol*. 2019;117:56-61.

232. Peng J, Ouyang Y, Fang WD, et al. Differentiation of intracranial tuberculomas and high grade gliomas using proton MR spectroscopy and diffusion MR imaging. *Eur J Radiol*. 2012;81(12):4057-4063.

233. Gupta RK, Roy R, Dev R, et al. Finger printing of mycobacterium tuberculosis in patients with intracranial tuberculomas by usingin vivo,ex vivo, andin vitro magnetic resonance spectroscopy. *Magn Reson Med*. 1996;36(6):829-833.

234. Morales H, Alfaro D, Martinot C, Fayed N, Gaskill-Shipley M. MR spectroscopy of intracranial tuberculomas: A singlet peak at 3.8 ppm as potential marker to differentiate them from malignant tumors. In: *Neuroradiology Journal*. 2015:294-302.

235. Kulanthaivelu K, Jabeen S, Saini J, et al. Amide proton transfer imaging for differentiation of tuberculomas from high-grade gliomas: Preliminary experience. *Neuroradiol J*. 2021;Epub:10.1177/19714009211002766.

236. McKenzie KP, Wong WM, Patterson SB, McDermott JH, Swamy NK, Hiles CL. Case of cerebral toxoplasmosis masquerading as high-grade glioma. *Interdiscip Neurosurg*. 2019;17:57-59.

237. Fard SA, Khajeh A, Khosravi A, et al. Fulminant and diffuse cerebral toxoplasmosis as the first manifestation of hiv infection: A case presentation and review of the literature. *Am J Case Rep*. 2020;21:e919624-1.

238. Vienne A, Dulou R, Bielle F, Baruteau M, Maison FL, Nikolova Yordanova Y. Awake surgery for isolated parenchymal degenerating neurocysticercosis – Case report and focused review of misdiagnosis of neurocysticercosis. *Neurochirurgie*. 2019;65(6):402-416.

239. Patil YP, Patel CR, Kuber RS, Sekhon RK. Characteristics of Ring enhancing lesions in brain in correlation with MRI and MR spectroscopy. *Int J Heal Clin Res*. 2021;4(1):120-127.

240. Chawla S, Asadollahi S, Gupta PK, Nath K, Brem S, Mohan S. Advanced magnetic resonance imaging and spectroscopy in a case of neurocysticercosis from North America. *Neuroradiol J*. 2021;Epub:10.1177/19714009211026889.

241. Ulett KB, Cockburn JWJ, Jeffree R, Woods ML. Cerebral cryptococcoma mimicking glioblastoma. *BMJ Case Rep*. 2017;2017:bcr2016218824.

242. Santander XA, Gutiérrez-González R, Cotúa C, Tejerina E, Rodríguez-Boto G. Intraventricular cryptococcoma mimicking a neoplastic lesion in an immunocompetent patient with hydrocephalus: A case report. *Surg Neurol Int*. 2021;10(115).

243. Kelly A, Mpanza P, Lekgwara P, Otto D. Multicentric Cryptococcomas Mimicking Neoplasia in Immunocompetent Patient. *World Neurosurg*. 2018;118:5-8.

244. Grüter BE, Reuss AM, Rushing EJ, Pangalu A, Oertel MF. An unexpected intracerebral lesion – case report of a superinfected aspergillosis mimicking a brain metastasis. *BMC Infect Dis*. 2021;21(1):1-5.

245. Neyaz Z, Singh V, Mehrotra A, Jain M. Cerebral Aspergillosis Mimicking a Neoplasm in an Immunocompetent Patient. *Int J Appl Basic Med Res*. 2018;8(4):269-271.

246. Dusak A, Hakyemez B, Kocaeli H, Bekar A. Magnetic resonance spectroscopy findings of pyogenic, tuberculous, and cryptococcus intracranial abscesses. *Neurochem Res*. 2012;37(2):233-237.

247. Luthra G, Parihar A, Nath K, et al. Comparative evaluation of fungal, tubercular, and pyogenic brain abscesses with conventional and diffusion MR imaging and proton MR spectroscopy. *Am J Neuroradiol*. 2007;28(7):1332-1338.

248. Nakayama M, Naganawa S, Ouyang M, et al. A review of clinical and imaging findings in tumefactive demyelination. *Am J Roentgenol*. 2021;217(1):186-197.

249. Lucchinetti CF, Gavrilova RH, Metz I, et al. Clinical and radiographic spectrum of pathologically confirmed tumefactive multiple sclerosis. *Brain*. 2008;131(7):1759-1775.

250. Saindane AM, Cha S, Law M, Xue X, Knopp EA, Zagzag D. Proton MR spectroscopy of tumefactive demyelinating lesions. *Am J Neuroradiol*. 2002;23(8):1378-1386.

251. Belfkih R, Khayat OG, H'Daidane H, El Amrani FZ. Pseudotumoral demyelinating lesions: A presentation of acute disseminated encephalomyelitis. *Case Rep Neurol*. 2021;13(2):289-296.

252. Paolilo RB, Deiva K, Neuteboom R, Rostásy K, Lim M. Acute Disseminated Encephalomyelitis: Current Perspectives. *Children*. 2020;7(11):210.

253. O´Sullivan C, Zach F, Moser T, et al. Misinterpretation of glioblastoma as ADEM: potentially harmful consequences of over-diagnosis of COVID-19 vaccine-associated adverse events. *J Neurol*. 2021;1:1-3.

254. Pradhan, Choudhury SS, Das A. Tumefactive acute disseminated encephalomyelitis. *Neurol India*. 2017;65(3):558.

255. Sammarra I, Barbagallo G, Labate A, et al. Value of multimodal imaging approach to diagnosis of neurosarcoidosis. *Brain Sci*. 2019;9(10):243.

256. Odaka M, Yuki N, Yamada M, et al. Bickerstaff's brainstem encephalitis: Clinical features of 62 cases and a subgroup associated with Guillain-Barré syndrome. *Brain*. 2003;126(10):2279-2290.

257. Ogawara K, Kuwabara S, Yuki N. Fisher syndrome or Bickerstaff brainstem encephalitis? Anti-GQ1b IgG antibody syndrome involving both the peripheral and central nervous systems. *Muscle Nerve*. 2002;26(6):845-849.

258. Yamamuro S, Yazawa G, Shiokawa R, et al. Erroneous resection of a cerebellar infarction – Lesson learned. *Interdiscip Neurosurg*. 2021;25:101196.

259. Zahid M, Yapor L, Niazi M, Adrish M, Hanif A. A Rare Case of Cerebellar Glioblastoma Mimicking Acute Stroke in an Elderly Patient. *Am J Case Rep*. 2020;21:e927031-1.

260. Remley W, Butala N. Glioblastoma Multiforme Masquerading as Stroke. *Cureus*. 2021;13(5).

261. Onyambu CK, Wajihi MN, Odhiambo AO. Clinical Application of Magnetic Resonance Spectroscopy in Diagnosis of Intracranial Mass Lesions. *Radiol Res Pract*. 2021;2021:1-10.

262. Adam G, Ferrier M, Patsoura S, et al. Magnetic resonance imaging of arterial stroke mimics: a pictorial review. *Insights Imaging*. 2018;9(5):815-831.

263. Soto JM, Lyon KA, Benardete EA. Glioblastoma multiforme presenting as cryptogenic intracerebral hemorrhage. *Baylor Univ Med Cent Proc*. 2018;31(4):516-518.

264. Jin H, Qu Y, Guo ZN, Cui GZ, Zhang FL, Yang Y. Primary Angiitis of the Central Nervous System Mimicking Glioblastoma: A Case Report and Literature Review. *Front Neurol*. 2019;10:1208.

265. Zhu DS, Yang XL, Lv HH, et al. Seizure syndrome as a first manifestation of solitary tumor-like mass lesion of PACNS: Two case reports. *Med (United States)*. 2017;96(9).

266. Kumar P, Rajesh A, Kandadai R, Purohit A, Sundaram C. Primary CNS vasculitis masquerading as glioblastoma: A case report and review. *Asian J Neurosurg*. 2017;12(1):69.

267. Panchal NJ, Niku S, Imbesi SG. Lymphocytic Vasculitis Mimicking Aggressive Multifocal Cerebral Neoplasm: MR Imaging and MR Spectroscopic Appearance. *AJNR Am J Neuroradiol*. 2005;26(3):642.

268. Arnett N, Pavlou A, Burke MP, Cucchiara BL, Rhee RL, Song JW. Vessel wall MR imaging of central nervous system vasculitis: a systematic review. *Neuroradiology*. 2021;1:1-16.

269. Welker K, Boxerman J, Kalnin A, Kaufmann T, Shiroishi M, Wintermark M. ASFNR recommendations for clinical performance of MR dynamic susceptibility contrast perfusion imaging of the brain. *Am J Neuroradiol*. 2015;36(6):E41-E51.

270. Clement P, Booth T, Borovečki F, et al. GliMR: Cross-Border Collaborations to Promote Advanced MRI Biomarkers for Glioma. *J Med Biol Eng*. 2021;41(2):115-125.

271. Pope WB, Brandal G. Conventional and advanced magnetic resonance imaging in patients with high-grade glioma. *Q J Nucl Med Mol Imaging*. 2018;62(3):239-253.

272. Talo M, Baloglu UB, Yıldırım Ö, Rajendra Acharya U. Application of deep transfer learning for automated brain abnormality classification using MR images. *Cogn Syst Res*. 2019;54:176-188.

273. Kurian KM, Jenkinson MD, Brennan PM, et al. Brain tumor research in the United Kingdom: Current perspective and future challenges. A strategy document from the NCRI brain tumor CSG. *Neuro-Oncology Pract*. 2018;5(1):10-17.

274. Enrique G-V, Irving S-R, Ricardo B-I, et al. Diagnosis and management of brain metastases: an updated review from a radiation oncology perspective. *J Cancer Metastasis Treat*. 2019;2019(5):54.

275. Cagney DN, Martin AM, Catalano PJ, et al. Incidence and prognosis of patients with brain metastases at diagnosis of systemic malignancy: a population-based study. *Neuro Oncol*. 2017;19(11):1511-1521.

276. Sacks P, Rahman M. Epidemiology of Brain Metastases. *Neurosurg Clin N Am*. 2020;31(4):481-488.

277. Skogen K, Schulz A, Helseth E, Ganeshan B, Dormagen JB, Server A. Texture analysis on diffusion tensor imaging: discriminating glioblastoma from single brain metastasis. *Acta radiol*. 2019;60(3):356-366.

278. Chartrand G, Cheng PM, Vorontsov E, et al. Deep Learning: A Primer for Radiologists. *RadioGraphics*. 2017;37(7):2113-2131.

279. Gillies RJ, Kinahan PE, Hricak H. Radiomics: Images are more than pictures, they are data. *Radiology*. 2016;278(2):563-577.

280. Varghese BA, Cen SY, Hwang DH, Duddalwar VA. Texture analysis of imaging: What radiologists need to know. *Am J Roentgenol*. 2019;212(3):520-528.

281. Acharya UR, Hagiwara Y, Sudarshan VK, Chan WY, Ng KH. Towards precision medicine: from quantitative imaging to radiomics. *J Zhejiang Univ Sci B*. 2018;19(1):6-24.

282. Erickson BJ, Korfiatis P, Akkus Z, Kline TL. Machine Learning for Medical Imaging. *RadioGraphics*. 2017;37(2):505-515.

283. van Griethuysen JJM, Fedorov A, Parmar C, et al. Computational Radiomics System to Decode the Radiographic Phenotype. *Cancer Res*. 2017;77(21):e104-e107.

284. Krstajic D, Buturovic LJ, Leahy DE, Thomas S. Cross-validation pitfalls when selecting and assessing regression and classification models. *J Cheminform*. 2014;6(1):1-15.

285. McKinney W. Data Structures for Statistical Computing in Python. *Proc 9th Python Sci Conf*. 2010:56-61.

286. Pedregosa F, Varoquaux G, Gramfort A, et al. Scikit-learn: Machine Learning in Python. *J Mach Learn Res*. 2011;12:2825-2830.

287. Demšar J, Erjavec A, Hočevar T, et al. Orange: Data Mining Toolbox in Python Tomaž Curk Matija Polajnar Laň Zagar. *J Mach Learn Res*. 2013;14:2349-2353.

288. Nayak L, Lee EQ, Wen PY. Epidemiology of Brain Metastases. *Curr Oncol Rep.* 2012;14(1):48-54.

289. Nussbaum ES, Djalilian HR, Cho KH, Hall WA. Brain metastases: Histology, multiplicity, surgery, and survival. *Cancer*. 1996;78(8):1781-1788.

290. Fiss I, Hussein A, Barrantes-Freer A, et al. Cerebral metastases: do size, peritumoral edema, or multiplicity predict infiltration into brain parenchyma? *Acta Neurochir*. 2019;161(5):1037-1045.

291. Artzi M, Bressler I, Ben Bashat D. Differentiation between glioblastoma, brain metastasis and subtypes using radiomics analysis. *J Magn Reson Imaging*. 2019;50(2):519-528.

292. Chen C, Ou X, Wang J, Guo W, Ma X. Radiomics-based machine learning in differentiation between glioblastoma and metastatic brain tumors. *Front Oncol*. 2019;9(AUG):806.

293. Qian Z, Li Y, Wang Y, et al. Differentiation of glioblastoma from solitary brain metastases using radiomic machine-learning classifiers. *Cancer Lett*. 2019;451:128-135.

294. Petrujkić K, Milošević N, Rajković N, et al. Computational quantitative MR image features - a potential useful tool in differentiating glioblastoma from solitary brain metastasis. *Eur J Radiol*. 2019;119:108634.

295. Tateishi M, Nakaura T, Kitajima M, et al. An initial experience of machine learning based on multi-sequence texture parameters in magnetic resonance imaging to differentiate glioblastoma from brain metastases. *J Neurol Sci*. 2020;410:116514.

296. Bae S, An C, Ahn SS, et al. Robust performance of deep learning for distinguishing glioblastoma from single brain metastasis using radiomic features: model development and validation. *Sci Reports*. 2020;10(1):1-10.

297. Blanchet L, Krooshof PWT, Postma GJ, et al. Discrimination between metastasis and glioblastoma multiforme based on morphometric analysis of MR images. *Am J Neuroradiol*. 2011;32(1):67-73.

298. Mouthuy N, Cosnard G, Abarca-Quinones J, Michoux N. Multiparametric magnetic resonance imaging to differentiate high-grade gliomas and brain metastases. *J Neuroradiol*. 2012;39(5):301-307.

299. Dikaios N. Deep learning magnetic resonance spectroscopy fingerprints of brain tumours using quantum mechanically synthesised data. *NMR Biomed*. 2021;34(4):e4479.

300. Lu Y, Patel M, Natarajan K, et al. Machine learning-based radiomic, clinical and semantic feature analysis for predicting overall survival and MGMT promoter methylation status in patients with glioblastoma. *Magn Reson Imaging*. 2020;74:161-170.

301. Dullea A, Marignol L. MGMT testing allows for personalised therapy in the temozolomide era. *Tumor Biol*. 2016;37(1):87-96.

302. Wick W, Weller M, Van Den Bent M, et al. MGMT testing - The challenges for biomarker-based glioma treatment. *Nat Rev Neurol*. 2014;10(7):372-385.

303. Weller M, Stupp R, Reifenberger G, et al. MGMT promoter methylation in malignant gliomas: Ready for personalized medicine? *Nat Rev Neurol*. 2010;6(1):39-51.

304. Binabaj MM, Bahrami A, ShahidSales S, et al. The prognostic value of MGMT promoter methylation in glioblastoma: A meta-analysis of clinical trials. *J Cell Physiol*. 2018;233(1):378-386.

305. Colquhoun A. Cell biology-metabolic crosstalk in glioma. *Int J Biochem Cell Biol*. 2017;89:171-181.

306. Quillien V, Lavenu A, Sanson M, et al. Outcome-based determination of optimal pyrosequencing assay for MGMT methylation detection in glioblastoma patients. *J Neurooncol*. 2014;116(3):487-496.

307. Rudie JD, Rauschecker AM, Bryan RN, Davatzikos C, Mohan S. Emerging Applications of Artificial Intelligence in Neuro-Oncology. *Radiology*. 2019;290(3):607-618.

308. Choy G, Khalilzadeh O, Michalski M, et al. Current applications and future impact of machine learning in radiology. *Radiology*. 2018;288(2):318-328.

309. Wei J, Yang G, Hao X, et al. A multi-sequence and habitat-based MRI radiomics signature for preoperative prediction of MGMT promoter methylation in astrocytomas with prognostic implication. *Eur Radiol*. 2019;29(2):877-888.

310. Yu P, Ning J, Xu B, et al. Histogram analysis of 11C-methionine integrated PET/MRI may facilitate to determine the O6-methylguanylmethyltransferase methylation status in gliomas. *Nucl Med Commun*. 2019;40(8):850-856.

311. Li ZC, Bai H, Sun Q, et al. Multiregional radiomics features from multiparametric MRI for prediction of MGMT methylation status in glioblastoma multiforme: A multicentre study. *Eur Radiol*. 2018;28(9):3640-3650.

312. Han Y, Yan LF, Wang X Bin, et al. Structural and advanced imaging in predicting MGMT promoter methylation of primary glioblastoma: A region of interest based analysis. *BMC Cancer*. 2018;18(1).

313. Sasaki T, Kinoshita M, Fujita K, et al. Radiomics and MGMT promoter methylation for prognostication of newly diagnosed glioblastoma. *Sci Rep*. 2019;9(1).

314. Xi Y Bin, Guo F, Xu ZL, et al. Radiomics signature: A potential biomarker for the prediction of MGMT promoter methylation in glioblastoma. *J Magn Reson Imaging*. 2018;47(5):1380-1387.

315. Korfiatis P, Kline TL, Coufalova L, et al. MRI texture features as biomarkers to predict MGMT methylation status in glioblastomas. *Med Phys*. 2016;43(6):2835-2844.

316. Brandes AA, Franceschi E, Paccapelo A, et al. Role of MGMT Methylation Status at Time of Diagnosis and Recurrence for Patients with Glioblastoma: Clinical Implications. *Oncologist*. 2017;22(4):432.

317. Zhou J, Reddy M V., Wilson BKJ, et al. MR Imaging Characteristics Associate with Tumor-Associated Macrophages in Glioblastoma and Provide an Improved Signature for Survival Prognostication. *Am J Neuroradiol*. 2018;39(2):252-259.

318. Wu G, Shi Z, Chen Y, et al. A sparse representation-based radiomics for outcome prediction of higher grade gliomas. *Med Phys*. 2019;46(1):250-261.

319. Tixier F, Um H, Bermudez D, et al. Preoperative MRI-radiomics features improve prediction of survival in glioblastoma patients over MGMT methylation status alone. *Oncotarget*. 2019;10(6):660-672.

320. Chaddad A, Sabri S, Niazi T, Abdulkarim B. Prediction of survival with multi-scale radiomic analysis in glioblastoma patients. *Med Biol Eng Comput*. 2018;56(12):2287-2300.

321. Sanghani P, Ang BT, King NKK, Ren H. Overall survival prediction in glioblastoma multiforme patients from volumetric, shape and texture features using machine learning. *Surg Oncol*. 2018;27(4):709-714.

322. Bae S, Choi YS, Ahn SS, et al. Radiomic MRI phenotyping of glioblastoma: Improving survival prediction. *Radiology*. 2018;289(3):797-806.

323. Lao J, Chen Y, Li ZC, et al. A Deep Learning-Based Radiomics Model for Prediction of Survival in Glioblastoma Multiforme. *Sci Rep*. 2017;7(1).

324. Davatzikos C, Rathore S, Bakas S, et al. Cancer imaging phenomics toolkit: quantitative imaging analytics for precision diagnostics and predictive modeling of clinical outcome. *J Med Imaging*. 2018;5(01):1.

325. Yushkevich PA, Piven J, Hazlett HC, et al. User-guided 3D active contour segmentation of anatomical structures: Significantly improved efficiency and reliability. *Neuroimage*. 2006;31(3):1116-1128.

326. wiki.cancerimagingarchive.net. VASARI Research Project - The Cancer Imaging Archive (TCIA) Public Access - Cancer Imaging Archive Wiki. Available at: https://wiki.cancerimagingarchive.net/display/Public/VASARI+Research+Project (Accessed 03-08-2021).

327. Rathore S, Akbari H, Rozycki M, et al. Radiomic MRI signature reveals three distinct subtypes of glioblastoma with different clinical and molecular characteristics, offering prognostic value beyond IDH1. *Sci Rep*. 2018;8(1):1-12.

328. Yan J, Zhang B, Zhang S, et al. Quantitative MRI-based radiomics for noninvasively predicting molecular subtypes and survival in glioma patients. *Precis Oncol*. 2021;5(1):1-9.

329. Andronesi OC, Rapalino O, Gerstner E, et al. Detection of oncogenic IDH1 mutations using magnetic resonance spectroscopy of 2-hydroxyglutarate. *J Clin Invest*. 2013;123(9):3659-3663.

330. Choi C, Ganji S, DeBerardinis RJ, et al. 2-hydroxyglutarate detection by magnetic resonance spectroscopy in IDH-mutated patients with gliomas. *Nat Med*. 2012;18(4):624-629.

331. Andronesi OC, Arrillaga-Romany IC, Ly KI, et al. Pharmacodynamics of mutant-IDH1 inhibitors in glioma patients probed by in vivo 3D MRS imaging of 2-hydroxyglutarate. *Nat Commun*. 2018;9(1):1-9.

332. Chang P, Grinband J, Weinberg BD, et al. Deep-learning convolutional neural networks accurately classify genetic mutations in gliomas. *Am J Neuroradiol*. 2018;39(7):1201-1207.

333. Sanghera P, Rampling R, Haylock B, et al. The Concepts, Diagnosis and Management of Early Imaging Changes after Therapy for Glioblastomas. *Clin Oncol*. 2012;24(3):216-227.

334. Brandsma D, Stalpers L, Taal W, Sminia P, van den Bent MJ. Clinical features, mechanisms, and management of pseudoprogression in malignant gliomas. *Lancet Oncol*. 2008;9(5):453-461.

335. Abbasi AW, Westerlaan HE, Holtman GA, Aden KM, van Laar PJ, van der Hoorn A. Incidence of Tumour Progression and Pseudoprogression in High-Grade Gliomas: a Systematic Review and Meta-Analysis. *Clin Neuroradiol*. 2018;28(3):401-411.

336. Brandes AA, Franceschi E, Tosoni A, et al. MGMT promoter methylation status can predict the incidence and outcome of pseudoprogression after concomitant radiochemotherapy in newly diagnosed glioblastoma patients. *J Clin Oncol*. 2008;26(13):2192-2197.

337. Taal W, Brandsma D, de Bruin HG, et al. Incidence of early pseudo-progression in a cohort of malignant glioma patients treated with chemoirradiation with temozolomide. *Cancer*. 2008;113(2):405-410.

338. Clarke JL, Iwamoto FM, Sul J, et al. Randomized phase II trial of chemoradiotherapy followed by either dose-dense or metronomic temozolomide for newly diagnosed glioblastoma. *J Clin Oncol*. 2009;27(23):3861-3867.

339. Chaskis C, Neyns B, Michotte A, De Ridder M, Everaert H. Pseudoprogression after radiotherapy with concurrent temozolomide for high-grade glioma: clinical observations and working recommendations. *Surg Neurol*. 2009;72(4):423-428.

340. Melguizo-Gavilanes I, Bruner JM, Guha-Thakurta N, Hess KR, Puduvalli VK. Characterization of pseudoprogression in patients with glioblastoma: is histology the gold standard? *J Neurooncol*. 2015;123(1):141-150.

341. Song YS, Choi SH, Park C-K, et al. True Progression versus Pseudoprogression in the Treatment of Glioblastomas: A Comparison Study of Normalized Cerebral Blood Volume and Apparent Diffusion Coefficient by Histogram Analysis. *Korean J Radiol*. 2013;14(4):662.

342. Prager AJ, Martinez N, Beal K, Omuro A, Zhang Z, Young RJ. Diffusion and Perfusion MRI to Differentiate Treatment-Related Changes Including Pseudoprogression from

Recurrent Tumors in High-Grade Gliomas with Histopathologic Evidence. *Am J Neuroradiol*. 2015;36(5):877-885.

343. Heidemans-Hazelaar C, Verbeek AY, Oosterkamp HM, Van der Kallen B, Vecht CJ. Use of perfusion MR imaging for differentiation between tumor progression and pseudo-progression in recurrent glioblastoma multiforme. *J Clin Oncol*. 2010;28(15_suppl):2026-2026.

344. Fink JR, Carr RB, Matsusue E, et al. Comparison of 3 Tesla proton MR spectroscopy, MR perfusion and MR diffusion for distinguishing glioma recurrence from posttreatment effects. *J Magn Reson Imaging*. 2012;35(1):56-63.

345. Rock JP, Hearshen D, Scarpace L, et al. Correlations between magnetic resonance spectroscopy and image-guided histopathology, with special attention to radiation necrosis. *Neurosurgery*. 2002;51(4):912-920.

346. Weybright P, Sundgren PC, Maly P, et al. Differentiation between brain tumor recurrence and radiation injury using MR spectroscopy. *Am J Roentgenol*. 2005;185(6):1471-1476.

347. Jain R, Scarpace LM, Ellika S, et al. Imaging response criteria for recurrent gliomas treated with bevacizumab: Role of diffusion weighted imaging as an imaging biomarker. *J Neurooncol*. 2010;96(3):423-431.

348. Kazda T, Bulik M, Pospisil P, et al. Advanced MRI increases the diagnostic accuracy of recurrent glioblastoma: Single institution thresholds and validation of MR spectroscopy and diffusion weighted MR imaging. *NeuroImage Clin*. 2016;11:316-321.

349. Bulik M, Kazda T, Slampa P, Jancalek R. The Diagnostic Ability of Follow-Up Imaging Biomarkers after Treatment of Glioblastoma in the Temozolomide Era: Implications from Proton MR Spectroscopy and Apparent Diffusion Coefficient Mapping. *Biomed Res Int*. 2015;2015(641023).

350. Alexiou GA, Zikou A, Tsiouris S, et al. Comparison of diffusion tensor, dynamic susceptibility contrast MRI and 99mTc-Tetrofosmin brain SPECT for the detection of recurrent high-grade glioma. *Magn Reson Imaging*. 2014;32(7):854-859.

351. Chu HH, Choi SH, Ryoo I, et al. Differentiation of true progression from pseudoprogression in glioblastoma treated with radiation therapy and concomitant temozolomide: Comparison study of standard and high-b-value diffusion-weighted imaging. *Radiology*. 2013;269(3):831-840.

352. Lee WJ, Choi SH, Park CK, et al. Diffusion-weighted MR Imaging for the Differentiation of True Progression from Pseudoprogression Following Concomitant Radiotherapy with Temozolomide in Patients with Newly Diagnosed High-grade Gliomas. *Acad Radiol*. 2012;19(11):1353-1361.

353. Hein PA, Eskey CJ, Dunn JF, Hug EB. Diffusion-Weighted Imaging in the Follow-up of Treated High-Grade Gliomas: Tumor Recurrence versus Radiation Injury. *Am J Neuroradiol*. 2004;25(2):201-209.

354. Zeng QS, Li CF, Liu H, Zhen JH, Feng DC. Distinction Between Recurrent Glioma and Radiation Injury Using Magnetic Resonance Spectroscopy in Combination With Diffusion-Weighted Imaging. *Int J Radiat Oncol*. 2007;68(1):151-158.

355. Sugahara T, Korogi Y, Tomiguchi S, et al. Posttherapeutic intraaxial brain tumor: the value of perfusion-sensitive contrast-enhanced MR imaging for differentiating tumor recurrence from nonneoplastic contrast-enhancing tissue. *Am J Neuroradiol*. 2000;21(5):901-909.

356. Hu LS, Baxter LC, Smith KA, et al. Relative Cerebral Blood Volume Values to Differentiate High-Grade Glioma Recurrence from Posttreatment Radiation Effect: Direct Correlation between Image-Guided Tissue Histopathology and Localized Dynamic Susceptibility-Weighted Contrast-Enhanced Perfusion MR Imaging Measurements. *Am J Neuroradiol*. 2009;30(3):552-558.

357. Xu JL, Li YL, Lian JM, et al. Distinction between postoperative recurrent glioma and radiation injury using MR diffusion tensor imaging. *Neuroradiology*. 2010;52(12):1193-1199.

358. Boxerman JL, Ellingson BM, Jeyapalan S, et al. Longitudinal DSC-MRI for distinguishing tumor recurrence from pseudoprogression in patients with a high-grade glioma. *Am J Clin Oncol Cancer Clin Trials*. 2017;40(3):228-234.

359. Wang S, Martinez-Lage M, Sakai Y, et al. Differentiating Tumor Progression from Pseudoprogression in Patients with Glioblastomas Using Diffusion Tensor Imaging and Dynamic Susceptibility Contrast MRI. *AJNR Am J Neuroradiol*. 2016;37(1):28-36.

360. D'Souza MM, Sharma R, Jaimini A, et al. 11C-MET PET/CT and advanced MRI in the evaluation of tumor recurrence in high-grade gliomas. *Clin Nucl Med*. 2014;39(9):791-798.

361. Seeger A, Braun C, Skardelly M, et al. Comparison of Three Different MR Perfusion Techniques and MR Spectroscopy for Multiparametric Assessment in Distinguishing Recurrent High-Grade Gliomas from Stable Disease. *Acad Radiol*. 2013;20(12):1557-1565.

362. Young RJ, Gupta A, Shah AD, et al. MRI perfusion in determining pseudoprogression in patients with glioblastoma. *Clin Imaging*. 2013;37(1):41-49.

363. Hu X, Wong KK, Young GS, Guo L, Wong ST. Support vector machine multiparametric MRI identification of pseudoprogression from tumor recurrence in patients with resected glioblastoma. *J Magn Reson Imaging*. 2011;33(2):296-305.

364. Barajas RF, Hamilton BE, Schwartz D, et al. Combined iron oxide nanoparticle ferumoxytol and gadolinium contrast enhanced MRI define glioblastoma pseudoprogression. *Neuro Oncol*. 2019;21(4):517-526.

365. Tsien C, Galbán CJ, Chenevert TL, et al. Parametric response map as an imaging biomarker to distinguish progression from pseudoprogression in high-grade glioma. *J Clin Oncol*. 2010;28(13):2293-2299.

366. Kong D-S, Kim ST, Kim E-H, et al. Diagnostic Dilemma of Pseudoprogression in the Treatment of Newly Diagnosed Glioblastomas: The Role of Assessing Relative Cerebral Blood Flow Volume and Oxygen-6-Methylguanine-DNA Methyltransferase Promoter Methylation Status. *Am J Neuroradiol*. 2011;32(2):382-387.

367. Sawlani V, Taylor R, Rowley K, Redfern R, Martin J, Poptani H. Magnetic resonance spectroscopy for differentiating pseudo-progression from true progression in GBM on concurrent chemoradiotherapy. *Neuroradiol J*. 2012;25(5):575-586.

368. Elias AE, Carlos RC, Smith EA, et al. MR Spectroscopy Using Normalized and Non-normalized Metabolite Ratios for Differentiating Recurrent Brain Tumor from Radiation Injury. *Acad Radiol*. 2011;18(9):1101-1108.

369. Smith EA, Carlos RC, Junck LR, Tsien CI, Elias A, Sundgren PC. Developing a Clinical Decision Model: MR Spectroscopy to Differentiate Between Recurrent Tumor and Radiation Change in Patients with New Contrast-Enhancing Lesions. *Am J Roentgenol*. 2009;192(2):W45-W52.

370. Plotkin M, Eisenacher J, Bruhn H, et al. 123I-IMT SPECT and 1H MR-spectroscopy at 3.0 T in the differential diagnosis of recurrent or residual gliomas: A comparative study. *J Neurooncol*. 2004;70(1):49-58.

371. Bobek-Billewicz B, Stasik-Pres G, Majchrzak H, Zarudzki Ł. Differentiation between brain tumor recurrence and radiation injury using perfusion, diffusion-weighted imaging and MR spectroscopy. *Folia Neuropathol Folia Neuropathol Folia Neuropathol*. 2010;48(482):81-92.

372. Fink J, Born D, Chamberlain MC. Pseudoprogression: Relevance with respect to treatment of high-grade gliomas. *Curr Treat Options Oncol*. 2011;12(3):240-252.

373. Cha J, Kim ST, Kim H-J, et al. Differentiation of Tumor Progression from Pseudoprogression in Patients with Posttreatment Glioblastoma Using Multiparametric Histogram Analysis. *Am J Neuroradiol*. 2014;35(7):1309-1317.

374. Hoffman WF, Levin VA, Wilson CB. Evaluation of malignant glioma patients during the postirradiation period. *J Neurosurg*. 1979;50(5):624-628.

375. Brandsma D, Van Den Bent MJ. Pseudoprogression and pseudoresponse in the treatment of gliomas. *Curr Opin Neurol*. 2009;22(6):633-638.

376. Linhares P, Carvalho B, Figueiredo R, Reis RM, Vaz R. Early pseudoprogression following chemoradiotherapy in glioblastoma patients: The value of RANO evaluation. *J Oncol*. 2013;2013:1-9.

377. Patel P, Baradaran H, Delgado D, et al. MR perfusion-weighted imaging in the evaluation of high-grade gliomas after treatment: A systematic review and meta-analysis. *Neuro Oncol*. 2017;19(1):118-127.

378. Hyare H, Thust S, Rees J. Advanced MRI Techniques in the Monitoring of Treatment of Gliomas. *Curr Treat Options Neurol*. 2017;19(3).

379. Song J, Kadaba P, Kravitz A, et al. Multiparametric MRI for early identification of therapeutic response in recurrent glioblastoma treated with immune checkpoint inhibitors. *Neuro Oncol*. 2020;22(11):1658-1666.

380. Park JE, Kim HS, Park SY, Jung SC, Kim JH, Heo H-Y. Identification of Early Response to Anti-Angiogenic Therapy in Recurrent Glioblastoma: Amide Proton Transfer–weighted and Perfusion-weighted MRI compared with Diffusion-weighted MRI. Radiology. 2020;295:(2):397-406.

381. Talati P, El-Abtah M, Kim D, et al. MR spectroscopic imaging predicts early response to anti-angiogenic therapy in recurrent glioblastoma. *Neuro-Oncology Adv*. 2021;3(1):1-10.

382. Zach L, Guez D, Last D, et al. Delayed contrast extravasation MRI: A new paradigm in neuro-oncology. *Neuro Oncol*. 2015;17(3):457-465.

383. Gahramanov S, Muldoon LL, Varallyay CG, et al. Pseudoprogression of glioblastoma after chemo- and radiation therapy: Diagnosis by using dynamic susceptibility-weighted contrast-enhanced perfusion MR imaging with ferumoxytol versus gadoteridol and correlation with survival. *Radiology*. 2013;266(3):842-852.

384. Ma B, Blakeley JO, Hong X, et al. Applying amide proton transfer-weighted MRI to distinguish pseudoprogression from true progression in malignant gliomas. *J Magn Reson Imaging*. 2016;44(2):456-462.

385. Albert NL, Weller M, Suchorska B, et al. Response Assessment in Neuro-Oncology working group and European Association for Neuro-Oncology recommendations for the clinical use of PET imaging in gliomas. *Neuro Oncol*. 2016;18(9):1199-1208.

386. Siakallis L, Sudre CH, Mulholland P, et al. Longitudinal structural and perfusion MRI enhanced by machine learning outperforms standalone modalities and radiological expertise in high-grade glioma surveillance. *Neuroradiology*. Published online May 28, 2021:1-10.

387. Booth TC, Akpinar B, Roman A, et al. Machine Learning and Glioblastoma: Treatment Response Monitoring Biomarkers in 2021. *Lect Notes Comput Sci*. 2020;12449 LNCS:212-228.

388. Kumar V, Gu Y, Basu S, et al. Radiomics: The process and the challenges. *Magn Reson Imaging*. 2012;30(9):1234-1248.

389. Chen X, Wei X, Zhang Z, Yang R, Zhu Y, Jiang X. Differentiation of true-progression from pseudoprogression in glioblastoma treated with radiation therapy and concomitant temozolomide by GLCM texture analysis of conventional MRI. *Clin Imaging*. 2015;39(5):775-780.

390. Ismail XM, Hill X V, Statsevych X V, et al. Shape features of the lesion habitat to differentiate brain tumor progression from pseudoprogression on routine multiparametric MRI: A multisite study. *Am J Neuroradiol*. 2018;39(12):2187-2193.

391. Kim J, Park JE, Jo Y, et al. Incorporating diffusion- and perfusion-weighted MRI into a radiomics model improves diagnostic performance for pseudoprogression in glioblastoma patients. *Neuro Oncol*. 2018;21(August):1-29.

392. Elshafeey N, Kotrotsou A, Hassan A, et al. Multicenter study demonstrates radiomic features derived from magnetic resonance perfusion images identify pseudoprogression in glioblastoma. *Nat Commun*. 2019;10(1):1-9.

393. Parekh VS, Laterra J, Bettegowda C, Bocchieri AE, Pillai JJ, Jacobs MA. Multiparametric Deep Learning and Radiomics for Tumor Grading and Treatment Response Assessment of Brain Cancer: Preliminary Results. Published online June 10, 2019. Available at: http://arxiv.org/abs/1906.04049 (Accessed 17-06-2020).

394. Kassner A, Thornhill RE. Texture Analysis: A Review of Neurologic MR Imaging Applications. *Am J Neuroradiol*. 2010;31(5):809-816.

395. Sala E, Mema E, Himoto Y, et al. Unravelling tumour heterogeneity using next-generation imaging: radiomics, radiogenomics, and habitat imaging. *Clin Radiol*. 2017;72(1):3-10.

396. Hopewell JW, Calvo W, Jaenke R, Reinhold HS, Robbins ME, Whitehouse EM. Microvasculature and radiation damage. In: *Recent Results in Cancer Research. Fortschritte Der Krebsforschung. Progrès Dans Les Recherches Sur Le Cancer*. Vol 130. Springer, Berlin, Heidelberg; 1993:1-16.

397. Chamberlain MC. Radiographic patterns of relapse in glioblastoma. *J Neurooncol*. 2011;101(2):319-323.

398. Mouraviev A, Detsky J, Sahgal A, et al. Use of radiomics for the prediction of local control of brain metastases after stereotactic radiosurgery. *Neuro Oncol*. 2020;22(6):797-805.

399. Ellingson BM, Wen PY, Cloughesy TF. Modified Criteria for Radiographic Response Assessment in Glioblastoma Clinical Trials. *Neurotherapeutics*. 2017;14(2):307-320.

400. Visser M, Müller DMJ, van Duijn RJM, et al. Inter-rater agreement in glioma segmentations on longitudinal MRI. *NeuroImage Clin*. 2019;22:101727.

401. Meier R, Knecht U, Loosli T, et al. Clinical Evaluation of a Fully-automatic Segmentation Method for Longitudinal Brain Tumor Volumetry. *Sci Rep*. 2016;6(1):1-11.

402. Varghese BA, Hwang D, Cen SY, et al. Reliability of CT-based texture features: Phantom study. *J Appl Clin Med Phys*. 2019;20(8):155-163.

403. Peeken JC, Hesse J, Haller B, Kessel KA, Nüsslin F, Combs SE. Semantic imaging features predict disease progression and survival in glioblastoma multiforme patients. *Strahlentherapie und Onkol*. 2018;194(6):580-590.

404. Yekula A, Muralidharan K, Rosh ZS, et al. Liquid Biopsy Strategies to Distinguish Progression from Pseudoprogression and Radiation Necrosis in Glioblastomas. *Adv Biosyst*. 2020;4(12):2000029.

405. Fornacon-Wood I, Mistry H, Ackermann CJ, et al. Reliability and prognostic value of radiomic features are highly dependent on choice of feature extraction platform. *Eur Radiol*. 2020;30(11):6241-6250.